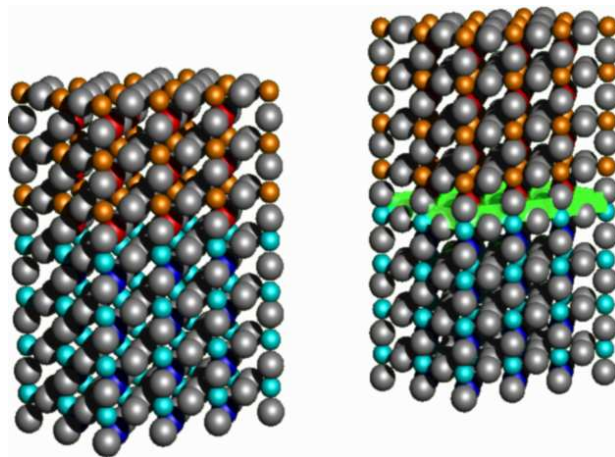


Study of Interface Properties in $\text{LaAlO}_3/\text{SrTiO}_3$ Heterostructures

Dissertation
zur Erlangung des Doktorgrades
der mathematisch-naturwissenschaftlichen Fakultät
der Universität Augsburg



vorgelegt von
Stefan Patrick Thiel

Augsburg, Januar 2009

Tag der mündlichen Prüfung: 19.2.2009

Erstgutachter:	Prof. Dr. Jochen Mannhart (Universität Augsburg)
Zweitgutachter:	Prof. Dr. Armin Reller (Universität Augsburg)
Drittgutachter:	Prof. Jean-Marc Triscone (Université de Genève)

Often, it may be said that the interface is the device.

H. Kroemer. *Review of Modern Physics*, **73**, 783 – 793, 2001

Contents

1	Introduction	1
2	Materials	5
2.1	Perovskites	5
2.2	SrTiO ₃	6
2.3	LaAlO ₃	8
2.4	LaAlO ₃ /SrTiO ₃ Interface	8
2.5	Summary	11
3	Experimental Methods	12
3.1	Substrate Preparation	12
3.2	Film Deposition by PLD	15
3.3	Film Growth	18
3.4	Growth Monitoring by RHEED	19
3.5	Film Characterization	24
3.6	Electronic Transport Measurements	32
3.7	Summary	34
4	Electronic Transport Properties of the LaAlO₃/SrTiO₃ Interface	35
4.1	Thickness Dependence of the Electronic Properties	40
4.2	Discussion of the Role of Oxygen Vacancies	44
4.3	Summary	48
5	Electric Field Effect Experiments	50
5.1	Electric Field Effect	50
5.2	Field Effect at <i>n</i> -Type LaAlO ₃ /SrTiO ₃ Interfaces	51
5.3	Field Effect Using a Top Gate Contact	62
5.4	High-Resolution Patterning Technique Using a Scanning Probe	64
5.5	Field Effect at <i>p</i> -Type LaAlO ₃ /SrTiO ₃ Interfaces	68
5.6	Summary	68
6	Development of a Technique to Pattern the Electron Gas at LaAlO₃/SrTiO₃ Interfaces	70
6.1	Preparation and Characterization of Patterned LaAlO ₃ /SrTiO ₃ Samples	70
6.2	Electronic Transport Properties of Patterned LaAlO ₃ /SrTiO ₃ Samples	74
6.3	Investigation of Other Patterning Techniques	77
6.4	Summary	78
7	Interface Superconductivity	79
7.1	Low Temperature Measurements of LaAlO ₃ /SrTiO ₃ Heterostructures	79
7.2	Berezinskii-Kosterlitz-Thouless Transition	84
7.3	Estimation of Superconducting Layer Thickness	87
7.4	Transport Properties and Ground State of LaAlO ₃ /SrTiO ₃ Samples Grown at High Oxygen Pressure	89
7.5	Summary	93

8	Electron Scattering at Dislocations	95
8.1	Grain Boundary Sample Preparation and Characterization	95
8.2	Transport Properties of the Grain Boundary Samples	101
8.3	Dislocations in SrTiO ₃ Substrates	105
8.4	Transport Properties of Samples with High Dislocation Density	108
8.5	Scattering at Dislocations	109
8.6	Summary	111
9	Summary and Outlook	113
	References	119
	Appendix A: List of Publications	129
	Appendix B: Ongoing Projects	131
	Appendix C: Danksagung	133
	Appendix D: Curriculum Vitae	135

1 Introduction

“Often, it may be said that the interface is the device.” [1] This quote from Nobel laureate H. Kroemer emphasizes that in many devices it is not the bulk properties of a material that generate the functionality, but rather the physics at the interfaces, where different materials meet. As we will see this is particularly true for the $\text{LaAlO}_3/\text{SrTiO}_3$ system studied in this thesis.

Devices the functionality of which is based on interface effects are common in everyday life. Modern electronics for example is not possible without semiconductor heterostructures. The semiconductor materials currently in use have been studied extensively over the last decades, yet their real success and incorporation in devices is not due to their bulk characteristics, which are rather simple. It is in the transport of charge carriers across or along interfaces between different materials or between semiconductors differing in doping level where the device functionality appears. Schottky contacts, p - n junctions, the interface between Si and SiO_2 , and various types of transistors are just a few examples of utilized heterostructures. The designs of devices became more and more sophisticated and by now complex structures are indispensable in modern electronics and are produced in huge amounts. For example, in 2007, the number of transistors fabricated amounted to 10^{19} . This success was triggered by big advancements in the preparation and growth of well defined semiconductor heterostructures. Nowadays modulation doping allows to tailor bandstructures and thus to generate special electronic systems, like the routinely used two-dimensional electron gases at interfaces.

The miniaturization to the nanoscale requires a deep understanding of the effects of surfaces and interfaces. But what is so special about them? At surfaces and interfaces the bulk electronic system can be altered due to many reasons. First of all the translational symmetry is broken, and if present also a rotational symmetry. Moreover the crystal lattice can be reconstructed, and atomic positions might be changed. This can directly affect crystal fields, lattice constants, and bonds between ions. Additionally point defects, dislocations, and stacking faults tend to be incorporated into the lattice at interfaces. Furthermore, the chemical composition at surfaces and interfaces can differ from that of the bulk. All this can modify bands at the interface and shift electronic states. Utilizing combinations of these interface effects therefore allows to design the transport properties of semiconductor heterostructures. This is what made them so successful.

All these effects may already occur at materials in which the electron system of the bulk is simply described by single particle physics with negligible interactions between charge carriers.

In the last decades another class of materials came into the focus of research: the oxides. In contrast to semiconductors these materials often have strongly correlated electrons and exhibit already in bulk a wealth of different intrinsic functionalities, like (anti)ferromagnetism, (anti)ferroelectricity, piezoelectricity, multiferroicity and superconductivity [2]. These properties are used in many different sensors and devices.

Additionally, the correlations can be strongly influenced, for example by doping the materials or by changing external parameters such as temperature or pressure. In this way the properties of oxide materials can be tuned to specific needs. This versatility

shows the potential lying in the utilization of bulk properties of oxides. The focus of this thesis is, however, on the physics of interfaces between different compounds.

What is so promising about them? In oxides, not only all the modifications at interfaces mentioned earlier in the context of semiconductors are possible, but also the interaction strengths are affected at surfaces or interfaces. As these correlations often govern the properties of the materials their modification can induce large functional changes.

Therefore it was soon realized that building heterostructures from correlated oxides can be even more interesting than solely exploiting their bulk properties. The as compared to semiconductors amazingly rich variety of properties present in oxides allows a vast number of combinations of different materials with different functionalities. As even structures made from semiconductor materials exhibiting comparably simple bulk properties can show fascinating effects like the quantum Hall effect (QHE) it is easy to see why the field of oxide electronics has attracted a lot of interest [3]. Therefore oxide surfaces, interfaces, and heterostructures have been intensely investigated [4], which has widened the understanding of oxide materials and shown their versatility.

Experimentally it turned out that the quality of the interfaces strongly influences their physical properties. Over the years the two main deposition techniques for oxides, Molecular Beam Epitaxy (MBE) and Pulsed Laser Deposition (PLD), have been improved to such an extent that today heterostructures can be grown with the same quality and precision on the atomic level previously achieved only in semiconductor multilayers. Consequently the field of oxide electronics is growing rapidly [5].

The possibility to control oxide film growth on the unit cell (uc) level opened an exciting new route for designing materials [6]. It enables the use of different oxide materials as building blocks in heterostructures with well defined interfaces. Such samples allowed to explore whether low dimensional electron systems, which are present in many semiconductor heterostructures, can also be generated at oxide interfaces, or, even more importantly, whether completely new effects arise at oxide interfaces.

During the last few years several groups reported experiments in which specific properties of oxide materials were improved by putting them adjacent to other building blocks in oxide heterostructures. For example in $\text{BaTiO}_3/\text{SrTiO}_3/\text{CaTiO}_3$ superlattices an enhanced ferroelectric polarization is found as compared to pure BaTiO_3 , which is caused by the inversion symmetry being broken in the heterostructure [7].

Building multilayers is not only possible to improve known properties of materials but also to generate completely new physical properties in multilayers, which are not found in the bulk of the constituting materials. In the past few years this phenomenon appeared in several spectacular examples. For instance, BaCuO_2 and SrCuO_2 are both non-superconducting, but a superlattice consisting of thin layers of both materials superconducts [8]. Neither SrZrO_3 nor SrTiO_3 are ferroelectric, but a superlattice of both is [9]. While CaMnO_3 is antiferromagnetic and CaRuO_3 is paramagnetic the interface between both is ferromagnetic [10]. A multilayer of the band insulator SrTiO_3 and the Mott-insulator LaTiO_3 shows metallic behavior [11]. Just a year ago a $\text{ZnO}/\text{Mg}_x\text{Zn}_{1-x}\text{O}$ heterostructure was found to display the QHE in its two-dimensional electron system [12].

These examples show that oxide heterostructures are a very active field of research. The burst of discoveries and startling results of oxide interfaces were even termed one of

the breakthroughs of the year by the Science magazine at the end of 2007.

In 2004 A. Ohtomo and H.Y. Hwang at Bell Laboratories were the first to observe the surprising properties of the $\text{LaAlO}_3/\text{SrTiO}_3$ heterostructure which was studied in this thesis. Both materials are band insulators, yet a conducting interface can be formed between them [13], depending on the precise atomic stacking.

Their discovery, only a short time before the beginning of this thesis, showed the importance of interface effects in this system. As the bulk properties of both building blocks, which are normal band insulators, are well known and investigated we decided to take LaAlO_3 films on SrTiO_3 substrates as a model system to study the effects of interface physics on electronic properties and gain a deeper understanding of the important mechanisms. It is noted here that although the used bulk oxide materials are not controlled by electron correlations, these might nevertheless play an important role, as right at the interface one unit cell of LaTiO_3 is formed, which is a correlated material.

Until the start of this thesis in 2005 only very few was known about this remarkable system and just two publications reported on $\text{LaAlO}_3/\text{SrTiO}_3$ samples [13,14]. The measured electronic transport properties still varied a lot and interpretation of the data was difficult. By now it has evolved into one of the most intensively studied interfaces in the field of oxide heterostructures.

Outline of the Thesis

Chapter 2 will start with a brief introduction to the two materials SrTiO_3 and LaAlO_3 , which are the building blocks of the studied heterostructure. Then the possible interfaces between both materials are discussed, which is crucial for the complete work. We will see that, as already stated in the first publication on this system, the observed conductivity between the two band-insulators can be explained by electronic reconstructions caused by a polarity discontinuity. All this information summarizes the state of knowledge about the $\text{LaAlO}_3/\text{SrTiO}_3$ interface at the beginning of this thesis.

The first goal was then to grow heterostructures of LaAlO_3 and SrTiO_3 with growth control down to the unit cell level in our laboratory, which before had not been done in our group. At the very beginning the idea was to study superlattices containing many $\text{LaAlO}_3/\text{SrTiO}_3$ interfaces, but soon it turned out that even the single interface shows amazing effects deserving a closer investigation, so all of the research of this thesis was devoted to the study of thin films of LaAlO_3 on SrTiO_3 substrates. Chapter 3 presents the applied experimental methods for fabricating the samples, which includes the termination procedures for substrate surfaces, film growth by Pulsed Laser Deposition, and growth monitoring by Reflection High Energy Electron Diffraction. Additionally the sample characterization by Atomic Force Microscopy, X-Ray Diffraction, and (Scanning) Transmission Electron Microscopy is covered. These experiments confirm the successful preparation of atomically sharp interfaces between substrates and films with a defined thickness of few unit cells. The chapter closes by describing the contact method that was developed to access the conducting layer, which is buried underneath the LaAlO_3 film.

Having the well defined heterostructures at hand, the rest of this thesis deals with the investigation of the electronic properties at the interface.

After reporting the sheet resistances and charge carrier densities in our samples, Chapter 4 will compare the data to previous reports and will emphasize the importance of using correct deposition conditions. One section will especially comment on a possible influence of oxygen vacancies in the substrate on the observed electronic properties, which is a scenario that has been discussed for years.

Upon studying the generation of the electron gas at the interface as a function of LaAlO₃ film thickness a remarkable change from insulating to conducting behavior is observed as the number of LaAlO₃ unit cells is increased from 3 to 4¹. This transition will be used in the rest of this thesis extensively.

The quasi two-dimensionality and the low charge carrier density of the conducting interface were promising for electric field effect experiments, which are described in Chapter 5. We will see that in a field-effect transistor geometry the conductivity of the LaAlO₃/SrTiO₃ interface can be tuned to a large extent. For insulating samples with 3 uc of LaAlO₃ it is even possible to induce an electric field driven transition to a conducting interface. Additionally this transition displays a pronounced memory behavior at room temperature.

The chapter closes by describing experiments where the metal-insulator transition is induced on the nanometer scale using a conducting AFM tip as gate electrode.

Initially it was only possible to study unpatterned samples in the experiments. A patterning technique for the electron gas at the interface developed within this work opened up new possibilities. As presented in Chapter 6 it is based on variation of the thickness of the epitaxial LaAlO₃ film. This patterning process was a prerequisite for most of the experiments covered in Chapter 7 and 8.

Chapter 7 describes the studies of the ground state of the LaAlO₃/SrTiO₃ interface, which has been unresolved yet. In our samples superconductivity is found for the first time at the LaAlO₃/SrTiO₃ interface. The measured critical temperature is $T_c \approx 200$ mK.

The last chapter reports on experimental investigations of the effects of microstructural defects and disorder on the electronic interface properties. It is found that the electron gas is strongly influenced by scattering at dislocations.

After summarizing the results an outlook will be given on the perspectives of oxide interfaces and electronics and on experiments or studies that potentially are necessary in the future development of the field.

¹An artistic sketch of that tremendous effect of one additional unit cell is shown on the cover of this thesis, with the electron gas generated at the interface shown in green.

2 Materials

For the investigation and identification of interface effects in heterostructures it is important to know the bulk properties of the constituting materials. Therefore this starting chapter of the thesis deals with the main oxides used in the experiments, discussing in particular their structural and electronic properties. After a brief introduction to perovskites, the two components from which heterostructures were fabricated, SrTiO₃ and LaAlO₃, are presented in detail. Both materials are well investigated band insulators. Finally the LaAlO₃/SrTiO₃ interface is described, which is found to be conducting. Then the polarity discontinuity model is described, which is the most widely used model to explain the observed conductivity in this heterostructure composed of band insulators.

As already mentioned in the introduction, transition metal oxides have attracted great attention in solid state physics in the past, in many cases due to the electronic correlations which often govern their properties. Among these oxides the perovskites have shown to be exceptionally versatile. Also the main materials used as building blocks for our samples belong to these materials, which are described next.

2.1 Perovskites

Perovskites have the general formula ABX_3 , where A stands for a large cation, B for a small cation, and X for an anion that bonds to both A and B . The anion X is usually oxygen or a halogen (in the following X will always be oxygen and is thus replaced by O). The chemical diversity of perovskites is enormous. The degree of freedom lies in the choice of elements on the A or B positions, the stabilization of vacancies, and the variation of the oxygen stoichiometry [15]. ABO_3 compounds can condense in a large diversity of crystal structures. Among others, cubic, orthorhombic, tetragonal, rhombohedral, and monoclinic structures occur. Additionally, structural phase transitions are often observed as a function of external parameters like temperature or pressure. This even increases the variety of physical and chemical properties. Perovskites can show, amongst others, insulating, semiconducting, metallic, superconducting, magnetic, piezoelectric, ferroelectric, and multiferroic behavior.

The cubic perovskite structure is shown in Fig. 2.1a. The unit cell drawn contains B ions at the corners, an A ion in the center, and O ions in the middle of the cube edges. As depicted in Fig. 2.1b the structure can be described as a network of corner-sharing BO_6 octahedra.

For this work the most instructive description of the perovskite structure is the one shown in Fig. 2.1c. Along the $\langle 001 \rangle$ direction a perovskite can be seen as a stacking of alternating AO and BO_2 layers. This view of the ABO_3 structure will be referred to later in this chapter when the LaAlO₃/SrTiO₃ interface is presented.

Both compounds of the studied heterostructure, SrTiO₃ and LaAlO₃ which are presented next, belong to the class of perovskites.

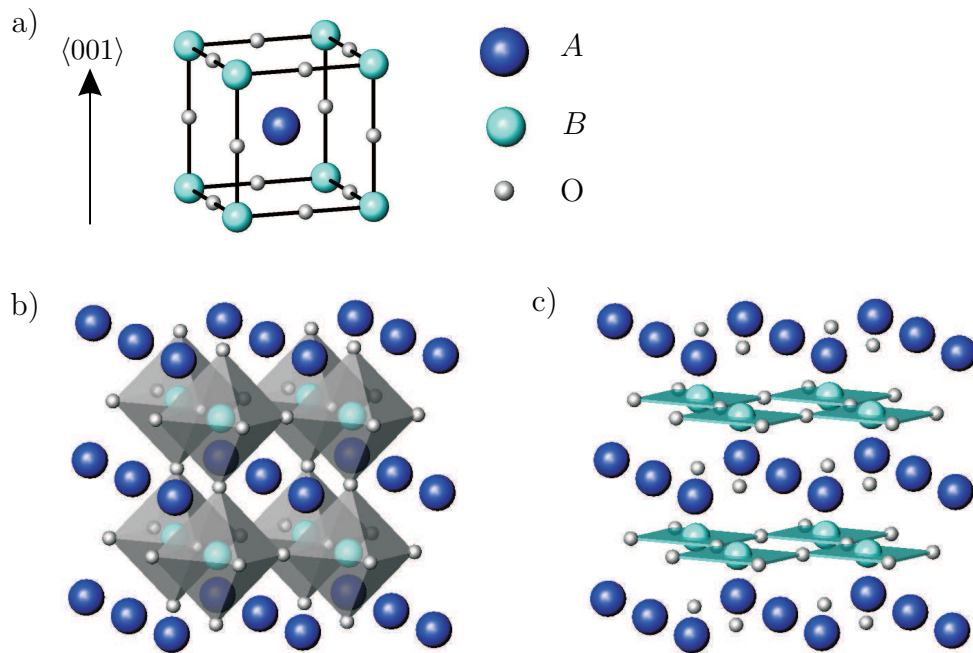


Figure 2.1: Schematic sketch of the perovskite ABO_3 structure. **a**, The cubic unit cell has B ions at the corners, an A ion in the center, and O ions in the middle of its edges. **b**, Perovskite structure with the BO_6 octahedra network highlighted. **c**, The ABO_3 compounds can also be viewed as a layered sequence of AO and BO_2 . This is the most instructive description for this thesis.

2.2 $SrTiO_3$

$SrTiO_3$ has been thoroughly investigated during the past decades. One reason for this scientific interest is that $SrTiO_3$ plays an important role as a standard substrate for many oxide materials. For example, it is possible to grow high- T_c superconductors [16], colossal magnetoresistance oxides or ferroelectrics epitaxially on $SrTiO_3$ due to the similarities in structure and lattice constant. Additionally $SrTiO_3$ is chemically inert. In many cases it does not react with the deposited materials. Also in this thesis it has been used as the standard substrate.

$SrTiO_3$ is cubic at room temperature (space group $Pm\bar{3}m$) with a lattice constant of 3.905 \AA . The TiO_6 octahedra have perfect 90° angles. At about 105 K neighboring TiO_6 octahedra are slightly rotated in opposite directions and $SrTiO_3$ is tetragonal (space group $I4/mcm$) [17] at lower temperatures.

Stoichiometric $SrTiO_3$ has a relatively large, indirect band gap of 3.25 eV . Therefore it can be viewed either as a band-insulator or a semiconductor. $SrTiO_3$ can be doped, even into a metallic state, by introducing oxygen vacancies [18, 19]. In samples doped to charge carrier densities of $10^{19} - 10^{21} \text{ cm}^{-3}$ even superconductivity was observed [20–22] with critical temperatures $< 300 \text{ mK}$. The concentration of oxygen vacancies can be carefully controlled in single crystals [23] and even in thin films. In the latter, doping profiles of $SrTiO_3$ with subnanometer abruptness have been prepared [24].

Experimentally, an oxygen deficiency in SrTiO_3 single crystals can easily be generated by heating to more than $\approx 800^\circ\text{C}$ in low oxygen pressures $\leq 10^{-6}$ mbar. Ar-ion etching also generates oxygen vacancies, and thus conductivity, in the exposed SrTiO_3 (see Fig. 2.2). This is an important point to consider when preparing samples which contain SrTiO_3 .

Metallic SrTiO_3 is formed not only if oxygen vacancies are present, but also forms upon substituting small amounts of La for Sr, or Nb for Ti, or other similar substitutions [19]. Unless otherwise stated in this work undoped, nominally fully oxidized SrTiO_3 is used.

Optically, SrTiO_3 single crystals are transparent with a slight yellowish hue, which sometimes is completely absent due to brightening dopants, which are introduced by the supplier on the ppm level for the use as an artificial gemstone. After a treatment in typical growth conditions (see Sec. 3.2) initially transparent, uncolored SrTiO_3 substrates often show a slight color hue. However these substrates are always found to be completely insulating. Therefore it is concluded that the color change is not due to an oxygen deficiency in SrTiO_3 , which would render the SrTiO_3 conducting, but rather caused by a change of the color centers induced by the brightening dopants.

Small concentrations of oxygen vacancies cause a greyish color in the substrate. When heavily doped, SrTiO_3 crystals are opaque with a black color.

SrTiO_3 has exceptional dielectric properties. It is an incipient ferroelectric [25], and remains paraelectric for $T \rightarrow 0$ K. The dielectric constant increases with decreasing temperature. Values from several hundred at 300 K to up to 25000 at 4 K in bulk samples [26–28] and up to 4000 in thin films [29, 30] have been reported. At low temperatures a strong reduction of the dielectric constant is found upon application of electric fields [31]. By the application of stress SrTiO_3 can be driven into a ferroelectric state [32].

Its high dielectric constant makes SrTiO_3 a good candidate as gate dielectric in field effect setups, which has been utilized in this work (see Chapter 5).

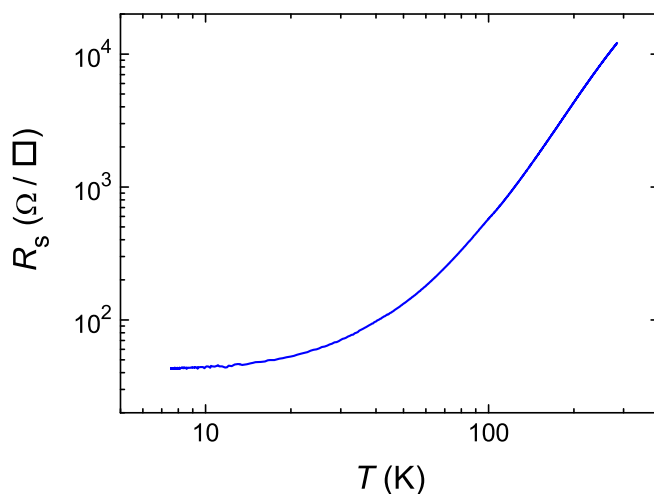


Figure 2.2: Sheet resistance as a function of temperature of a SrTiO_3 substrate after a standard Ar-ion etching process (acceleration voltage 500 V, beam current 10 mA, etching time 3 min). For this measurement a current of $10\ \mu\text{A}$ was used.

2.3 LaAlO₃

LaAlO₃ is the second building block of the studied heterostructure. Just like SrTiO₃ it has a good lattice matching with many oxide materials and because of this was also thoroughly studied as substrate material [33]. In LaAlO₃ single crystal substrates twinning domains (orthogonal twin planes along $\langle 100 \rangle$) are present. The twinning results in a roof- and valley-like buckling of the crystal surface at the twin-boundaries. This LaAlO₃ surface is ill defined compared to the untwinned SrTiO₃ substrate surface. Therefore LaAlO₃ was used in this thesis only as thin film on SrTiO₃ substrates.

At high temperatures LaAlO₃ has the cubic perovskite structure (space group $Pm\bar{3}m$). At ≈ 813 K it undergoes a transition to a rhombohedrally distorted perovskite structure (space group $R\bar{3}c$) [34]. In this work LaAlO₃ is always in the lower temperature range, where the structure differs from the cubic perovskite only by small antiphase rotations of AlO₆ octahedra. It can be described as pseudocubic with a lattice constant of 3.791 Å [35]. The reasonably small lattice mismatch of 3% to SrTiO₃ and the similarity of the thermal expansion coefficients [36, 37] allow the epitaxial growth of LaAlO₃ films on SrTiO₃.

Optically, LaAlO₃ single crystals are yellowish transparent. Twin boundaries are clearly visible. LaAlO₃ is a band insulator with a wide gap of 5.6 eV. Like SrTiO₃ it belongs to the high κ oxides, having a dielectric constant of about 25 for temperatures between 300 K and 4 K [33, 38]. The relatively high value of κ was utilized in this thesis in field effect devices with LaAlO₃ as the gate dielectric (see Sec. 5.3).

2.4 LaAlO₃/SrTiO₃ Interface

As presented before, the bulk properties of both SrTiO₃ and LaAlO₃ the building blocks of the heterostructure, are well known. This section will now introduce the LaAlO₃/SrTiO₃ interface system. The investigation of the observed new effects and properties of the LaAlO₃/SrTiO₃ heterostructure, which are not found in the bulk properties of the constituting materials, is the central topic of this work.

The report which triggered the studies of this thesis was published in 2004 by A. Ohtomo and H.Y. Hwang from Bell Labs (USA). They analyzed the interface between LaAlO₃ and SrTiO₃ [13]. Two different stackings were prepared by Pulsed Laser Deposition (PLD) on (001) oriented SrTiO₃ substrates. For this orientation ABO_3 perovskites can be described as being composed of alternating AO and BO_2 layers (see Fig. 2.1). An illustrative sketch of both configurations is shown in Fig. 2.3.

In the first configuration, LaAlO₃ is grown epitaxially on a (001) oriented SrTiO₃ substrate, terminated by a TiO₂ layer. For the second configuration an additional monolayer of SrO is inserted before growing the LaAlO₃. These procedures result in a TiO₂/LaO and a SrO/AlO₂ stacking, respectively, at the interface. The surprising result of electronic transport measurements of these samples was, that one setup (TiO₂/LaO stacking) was highly conducting at the interface, while the other sequence (SrO/AlO₂ stacking) was found to be insulating. This is definitely worth a deeper investigation for two reasons. First, one stacking sequence results in a well conducting interface, although the sample is entirely composed of band insulators. Second, depending on the stacking sequence at

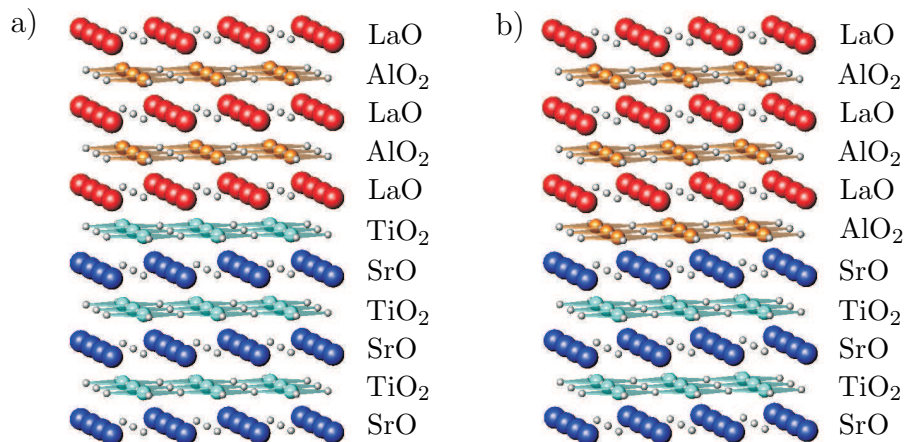


Figure 2.3: Illustration of the two possible stackings for atomically abrupt interfaces between LaAlO₃ and SrTiO₃ in the (001) orientation. Color legend: La (red), Al (orange), Sr (blue), Ti (cyan), O (grey). **a**, The LaAlO₃ films starts with a layer of LaO on the final TiO₂ layer of SrTiO₃. **b**, The LaAlO₃ films starts with a layer of AlO₂ on the last SrO layer of SrTiO₃.

the interface, the electronic properties of the heterostructure differ from conducting to insulating. It is remarkable that the insertion of one atomic layer of SrO during sample growth leads to such a tremendous difference.

To explain the special situation at the interface, which causes the conductivity, one first has to look at the two building blocks LaAlO₃ and SrTiO₃ separately. A difference is given by the stacking sequence of both materials and their formal valence states (Sr²⁺, Ti⁴⁺, La³⁺, Al³⁺, O²⁻). While SrTiO₃ is composed of alternating layers of (SrO)⁰ and (TiO₂)⁰, which are charge neutral, LaAlO₃ has alternating sheets of (LaO)⁺ and (AlO₂)⁻, which have a non-zero net charge.

The LaAlO₃/SrTiO₃ interface is special as here charge neutral layers and charged layers adjoin. As can be deduced from Fig. 2.4, and will be discussed in the following paragraphs, this is an unfavorable situation. The consequences of such a sequencing were first discussed by G.A. Baraff *et al.* [39] and W.A. Harrison *et al.* [40] in the 1980s for semiconductor Ge/GaAs heterojunctions.

Let us first apply the argumentation of Baraff *et al.* and Harrison *et al.* to the heterostructure with a TiO₂/LaO stacking sequence at the interface (Fig. 2.4a). The charged sublayers produce an electric field E , which leads to an electric potential V that diverges with the thickness of the LaAlO₃ film. For semiconductor heterostructures with charge neutral sheets followed by charged sheets it was shown that the system can avoid this so called polar catastrophe (or polarity discontinuity) by redistributing the atoms at the interface, which causes roughening of the interface. An analogous argumentation explains why crystals with polar planes need to have atomic reconstructions at their surface. Conventional semiconductor ions have a fixed valence, so a spatial redistribution of ions, which leads to a roughening of the interface, is their only option to avoid the divergence of the electrostatic potential. But the complex oxides, like LaAlO₃ and SrTiO₃, have an additional option. The mixed valence states available allow for a charge compensation by moving electrons, which happens if it is energetically favorable compared to a redistribu-

tion of ions [41]. The effect of rearranging the electron distribution is shown in Fig. 2.4b. Illustratively, one can construct the system from neutral atoms and then transfer half an electron from the LaO layers to those above and below. During this reconstruction the total structure remains charge neutral, only the Ti at the interface becomes $\text{Ti}^{3.5+}$. This redistribution eliminates the divergence of the electrostatic potential V . The resulting V oscillates around a finite value.

The induced additional half electron at the TiO_2/LaO interface results in n -type conductivity, which was indeed observed experimentally. In the following the interface with this stacking sequence will thus be termed n -type. It is due to electronic reconstructions that metallic behavior appears at the interface.

Figures 2.4c and d show that the same argumentation predicts a p -type conductivity for the SrO/AlO_2 interface (termed p -type interface in the following). Experimentally such $\text{LaAlO}_3/\text{SrTiO}_3$ heterostructures were found to be insulating, however ² [13, 14].

This admittedly simple model provides a good explanation on how electronic reconstructions can lead to a metallic interface in the $\text{LaAlO}_3/\text{SrTiO}_3$ heterostructure. However it seems to be oversimplified, as, e.g., the insulating behavior of the p -type interface observed experimentally is not captured in this approach. More sophisticated models and

²It is noted here that the term “insulating” is used throughout this thesis to characterize resistances that exceed the measurement limit ($10^9 \Omega$) of the used setup, and not, as is usually done, to describe resistances that increase with decreasing temperature.

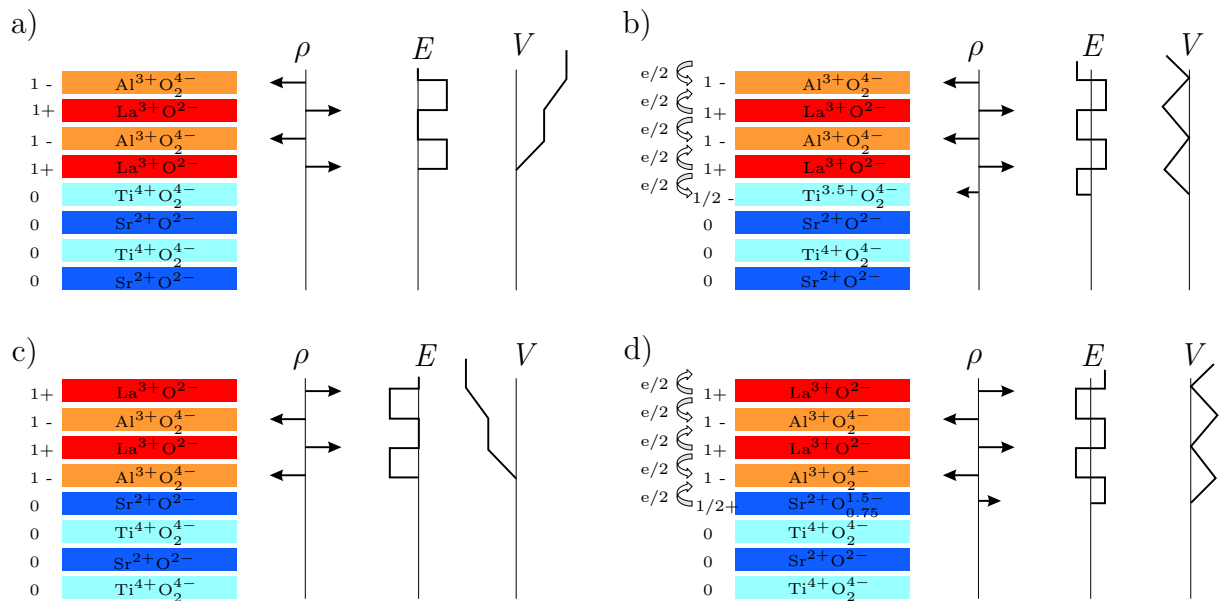


Figure 2.4: Illustration of the polar catastrophe occurring between LaAlO_3 and SrTiO_3 . Superscripts denote the oxidation numbers for the different elements. In the diagrams ρ is the net charge of the layers, which leads to the electric field E , that produces the electric potential V . **a**, The unreconstructed n -type interface (TiO_2/LaO stacking) leads to a diverging potential V due to the polarity discontinuity. **b**, If electrons are redistributed such that half an electron enters into the last TiO_2 plane the potential stays finite. **c**, The potential of the unreconstructed p -type interface (SrO/AlO_2 stacking) diverges negatively. **d**, Removal of half an electron from the SrO plane can avoid this divergence (adopted from Ref. [41]).

calculations are needed.

During the past few years interfaces between different, in some cases even correlated systems have been theoretically studied, e.g. $\text{LaTiO}_3/\text{SrTiO}_3$ heterostructures [42, 43]. Materials that are governed by correlations offer of course a large potential for fundamental physics, due to their susceptibility to all kinds of perturbations. The focus of the calculations was therefore directed on that field. From this point of view SrTiO_3 as well as LaAlO_3 are not of particular interest, because correlation effects can be neglected, and both are well described as rather simple band insulators. At the $\text{LaAlO}_3/\text{SrTiO}_3$ interface, however, the stacking of LaO on top of TiO_2 equals a unit cell of LaTiO_3 , which is a correlated material. Stoichiometric LaTiO_3 is a Mott-insulator with semiconducting transport properties [44, 45]. The presence of one unit cell of LaTiO_3 at the interface might bring correlation effects into the transport properties of $\text{LaAlO}_3/\text{SrTiO}_3$ heterostructures.

Theoretical studies of $\text{LaAlO}_3/\text{SrTiO}_3$ heterostructures were conducted by several groups, see, e.g., [46–52], perhaps motivated by the results described in this thesis. The calculations mainly used Density Functional Theory (DFT) in the Local Density Approximation (LDA), partly extended to LDA+U. Due to computational limitations rather thin stacks of about 2–4 uc of LaAlO_3 on 2–4 uc of SrTiO_3 were used as the repeating unit of the investigated $\text{LaAlO}_3/\text{SrTiO}_3$ heterostructure. A $\text{LaAlO}_3/\text{vacuum}$ interface terminating the top of the $\text{SrTiO}_3/\text{LaAlO}_3$ stack, as present in the samples analyzed experimentally, is up to now included only in Ref. [51]. The common result of those calculations is that the n -type interface is expected to be conducting. When it comes to predictions of slight atomic displacements in the heterostructure and the calculated band structure the publications still show large differences, which makes it difficult to obtain from the theoretical investigations a more complete picture. Further calculations are in progress and will potentially help to clarify the band structure at $\text{LaAlO}_3/\text{SrTiO}_3$ interfaces.

As will be discussed in Chapter 3 experimental difficulties were experienced in preparing p -type $\text{LaAlO}_3/\text{SrTiO}_3$ samples, therefore the focus of this thesis is on the electronic system of n -type $\text{LaAlO}_3/\text{SrTiO}_3$ interfaces. For the conducting layer the term “quasi two-dimensional electron gas” (q2-DEG) will be used.

2.5 Summary

In this chapter the two perovskites SrTiO_3 and LaAlO_3 have been introduced. The bulk properties of both materials are well explored. In particular, they both are band insulators. Strikingly, in $\text{LaAlO}_3/\text{SrTiO}_3$ heterostructures with a TiO_2/LaO stacking at the interface a conducting electron gas is formed. As shown, the polarity discontinuity model offers a possible explanation for the observed n -type conductivity.

3 Experimental Methods

After the constituent materials have been described in the previous chapter, now the experimental methods employed for fabrication and structural characterization of the $\text{LaAlO}_3/\text{SrTiO}_3$ samples will be presented. This part covers techniques for substrate preparation and film deposition, and results of Atomic Force Microscopy, X-ray diffraction, and transmission electron microscopy.

Finally the setup for electronic transport measurements is presented. The results obtained will be discussed in the subsequent chapters in detail.

3.1 Substrate Preparation

3.1.1 Preparation of SrTiO_3 Substrates

The substrate commonly used in this thesis is (001) oriented single-crystalline SrTiO_3 . The substrates were bought from CrysTec in Berlin (Germany). Typical dimensions are $10 \times 10 \times 1 \text{ mm}^3$ and $5 \times 5 \times 1 \text{ mm}^3$.

As-supplied substrates are first treated by ultrasonic cleaning in acetone for 10 min, then wiped on soft lens cleaning tissue (Whatman) followed by two more ultrasonic cleaning steps, first for 10 min in acetone and then for 10 min in isopropanol.

After this procedure the substrates still have a mixed surface termination of SrO and TiO_2 . To obtain a pure TiO_2 -termination of (001) oriented SrTiO_3 a well established recipe is used [53,54]. The SrTiO_3 substrate is dipped in an ultrasonic bath of bi-distilled water for 10 minutes. It is assumed that during this treatment the SrO on the SrO-terminated surface areas forms a Sr-hydroxide complex.

In contrast, the TiO_2 terminated areas are chemically very stable and remain unaffected by the bi-distilled water. Because the Sr-hydroxide complex dissolves in acidic solutions, the substrates are then brought in an ultrasonic bath of commercially available buffered HF solution ($\text{NH}_4\text{F}:\text{HF} = 87.5:12.5$, Merck) for 30 seconds. It is possible to obtain TiO_2 -terminated SrTiO_3 by using the last etching step in buffered HF only, but the performed hydroxidizing process minimizes the severe dependence of termination reproducibility on the pH value of the used acid and additionally prevents the formation of deep etch pits. The substrates are then rinsed with bi-distilled water and blown dry with nitrogen. To remove residuals of the previous treatment steps and to improve recrystallization a final annealing step is performed in a tube-furnace in flowing oxygen gas. The substrates are heated to $950 \text{ }^\circ\text{C}$ within 2 hours and kept at that temperature for 10 hours before the furnace is switched off to cool. In Ref. [54] it was shown by Lateral Force Microscopy (LFM) that SrTiO_3 treated in this manner is terminated by TiO_2 . This result was confirmed by a different method, coaxial impact-collision ion scattering spectroscopy, in Ref. [55].

It was not possible to check the substrate termination composition with the equipment available in our group. But as the recipe is commonly used as a standard method we relied on the previously mentioned experiments which revealed a TiO_2 surface. AFM measurements, which were done on the substrates after the termination procedure do not

reveal whether the surface is terminated by SrO or TiO₂, but it is possible to verify if only one termination is present on the substrate.

Every terminated substrate was analyzed by Atomic Force Microscopy (AFM) prior to thin film deposition. The experiments were mainly performed using a Multimode Microscope (Digital Instruments) in tapping mode. Silicon cantilevers and probes (NanosensorsTM) with resonance frequencies of 200–500 kHz and force constants of 10–130 N/m were used. The cantilevers were coated with Al for high reflectivity and had a tip radius of curvature of < 10 nm (PPP-NCHR) or even \approx 2 nm (SSS-NCHR). The scanning size is limited to $14 \times 14 \mu\text{m}^2$ with this device, but it allows to resolve topographic features, which are only few Å high. To reduce the effect of vibrations on the measurement the AFM was usually operated on a stone plate, which was suspended from a tripod using rubber straps.

Whenever larger scale images of samples were needed a Park Scientific Autoprobe cp AFM was used, which has a lower resolution for topography as compared to the Multimode Microscope.

Figure 3.1 shows an AFM image of a typical SrTiO₃ substrate. The topography shows a smooth step-and-terrace structure with surface steps that are one unit cell (uc) high (3.9 Å). Features of half this height were not observed, which confirms that only one termination is present. The terrace orientation and width are determined by the unavoidable misalignment (usually around 0.1°) of the substrate’s cutting plane with the SrTiO₃ crystal planes. Therefore the terrace geometry remains the same over a complete substrate area of $10 \times 10 \text{ mm}^2$.

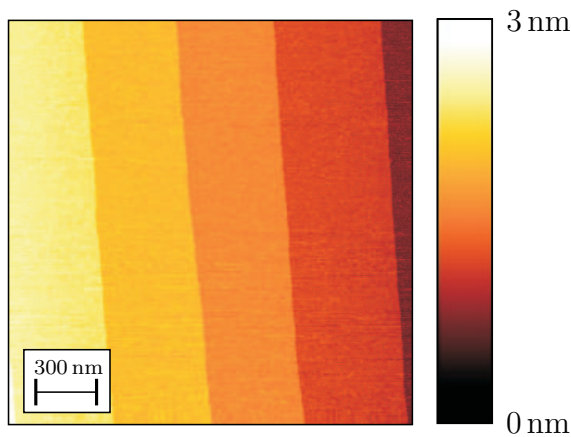


Figure 3.1: Topographic AFM image of a typical TiO₂-terminated SrTiO₃ substrate. A step-and-terrace structure with smooth step-ledges is observed. The step height corresponds to one unit cell (3.9 Å).

Only single-crystalline substrates with a clean step-and-terrace structure, one unit cell high steps, and a minimum terrace width of 50 nm were used for the experiments.

Several topographic features indicate when a terminated substrate should not be used. During the annealing process the step ledges of the substrate change from rough to straight due to material diffusion. If the terrace width is longer than the diffusion length the perfect step-and-terrace structure cannot be formed and holes with a depth of 1 uc remain in some areas (Fig. 3.2a). If the terrace width is too short (caused by a large miscut) the diffusion can lead to steps with a height of several unit cells.

Step bunches (several single unit cell steps merging into one larger step, see Fig. 3.2b) are another indicator for insufficient substrate quality. Such features were only observed on part of the SrTiO_3 single crystals during the second half of this thesis, which can only be explained by a change in the production of SrTiO_3 boules or the subsequent cutting and polishing processes. This observation emphasizes the importance of controlling all substrate surfaces after the termination procedure. As we will see later, the occurrence of these step bunches is often linked to dislocations in the substrate, which strongly affect the electronic transport properties of the conducting interface (see Chapter 8).

Hence, only SrTiO_3 single crystals with perfect step-and-terrace structure, one unit cell high steps, and without step-bunches were used as substrates for $\text{LaAlO}_3/\text{SrTiO}_3$ heterostructure growth.

The previously listed topographic features on SrTiO_3 single crystals can also have detrimental effects on the properties of other thin film samples using SrTiO_3 substrates. Therefore the quality of the SrTiO_3 needs to be always tested prior to experiments.

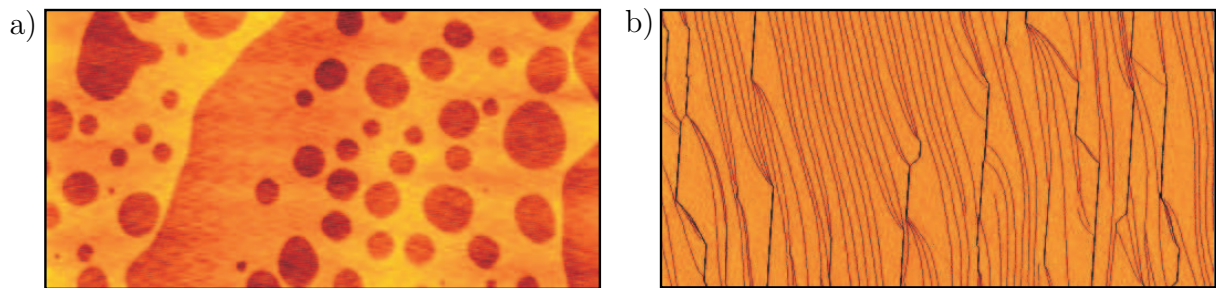


Figure 3.2: Analysis of SrTiO_3 substrate quality after treatment for TiO_2 termination. **a**, (topographic AFM image, $5 \times 10 \mu\text{m}^2$) One unit cell deep holes remain if the terrace width is longer than $\approx 1 \mu\text{m}$. **b**, (AFM amplitude error image, $5 \times 10 \mu\text{m}^2$) Step bunches are observed on SrTiO_3 substrates with a high density of dislocations.

This part closes with brief descriptions of occasionally used perovskite-type substrates and appropriate termination procedures, which were tested in the course of this thesis.

3.1.2 Preparation of Nb-doped SrTiO_3 Substrates

When doped with $\approx 0.05\%$ of niobium SrTiO_3 becomes conducting. The termination procedure used for pure SrTiO_3 also works for Nb-doped SrTiO_3 and leads to a clear step-and-terrace structure. On these substrate-surfaces, however, step-bunching was very common.

3.1.3 Preparation of LaAlO_3 Substrates

A specific termination (probably by AlO_2) of LaAlO_3 (001) substrates can be achieved by dipping the crystals in boiling water in an ultrasonic bath for 15 min, and then annealing them for 10 hours at 1100°C . Terraces with a step height of one unit cell are formed. Additionally the common twin-boundaries in LaAlO_3 clearly show up in topography (see Fig. 3.3a).

3.1.4 Preparation of DyScO₃ Substrates

DyScO₃, an insulating material, has the so called GdFeO₃ structure, which is a distorted perovskite, in which essentially rigid ScO₆ octahedra are tilted. The crystal is orthorhombic (space group Pnma) with the (110) orientation having the appropriate lattice constant (3.944 Å) for epitaxial growth with various oxides.

Only single unit cell-steps with smooth ledges are observed on DyScO₃ (110) single crystal substrates after cleaning with acetone and isopropanol and annealing at 1000 °C for 14 hours (see Fig. 3.3b) [56].

3.1.5 Preparation of NdGaO₃ Substrates

NdGaO₃ is also insulating and has the same structure as DyScO₃ (orthorhombic, space-group Pnma). The pseudocubic lattice constant for the (110) orientation is 3.867 Å.

As shown in Fig. 3.3c, a clear step-and-terrace structure with 1 uc high steps of NdGaO₃ (110) is achieved by cleaning in acetone and isopropanol and annealing at 950 °C for one hour [57, 58].

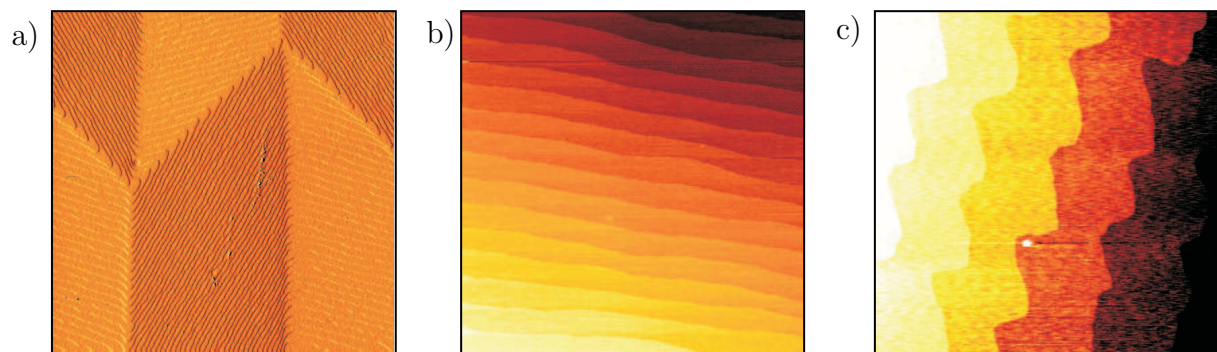


Figure 3.3: AFM images of several terminated substrate surfaces. **a**, (001) LaAlO₃ (amplitude error signal, 10×10 μm²). **b**, (110) DyScO₃ (topographic signal, 5×5 μm²). **c**, (110) NdGaO₃ (topographic signal, 2×2 μm²).

3.2 Film Deposition by PLD

In the following the deposition of thin films on the terminated substrates is discussed. Pulsed Laser Deposition (PLD) was used in this work. This method will be described in general, discussing in particular the procedures and standard parameters used for the growth of LaAlO₃ films on SrTiO₃ substrates.

PLD is a very popular and advanced technique for growing thin films in a research environment. The big advantages of PLD over competing techniques are that many materials can be ablated, that the growth rate is well controlled, and if optimal conditions are used, that even for complex materials the stoichiometry of the film is preserved from the starting material. Larger costs, slower deposition rates, and smaller coated areas in

comparison to other growth techniques are disadvantages, which usually can be tolerated in research, but hamper the use of PLD for industrial applications.

Figure 3.4a shows a sketch of the operation principle. High energy laser pulses, having a duration of 25 ns, are directed into a high-vacuum chamber and focused on the target material (poly- or single-crystalline). The energy is absorbed below the target surface. If the threshold value for ablation is exceeded the material gets removed, ionized, and accelerated away from the target surface. A plasma plume is thereby formed. At the end of the plume the heated substrate is positioned. The ablated target material is deposited on the substrate [59]. If the deposition parameters such as energy density on the target, background pressure, and substrate temperature are adjusted correctly, the stoichiometry of the target material and the deposited film match. This stoichiometric material transfer is one of the big advantages of PLD over other deposition techniques, and thus PLD is widely used for the film growth of complex materials.

In our setup (see Fig. 3.4b) a KrF Excimer Laser ($\lambda = 248$ nm, pulse width 25 ns, LPX300, Lambda Physik) is used. The homogeneous part of the laser beam profile is selected by an aperture and optically mapped in a 4:1 ratio on the target surface. For the typically used pulse energy of 450 mJ an energy density of ≈ 0.8 J/cm² is obtained on the target surface. By changing the size of the aperture the energy density on the target is kept fixed, but the laser spot size on the target is changed. This change allows to adjust the amount of ablated material.

The PLD high vacuum chamber (base pressure $< 10^{-7}$ mbar) is connected to a transfer chamber and a load lock, so that targets and substrates fixed to heaters can be mounted and exchanged without breaking the vacuum of the deposition chamber.

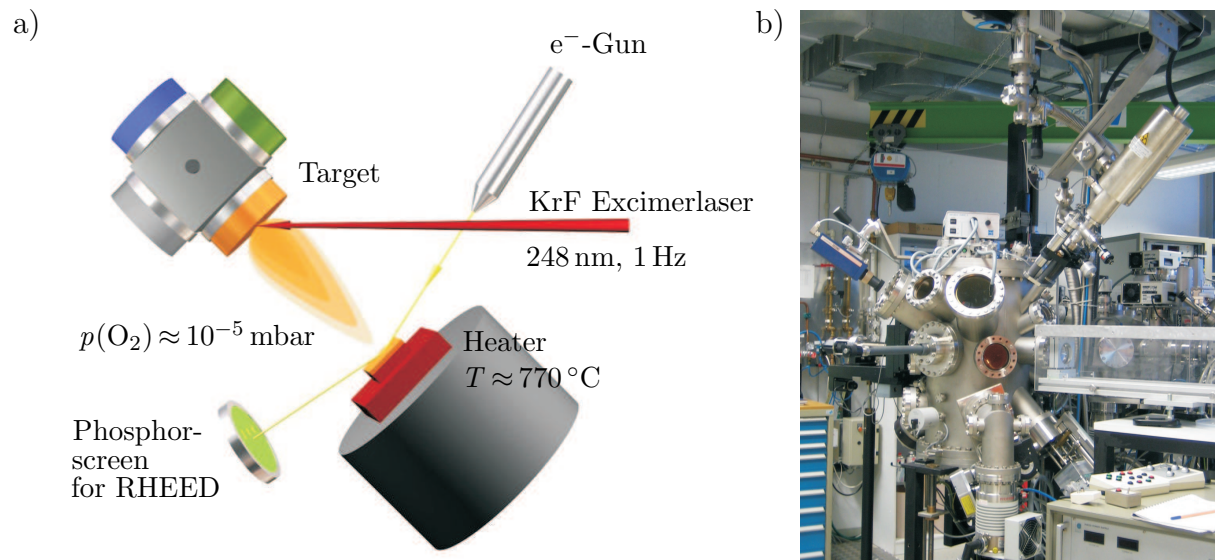


Figure 3.4: Film deposition by PLD. **a**, Sketch of the deposition principle. The noted parameters are the standard values used for the growth of LaAlO₃ on SrTiO₃ in this thesis. (Sketch by A. Herrnberger) **b**, Photo of the deposition chamber with the attached RHEED system (top right). A detailed description of this system can be found in Ref. [60].

Prior to every deposition the target, a stoichiometric LaAlO_3 single crystal, is polished on fine sandpaper (grade 400, VSM), wiped on a hard lens tissue (Mackerey-Nagel), rinsed with isopropanol, and blown dry with nitrogen. Then the target is transferred to the deposition chamber and mounted on the turnable multi-target holder, which carries up to four different targets for the *in situ* growth of complex heterostructures. To avoid cross-contamination between the target materials, a metal cap (not shown in Fig. 3.4) shields the targets not currently in use. As a final cleaning step a preablation is performed using the same parameters later used for the film deposition. By meandering the target holder the laser spot is scanned across the target surface on an area of approximately $8 \times 6 \text{ mm}^2$.

The prepared substrate is glued to a heater by silver paint (G3303A, Plano GmbH, drying at 70°C for 30 min) to assure good thermal contact. After transferring the mounted substrate to the deposition chamber the temperature of the resistive heater is ramped up computer controlled and measured with a pyroscope (Kleiber, 270B) pointing at a black area of the heater. This heating process is performed at the same oxygen background pressure later used for the film deposition ($p(\text{O}_2) \approx 10^{-5} \text{ mbar}$ for the deposition of LaAlO_3 , adjusted by a controlled flow of oxygen via a flowcontroller (mks PR4000)). The high substrate temperatures ($\approx 770^\circ\text{C}$ for the deposition of LaAlO_3) are necessary to ensure high quality epitaxial growth of the film. Figure 3.5 shows the typical temperature and pressure sequences used in the complete deposition process.

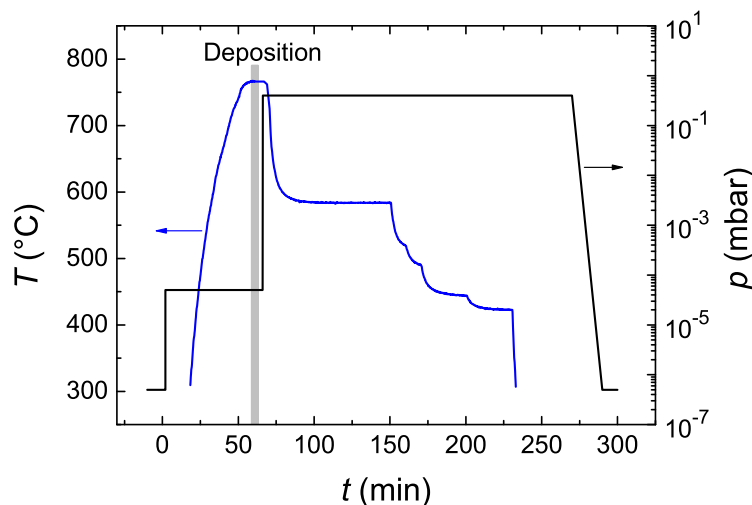


Figure 3.5: Typical time sequences of the temperature and the oxygen pressure used in this work for the pulsed laser deposition of LaAlO_3 on SrTiO_3 .

When the deposition temperature is stabilized, the film growth by laser ablation is performed, typically at a laser pulse rate of 1 Hz. The target to substrate distance is $\approx 5 \text{ cm}$. Again the laser spot is scanned across the target surface by meandering the target holder. As described in the next paragraphs, the growth is monitored in real time via Reflection High-Energy Electron Diffraction (RHEED). This technique is very sensitive to vibrations, therefore it is necessary to reduce the speed of the meandering target holder by a factor 10, as compared to the velocity used in the preablation.

Directly after the deposition the oxygen background pressure in the PLD chamber is raised to 400 mbar and the cooldown over several hours is started, during which the

current through the resistive heating block is reduced stepwise.

For the growth of LaAlO_3 films the 2.5 hour cooldown includes a one hour oxidation step at $\approx 600^\circ\text{C}$. In the rest of this work the parameters noted in the previous paragraphs will be referred to as the standard values for the deposition of LaAlO_3 ($p(\text{O}_2) \approx 10^{-5}$ mbar, $T \approx 770^\circ\text{C}$, energy density $\approx 0.8 \text{ J/cm}^2$, cooldown in 400 mbar of oxygen including a one hour step at $\approx 600^\circ\text{C}$).

3.3 Film Growth

When a laser pulse ablates material from the target surface, many atoms, ions, and molecules reach the substrate surface. There, several processes may occur. The particles are either elastically reflected or captured on the sample by transferring their kinetic energy to the surface molecules. Then the particles are subject to desorption and adsorption, diffusion on the surface and along steps, and finally they are incorporated into the film. As a result of this process the film grows.

Historically, four different growth modes (see Fig. 3.6) are distinguished, depending on the free energies of the substrate surface, film surface, and film-substrate interface. Significant wetting will appear if the total free energy of the film surface and the interface is lower than the free energy of the substrate surface. In this situation layer-by-layer growth, also called Frank-Van der Merwe growth [61] (Fig. 3.6a) occurs. When the bonding between substrate and film is weak and hence enlarging the interface yields no gain in free energy discrete three-dimensional islands will grow and finally coalesce (Volmer-Weber growth [62], Fig. 3.6b). Stranski-Krastanov growth [63] (Fig. 3.6c) describes the intermediate case when strong substrate-film interactions at first lead to some continuous monolayers, followed by the growth of discrete islands. Another important growth mode (step-flow, Fig. 3.6d) is found if the diffusion of atoms on a terrace is very fast. Then the adsorbed particles move to the step edges and nucleation on a terrace is prevented. No island growth is observed in this case.

Due to the large laser pulse energies the PLD process works far from thermal equilibrium. Therefore the distinction of growth modes by thermodynamic energy considerations, as described in the preceding paragraph, just treats limiting cases. The growth modes depend additionally on substrate temperature, background pressure, nucleation density of particles on the sample surface, and substrate miscut. This dependence implies that different modes can be induced for the same film-substrate material combination. Sometimes the so called Pulsed Laser Interval Deposition (PLID) [64–66] can be used to

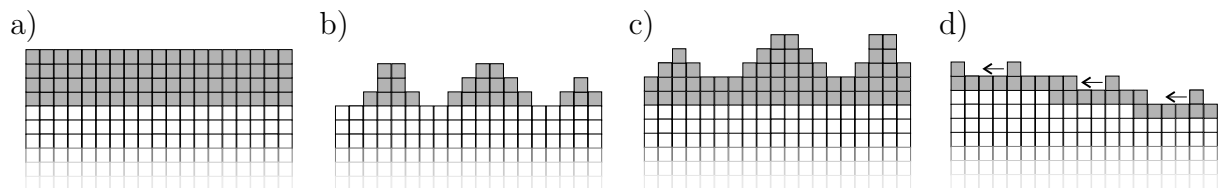


Figure 3.6: Sketch of different film growth modes. **a**, Frank-Van der Merwe, or layer-by-layer. **b**, Volmer-Weber. **c**, Stranski-Krastanov. **d**, step-flow growth modes.

impose layer-by-layer growth. In PLID the film is grown by repeating two steps until the desired thickness is reached. First, the complete material needed for one monolayer is deposited in a time interval shorter than the characteristic relaxation time of the material on the sample surface and then a longer pause allows for material rearrangement.

For heteroepitaxial growth, the crystallographic lattice mismatch between film and substrate is another important factor to consider. Biaxial strain will lead to elastic energy growing as the film thickness increases. At some critical thickness misfit dislocations and sometimes even cracks are formed to relieve the strain (see Fig. 3.12).

3.4 Growth Monitoring by RHEED

Reflection High-Energy Electron Diffraction (RHEED) is a versatile technique for *in situ* studies of the surface and growth of thin films [67]. As already mentioned, it was always used during the deposition of LaAlO_3 films on SrTiO_3 substrates in this thesis.

A schematical view of the RHEED geometry is shown in Fig. 3.7a. An electron beam (electron gun STAIB RH30, 30 kV acceleration voltage) is directed onto the sample surface. To enable RHEED in the high gas pressures necessary for the deposition of oxides a two-stage differentially pumped setup is used [68], where the electron beam is directed through a pumped extension tube to reduce its travel distance in the high oxygen pressure of the deposition chamber to about 20 cm. A four-axis goniometer provides one translational and three rotational degrees of freedom for precise alignment of the sample with the beam [60] at a small angle of incidence θ of 0.5° – 3° (see Fig. 3.4a and Fig. 3.7a). The diffracted electron beam intensity is monitored via a phosphor screen and a CCD camera, with the screen shielded from the ablation plume by a metal grid.

For well oriented crystalline surfaces a characteristic, symmetric spot pattern is observed. In kinematical scattering theory intensity maxima in the reflections are expected where the wavevectors of the incident and diffracted beams differ by a reciprocal lattice vector. The solutions to this condition can be constructed geometrically using the Ewald sphere. In this construction the tip of the incident wave vector \vec{k}_0 is attached to a reciprocal lattice point, and a sphere is drawn around the tail of \vec{k}_0 with radius $|\vec{k}_0|$. Every intersection of this Ewald sphere with a reciprocal lattice point corresponds to one reflection. The low angle of incidence corresponds to a small component of \vec{k}_0 perpendicular to the sample surface, and thus only a small penetration depth. For a perfectly flat surface this implies that only the sample surface is probed. In this case the probed reciprocal lattice consists of one dimensional rods perpendicular to the surface. These rods are intersected by the Ewald sphere, which has a large radius ($\approx 900 \text{ nm}^{-1}$) compared to the typical reciprocal lattice vectors ($\approx 16 \text{ nm}^{-1}$), so that only few reflections, lying on a circle, are observed on the screen. The intersection with the (00) rod is the specular reflection, which is the spot monitored most frequently in the RHEED experiments described in this thesis. Such a spot-like pattern being observable is an indicator of a flat surface with almost perfect crystalline order on an area of thousands of unit cells on the surface.

Because the distance between the first order diffraction spots is related to the reciprocal lattice parameters, one can in principle extract the lattice constants and their temporal evolution, if the electron wavelength is known precisely. This analysis was not done in the

experiments described in this work due to the insufficient resolution of the spot distances on the screen by the CCD camera of our RHEED setup.

Surface irregularities and steps lead to a broadening of the reciprocal rods, and streaks appear in the RHEED pattern. When the surface gets rougher and more three-dimensional the diffraction pattern also contains spots from transmission-diffraction through islands and large particles on the surface, which gives rise to a superimposed rectangular pattern.

RHEED not only allows to investigate the surface morphology of sample surfaces, but also allows to resolve surface reconstructions. These change the symmetry of the reciprocal lattice, so that additional spots are observed. Another feature in RHEED patterns, which are caused by inelastic scattering processes, are the Kikuchi lines [69] (see Fig. 3.7b), whose presence indicates very flat surfaces.

A typical RHEED image after a thin film deposition of 10 uc of LaAlO_3 on SrTiO_3 is shown in Fig. 3.7b. Clearly a spot pattern with additional Kikuchi lines is observed. This image proves that the perfectly flat substrate surface and its single-crystallinity is maintained throughout the LaAlO_3 film growth, which proceeds layer-by-layer. Also no reconstruction induced additional spots are found.

As described next, even more information about film growth can be deduced from the temporal evolution of the RHEED signal during film deposition.

For the exploration of growth dynamics the spot intensity is monitored as a function of time. In 1981 for the first time oscillations in the spot intensity of the RHEED pattern were observed [70] and related to the successive growth of one complete unit cell thick layer after the other.

Several models exist to explain the intensity modulations. Often the step-density model is used, where steps on the surface are taken as diffuse scatterers, which reduce the intensity at the specular reflection. While this model well explains the periodic variation, it is by far oversimplified and cannot explain many experimental results. In any realistic

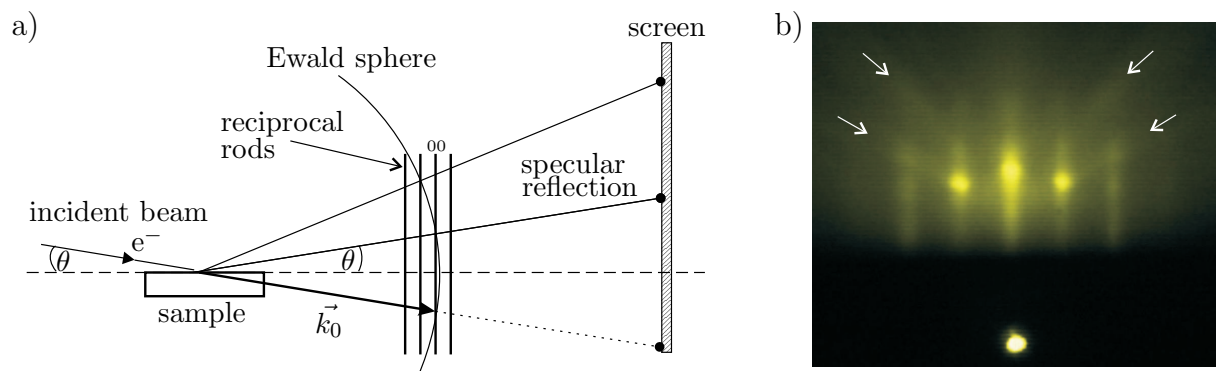


Figure 3.7: Illustration of the study of film surfaces by RHEED. **a**, Sketch of the RHEED geometry. Reflections occur in directions defined by the intersections of the Ewald sphere with the reciprocal lattice rods. **b**, RHEED image after deposition of a 10 uc thick LaAlO_3 film on SrTiO_3 . The direct beam is found at the bottom of the image, the specular reflection and the adjacent first order spots are also clearly visible, indicating a very flat surface after film growth. Additionally, Kikuchi lines are observed (marked by arrows).

model both diffraction effects and microscopic growth mechanisms have to be taken into account.

When RHEED oscillations are observed during film growth the temporal periodicity of RHEED intensity always corresponds well to the temporal periodicity of unit cells being completed. However, RHEED intensity and unit cell completeness have no fixed phase relation. The phase difference depends on the incident angle of the electron beam [71]. For this reason we used fixed diffraction conditions for the growth of LaAlO_3 on SrTiO_3 . To obtain always the same conditions the (100) direction is aligned with the electron beam to get a symmetric diffraction pattern and then the incident angle θ is increased from 0° until the intensity of the specular reflection is maximal for the first time after the first-order reflections appear. This procedure leads to reproducible RHEED signals for LaAlO_3 growth, where maxima in the intensity correspond to completed unit cell layers (see later).

The measured intensity of the electron beam on the screen is sensitive to vibrations of the vacuum chamber. To reduce their influence, in this thesis several precautions were taken. The flexible tubes from the scroll-pumps to the turbomolecular pumps of the deposition chamber were fixed using heavy weights damping their vibrations. Additionally the RHEED electron gun was fixed by using a stiff setup to the ceiling of the laboratory. Prior to the depositions, the electron beam direction is adjusted electrically to the center of the extension tube for optimal performance.

3.4.1 RHEED Signals Occurring During the Preparation of *n*-Type $\text{LaAlO}_3/\text{SrTiO}_3$ Interfaces

Figure 3.8 shows the typical RHEED oscillations seen during the deposition of 15 uc of LaAlO_3 on TiO_2 -terminated SrTiO_3 . In the graph the peak intensity of the (00) spot is plotted as a function of time. After the start of the film growth the intensity drops sharply, then recovers, but at the first maximum does not reach the initial value again. The intensities at the second and third maxima are still slightly smaller, so that usually here the RHEED intensity is increased manually by increasing the filament current in the electron gun. After several more oscillations the height of the maxima reaches an approximately constant value. The characteristic drop of the intensity at the beginning of the deposition is probably related to an altered optimum condition for the incident angle θ upon deposition of LaAlO_3 . When this angle is initially adjusted to obtain a maximum in the specular spot intensity, the electron beam probes a SrTiO_3 surface, while it is LaAlO_3 that determines the diffraction conditions after the deposition of one unit cell. Therefore, if the deposition is interrupted after one or two unit cells of LaAlO_3 , and θ is then adjusted to obtain a maximal specular spot intensity like at the beginning, one observes RHEED maxima of almost constant intensity. The effect of such an adjustment can be seen for example in Chapter 6, where the RHEED signal during film growth using the developed patterning process is presented.

These characteristic modulations of the specular spot intensity are found reproducibly for all samples which were initially adjusted to the standard condition for θ , as described before.

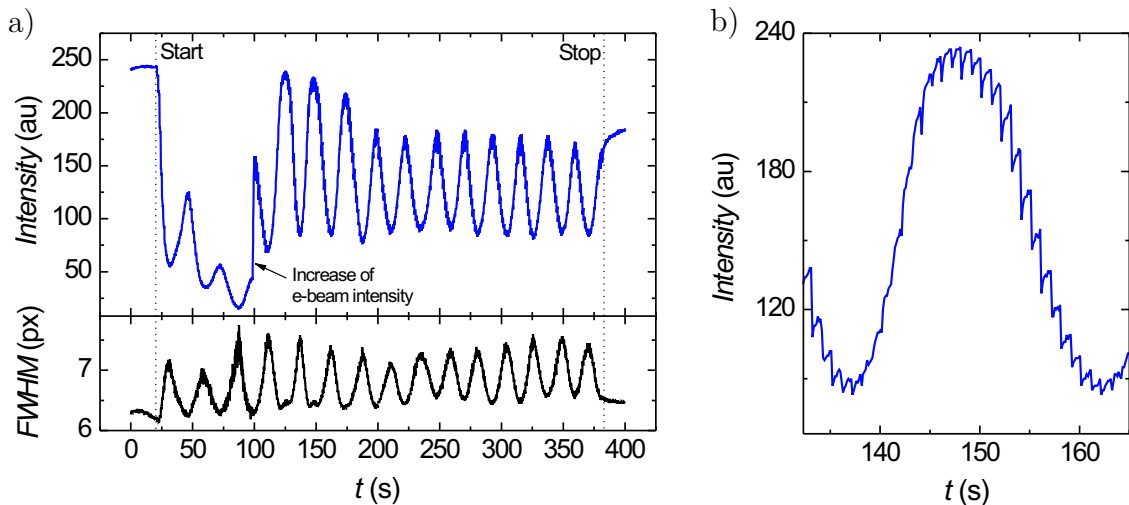


Figure 3.8: RHEED oscillations for the growth of 15 uc of LaAlO_3 on TiO_2 -terminated SrTiO_3 (sample L116). **a**, Intensity (top) and full-width at half maximum FWHM (bottom) of the specular reflection spot. **b**, Enlarged view of the intensity oscillation around the fifth maximum.

By using a laser pulse rate of 1 Hz during PLD one unit cell is deposited in about 25 seconds, corresponding to a typical growth rate of ≈ 1 nm/min. This timescale allows to stop the film deposition at the desired moment during the evolution of the signal, usually at a certain maximum in intensity. As noted before, the period of the oscillations always corresponds to the growth of one unit cell. This is confirmed by transmission electron microscopy images of the samples (see Sec. 3.5.3), which show LaAlO_3 film thicknesses that correspond exactly to the number of RHEED oscillations during the film deposition. Additionally the fact that the time from the start of the LaAlO_3 deposition to the first maximum in RHEED intensity is as long as the time interval between subsequent maxima proves that maxima in the intensity correspond to completed unit cells and not to some incomplete coverage.

The enlarged view of the intensity oscillations during the deposition of the fifth LaAlO_3 layer (Fig. 3.8b) shows that every single laser pulse is detected, with a characteristic, rapid drop in RHEED intensity directly after a laser pulse, followed by a slower increase in intensity. The drop is caused by the particles that are deposited by the pulse and then diffuse on the surface. Before the particles attach at step edges of present one unit cell high islands they act as additional diffuse scatterers [72, 73].

The unit cell oscillations are also visible in the full-width at half maximum (FWHM) of the specular spot intensity peak (shown in the bottom part of Fig. 3.8a). The peak width broadens periodically with the step-edge density on the surface, and thus the FWHM shows maxima for half covered layers and minima for complete coverage.

RHEED oscillations are observed for the growth of LaAlO_3 on SrTiO_3 for the deposition of at least 180 unit cells, which implies that up to this thickness the growth mode does not change from layer-by-layer to a three-dimensional mode. In our setup an addi-

tional small modulation of the RHEED intensity is caused by the vibrations due to target holder step-motor movement.

As RHEED allows to monitor the film thickness only at a certain position on the surface, it had to be investigated how homogeneous the film deposition is across the sample. For this reason a ≈ 180 nm thick reference film of $\text{YBa}_2\text{Cu}_3\text{O}_{7-\delta}$ was grown on a standard $5 \times 5 \text{ mm}^2$ SrTiO_3 substrate and patterned by photolithography and phosphorous acid. This test was not performed using a LaAlO_3 film, because, as discussed in detail in Chapter 6, LaAlO_3 can not be etched chemically in an appropriate manner. The step heights were then determined by AFM measurements and found to vary by less than 5%. Therefore I conclude that the film deposition by PLD is sufficiently homogeneous, so that the number of unit cells as measured by RHEED at one location applies with 5% accuracy to the complete sample surface and can therefore be reliably taken as the film thickness.

3.4.2 RHEED Signal Occurring During the Preparation of *p*-Type $\text{LaAlO}_3/\text{SrTiO}_3$ Interfaces

By the growth of a monolayer of SrO the termination of a treated SrTiO_3 substrate can be switched from TiO_2 to SrO. After growing a LaAlO_3 film the stacking sequence right at the interface is then SrO/ AlO_2 , which the polarity discontinuity model predicts to show *p*-type behavior. This insertion of a monolayer of SrO was already used in the first publications on the $\text{LaAlO}_3/\text{SrTiO}_3$ interface [13, 14] to investigate both *n*-type and *p*-type stacking sequences. As this method allows an important, optional modification of the heterostructure, it was also investigated if a monolayer of SrO can be successfully grown in our deposition chamber.

As SrO tends to grow in islands at high deposition temperatures, the PLID method was employed to impose layer-by-layer growth [74]. First SrO is deposited from a single-crystalline target on a SrTiO_3 substrate by standard PLD (500 mJ, $p(\text{O}_2) = 0.1$ mbar) at a lower temperature (400 °C). Under these conditions SrO grows in a layer-by-layer mode and the necessary number of pulses for the deposition of one SrO unit cell is taken from the first oscillation in the RHEED intensity of the (01) spot. Usually the determined number was a factor of 18 higher as compared to the deposition of 1 uc LaAlO_3 . On a new TiO_2 -terminated SrTiO_3 substrate a monolayer of SrO was then rapidly deposited by PLID (770 °C, 500 mJ, $p(\text{O}_2) = 0.1$ mbar) taking the previously determined number of pulses and using a laser pulse repetition frequency of 50 Hz (50 Hz is the maximum repetition frequency of the laser in use). For this high frequency operating the laser in constant high-voltage mode assures the necessary high pulse-to-pulse stability. Finally LaAlO_3 was deposited with the standard PLD parameters.

Figure 3.9 shows the RHEED intensity for the growth of such a *p*-type $\text{LaAlO}_3/\text{SrTiO}_3$ heterostructure. After the deposition of SrO the intensity dropped to about 20% of the initial value and was therefore manually increased. At the beginning of the LaAlO_3 deposition a clear difference is found compared to the *n*-type $\text{LaAlO}_3/\text{SrTiO}_3$ heterostructure growth. The RHEED signal first increases to a maximum before the oscillations, known from the *n*-type samples, start. This indicates that the substrate termination was indeed changed by the growth of SrO and that LaAlO_3 grows in layer-by-layer mode also on SrO-terminated SrTiO_3 substrates. While these RHEED signals indicate that a very flat

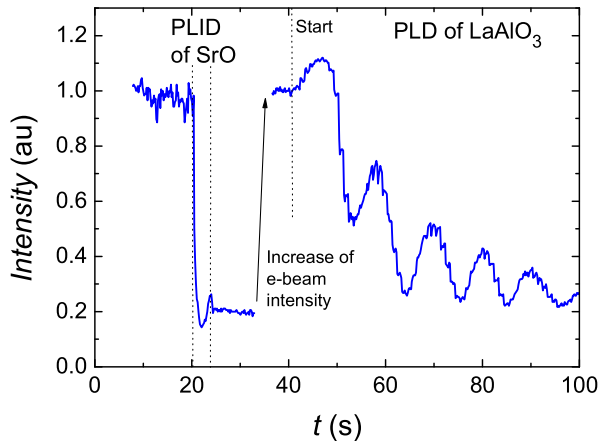


Figure 3.9: RHEED intensity for the deposition of a *p*-type $\text{LaAlO}_3/\text{SrTiO}_3$ heterostructure (sample L87). A large drop is observed after the PLID of SrO. In contrast to the *n*-type interface an initial increase in the RHEED intensity is observed for the PLD of LaAlO_3 before the usual oscillations set in.

SrO monolayer was grown, we will see in the following discussion on sample topography that the *p*-type samples have a larger surface roughness than the *n*-type samples.

3.5 Film Characterization

3.5.1 AFM

The surface topography shown by the samples after the deposition of LaAlO_3 films on TiO_2 -terminated SrTiO_3 was regularly checked by AFM. For these experiments the microscope employed for the analysis of the substrate surface topography was used. Figure 3.10 shows typical micrographs. It can be clearly seen that the terraced structure observed on the substrate surface with one unit cell high steps is preserved throughout the LaAlO_3 film growth. A low roughness of ≈ 0.1 nm (RMS value) is obtained. Half unit cell high features are not observed, which shows that also on the LaAlO_3 surface only one termination is present, which presumably is AlO_2 .

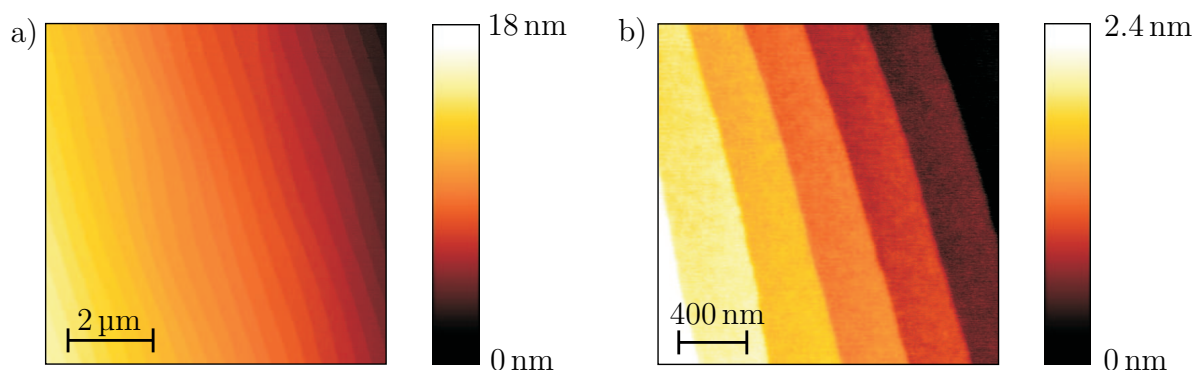


Figure 3.10: Topographic AFM image of a 5 uc thick film of LaAlO_3 on TiO_2 -terminated SrTiO_3 (sample L29). The step-and-terrace structure of the substrate is preserved throughout the growth of the LaAlO_3 film. Fig. **a**, $8 \times 8 \mu\text{m}^2$ image **b**, $2 \times 2 \mu\text{m}^2$ image. Published in Ref. [75].

AFM images of LaAlO_3 grown on SrO-terminated SrTiO_3 also show a clear step-and-terrace structure (see Fig. 3.11). But here many tiny islands are found in addition, which are not present for n -type interface samples. Correspondingly the RMS roughness, ≈ 0.25 nm, is higher. These islands indicate that the SrO was not grown as an ideal monolayer, although the RHEED oscillations signalled that the termination of the substrate was switched from TiO_2 to SrO. The consequence of a non-ideal, rough layer of SrO is, that the interface to the subsequently deposited LaAlO_3 film is ill defined and certainly not atomically sharp. This rough interface makes any interpretations of transport properties quite speculative. For this reason mainly the n -type interface samples are studied in this work.

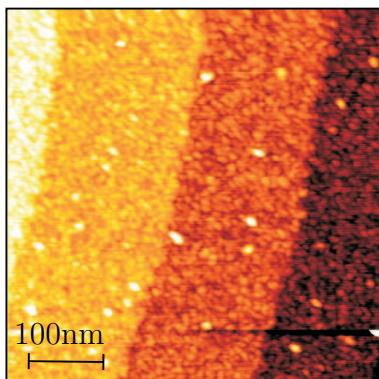


Figure 3.11: AFM image (topographic signal, $500 \times 500 \text{ nm}^2$) of a 10 uc thick film of LaAlO_3 on SrO-terminated SrTiO_3 (sample L87).

Due to the large lattice mismatch of $\approx 3\%$ between LaAlO_3 and SrTiO_3 strain builds up rapidly with increasing thickness of the film. This strain relaxes when the so called critical thickness is exceeded [76]. In general, strain relaxation of films with a rough surface occurs by twinning or by formation of dislocations, while smooth films, like the ones of our samples, relax by cracking [77]. Such cracks are indeed observed in our $\text{LaAlO}_3/\text{SrTiO}_3$ heterostructures. For these samples the critical thickness measured is 25 unit cells (see Fig. 3.12). The thicker the LaAlO_3 film the higher the density of the cracks. The cracks are predominantly oriented along the main crystallographic axes (horizontal and vertical direction in Fig. 3.12a–c). Between the cracks the step-and-terrace structure can still be clearly seen. Figure 3.12d shows a linescan across a crack in a 46 uc thick LaAlO_3 film on SrTiO_3 . Up to a distance of ≈ 25 nm from the crack the LaAlO_3 delaminates from the substrate and bends up from the surface of the film. A gap of about 7 nm is formed right at the crack. If the cracks already form upon film growth at high T or during the cooldown process can not be decided from our experiments.

We will see later in Chapter 4 that no conductivity was found in $\text{LaAlO}_3/\text{SrTiO}_3$ samples which show cracks, therefore in the samples discussed in the following chapters the thickness of the LaAlO_3 films was kept well below the critical value of 25 uc.

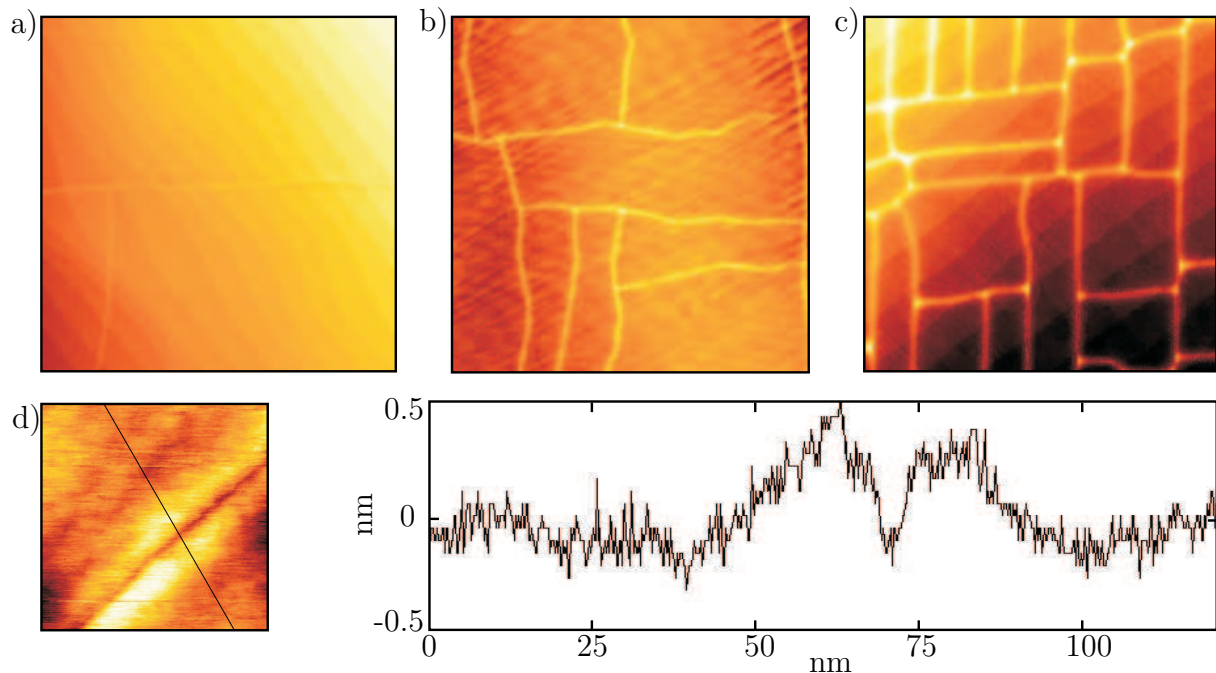


Figure 3.12: Topographic AFM images of LaAlO_3 films on TiO_2 -terminated SrTiO_3 with a film thickness larger than the critical value (25 uc) for crack formation: **a**, 31 uc (sample L19) **b**, 46 uc (sample LGB1) **c**, 102 uc (sample L18) (all images are $5 \times 5 \mu\text{m}^2$) **d**, Linescan across a crack in the 46 uc thick film (linescan as indicated on the left $100 \times 100 \text{nm}^2$ AFM topographic image).

3.5.2 X-Ray Diffraction

X-Ray Diffraction (XRD, performed with a Philips X'Pert MPD System) was used to check the crystalline structure of the samples. As shown in Fig. 3.13a only (h00) reflections of the SrTiO_3 substrate and the LaAlO_3 film are observed in a $\theta - 2\theta$ -scan, which proves c -axis oriented growth of the LaAlO_3 . From the θ -values of several peaks the c -axis lattice constant is determined to 3.74 \AA , slightly smaller than the bulk value for LaAlO_3 (3.791 \AA). The TEM images in the next section will show that in our samples the LaAlO_3 grows cube-on-cube on SrTiO_3 with the in-plane lattice constant of the LaAlO_3 film equal to the lattice constant of SrTiO_3 . This clamping to the substrate probably causes the slightly shortened lattice constant of the LaAlO_3 film in c -direction

In a detailed view on the (100) reflection (see Fig. 3.13b) clear Laue fringes can be seen. Their presence indicates a high quality thin film with a homogeneous thickness between two well defined interfaces ($\text{SrTiO}_3/\text{LaAlO}_3$ and $\text{LaAlO}_3/\text{air}$). The function describing the intensity I of this special diffraction pattern (disregarding the substrate peak) can be calculated by assuming Laue-conditions for the LaAlO_3 film only for the two in-plane directions [78]:

$$I = I_0 \frac{\sin^2(\frac{1}{2}Nq_z c)}{\sin^2(\frac{1}{2}q_z c)} \quad (3.1)$$

Here $q_z = 4\pi \sin(\theta)/\lambda$ is the projection of the scattering vector perpendicular to the

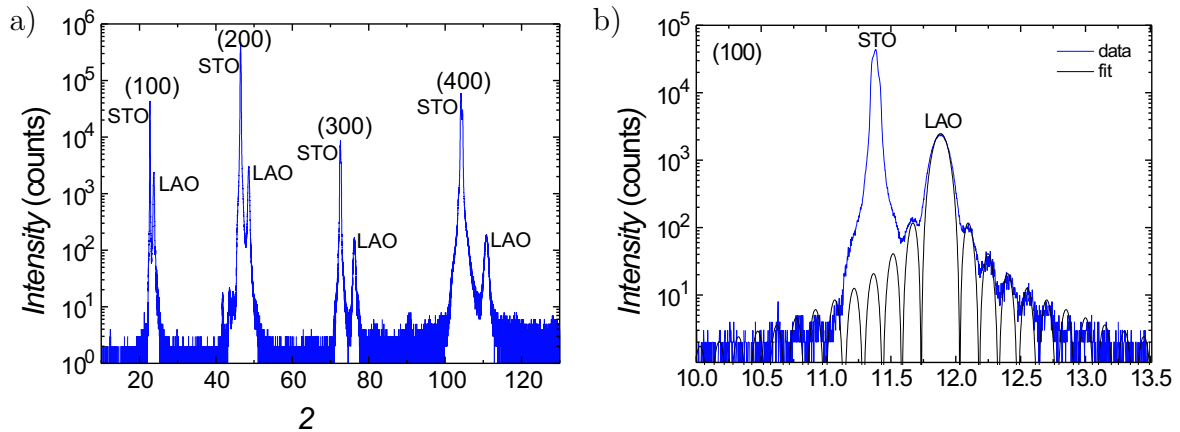


Figure 3.13: XRD data for a 81 uc thick film (sample L18) of LaAlO_3 (LAO) on SrTiO_3 (STO). **a**, $\theta - 2\theta$ -scan, showing only (h00) reflections of the film and the substrate. **b**, Enlarged view of the (100) peak. Clear Laue fringes are observed around the LaAlO_3 peak, which can be fitted to Eq. 3.1.

film surface, c is the lattice constant, and N is the number of unit cells of the LaAlO_3 in z -direction. With the correct parameters the measured data can be fitted very well, as shown in Fig. 3.13b for a film thickness of $N = 81$ uc, as taken from the observed RHEED oscillations for this sample. However, similarly good fits can be obtained by assuming LaAlO_3 thicknesses two unit cells larger or smaller, so the XRD measurements can not be used for the exact determination of the film thickness. Therefore, as mentioned before, we use the number of RHEED oscillations during film growth as the precise value of the LaAlO_3 film thickness.

As films of a thickness of 25 uc and more have been shown to contain cracks, the 81 uc sample used for the XRD experiments also had many cracks in the LaAlO_3 layer. The observation of a clear XRD pattern with Laue fringes therefore proves that the delamination of the LaAlO_3 film is limited to the area directly next to the cracks, keeping the large majority of the film unaffected. Due to the resolution of our XRD device it was impossible to study thin, uncracked LaAlO_3 films. In an ongoing collaboration (see Appendix B) samples with 2 uc, 3 uc, and 5 uc of LaAlO_3 on SrTiO_3 are studied in detail by Surface X-Ray Diffraction by S.A. Pauli and P.R. Willmott at the Paul-Scherrer-Institute in Villigen (Switzerland). They expect to be able to resolve the atom positions in the samples with high precision. This structural information will also be important for theoretical calculations like DFT.

3.5.3 Transmission Electron Microscopy

To obtain more information on the microstructure of our heterostructures, the samples were investigated by transmission electron microscopy (TEM) and scanning TEM (STEM) by Lena Fitting Kourkoutis and Dave A. Muller at the University of Cornell (USA).

These studies were performed on reference $\text{LaAlO}_3/\text{SrTiO}_3$ samples grown under the

standard conditions ($p(\text{O})_2 = 4 \times 10^{-5}$ mbar, 770 °C). To protect the film surface during TEM specimen preparation an additional capping is needed. Therefore in the first experiments a 5 nm thick layer of amorphous Al_2O_3 was deposited on the $\text{LaAlO}_3/\text{SrTiO}_3$ heterostructure by PLD at room temperature as final layer. Cross sectional cuts were then prepared by mechanical polishing followed by low-energy, low-angle ion milling.

The TEM and STEM investigations were performed on a monochromated 200 kV FEI Tecnai F20-ST STEM with a minimum probe size of ≈ 1.6 Å and a convergence semiangle of (10 ± 1) mrad. Annular Dark Field (ADF) detectors were used, which register signals from electrons scattered to large angles. The high angle annular dark field (HAADF) images were recorded at an inner detector angle of ≈ 65 mrad. HAADF images are well suited to distinguish different chemical elements, as the intensity is proportional to Z^n , with Z as the atomic number and n having a value of $\approx 1-2$. Therefore, detecting the HAADF signals is often referred to as Z -contrast imaging.

To increase signal to noise and average out the scan noise, 8 successive images, each recorded at 16 microseconds per pixel, were cross-correlated and averaged. The 1024×1024 pixel images were subsequently rebinned to 512×512 pixels.

Figure 3.14 shows STEM images of samples with 3 uc and 5 uc of LaAlO_3 on TiO_2 -terminated SrTiO_3 . In all following STEM images the dark area in the top corresponds to the amorphous capping layer. Below this stripe, the epitaxial LaAlO_3 film can be seen, followed by the SrTiO_3 substrate. Due to their high atomic numbers La ($Z = 57$) and Sr ($Z = 38$) atoms appear brightest in these HAADF images, with La atoms providing the highest intensity. Al ($Z = 13$) and Ti ($Z = 22$) atoms can additionally be resolved in between La and Sr atoms, respectively. The micrographs clearly show that an abrupt interface formed between SrTiO_3 and LaAlO_3 , while the interface between LaAlO_3 and the amorphous capping layer of Al_2O_3 is rough.

Below this rough capping sheet no difference in the microstructure is observed for samples with 3 uc and 5 uc of LaAlO_3 . This is stated explicitly here, as we will see later in Sec. 4.1 that the electronic transport properties of the interfaces differ dramatically as a function of the LaAlO_3 thickness.

An analysis by Electron Energy Loss Spectroscopy (EELS) reveals that the La concentration drops sharply at the $\text{LaAlO}_3/\text{SrTiO}_3$ interface as is expected from the abrupt interface in the ADF images. But La is also found in the capping, which is probably caused by La diffusion into the Al_2O_3 , or even by chemical reactions between both materials. This La diffusion explains why the number of uniform LaAlO_3 layers in the STEM images does not correspond to the number of RHEED oscillations during LaAlO_3 film growth. Additionally, the EELS data revealed diffusion of Ti into the LaAlO_3 film as well as into the cap.

A tiny signature of fluorine, present in the EELS signal of the first TEM samples, was not found in later samples when transport boxes made of non-fluorine-containing plastics were used.

The O-K EELS spectra are presented and discussed in the next chapter (see Sec. 4.2).

To reduce La diffusion into the capping layer, capping layers consisting of 5 nm of amorphous SrTiO_3 , grown by PLD at room-temperature, were used from then on. This

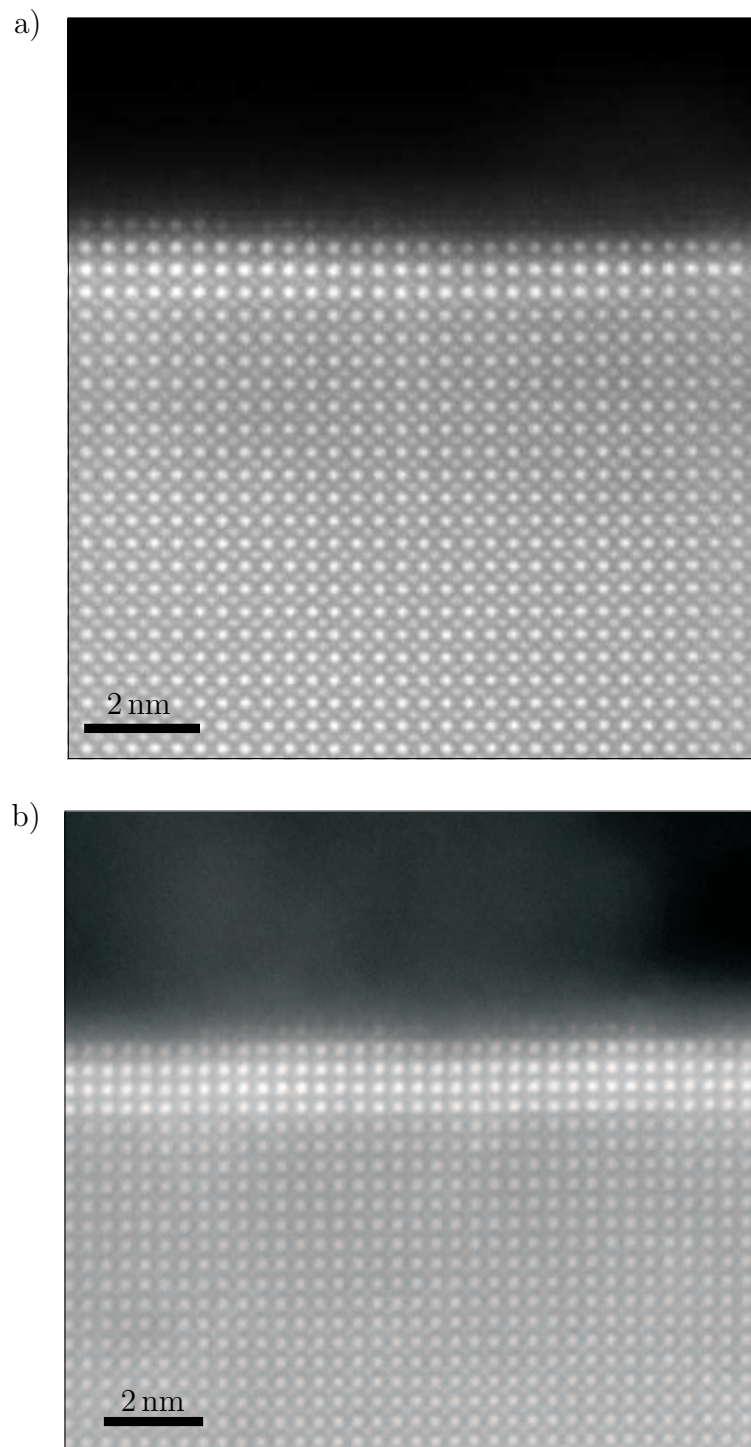


Figure 3.14: Cross-sectional STEM HAADF images of samples with an amorphous Al_2O_3 capping layer. **a**, 3 uc (sample L58) and **b**, 5 uc (sample L56) of LaAlO_3 on SrTiO_3 . An atomically abrupt interface between SrTiO_3 and LaAlO_3 is observed, while the top LaAlO_3 layer is very rough for both samples due to interdiffusion or chemical reaction with Al_2O_3 . For this reason also the number of LaAlO_3 unit cells does not correspond to the observed RHEED oscillations during deposition. The STEM experiments were done by L. Fitting Kourkoutis and D.A. Muller at the University of Cornell (USA).

capping resulted in much clearer STEM images with sharp top and bottom interfaces of the LaAlO_3 film. The corresponding images are shown in Fig. 3.15 for a 15 uc sample and in Fig. 3.16 for a 5 uc thick film on SrTiO_3 . Fig. 3.17 shows an enlarged view of the $\text{LaAlO}_3/\text{SrTiO}_3$ interface. In this STEM image a colored sketch of the atomic structure at the interface is shown for illustration.

As already expected from the XRD measurements which showed Laue fringes, a homogenous, bright LaAlO_3 film can be clearly seen above the greyish SrTiO_3 with an atomically sharp interface inbetween. In samples with amorphous SrTiO_3 as capping layer the number of LaAlO_3 unit cells visible in STEM images fits exactly to the number of observed maxima in the RHEED oscillations during growth. This correspondence finally proves the previously applied interpretation of the oscillating RHEED signal as being caused by the layer-by-layer growth of the LaAlO_3 film.

For the sample with 5 uc of LaAlO_3 the lattice constants were analyzed in detail. C -axis oriented growth was already checked by XRD, but the STEM images now confirm that the LaAlO_3 film grows epitaxially on the SrTiO_3 substrate. The film is found to be coherent with the substrate (in-plane lattice constant 3.91 \AA). No obvious defects or dislocations were found at the interface, resulting in biaxial tensile strain of $\approx 3\%$. At thicknesses of ≈ 25 uc the film begins to relax this strain by the formation of cracks, as

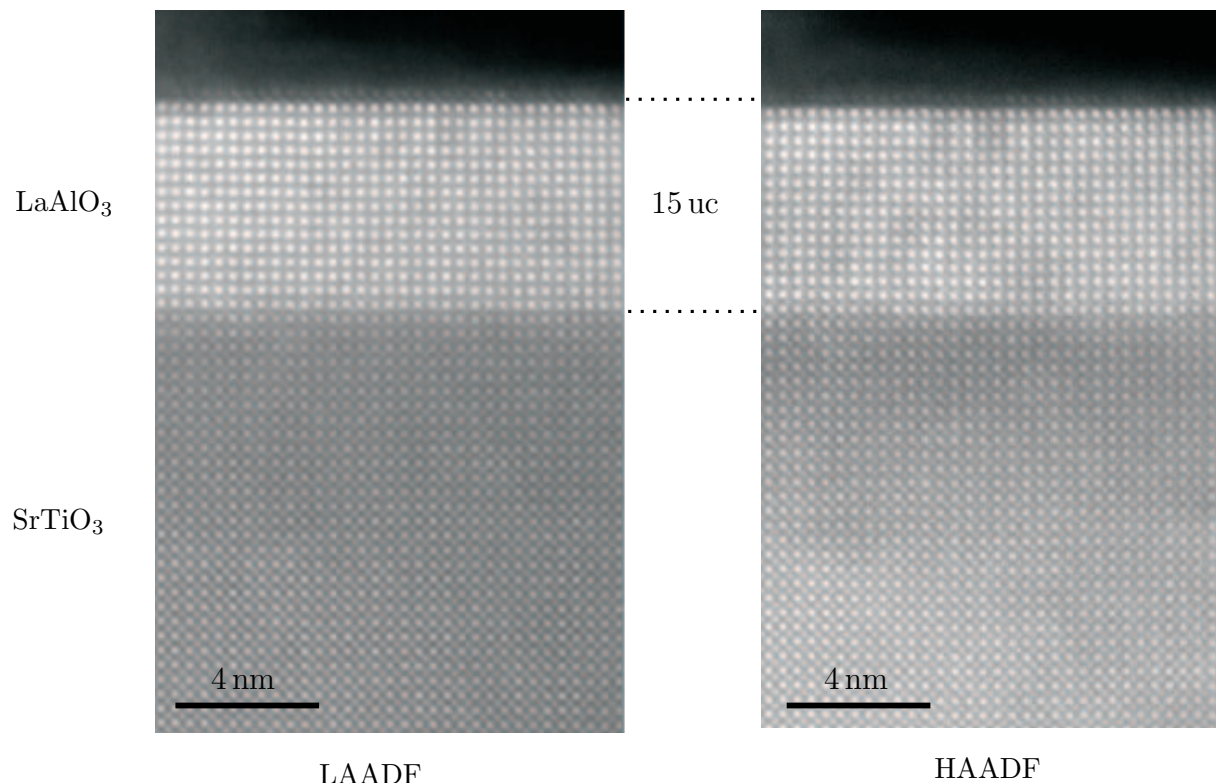


Figure 3.15: Cross-sectional STEM images of a sample with 15 uc of LaAlO_3 (sample L121). Both Low-Angle ADF (LAADF) and High-Angle ADF (HAADF) images are shown. The STEM experiments were done by L. Fitting Kourkoutis and D.A. Muller at the University of Cornell (USA).

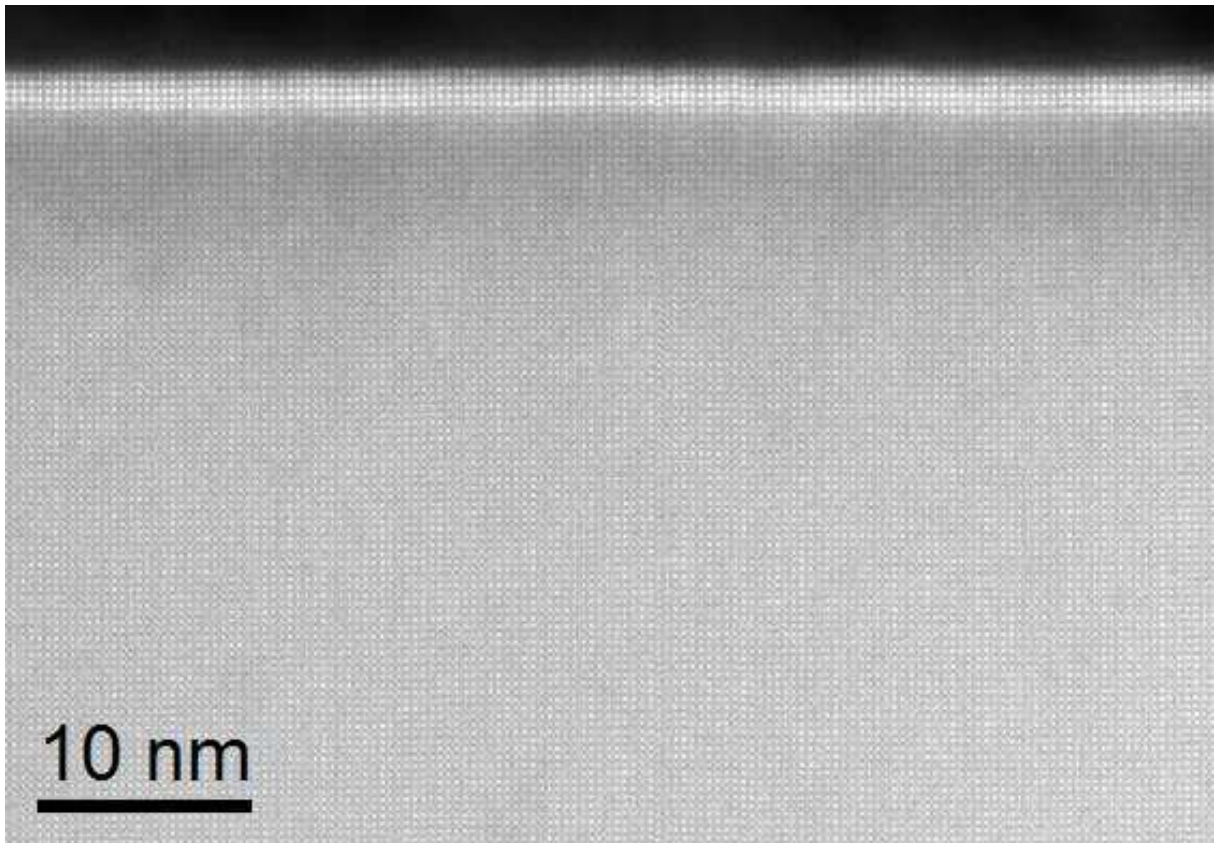


Figure 3.16: Cross-sectional STEM HAADF image ($40 \times 60 \text{ nm}^2$) of a 5 uc thick film of LaAlO_3 (bright) on a SrTiO_3 substrate (greyish) with a capping of amorphous SrTiO_3 (sample L85). La and Sr atoms appear brightest in this image. The STEM experiments were done by L. Fitting Kourkoutis and D.A. Muller at the University of Cornell (USA).

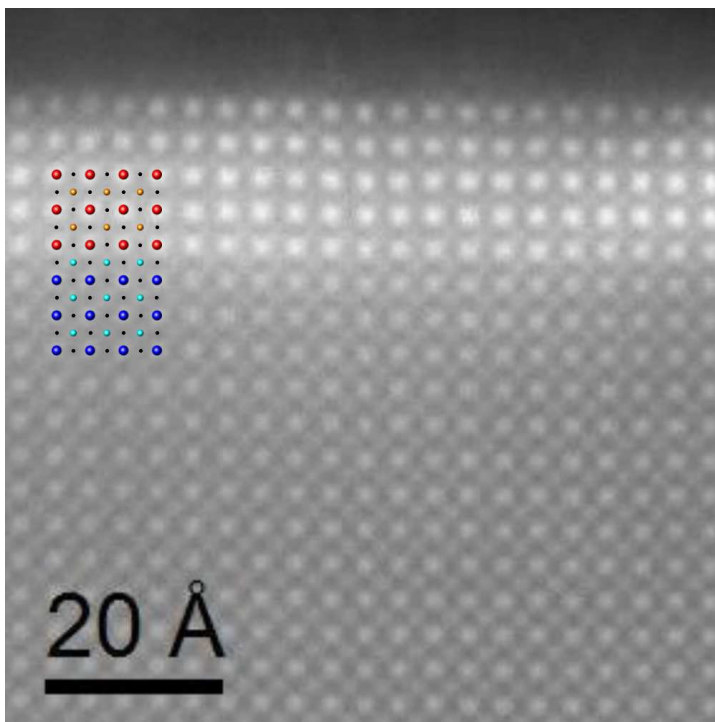


Figure 3.17: Cross-sectional STEM LAADF image ($80 \times 80 \text{ \AA}^2$) of a 5 uc thick film of LaAlO_3 (bright) on a SrTiO_3 substrate (greyish) (sample L85). On the left a sketch of the atomic structure at the interface is shown for illustration (La: red, Al: orange, Sr: blue, Ti: cyan, O: black). The STEM experiments were done by L. Fitting Kourkoutis and D.A. Muller at the University of Cornell (USA).

seen in AFM.

From the STEM images the out-of-plane lattice constant is found to equal 3.78 \AA , in accordance with the XRD experiments. This value suggests either a rather small Poisson ratio as previously reported [79] or out-of-plane relaxation in the thin film [80].

3.6 Electronic Transport Measurements

This chapter concludes with a description of the general experimental setup for the measurement of electronic transport properties. In the next chapters the detailed sample structures and corresponding results will be presented .

3.6.1 Contacts

Since the electronically conducting interface between LaAlO_3 and SrTiO_3 is encapsulated by insulators, special care has to be taken to provide good electrical contacts.

Several contacting methods have been reported. A. Ohtomo *et al.* [13] used laser-annealed, ohmic contacts to reach the buried interface. M. Huijben *et al.* [81] applied wire-bonded contacts to the samples, which were found to also work for our $\text{LaAlO}_3/\text{SrTiO}_3$ heterostructures. Gold pads, which were sputtered on a Ti adhesion layer on the sample, were used by A. Kalabukhov *et al.* [82]. Although these approaches seem all to work, they rely either on micro cracks of ill-defined density and depth (for laser-annealing and wire-bonding) or on unknown Ti diffusion through the LaAlO_3 . To avoid these uncertainties a different contact method was developed for our samples (see Fig. 3.18). Lithographically defined holes of some $100 \mu\text{m}$ length and $\approx 80 \text{ nm}$ depth were Ar-ion etched (ion gun from Commonwealth Scientific Corp., beam voltage 500 V) and then filled by *ex situ* sputter deposition of Au (Agar Sputter Coater 103). This technique leads to a defined contact to the electron gas at the interface, and was therefore employed for all the samples described in this thesis. It is noted here that the contact to the q2-DEG is not only mediated by the sputtered gold, but also by a thin sheet of ion-etched SrTiO_3 which is formed at the inner surface of the generated holes (as ion-etching causes oxygen deficiency, and thus conductivity in $\text{SrTiO}_{3-\delta}$).

For contacting the surface of the LaAlO_3 film, or for fabricating a gate electrode, gold was sputtered without prior ion etching.

3.6.2 Measurement setup

After the contacts were made, the samples were mounted on connector boards (see Fig. 3.19a), which are designed to fit into the various experimental setups of our labs. From the boards the contacts on the sample are connected with up to ten contact pads via wire bonds (Al-Si 1% wires, bonder from Marpet Enterprises Inc., Model 1204W). The boards with the samples are then mounted on a probe, consisting of a room-temperature connector box, a steel tube and a low temperature sensor head. Ten elastically supported contact pins connect the board electrically with the wires coming from the room temperature environment, while the sample remains thermally decoupled. Further parts of the

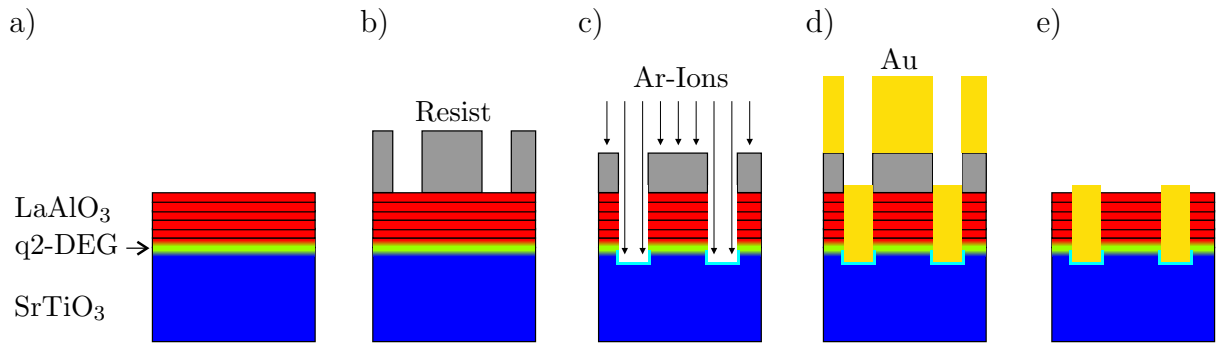


Figure 3.18: Illustration of the developed contacting method. **a**, The conducting interface is buried underneath the LaAlO_3 film. **b**, Contact areas are defined by lithography. **c**, Ar-ion etching creates holes reaching down to the interface. At the inner surface of the holes in the substrate a thin layer of conducting $\text{SrTiO}_{3-\delta}$ (shown in cyan) is generated by the ion-etching process. **d**, The holes are filled *ex situ* with sputtered Au. **e**, A final lift-off step removes the resist, and the buried electron gas can now be contacted from the sample surface.

sensor head are a temperature-sensor (Si-Diode, GaAs-Diode or Cernox) and a resistive heater, which are connected to a temperature controller (Lakeshore 340).

The setup for transport measurements is shown schematically in Fig. 3.19b. Electronic sample properties are analyzed using computer controlled current and voltage sources (Keithley model 238 and 2400) and multimeters (Keithley model 2000 and 2182), which are connected to the sample probe via shielded BNC cables. Different setups were used for temperature dependent measurements from 300 K to 4.2 K. To vary the temperature the probe can either be set in different heights in a dewar with liquid helium or be mounted

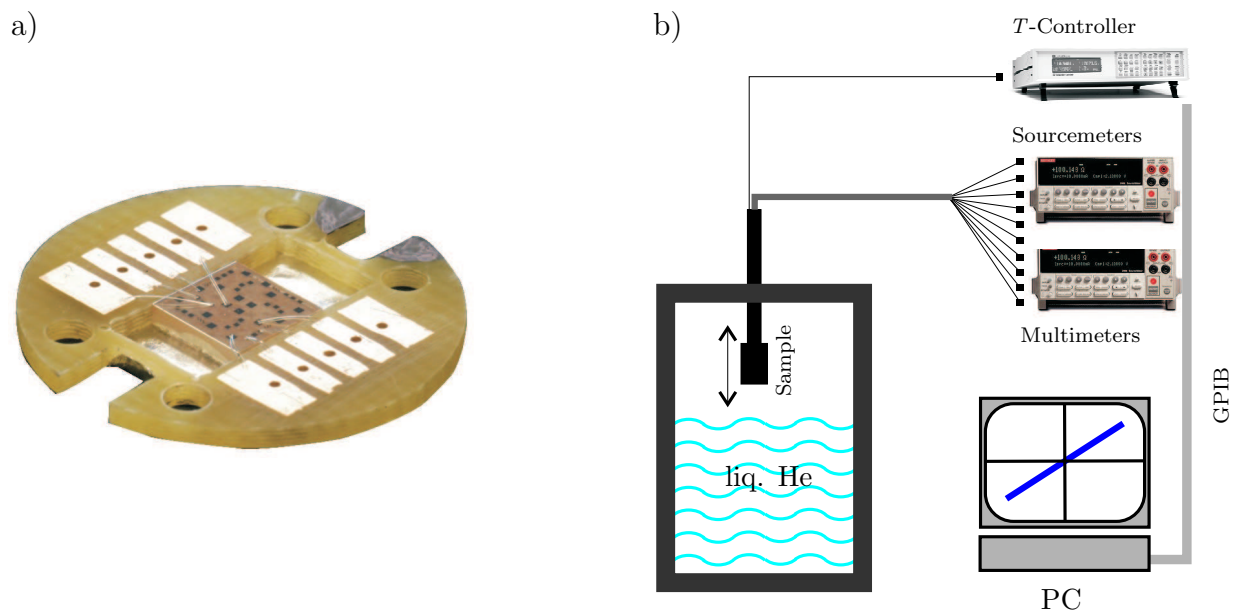


Figure 3.19: Setup for electronic transport measurements. **a**, Photo of a sample mounted on a connector board and contacted by wire bonds. **b**, Sketch of the experimental setup used for the transport measurements.

into a flow cryostat (Oxford Instruments). In the latter, temperatures between ≈ 4 K and 310 K can be stabilized by controlling the flow of preheated He-gas around the sample. Additionally magnetic fields up to ± 8 T can be applied either in parallel or perpendicular direction to the sample surface, enabling magnetoresistance and Hall effect experiments.

3.7 Summary

This chapter presented the experimental methods employed in the work of this thesis for the preparation of the $\text{LaAlO}_3/\text{SrTiO}_3$ heterostructures.

A special termination procedure creates atomically flat, TiO_2 -terminated SrTiO_3 substrates, with 1 uc high steps and terraces. On these substrates films of LaAlO_3 are grown by PLD to a thickness of several unit cells. The film thicknesses are controlled by monitoring the RHEED oscillations, which are caused by the layer-by-layer growth of LaAlO_3 . At the interface between film and substrate this procedure leads to a TiO_2/LaO stacking sequence. Unless otherwise stated only such n -type interfaces are discussed in the rest of this work. Standard parameters for the film growth by PLD are a deposition temperature of $\approx 770^\circ\text{C}$, an energy density on the target of ≈ 0.8 J/cm², and an oxygen pressure of $\approx 10^{-5}$ mbar.

The sample characterization performed after film deposition reveals a high quality of the prepared $\text{LaAlO}_3/\text{SrTiO}_3$ heterostructures. For a film thickness $d_{\text{LAO}} < 25$ uc AFM micrographs show the same step-and-terrace structure of the sample surface as found for the TiO_2 -terminated substrate. Thicker films show cracks, caused by relaxation of the strain due to 3% lattice mismatch between LaAlO_3 and SrTiO_3 . XRD and STEM confirm the epitaxial growth of the films and reveal a homogenous film thickness. The number of LaAlO_3 unit cells equals the number of observed RHEED oscillations during film growth. The interface to the SrTiO_3 substrate is found to be atomically sharp.

The first goal of this thesis to grow such heterostructures with the film thicknesses controlled on the unit cell level and with defined interfaces has therefore been reached. The described sample preparation led to reproducible sample properties over the complete duration of this thesis. All these achievements now opened the route to study the interface between LaAlO_3 and SrTiO_3 in detail.

To electronically access the $\text{LaAlO}_3/\text{SrTiO}_3$ interface, which is buried underneath the insulating LaAlO_3 , a new method for contacting was developed. It uses lithographically defined holes generated by Ar-ion etching, filled with gold by sputtering.

Finally the electronic transport measurement setup was presented, which was used in the experiments described in the following chapters to analyze the heterostructure properties and to study the effects governing the conductivity generated at the interface between the band-insulators LaAlO_3 and SrTiO_3 .

4 Electronic Transport Properties of the $\text{LaAlO}_3/\text{SrTiO}_3$ Interface

As described in the previous chapter, the $\text{LaAlO}_3/\text{SrTiO}_3$ heterostructure can be prepared reproducibly with precision on the atomic level. The focus of this chapter is on the studies of the electronic properties of $\text{LaAlO}_3/\text{SrTiO}_3$ samples ³.

The structure of this chapter is as follows. After introducing the contact arrangements used, the conductivities and charge carrier densities of the samples grown under the standard conditions used in this work will be discussed. Additionally the large effects on the electrical conductivity by varying the LaAlO_3 film thickness are shown.

Because interfaces in this heterostructure are a novel research topic only few publications reported on it. Obviously it was important to establish how far, and under which conditions samples from different groups can be compared, and how well the transport properties match. Therefore it will subsequently be discussed why the used deposition parameters were chosen, and it will be shown that the electronic properties of the samples are in accordance with the polarity discontinuity model.

At the start of this thesis all groups working on $\text{LaAlO}_3/\text{SrTiO}_3$ interfaces were restricted to study unpatterned samples. Always the LaAlO_3 film, and thus also the electron gas at the interface, extended over the complete sample area. Such unpatterned samples were contacted in two different geometries.

The first option is to use a van-der-Pauw configuration [83], which has contacts at the boundary of the sample (see Fig. 4.1a). This method allows to obtain the specific resistance or the sheet resistance ⁴ of almost any arbitrarily shaped sample, by measuring the resistance of different configurations for current and voltage contacts. For Hall measurements, voltage contacts perpendicular to the current direction were chosen. From the sign of the Hall voltage the charge carriers can be identified to be electrons (n -type) or holes (p -type). The sheet carrier density n_s is obtained via

$$n_s = \frac{BI}{qV_H} \quad (4.1)$$

with B the applied perpendicular magnetic field, and q the charge of the carriers.

The second option for the contact geometry is shown in Fig. 4.1b, with two voltage contacts between the two current contacts. Note that the voltage contacts were set off by $500\ \mu\text{m}$ from the straight line connecting the current contacts to reduce the flow of charges across the contact Au. Preparing several of such setups on different positions on the sample and measuring the resistance allows to check the spatial homogeneity of the electronic transport properties. A clear disadvantage is that Hall measurements are not possible. For these contacts the sheet resistance was calculated as $R_s = \sigma_s^{-1} = 4.3 R$ from the measured resistance R . The factor 4.3 was determined from three reference

³Unless otherwise stated only n -type interfaces (TiO_2/LaO stacking) are discussed.

⁴As the precise thickness of the conducting layer is not known, sheet resistances R_s are always calculated in units of Ω/\square . The unit distinguishes R_s from the measured resistances R . For a bar of length l and width b one finds the relation $R = R_s l/b$.

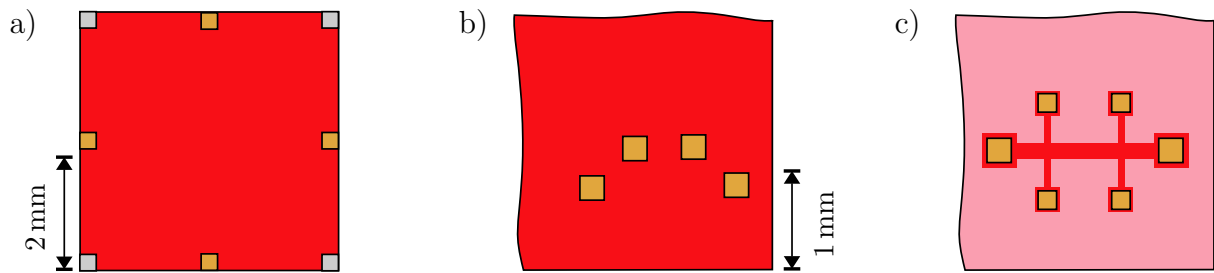


Figure 4.1: Sketch of different contact configurations, which were used for resistance and Hall effect measurements. **a**, Van-der-Pauw setup. The contacts shown in orange or those shown in grey were used as alternative options. **b**, Setup with voltage contacts set off the line connecting the current contacts. **c**, Contacts on patterned bridges (see Sec. 6) with defined geometries of different sizes.

samples of $\text{YBa}_2\text{Cu}_3\text{O}_{7-\delta}$, which were measured with this contact setup and again after patterning defined bridges (using photolithography and phosphorous acid) to obtain the specific resistance.

After a patterning process was successfully developed in the course of this thesis (see Chapter 6) structured bridges were used, as shown schematically in Fig. 4.1c. For the first time sheet resistances and Hall voltages were then measured on bridges with well defined geometries.

All the configurations discussed before allow for four-point measurements of the conductivity without contributions from contact resistances.

Control measurements revealed that under ambient light charge carriers were generated in the samples by photodoping. This photodoping was measured as a function of wavelength by M. Huijben [84] who observed an abrupt change in conductance upon illumination at a wavelength that precisely corresponds to the bandgap of SrTiO_3 ($\lambda < 380$ nm). This suggests an intrinsic optical absorption with an electron excited from the valence band into the conduction band. To avoid an influence of this additional photo-generated conductivity ($\approx 10\%$ of the measured conductivity in light at 300 K), which decays over several hours, the samples were always kept in dark cryostats for at least 24 hours prior measurements. The additional photoconductivity has to be taken into account whenever the sample is exposed to photons with an energy larger than the SrTiO_3 bandgap, as for example in spectroscopic studies using X-rays.

The results of these transport measurements using the described contact setups will be discussed next.

Like the first report by Ohtomo and Hwang [13] on the $\text{LaAlO}_3/\text{SrTiO}_3$ heterostructure, and as predicted by the polar catastrophe scenario, a conducting electron gas was found at the interface between TiO_2 -terminated SrTiO_3 and LaAlO_3 in our samples. The following data on electronic transport measurements summarize the properties of samples grown under the standard deposition conditions, which were described in the previous chapter.

The $R_s - T$ curves of samples with different thicknesses of LaAlO_3 are shown in Fig. 4.2. Conducting interfaces are observed with a typical drop in sheet resistance of more than

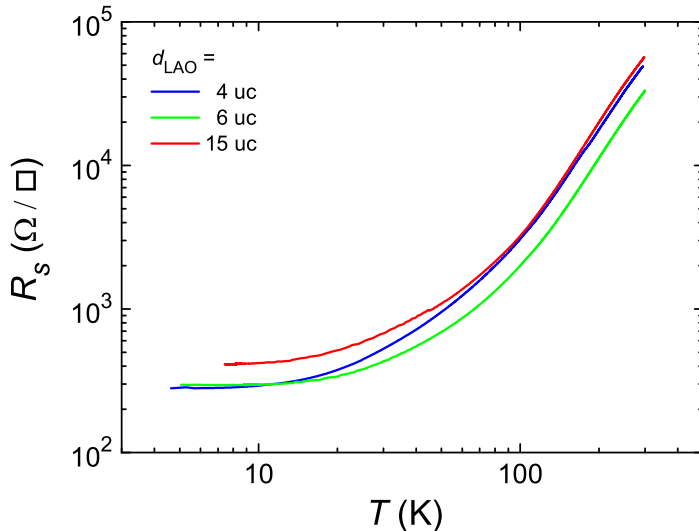


Figure 4.2: R_s - T dependence measured on n -type samples with 4 uc (sample L35), 6 uc (sample L80), and 15 uc (sample L102) of LaAlO_3 grown under the standard conditions ($p(\text{O}_2) = 2 \times 10^{-5}$ mbar, $T = 770^\circ\text{C}$). For these measurements bias currents of $10\ \mu\text{A}$ were used.

two orders of magnitude from 300 K down to 4.2 K. No minima are observed in the $R(T)$ curves. The corresponding sheet conductances are $\sigma_s \approx 2 \times 10^{-5}\ \Omega^{-1}$ (at 300 K) and $\sigma_s \approx 3 \times 10^{-3}\ \Omega^{-1}$ (at 4.2 K). Reported values in literature are of the same order of magnitude [14, 81, 85]. Section 4.2 will discuss in more detail the problems of comparing experimental results with those of other groups.

A critical point, which had to be clarified, was the location of the conducting layer in the sample.

In studies on samples contacted without Ar ion-etched holes, Au being sputtered directly onto the LaAlO_3 surface, insulating behavior was found, which confirmed that the conducting layer is not located on the surface of the LaAlO_3 .

The sheet resistances of the samples shown in Fig. 4.2 are independent of the thickness of the LaAlO_3 film. If the film itself was conducting R_s would likely scale with the number of unit cells⁵.

To test for bulk conduction deep in the SrTiO_3 substrate the surface layer ($\approx 10\ \mu\text{m}$) of a conducting sample was removed by polishing (polishing machine 1PM51, Logitech) with $0.25\ \mu\text{m}$ grained diamond paste. The remaining substrate was insulating.

Therefore it is concluded that the observed transport properties are indeed caused by a conducting layer which is located at the interface or very close to it.

In another experiment, the role of the SrTiO_3 substrates was investigated. As already stated in Chapter 2, those single crystals usually contain a tiny amount of dopants, which make the SrTiO_3 perfectly transparent without any hue, so that the crystals can also be used as synthetic gems. To exclude any influence from these dopants LaAlO_3 films were also grown on special SrTiO_3 substrates, which were fabricated without any additional elements⁶. These substrates show a yellowish hue, typical for pure SrTiO_3 single crystals.

⁵The special case of samples with up to 3 uc of LaAlO_3 is discussed in detail in Sec. 4.1

⁶Substrates obtained from eSCeTe Single Crystal Technology B.V., Enschede, Netherlands

The transport properties of these n -type $\text{LaAlO}_3/\text{SrTiO}_3$ heterostructure samples were not affected by the different SrTiO_3 substrates. It is therefore concluded that these dopants in SrTiO_3 have no detectable influence on the electron gas at the interface. For this reason for the rest of the experiments the standard SrTiO_3 substrates were used.

With the conductivity found to be confined to the $\text{LaAlO}_3/\text{SrTiO}_3$ interface, it is necessary to clarify if the present one unit cell high steps affect the transport properties.

If the electron gas only forms directly on terraces the intra-terrace resistance is likely lower than the inter-terrace resistance. It was not possible to check for an influence on unstructured samples, so this experiment was delayed until patterning of defined tracks of the electron gas became possible (see Chapter 6). Then the influence of the step-orientation on the transport properties was investigated by varying the angle between the measurement bridge and the steps. The experiments showed that effects from the step-orientation are, if present at all, smaller than the standard scatter of 10% found for the resistance on different positions on one sample. The electron gas at the interface thus couples across the unit cell steps.

According to Hall measurements at all temperatures the carriers are negatively charged with sheet densities $n_s \approx 10^{13} \text{ cm}^{-2}$. The exact value of the carrier density was found to vary slightly over years, with n_s ranging from $1 \times 10^{13} \text{ cm}^{-2}$ to $7 \times 10^{13} \text{ cm}^{-2}$. Figure 4.3 shows the typical temperature dependence of n_s with a maximum carrier density around 100 K followed by a decrease to the lowest values at 4.2 K.

The sign of the charge of the carriers was never disputed in literature, in contrast to the value of the magnitude. Reported carrier densities of $\text{LaAlO}_3/\text{SrTiO}_3$ samples grown under similar conditions usually are approximately a factor of 5 higher, especially for $T \approx 300 \text{ K}$ [14, 81, 85] (see also the discussion on oxygen vacancies at the end of this section).

From the simple polarity discontinuity model, a planar density of half an electron per unit cell is expected, which corresponds to $n_s = 5 \times 10^{14} \text{ cm}^{-2}$, but this value just provides

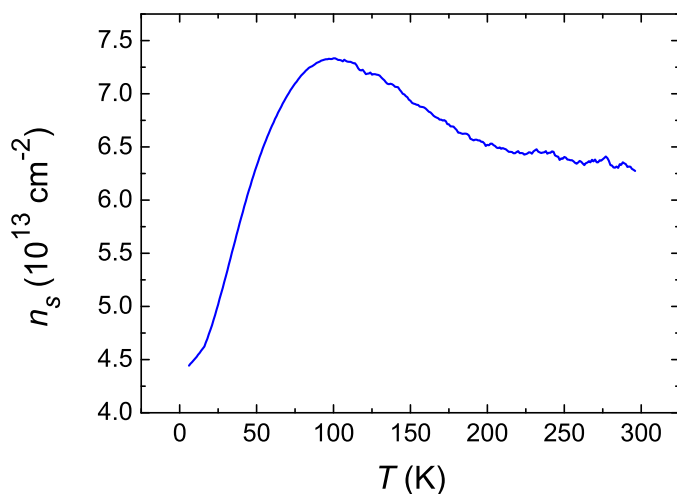


Figure 4.3: Plot of the sheet carrier density as a function of temperature for a sample with 5 uc of LaAlO_3 (sample L51) grown under standard conditions. The sheet charge carrier density is $n_s \approx 10^{13} \text{ cm}^{-2}$. According to the sign of the Hall voltage the charge carriers are electrons.

an upper limit and might be reduced in a more complex model. The measured charge carrier density in our samples corresponds to $\approx 1/20$ electron per unit cell in the plane.

The corresponding mobilities $\mu = (n_s R_s q)^{-1}$ are $\approx 500 \text{ cm}^2 \text{ V}^{-1} \text{ s}^{-1}$ and $\approx 2 \text{ cm}^2 \text{ V}^{-1} \text{ s}^{-1}$ at 4.2 K and 300 K respectively. These mobilities are high, but smaller than the best values reported in literature [13, 82, 86], probably because of the growth conditions used, as discussed at the end of this section.

Upon application of a magnetic field oriented parallel to the surface normal the resistance increases (see Fig. 4.4), predominantly at low temperatures. At $T = 4 \text{ K}$ a pronounced magnetoresistance (MR) is observed (Fig. 4.5). By applying the magnetic field B in this direction a positive MR of some 10 % at 8 T is observed, with a parabolic dependence for fields up to $\approx 4 \text{ T}$ (see Fig. 4.5a). Remarkably, a negative MR is found for B parallel to the interface plane. Depending on the direction of the measurement current I with respect to B the MR at 8 T is $\approx -1.5 \%$ ($B \parallel I$) or $\approx -5 \%$ ($B \perp I$) (see Fig. 4.5b).

For a two-dimensional electron system with sufficiently high mobility signatures of quantum Hall effect (QHE) and Shubnikov-de Haas (SdH) oscillations are expected in the transport measurements at low temperatures and high magnetic fields. These features have been observed in semiconductor heterostructures and in $\text{ZnO}/\text{Mg}_x\text{Zn}_{1-x}\text{O}$ oxide multilayers [12]. One detrimental fact for the observation of the QHE in our samples is that due to the larger carrier density of the oxide q2-DEG, as compared to semiconductors, the fill factor ν of Landau levels in magnetic fields is proportionally larger ($\nu = n\phi_0/B$, with ϕ_0 the magnetic flux quantum and B the applied magnetic flux density), so that QHE induced oscillations are expected to occur at very large field strengths only. Compared to our $\text{LaAlO}_3/\text{SrTiO}_3$ heterostructures, in the $\text{ZnO}/\text{Mg}_x\text{Zn}_{1-x}\text{O}$ system the charge carrier densities are at least one order of magnitude smaller, and the mobility is larger by a factor of 5–10 at low temperatures, which facilitates the observation of the QHE.

None of the $\text{LaAlO}_3/\text{SrTiO}_3$ samples prepared in the course of this work showed oscillations in R - B measurements at 4 K for magnetic fields up to 8 T. The absence

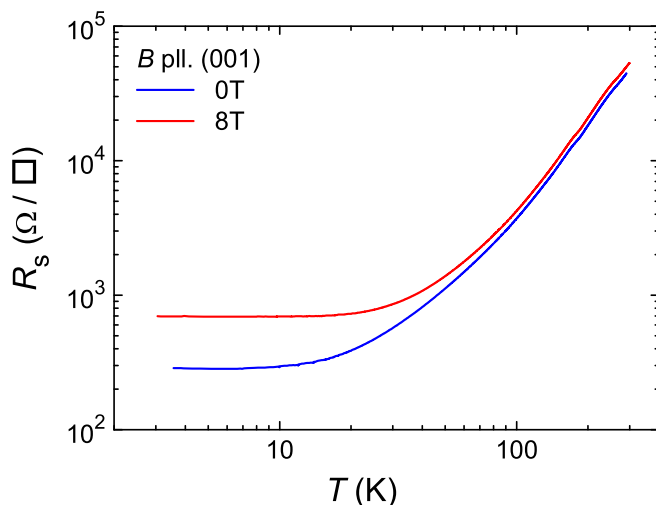


Figure 4.4: Sheet resistance as a function of temperature for a sample with 14 uc of LaAlO_3 (sample LGB3) measured with no magnetic field applied and with 8 T applied parallel to the interface normal. For this measurement a current of $10 \mu\text{A}$ was used.

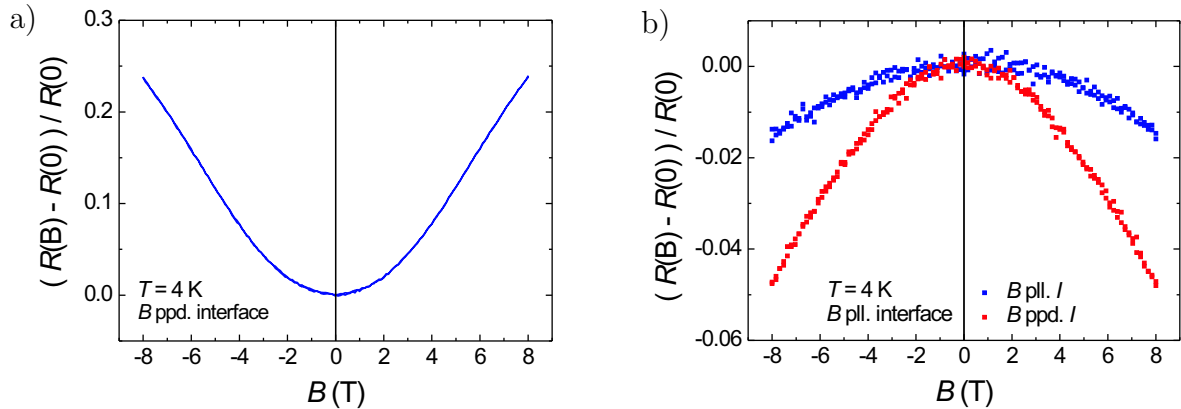


Figure 4.5: Magnetoresistance (MR) for a standard sample with 10 uc of LaAlO_3 on SrTiO_3 (sample LGB10, bridge of $5 \mu\text{m}$ width and $35 \mu\text{m}$ length, for patterning process see Chapter 6) at $T = 4$ K. **a**, MR for B perpendicular to the interface. **b**, MR for B parallel to the interface, with $B \perp I$ and $B \parallel I$. For this measurement a current of 50 nA was used. The sheet resistance with no magnetic field applied is $R_s(0 \text{ T}) = 460 \Omega/\square$.

of oscillations was additionally checked by G. Koster (Stanford University, USA) on one of our samples (sample L57, 5 uc of LaAlO_3) at 1.8 K up to 14 T with the same result. In contrast to this, A. Ohtomo *et al.* [13] and G. Herranz *et al.* [87] reported MR oscillations in the $\text{LaAlO}_3/\text{SrTiO}_3$ system. As discussed later, the differences are related to the used growth conditions.

For our samples all the transport properties described before were checked to be stable over a timespan of at least a year. The samples were thereby stored in dryboxes.

4.1 Thickness Dependence of the Electronic Properties

It was already shown that the sheet resistance of conducting samples is independent of the LaAlO_3 film thickness. This is in agreement with the simple polarity discontinuity model, which predicts that always the same density of electrons is found at the interface in order to avoid the diverging potential in the sample.

Experimentally, our study of conducting $\text{LaAlO}_3/\text{SrTiO}_3$ interfaces was limited by the upper critical thickness of the LaAlO_3 layer. If the films are grown too thick, $d_{\text{LAO}} > 25$ uc, the samples are insulating, which is probably caused by the appearance of strain-related cracks (see Fig. 3.12). Such samples do not even show photoconductivity when exposed to light. Because the area between the cracks ($\approx \mu\text{m}^2$) was too small to be measured separately, it was not possible to check if the conducting interface is interrupted only at the cracks, or if the whole sample becomes insulating. Therefore the investigation of conducting samples is limited to $\text{LaAlO}_3/\text{SrTiO}_3$ heterostructures with the number of LaAlO_3 unit cells lower than the upper critical thickness of ≈ 25 uc.

It was already shown that samples with 4 uc, 6 uc, and 15 uc of LaAlO_3 have a conducting interface with similar conductivities. It was also found that samples of bulk SrTiO_3 ,

with no LaAlO_3 film deposited, are insulating. Raising the question of how the transition between these two fundamentally different transport properties occurs upon increasing the film thickness led to an amazing discovery, which triggered many of the experiments in this thesis.

Experimentally, the transition was investigated by growing samples with varying LaAlO_3 thicknesses, controlled on the unit cell level, and measuring the sheet conductivities and carrier densities. The corresponding data, shown in Fig. 4.6, have a surprising result: the interface conductivity does not rise continuously as a function of the number of LaAlO_3 unit cells.

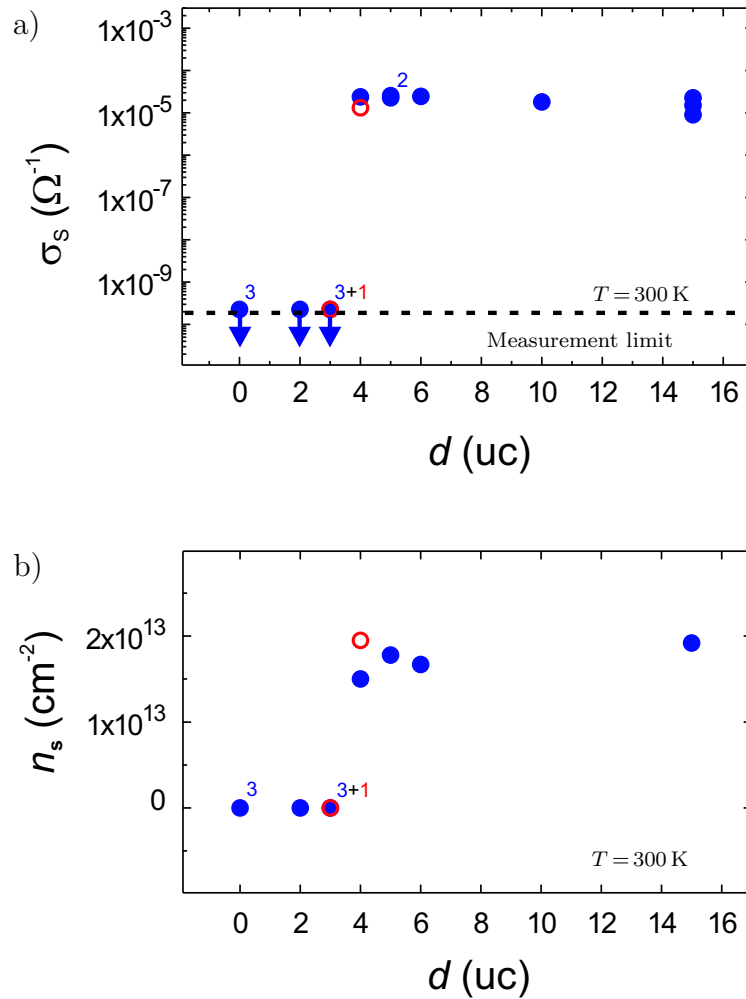


Figure 4.6: Influence of LaAlO_3 thickness on the electronic properties of the $\text{LaAlO}_3/\text{SrTiO}_3$ interfaces. The data were taken at 300 K. **a**, Sheet conductivity and **b**, Carrier density of the heterostructures plotted as a function of the number of their LaAlO_3 unit cells. The data shown in blue and red are those of samples grown at 770°C and 815°C , respectively. The numbers next to the data points indicate the number of samples with values that are indistinguishable in this plot. Published in Ref. [75].

At a critical LaAlO₃ film thickness of $d_c = 4$ uc the conductivity changes strongly. All our samples with $d < 4$ uc are insulating for all T ($\sigma_s < 2 \times 10^{-10} \Omega^{-1}$, limited by the measurement setup) and all those with $d \geq 4$ uc are conducting with conductivities of $\sigma_s \approx 2 \times 10^{-5} \Omega^{-1}$ (at 300 K) and $\sigma_s \approx 3 \times 10^{-3} \Omega^{-1}$ (at 4.2 K), and sheet charge carrier densities of the order of 10^{13} cm^{-2} at all T . By increasing the LaAlO₃ film thickness by only one single unit cell from 3 uc to 4 uc an electron gas is generated at the LaAlO₃/SrTiO₃ interface.

Once the conducting interface is formed, the transport properties were not found to change with increasing thickness of the LaAlO₃ film. This step-like dependence was reproducibly found during the duration of this thesis.

Can the observed critical thickness phenomenon be understood in the framework of electronic reconstructions at the interface? To answer this question, let us first recall the driving mechanism in the polarity discontinuity model. The polar catastrophe leads to an electric potential, V_{LAO} , across the LaAlO₃ that diverges with the number of unit cells, n . By moving electrons into the interface the heterostructure can avoid this divergence. Assuming that the energy needed to activate electrons in LaAlO₃ such that they can move, ΔE_{mobile} , does not depend on n suggests that the number of unit cells has to exceed a critical value, n_c , for the electronic reconstruction to become energetically favorable:

$$V_{\text{LAO}} = nV_{\text{uc}} > \Delta E_{\text{mobile}} \quad \Rightarrow \quad n_c \approx \frac{\Delta E_{\text{mobile}}}{V_{\text{uc}}} \quad (4.2)$$

These simple considerations predict the existence of a critical thickness d_c for the interface to become conducting, thus as is observed in the experiments.

To investigate whether the transport properties of the samples, and especially the metal-insulator transition, depend on the film growth conditions and the related specific sample microstructure, several LaAlO₃ films were also deposited at an elevated temperature (815°C as compared to the standard value of 770°C). It was not possible to obtain higher temperatures with the resistive heater used. The data for those samples are shown by red circles in Fig. 4.6 and reveal that the electronic properties of the electron gases are virtually identical, independent of the deposition temperature.

In another set of experiments the growth rate of the LaAlO₃ film, and thus the time which the samples stay at the deposition temperature, was varied from 0.6 nm/min to 2.4 nm/min. No changes in the electronic properties or the critical thickness of the samples were found.

In the years that followed, this step-like change from insulating to conducting behavior exactly between three and four unit cells of LaAlO₃ was reproduced by groups at the universities of Stanford (USA), Chalmers (Sweden), Twente (Netherlands), Geneva (Switzerland), Tokyo (Japan), and Naples (Italy).

Therefore one can conclude that the transition is robust against changes in deposition temperature or deposition rate and also it is independent of the details of the PLD system used.

A film thickness dependence of the transport properties was also observed for samples measured in light. While for LaAlO₃ layers up to 2 uc no photoconductivity is induced,

heterostructures with 3 uc of LaAlO_3 are conducting in light with sheet resistances of some $100\text{ k}\Omega$. They become insulating again when brought back to darkness. This result suggests that already for a subcritical film thickness of 3 uc the formation of a conducting interface is strongly supported, but no mobile charge carriers are present, so that conducting behavior is only found when additional photo-generated electrons are induced from the SrTiO_3 .

Furthermore, control measurements were performed to exclude that the critical-thickness phenomenon is simply caused by an effect that is generated by the contact between the Au, the ion-etched SrTiO_3 , and the q2-DEG. To check for a possible influence, transport properties were studied on samples that were patterned to have conducting interfaces with 5 uc thick LaAlO_3 layers in the areas in which the contacts were placed and subcritical, 2 uc or 3 uc thick LaAlO_3 on the bridges connecting these areas (for details of the applied patterning process see Chapter 6). So the contact to the 2 uc or 3 uc thick areas was now via the interfacial electron gas. The subcritical areas were found to be insulating and thereby provided evidence that the metal insulator transition is not contact related, but indeed is a property of the q2-DEG.

In $\text{SrTiO}_3/\text{LaAlO}_3/\text{SrTiO}_3$ heterostructures containing stacked p - and n -type interfaces the effect of changing the LaAlO_3 thickness was studied before by M. Huijben *et al.* [81]. A reduced conductivity was found for samples in which the two interfaces were spaced by less than 6 uc, but in strong contrast to our results in these experiments even samples with only one unit cell of LaAlO_3 were well conducting. To explicitly check if an additional layer of epitaxial SrTiO_3 on top drives samples with a subcritical thickness of LaAlO_3 conducting one sample was grown with 2 uc of LaAlO_3 covered by 10 uc of SrTiO_3 (sample L175). Also for this heterostructure insulating behavior was found.

Until 2007 the $\text{LaAlO}_3/\text{SrTiO}_3$ system was the only one known to show such a striking thickness dependence of the conductivity. Then Y. Hotta *et al.* [88, 89] reported on their experiments on $\text{LaVO}_3/\text{SrTiO}_3$ interfaces. In the ionic limit this system presents a similar polarity discontinuity as in $\text{LaAlO}_3/\text{SrTiO}_3$ with TiO_2^0 on the substrate surface followed by LaO^+ and then VO_2^- in the film. Notable differences between both systems are that LaVO_3 is a Mott-insulator, as compared to band-insulating LaAlO_3 , and the large range of valence states (2+ to 5+) for vanadium oxides as compared to the few degrees of freedom for LaAlO_3 . Also in the $\text{LaVO}_3/\text{SrTiO}_3$ system a conducting interface is formed and a critical thickness of $d_c = 5$ uc of the LaVO_3 film was found for the interface to become conducting.

The simple polarity discontinuity model might not capture all of the physics governing the interface properties. To gain more insight into the mechanism causing the critical thickness behavior it would be helpful to have more sophisticated theoretical calculations. As already stated in Sec. 2.4, several groups performed DFT calculations and found the $\text{LaAlO}_3/\text{SrTiO}_3$ interface to be conducting. Unfortunately, only few of these theoretical studies considered several film thicknesses.

In 2008, U. Schwingenschlöggl *et al.* [51] reported a strong dependence of the transport properties on d_{LAO} , with good qualitative agreement to the experiments (enhanced conductivity for thicker films). However in their calculations also samples with 3 uc of LaAlO_3 and less are found conducting. These authors state that this quantitative disagreement

is probably related to the underestimation of the band gap in pure SrTiO₃ by the LDA method.

A theoretical study of S. Hellberg in the supplementary material of Ref. [52] reports a transition from insulating to conducting behavior upon increasing the LaAlO₃ thickness from 3 uc to 4 uc.

For direct comparison of the experimental data with theoretical studies it will be essential to wait for a common picture to emerge from the various calculations, which up to now differ a lot in the applied methods, assumptions, and parameters, and thus also in the results.

Care has to be taken for the comparison of the electronic properties of the samples grown in our lab with those of other reports in literature. It turned out that the sample preparation conditions are an important parameter for the LaAlO₃/SrTiO₃ heterostructures. If improperly chosen, the observation of a q2-DEG at the interface can be impeded by a much larger electronic contribution from the bulk, which led to considerable confusion in the scientific community. In the next section the effects of sample preparation parameters will be discussed and it will be demonstrated that our sample properties are indeed caused by a q2-DEG at the interface.

4.2 Discussion of the Role of Oxygen Vacancies

Several groups claim that the observed conductivity in the samples is caused by oxygen vacancies in the SrTiO₃ substrate, and not related to electronic reconstructions caused by the presence of the LaAlO₃ film. In the following, a possible influence of the oxygen vacancies on the electronic transport properties of the samples will be discussed.

Oxygen vacancies are known to lead to conductivity in SrTiO₃ (see Sec. 2.2). This doping mechanism has been known for a long time [18, 19] and was also claimed to be crucial for the LaAlO₃/SrTiO₃ system. Several groups have analyzed samples with LaAlO₃ films grown at $p(O_2) \leq 10^{-6}$ mbar and looked for oxygen deficiency in the SrTiO₃ substrate. Several techniques, such as *in situ* ultraviolet photoelectron spectroscopy (UPS) [86], MR measurements [87], and cathode- and photoluminescence measurements [82] were applied in those studies. All these methods found the conductivity to be caused by oxygen reduced SrTiO₃. For such samples grown in the “low pressure regime”, the measured resistances are orders of magnitude lower, and the sheet charge carrier densities are orders of magnitude larger than those found for our standard samples. These doped samples exhibit very high mobilities of up to 10⁴ cm²/Vs at 4 K, which attracted considerable attention over the years that followed. Additionally the resistance ratio $R(300\text{ K})/R(4.2\text{ K})$ is about 10³ for these samples, as compared to ≈ 150 for our samples grown under standard conditions. Furthermore oscillations in MR were observed and attributed to doped SrTiO₃ [87].

Such values, which clearly differ from those for standard heterostructures in this work, were already found in the first paper on LaAlO₃/SrTiO₃ interfaces by A. Ohtomo and H.Y. Hwang [13]. Even with a typographic error corrected (Ω instead of m Ω in Fig. 2 of Ref. [13]), the resistances of 26 nm thick LaAlO₃ films on SrTiO₃ are 3 orders lower than those of our samples. They also found much higher carrier densities of up to 10¹⁷ cm⁻². It is already stated in the publication that such a high sheet carrier density would imply

unphysical densities of ≈ 1000 electrons per two-dimensional unit cell if the charges resided at the interface.

These experiments reveal that obviously $\text{LaAlO}_3/\text{SrTiO}_3$ samples grown in the “low pressure regime” contain a large number of oxygen vacancies in the substrate. This causes high bulk conductivity in the SrTiO_3 and hides the much smaller contribution from the electronic reconstruction at the interface, which probably is still present.

Just like in all these reports, also samples grown in our deposition chamber under such a low pressure ($p(\text{O}_2) = 1 \times 10^{-6}$ mbar) have resistances one order of magnitude lower, and charge carrier densities one order of magnitude larger than our samples grown under standard conditions. These values clearly show that oxygen vacancies dominate the electronic transport properties also in our samples grown at $p(\text{O}_2) \leq 10^{-6}$ mbar. It is interesting to note that even when trying to induce oxygen deficiency in the substrate on purpose by growing the LaAlO_3 films in vacuum and at 800°C the obtained sheet resistances were not as small as reported by other groups for similar deposition conditions.

The crucial question obviously is whether in all $\text{LaAlO}_3/\text{SrTiO}_3$ samples the conductivity is exclusively caused by oxygen defects in the substrate, and if electronic reconstruction really leads to interface conductivity if no such doping of the substrate is present.

To clarify this, several experiments were done to gain information on the strength of doping by oxygen defects for $\text{LaAlO}_3/\text{SrTiO}_3$ heterostructures grown at $p(\text{O}_2) \approx 10^{-5}$ mbar. These studies are discussed in the following.

A first hint to the origin of the charge carriers comes from an optical check. Heavily doped SrTiO_3 , which has a greyish to black color (depending on the amount of doping), can already be excluded to be present by the transparency of our samples (see Fig. 4.7).

Insulating behavior, even in light, is found in bare SrTiO_3 substrates exposed to the standard pressure and temperature cycle used for LaAlO_3 film deposition. This insulating behavior remains when the cooldown process is done in the deposition pressure of $\approx 10^{-5}$ mbar instead of the standard pressure of 400 mbar.

Furthermore, one sample with a film thickness of $d = 6$ uc (sample L41) was analyzed by A. Kalabukhov at Chalmers University (Sweden) using cathode-luminescence. Upon irradiation with an electron beam, oxygen reduced SrTiO_3 is known to show a character-

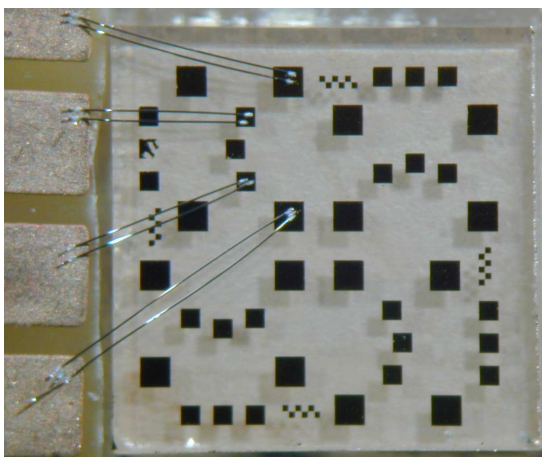


Figure 4.7: Photo of a sample with 5 uc of LaAlO_3 on TiO_2 -terminated SrTiO_3 (sample L34) with contacts via Ar-ion etching and Au sputtering. On the left side a part of the sample holder is visible with wire-bond connections to contacts on the sample.

istic blue light emission [90]. In the investigated sample no indications of oxygen defects were observed under standard measurement conditions [82].

Additionally, a reference sample with 15 uc of LaAlO_3 on SrTiO_3 and a 5 nm capping of amorphous SrTiO_3 was sent to L. Fitting Kourkoutis and D.A. Muller at the University of Cornell (USA) for scanning transmission electron microscopy (STEM) studies [91]. Figure 4.8a shows a high angle annular dark field (HAADF) STEM image of the atomically sharp interface between the LaAlO_3 film and the SrTiO_3 substrate. The image reveals a dark band in the SrTiO_3 close to the interface.

This reduced HAADF intensity at the interface has to be interpreted with care. Bending and tilting of the crystal in that region or distortions of the thin TEM foil due to strain relaxation can result in a reduction of the HAADF intensity [92], and a local tilting of 5-10 mrad of the foil is indeed detected in the thinner regions. A similar tilting was also reported by Maurice *et al.* [79]. This buckling of the sample can lead to a dark band at the interface due to dechanneling of the electron beam. While the presence of oxygen

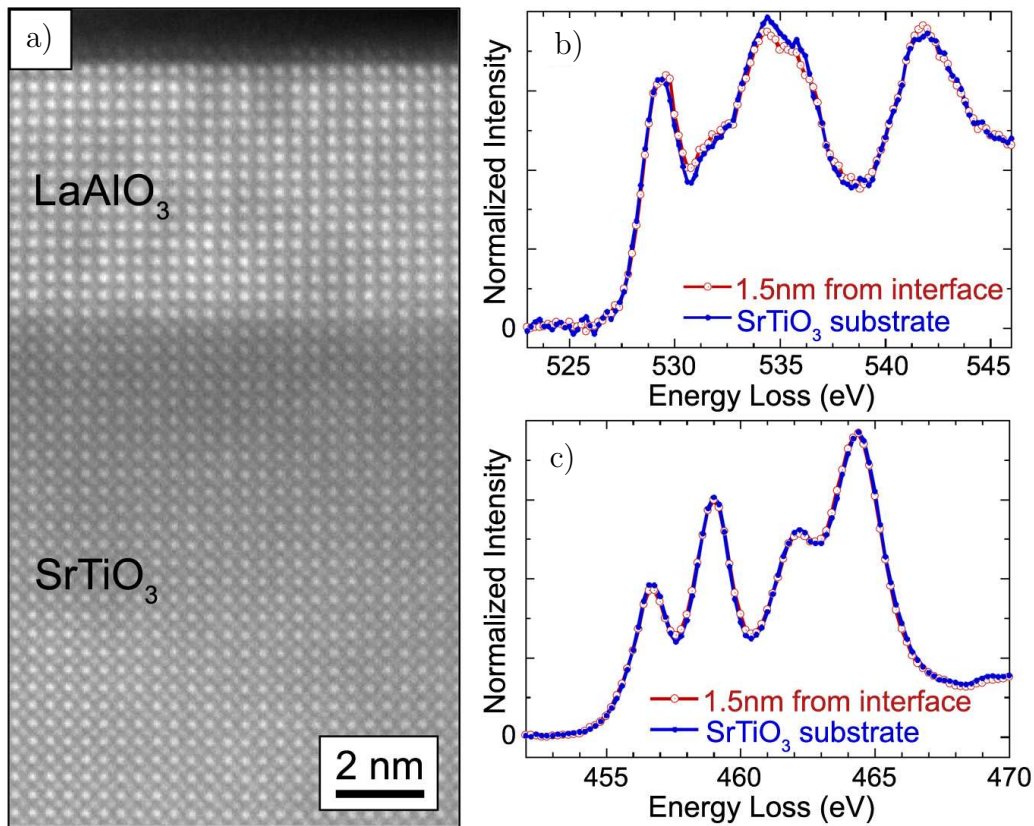


Figure 4.8: STEM and EELS data of a 15 uc thick film of LaAlO_3 on SrTiO_3 (sample L121) grown at $p(\text{O}_2) \approx 10^{-5}$ mbar. **a**, HAADF image showing a coherent interface. **b**, O-K EELS spectra of the SrTiO_3 close to (1.5 nm) and far away from the interface. Even at 1.5 nm from the interface, the O-K fine structure is only very slightly damped compared with with the bulk. **c**, Small changes of the Ti-L_{2,3} fine structure close to the interface are consistent with a small concentration of Ti^{3+} , which falls below the detection limit by 6 nm from the interface and beyond. Measurements were done by L. Fitting Kourkoutis and D.A. Muller at the University of Cornell (USA). Published in Ref. [91].

vacancies in SrTiO₃ can also lead to a reduced HAADF intensity [24], the contrast at low oxygen vacancy concentrations is expected to be patchier than found here, as single vacancies would be observed. Furthermore, a band of oxygen deficient SrTiO₃ would cause an increase in the low angle annular dark field STEM signal in that region, which was not found. Additionally, it is noted that this dark band is also observed for a sample with 3 uc of LaAlO₃ (see Fig. 3.14a), which is insulating. Therefore it is unlikely that the observed contrast is related to the conductivity at the interface.

These considerations lead to the conclusion that the dominant contribution to the observed dark band is the local tilting of the film, and not oxygen vacancies, whose signal would be hidden beneath this much larger contribution. To obtain an upper limit on the extent of changes in electronic structure and composition in the vicinity of the interface electron energy-loss spectroscopy (EELS) in the STEM was used to probe the chemistry of the heterostructure at the atomic scale. For the EELS measurements, the STEM (Tecnai F20-ST) is equipped with a Gatan imaging filter 865-ER. The energy resolution was ≈ 0.6 eV as measured from the FWHM of the zero loss peak at 0.2 eV/channel. The Ti-L_{2,3} and O-K spectra were recorded simultaneously on a 2048 \times 2048 pixel CCD. To increase the signal to noise ratio, five successive spectra, each recorded for 5 s, were averaged. The spectra of these edges close to and far away from the interface are shown in Fig. 4.8b and c. At a distance of 1.5 nm from the interface, the changes in the O-K edge are only very slight, suggesting an upper limit to the oxygen vacancy concentration of 3%. At a distance of 6 nm away from the interface, the changes in the O-K and Ti-L_{2,3} edges compared with bulk SrTiO₃ fall below the noise level ($< 1\%$ oxygen vacancy concentration). The small changes of the Ti-L_{2,3} edges are consistent with a small concentration of Ti³⁺, which can be attributed either to an oxygen deficiency or a compensating interface charge.

While these STEM and EELS experiments can only provide an upper limit on a possible oxygen vacancy concentration, other experimental results are hard to reconcile with a scenario where reduced SrTiO₃ has an effect at all.

One of these results is the insulating behavior found for samples with cracks in the LaAlO₃ film, which delaminated from the substrate in the vicinity of the crack (see Sec. 3.5.1). A substrate conductivity would not be affected by such cracks.

Another evidence against doping by oxygen defects comes from the study of heterostructures containing *p*-type interface. These samples are grown by first depositing a monolayer of SrO on the TiO₂-terminated SrTiO₃ and then depositing the LaAlO₃ film. As described in the experimental section, for the final sample a rougher surface topography in comparison to *n*-type samples is observed in AFM. This roughness indicates that not an atomically flat monolayer of SrO was grown in our experiments, which results in an ill-defined LaAlO₃/SrTiO₃ interface. Therefore heterostructures with *p*-type interface stacking sequences have not been studied in detail. The transport properties of several such samples have been measured nevertheless. All *p*-type interfaces are completely insulating, which provides information on possible doping of the substrate, because any mechanism leading to oxygen vacancy doping in the SrTiO₃ is not expected to be altered by the insertion of a monolayer of SrO in the LaAlO₃/SrTiO₃ heterostructure. This insulating behavior of *p*-type samples was also reported by other groups [13, 84]. J. Nishimura *et al.* [14] studied the transport properties of LaAlO₃ films grown on SrTiO₃ substrates with different coverage of SrO and found that in this way the generation of carriers at the

interface can be systematically controlled. It is not yet clarified why the SrO/AlO₂ interfaces do not display *p*-type conductivity, as predicted by the polarity discontinuity model. The rougher topography and the correspondingly ill-defined interface to the LaAlO₃ film in our samples puts the applicability of the model in question. Insulating behavior also results if holes are present at the interface, but are localized. Another possible explanation is that a tiny number of electrons originating from oxygen vacancies, which are not sufficient to cause conducting behavior in *p*-type LaAlO₃/SrTiO₃ heterostructures, compensates the small positive charge built up by the electronic reconstruction.

Finally the step-like dependence of the interface conductivity on LaAlO₃ film thickness can only be accounted for by doping from growth-induced oxygen defects, if during the sample fabrication oxygen can diffuse well through 3uc thick layers but not through 4uc thick ones. For this case one has to expect that $d \geq 4$ uc samples can be turned into insulators, too, if the diffusion of oxygen through their LaAlO₃ layers is enhanced. To test this prediction a 4uc sample was annealed for 7 days at 400 °C in 20 bar of O₂ (sample L35). This oxidation step did not result in an insulating interface, but reduced the conductance by a factor of 5 for all T . For the interpretation of the annealing experiment one has to keep in mind that apart from possible oxygen vacancy filling also other processes like interdiffusion or modifications of the microstructure can change the resistance. While a tiny amount of oxygen vacancies can not be excluded, it is clear that the dependence of the interface conductivity on the LaAlO₃ thickness together with the annealing experiment result agrees with the behavior predicted for doping by the polarity discontinuity and not with a behavior caused by doping of the substrate. Therefore a good method to check if oxygen vacancies are present in the samples and contribute to the conductivity is to check if samples with 3uc of LaAlO₃ on SrTiO₃ are insulating.

In summary, the electronic transport properties of LaAlO₃/SrTiO₃ samples are dominated by oxygen vacancies in the substrate for deposition pressures $p(O_2) \leq 10^{-6}$ mbar (low pressure regime).

As shown by the various experiments described before, the mobile electrons observed in samples grown at $p(O_2) \geq 10^{-5}$ mbar (high pressure regime), can not be explained by reduced SrTiO₃ and are thus attributed to the electronic reconstruction at the LaAlO₃/SrTiO₃ interface.

The conclusion that several mechanisms are causing the observed conductivity depending on the pressure ranges used during film growth has also been drawn by other groups [85, 93–95] and needs to be kept in mind when comparing transport properties with reports in literature.

4.3 Summary

After the controlled growth of high quality *n*-type LaAlO₃/SrTiO₃ heterostructures was demonstrated in Chapter 3, this chapter dealt with the detailed study of the electronic transport properties. In accordance with the polarity discontinuity model a conducting quasi two-dimensional electron gas is found at the interface in our samples. Several experiments revealed and confirmed that the interface is providing the conductance.

The sheet resistance R_s decreases by slightly more than two orders of magnitude from $\approx 50 \text{ k}\Omega$ at 300 K down to $\approx 300 \Omega$ at 4 K, with a charge carrier density of the order of 10^{13} cm^{-2} for all temperatures. These transport properties are reproducibly obtained for the complete duration of this thesis for samples grown under our standard conditions.

In comparison to values reported for these interfaces, our samples exhibit higher R_s and lower carrier density. This clear difference was traced to the deposition conditions used. It is found that for samples grown in “low” oxygen pressures $\leq 10^{-6}$ mbar oxygen vacancies are induced in the SrTiO_3 , which render it conducting. Several experiments confirmed that this doping of the substrate is not present in samples grown at “high” $p(\text{O}_2) \geq 10^{-5}$ mbar, as used in this work.

For the experimentally accessible parameters of $T = 1.8 \text{ K}$ and $B = 15 \text{ T}$ no quantum Hall effects are observed in the samples, which is not astounding, considering the higher carrier density and lower mobility of the oxide electron gas as compared to electron gases in semiconductors.

While this well known effect of low-dimensional electron systems was not found yet, an amazing phenomenon was revealed when studying the generation of the q2-DEG as a function of LaAlO_3 film thickness. Starting from an insulating substrate the electron gas is not generated continuously upon the deposition of one unit cell of LaAlO_3 at a time, but shows a sharp insulator-to-metal transition. All samples with 3 uc of LaAlO_3 or less are insulating and all samples with 4 uc or more are conducting. For the conducting samples the resistances and charge carrier densities are independent of the number of LaAlO_3 layers. This step in conductivity for film thicknesses exactly between 3 uc and 4 uc has by now been reproduced by several groups worldwide.

The observed metal-insulator transition, which is unknown for semiconductors, shows great potential for oxide heterostructures. Due to the available mixed valence states in oxides, electronic reconstructions can lead to novel phenomena at interfaces.

While the dependence of interface conductivity on film thickness is striking, the reversible change from the insulating to the conducting state by the deposition and removal of material is difficult to realize experimentally. Nevertheless a tuning between these drastically different phases would offer many possibilities, both for applications and fundamental research. Therefore, the electronic tunability of the transport properties in $\text{LaAlO}_3/\text{SrTiO}_3$ samples was investigated, which is the topic of the following chapter.

5 Electric Field Effect Experiments

This chapter presents the studies on the tunability of the electron gas formed at the $\text{LaAlO}_3/\text{SrTiO}_3$ interface by applying electric fields. A special focus is set on heterostructures with LaAlO_3 film thicknesses of 3 uc and 4 uc, which are in proximity to the previously described metal-insulator-transition. Before the experimental results on our samples are discussed in detail, a short introduction to electric field effects is given.

5.1 Electric Field Effect

Devices utilizing the electric field effect, in particular field effect transistors (FETs) are found in a tremendous number in our daily life, as semiconducting FETs are used e.g. in cell phones, cars and of course in computers. About 10^{19} of such transistors are manufactured each year [96]. These FETs consist of a thin conducting channel from the source- (S) to the drain-electrode (D). This channel is separated from a gate electrode by a dielectric layer. Channel and gate form a plate capacitor, and upon application of a gate voltage between both plates charges are accumulated in the channel. These charges change the carrier density and thus the resistance of the conducting channel.

This successful principle offers also for fundamental science a wealth of options because different compounds can be used as channel materials.

Many materials, like, e.g., oxides, or correlated systems in general, have a larger diversity of electronic and magnetic properties as compared to semiconductors. Additionally these materials often show phase transitions as a function of charge carrier density (see Fig. 5.1) which gave rise to intense research over the last decade.

In many cases chemical doping is used to tune the carrier density, but this approach has disadvantages. The samples are chemically and structurally altered, and the degree of disorder can be changed. Moreover, chemical doping is not tunable, so that in general for every carrier density a new sample with a different composition is needed. In contrast to this, electric field effect experiments allow controlled and reversible changes of the carrier

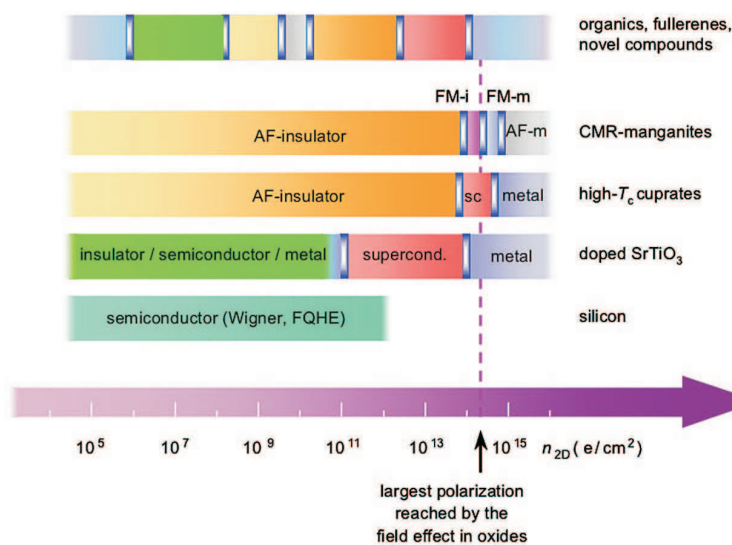


Figure 5.1: Illustration of the zero-temperature behavior of various correlated materials as a function of sheet charge density. Silicon is shown as a reference. The bars on top are drawn to schematically show the richness of materials available for field-effect tuning and the spectrum of their phases. AF, FM, i, m, and sc stand for antiferromagnetic, ferromagnetic, insulating, metallic, and superconducting respectively. From Ref. [96].

density in a single sample. A more detailed review on electrostatic modifications of novel materials can be found in the articles by C. Ahn *et al.* [96,97].

It is not only their proximity to phase transitions, which makes correlated systems so interesting from the scientific point of view, but it also is the small charge carrier density, which is often found. A low number of carriers is experimentally advantageous for field-effect experiments because the layer of charge accumulation or depletion in the channel, which is induced by the electric field, has a characteristic width which is given by the electrostatic screening length λ_{el} . In the semiclassical, metallic limit, λ_{el} is the Thomas-Fermi length $\lambda_{TF} = (\epsilon_r \epsilon_0 / e^2 n)^{1/2}$, with ϵ_r and ϵ_0 being the dielectric constants of the conductor and vacuum, respectively, e the elementary charge, and n the effective density of charge carriers screening the applied field. In typical metallic systems this screening length is extremely short, only parts of an atomic diameter, and therefore only tiny electric field effects are observed. In semiconductors with typical carrier densities of 10^{18} cm^{-3} , which corresponds to an areal density of 10^{12} cm^{-2} for a film thickness of 10 nm, the screening length equals tens of nanometers. Therefore in several nm thick semiconductor channels correspondingly large field effects are found, which is one of the reasons why semiconductors rather than metals are used as FET. Oxide materials have carrier densities and screening lengths intermediate between those of metals and semiconductors, which makes oxides good candidates for field effect experiments. There are mainly two options for achieving a substantial carrier density modulation in the DS-channels. The first is to use very thin films, and the second is to induce large areal charge densities or polarizations in the channel. For the latter option, one has to apply large electric fields, which requires high breakdown strength of the dielectric material. Additionally, a large dielectric constant increases the charge on the plate-capacitor, formed by gate and channel, and thus increases the induced electric field effect. These considerations show that the carrier concentrations achievable by electric field are mainly limited by the physical properties of the gate insulator. With the standard dielectric SiO_2 , polarizations of $\approx 3 \mu\text{C}/\text{cm}^2$ can be induced. By using SrTiO_3 with its larger dielectric constant even 10-40 $\mu\text{C}/\text{cm}^2$ are possible. This value corresponds to an areal density of $\approx 10^{13} - 10^{14} \text{ cm}^{-2}$. Such high polarizations can also be achieved by using a ferroelectric layer, like $\text{Pb}(\text{Zr},\text{Ti})\text{O}_3$, between gate and channel. In such devices the spontaneous polarization of the material, and thus the induced change of carrier density of the channel, is switchable upon application of an external electric field and remains stable even if the gate voltage is switched off (ferroelectric field effect) [96].

5.2 Field Effect at *n*-Type $\text{LaAlO}_3/\text{SrTiO}_3$ Interfaces

After the discovery of the step-like dependence of conductivity on LaAlO_3 film thickness experiments were performed to study the tunability of the transition by electric field. From the considerations before it is obvious that the conducting interface between LaAlO_3 and SrTiO_3 , with a sheet carrier density of $\approx 10^{13} \text{ cm}^{-2}$ of the quasi two-dimensional electron gas, is ideally suited for experiments, where the transport properties are controlled by electric field, because the possible modulation of the amount of charge carriers is close to the total number of charge carriers in the system. Additionally, one can expect a pronounced electric field effect, because due to the weak electrostatic screening of the

ultrathin electron gas the field affects the conducting channel over its entire thickness.

Samples for field effect experiments were fabricated with our standard conditions and the techniques described in previous chapters. A schematic view of such a sample is shown in Fig. 5.2. As usual, the interface was contacted by Ar-ion etching followed by gold sputtering. In Fig. 5.2 the left side of the sample sketch is a cross-sectional cut and shows one contact through the insulating LaAlO_3 to the interface. The resistance of the electron gas is measured in a four-point configuration (like shown in Fig. 4.1b). Electric fields were induced either across the SrTiO_3 substrate by applying gate voltages $V_{G,b}$ to backside contacts made by silver paint (back gate setup), or across the LaAlO_3 film by applying $V_{G,f}$ to small test contacts silverpainted on top of the LaAlO_3 (top gate setup). The gate voltages were applied by Keithley sourcemeter models 2400 or 238 with the current compliance set to a few nA. For all LaAlO_3 layers the gate resistances, measured between the top gate-electrode and the electron gas, were very large ($> 2 \text{ M}\Omega\text{cm}^{-2}$, see also Sec. 5.3). This shows that the LaAlO_3 layers are excellent insulators and suggests that they are grown pinhole-poor, or even pinhole-free.

Unless otherwise stated, all experiments presented in the following utilize a back-gate electrode. The polarity of the gate contacts is defined such that the plus terminal is on the gate electrode and the minus terminal reaches down to the interface. Accordingly, for a positive gate voltage the interface is the negatively charged plate (accumulation of electrons) and for negative gate voltages it is the positively charged plate (depletion of electrons).

The starting point of our studies of the tunability of interface conductivity by electric field were samples with $d_{\text{LAO}} \geq 4 \text{ uc}$, which are conducting without any gate voltage applied.

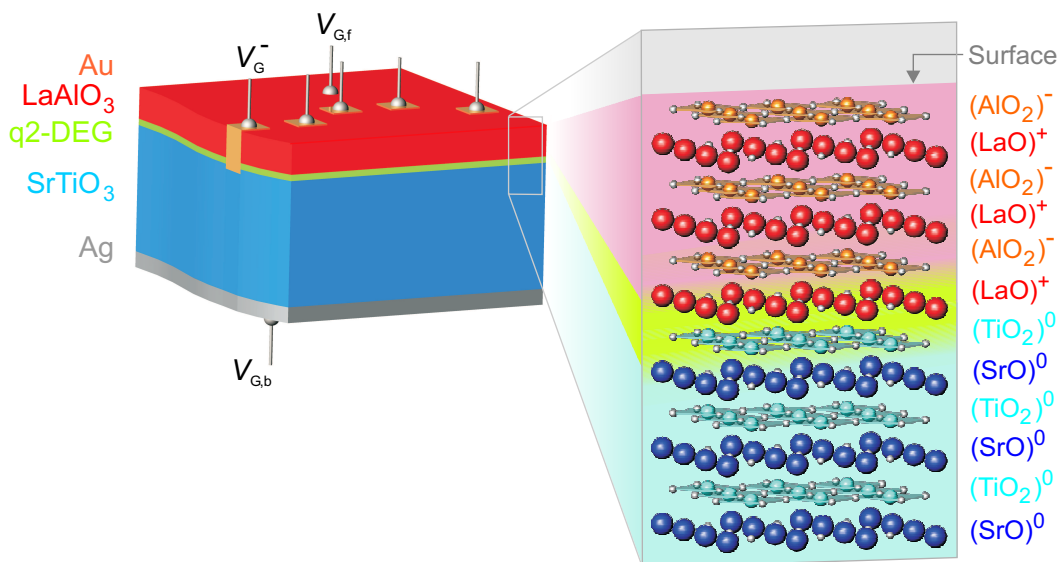


Figure 5.2: Sketch of a 3 uc thick sample with top and back gate contacts. The SrTiO_3 substrate is 1 mm thick. A cross sectional cut is shown on the left side of the sample sketch with one contact going through the insulating LaAlO_3 down to the interface. The charges listed in the atomic lattice sketch represent the unrelaxed charge distribution.

Figure 5.3 shows the change in resistance of a 5 uc thick sample as a function of applied gate voltage at $T = 4\text{ K}$. As expected, the field effect is large, with modulations from +170% to -60% for back gate voltages between -100 V and +100 V. Larger gate voltages were not used to avoid breakdown of the dielectric material, SrTiO_3 , by creating permanent conducting paths from channel to gate. For this magnitude of $V_{\text{G,b}}$ the gate currents ($< 1\text{ nA}$) are much smaller than the drain-source (DS) current ($10\text{ }\mu\text{A}$) and therefore affect the measurements only marginally.

From the sign of the resistance change one obtains an additional independent determination, apart from Hall measurements, of the type of charge carriers in the channel. The observed reduced resistance with a positive gate voltage is again in accordance with the formation of a n -doped electron system at the interface.

Such large effects are only expected if the gate voltage induced polarization via the SrTiO_3 substrate notably changes the charge carrier density in the channel. This is indeed the case, as found by measuring the gate-voltage dependent polarization of this sample with a Precision Materials Analyzer (Precision Pro, Radiant Technologies, Inc.). The data are shown in Fig. 5.4. A linear dependence is observed for voltages from -100 V to +100 V. The value of $1.45\text{ }\mu\text{C}$ at 100 V corresponds to a sheet charge carrier density of $9 \times 10^{12}\text{ cm}^{-2}$, which is only slightly lower than the density initially present at the interface ($\approx 10^{13}\text{ cm}^{-2}$), without any gate voltage applied. The large value for the induced sheet carrier density explains why the conductivity is tunable over such a large range, but the fact that it is still lower than the total n_s also implies that it will be difficult to deplete the electron gas completely by electric field to get an insulating interface.

For samples with a lower LaAlO_3 film thickness of 4 uc the interface is close to the metal-insulator transition, which occurs between film thicknesses of 3 uc and 4 uc. However, as reported before, once it is formed the charge carrier density of the q2-DEG is independent of the number of LaAlO_3 unit cells. So also for this reduced thickness a similar field effect like for the 5 uc sample is expected. Figure 5.5 shows I - V characteristics of such a 4 uc sample measured at 4 K for different gate voltages from -20 V to +20 V.

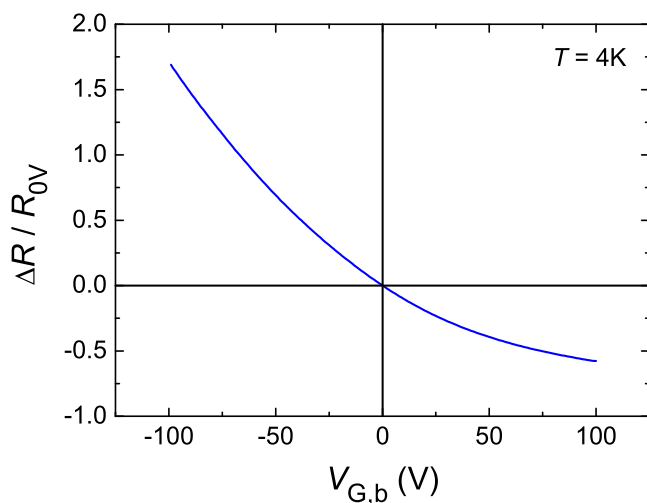


Figure 5.3: Electric field induced change of the resistance of the DS-channel of a sample with 5 uc of LaAlO_3 (sample L34) for back gate voltages $V_{\text{G,b}}$ from -100 V to +100 V. The measurement was done at $T = 4\text{ K}$ using a DS-current of $10\text{ }\mu\text{A}$. A strong tunability of the resistance from +170% to -60% is observed. The sheet resistance at $V_{\text{G,b}} = 0\text{ V}$ is $R_s(0\text{ V}) = 720\text{ }\Omega/\square$.

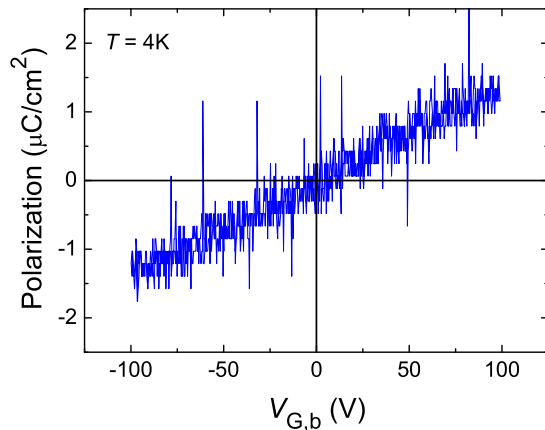


Figure 5.4: Induced polarization in a sample with 5 uc of LaAlO_3 (sample L34) via the SrTiO_3 substrate for back gate voltages from -100 V to +100 V. The measurement was done at $T = 4$ K.

As in the 5 uc sample, the resistance can be tuned to a large extent, and the DS-channel can again not be driven into the insulating state within the available range of back gate voltages. This behavior is found for all the 4 uc samples studied.

All the measurements discussed above were taken at $T = 4$ K. At this low temperature the samples behave as anticipated for a standard electric field effect with instantaneous changes of conductivity with applied gate voltages.

The behavior changes dramatically for field effect measurements performed at room-temperature. In comparison to the 4 K experiments the charge carrier density is only slightly higher (approximately by a factor 1.5), so in principle a similar dependence on $V_{G,b}$ is expected. Experimentally it is found, that gate voltages still tune the resistance, but, in contrast to the low temperature measurements, longer timescales and a memory behavior are observed. When the back gate voltage is switched on, the resistance does not instantaneously reach the final value but keeps changing over a timescale of minutes.

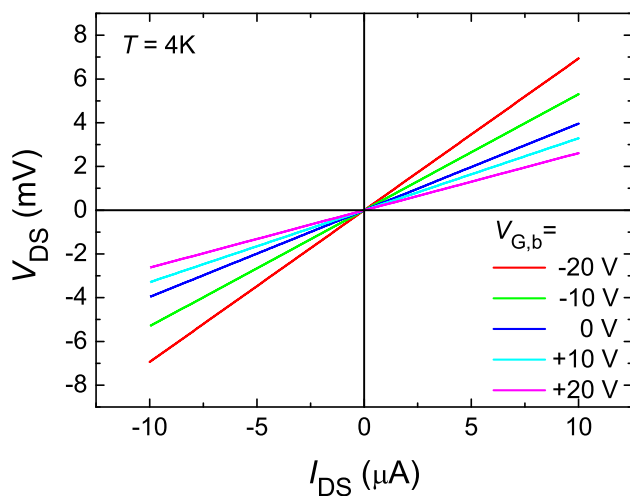


Figure 5.5: I - V characteristics of a sample with 4 uc of LaAlO_3 (sample L35) for different applied $V_{G,b}$. The measurement was done at $T = 4$ K. A large tunability is observed.

After switching off the gate voltage the sample conductance also does not return to the value which it had before $V_{G,b}$ was applied.

Figure 5.6 shows the typical behavior of the resistance as a function of time, while the gate voltage is changed. Initially the gate voltage is off and R stays constantly at $9.3\text{ k}\Omega$. By applying $V_{G,b} = +100\text{ V}$ the resistance drops to $7.7\text{ k}\Omega$ over 80 s . After switching off $V_{G,b}$ the sample resistance increases during 60 s again to $8.2\text{ k}\Omega$. By applying the opposite polarity ($V_{G,b} = -100\text{ V}$) charge carriers are effectively withdrawn from the interface and the resistance increases to $9.9\text{ k}\Omega$ over 60 s . Finally, after switching off the gate voltage, R decreases to $9.3\text{ k}\Omega$.

This behavior does not fit to the fast timescales of electronic reactions expected in the standard picture for electric field effects. Possible interpretations and explanations for such a memory effect will be discussed later in this chapter.

So far the initial idea, to tune the metal-insulator phase transition, which occurs as a function of film thickness, by electric fields was not realized in the experiments. Up to now only conducting $\text{LaAlO}_3/\text{SrTiO}_3$ samples with more than 3 uc of LaAlO_3 were used. Therefore it was tried to induce the phase transition by starting from insulating samples. Samples where the number of LaAlO_3 unit cells was below the critical thickness were investigated. In the following, the electric field effect on samples with 3 uc of LaAlO_3 will be presented and discussed. The big difference to the heterostructures studied before is that here no electron gas is initially present at the interface. If now charge carriers can be induced by electric field the relative change of the carrier density is enormous and a conducting interface can be formed. As noted before, the samples with 3 uc of LaAlO_3 show a large susceptibility to UV light, with light induced sheet resistances of $100\text{ k}\Omega$. This observation of conducting interfaces in 3 uc samples makes them promising structures for inducing the phase transition also by electric field.

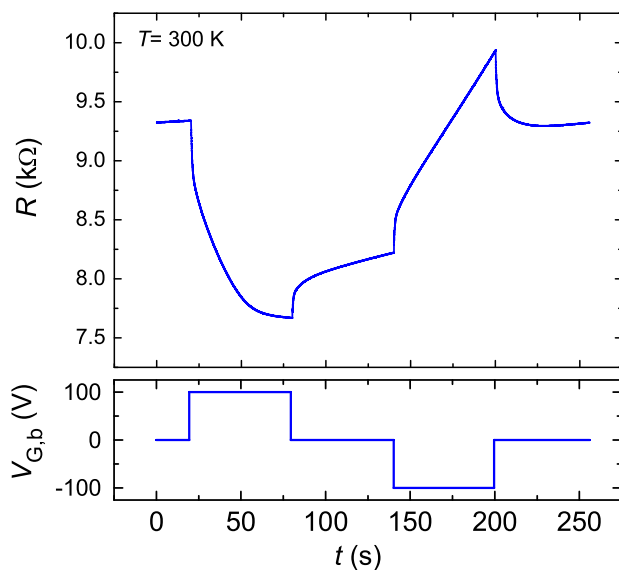


Figure 5.6: Resistance of a sample with 5 uc of LaAlO_3 (sample L34) as a function of time (upper panel). The back gate voltage was changed as plotted in the lower panel. This measurement, taken at $T = 300\text{ K}$ using a DC-current of $10\text{ }\mu\text{A}$, shows the long timescales and the memory behavior typically observed for field effect experiments at high temperatures.

Like for the initially conducting samples with $d \geq 4$ uc, which were described before, the focus will first be on the low temperature properties at 4.2 K. As shown in Fig. 5.7, by applying a sufficiently high positive gate voltage the electron gas is indeed induced at the initially insulating interface. For gate voltages between 0 V and 60 V the current-voltage characteristics of the channel were measured in a two-point configuration, because the resistance was too high to produce a steady voltage between the two voltage contacts of the four-point setup (shown in Fig. 4.1b), which were just floating. Increasing the gate voltage to 70 V drives the interface into a conducting state, which was now measured in a four-point configuration. By going up to $V_{G,b} = 100$ V the resistance can be reduced further. This implies that finally the gate field has generated a metal-insulator transition with conductance changes exceeding seven orders of magnitude.

These electron gases, which are induced at the interfaces of the 3 uc samples, have sheet conductances as high as $\sigma_s = 5 \times 10^{-3} \Omega^{-1}$ at 4.2 K ($5 \times 10^{-6} \Omega^{-1}$ at 300 K). Again the sign of the field effect is in accordance with the formation of n -doped electron systems. Several V - I curves display a curvature and an asymmetry, which we observed frequently for high-resistance samples grown on SrTiO₃ [98]. These deviations from linear behavior are attributed to non-ideal and non-identical contacts, and to the non-ideal four-point configuration.

Furthermore, heterostructures with 2 uc of LaAlO₃ were studied. It was not possible to switch those samples into the conducting state. These experiments bear similarities to the investigation of the photoconductivity mentioned earlier in this thesis. The fact that in 2 uc samples the electron gas can not be induced shows that the LaAlO₃ layers with

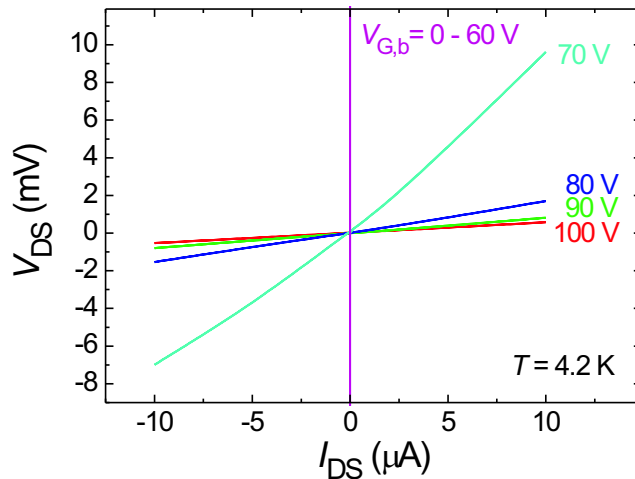


Figure 5.7: Voltage-current characteristics of a heterostructure with 3 uc of LaAlO₃ on SrTiO₃ (sample L32), measured at 4.2 K with various voltages applied to its back gate. The sample shows a large field-effect response with a conductance change of seven orders of magnitude. The curves taken at $V_{G,b} = 0$ V - 60 V was measured in a two-point configuration, because the resistance was too high to produce a steady voltage between the two voltage contacts of the four-point configuration, which was used for all other measurements. Published in Ref. [75].

the subcritical thickness of $d = 3$ uc still support the formation of the q2-DEG, whether by light or by electric field.

Continuing the investigation of the importance of the presence of the LaAlO_3 film on the samples also a TiO_2 -terminated SrTiO_3 substrate was exposed to the standard deposition procedure, yet without depositing any LaAlO_3 film. It was also not possible to induce conductivity in this substrate by electric field.

On one 3 uc sample, contacts were made by ion-etching followed by sputtering Al, which was finally protected with a thin Au-film to avoid oxidation (sample L73). Also in this sample it was possible to induce the metal-insulator transition by electric field, which excludes any influence from the contact material.

The R_s - T curve of such a field-induced q2-DEG in a sample with 3 uc of LaAlO_3 was also measured. It is shown in Fig. 5.8. Obviously, the electron gas is generated over the entire temperature range from 4 K to 300 K. The temperature dependence of the resistance of the field-induced electron gas is reminiscent of the properties of the electron gases that are present in all samples with $d \geq d_c$, as shown for two samples with 4 uc and 6 uc of LaAlO_3 in Fig. 5.8. The same observation is made for Hall measurements (see Fig. 5.9), which show a carrier density of the field-induced q2-DEGs of $n_s \approx 3\text{-}4 \times 10^{12} \text{ cm}^{-2}$. This value is only slightly lower than the typical 10^{13} cm^{-2} found for thicker samples.

At 4.2 K the R_s and n_s values for the induced electron gas correspond to a high mobility of almost 10^4 Vs/cm^2 . This high number allows to view these field effect devices as an analog to high electron mobility transistors (HEMTs) built from conventional semiconductors [99]. Such HEMTs consist of modulation doped heterojunctions with a two dimensional electron gas at an atomically sharp interface (e.g. GaAs/AlGaAs or GaN/AlGaN) which is separated from a doping layer by $\approx 100 \text{ nm}$. The additional electrons which come from the dopants move, due to the designed band structure, to a quantum well at the interface. Here the electrons can move practically unimpeded by their parent doping impurities, which is the big advantage compared to Silicon MOSFETs (mobility increased

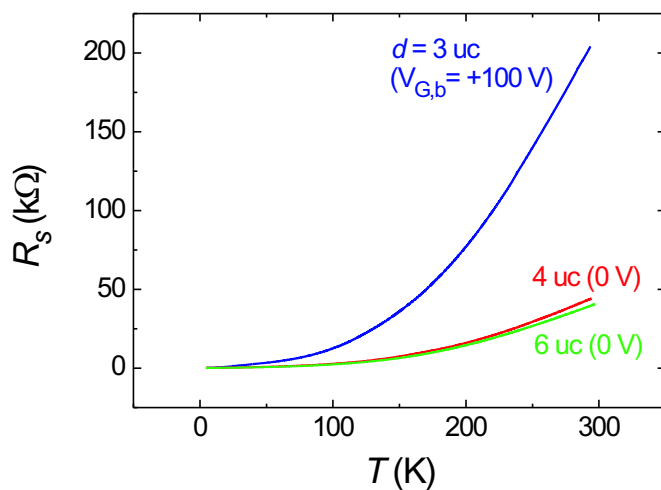


Figure 5.8: Sheet resistance measured as a function of temperature for two samples with $d \geq d_c$ at $V_{G,b} = 0 \text{ V}$ (samples L35 (4 uc) and L29(6 uc)) and for one sample with $d = 3 \text{ uc} < d_c$ (sample L32), in which the q2-DEG was induced by $V_{G,b} = 100 \text{ V}$. In this measurement a DS current of $1 \mu\text{A}$ was used. Published in Ref. [75].

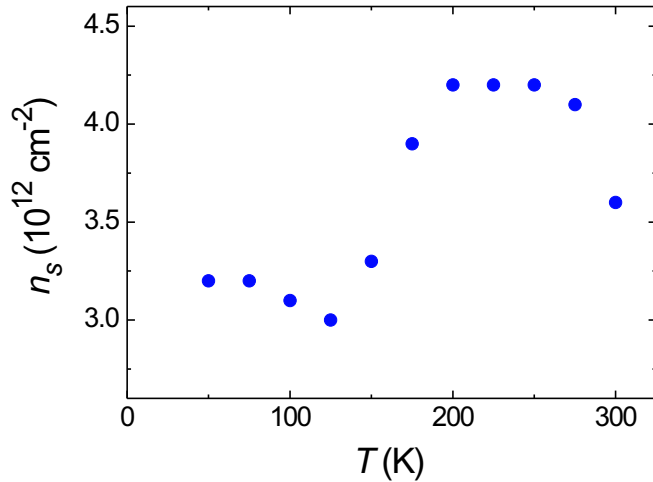


Figure 5.9: Carrier density of the electron gas, which was induced by electric field ($V_{G,b} = +100$ V) in a sample with 3 uc of LaAlO_3 (sample L32), for different temperatures as obtained from Hall measurements ($I_{DS} = 1 \mu\text{A}$, B field 8 T). Published in Ref. [75].

by a factor of 1000). The high mobility boosted the extensive use of these low-noise, high-frequency HEMTs. In the $\text{LaAlO}_3/\text{SrTiO}_3$ structure no spacer layer is included, but the channel carriers are doped from the LaAlO_3 layers, which are spatially separated from the DS channel. These heterostructures therefore embody the concept of modulation doping.

Yet, there are clear differences between both systems. On the one hand, the mobilities in the semiconducting interfaces exceed those in the current oxide interfaces by three orders of magnitude, and the carrier densities of the q2-DEG in the oxides exceed those of their semiconductor counterparts by orders of magnitude. Therefore, as discussed earlier for the magnetoresistance experiments, quantum Hall effect-induced resistance oscillations can only be expected to occur at very large field strengths, due to the proportionally larger fill factor $\nu = nh/eB$ (n is the carrier density, h is Planck's constant, e the elementary charge and B the applied magnetic flux density). One reason for the low mobility in the $\text{LaAlO}_3/\text{SrTiO}_3$ system is its pronounced sensitivity to the substrate quality, which is discussed in Chapter 8. On the other hand, the concept of modulation doping of oxides is of course not restricted to SrTiO_3 and LaAlO_3 and can be done using many compounds with strongly correlated electron systems. Interactions between the q2-DEG and the correlated electron systems of the bulk may therefore create electronic systems with unique properties.

The field effects shown by the samples are enormous. Field effect devices that use either doped SrTiO_3 [100, 101] or the SrTiO_3 surface [102, 103] as a DS channel have been fabricated with fine characteristics, yet the on/off ratios of our samples exceed those of these earlier devices by orders of magnitude. There are several reasons: First, the q2-DEG structures, which are used in our experiments, are close to optimal to achieve large electric-field effects, because the DS-channels consist of ultrathin, and therefore weakly screening, electron gases in which a metal-insulator phase transition can be induced by the field. Second, the gate insulator SrTiO_3 has a very large electric permittivity [26, 28, 29], which enhances the field response, especially at low temperatures. Third, because there is no conducting DS channel when the sample is insulating, the gate field lines initially

end at the drain and source contacts. Once the gate voltage exceeds a threshold value, the DS channel grows in a bootstrapping mode. This nonlinear process is expected to contribute to the abrupt change of resistance with gate field (Fig. 5.7).

For employing the field-induced electron gas at interfaces in samples with 3 uc of LaAlO_3 in devices, it is important to investigate the behavior at room temperature. Therefore the field-effect experiments using such samples at $T = 300$ K are presented next.

At such high temperatures the electric field-induced q2-DEG was found to display unusual behavior, in particular in samples that over minutes or hours had been subjected to a large $V_{G,b}$ (> 70 V). Similar to the results for the 4 uc samples (Fig. 5.6), but with an effect orders of magnitude larger, a memory effect is observed (Fig. 5.10). Varying $V_{G,b}$ causes the conductance to react rapidly by a small amount, followed by a larger, but very slow change. If the gate is switched, for instance from $V_{G,b} > 70$ V to $V_{G,b} = 0$ V, the samples with 3 uc ($< d_c$) retain for hours a high and only slowly diminishing conductance. By application of a negative $V_{G,b}$ this conductance is instantaneously switched off.

Figure 5.11 shows the memory effect of another 3 uc sample. The resistance of the induced electron gas is slightly higher, but the general behavior is the same as shown in Fig. 5.10.

This memory effect is unexpected from the standard electric field effect scenario, which predicts fast electronic reactions upon change of a gate voltage. Therefore it will be

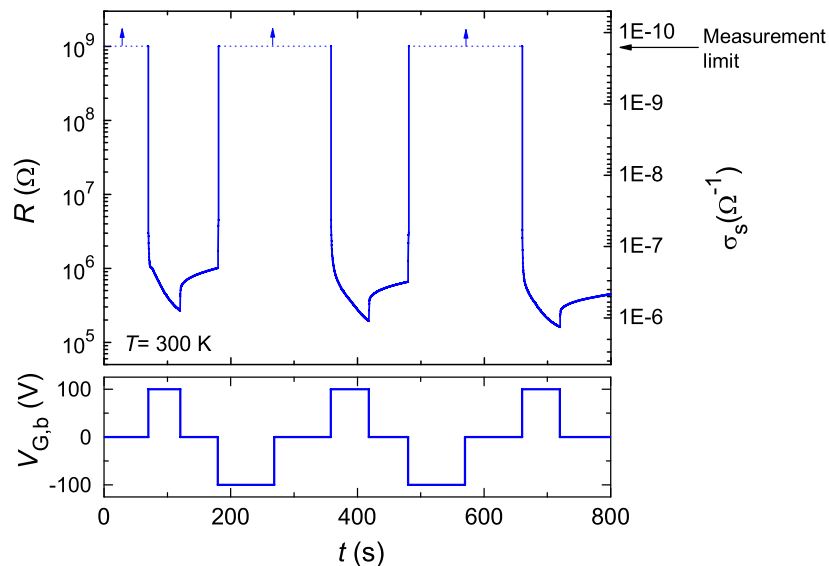


Figure 5.10: Memory behavior of the q2-DEG measured at 300 K. The resistance and sheet-conductivities (upper panel) of an initially insulating 3 uc sample (sample L32) and the applied back gate voltage (lower panel) are plotted as a function of time. By applying the gate voltage pulses, the sheet conductance was reversibly switched between $\approx 1 \times 10^{-6} \Omega^{-1}$ and an unmeasurable value $< 2 \times 10^{-10} \Omega^{-1}$. The data were measured in four-point configuration using a DS current of $1 \mu\text{A}$. Published in Ref. [75].

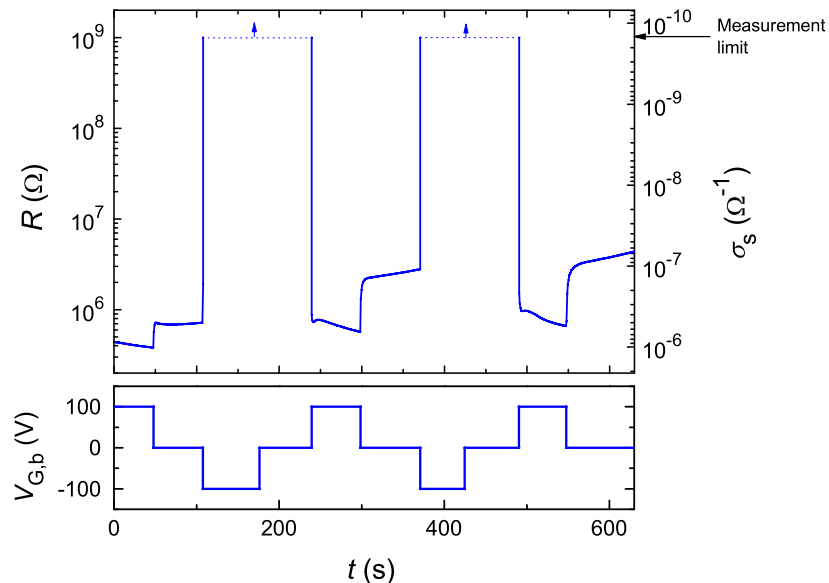


Figure 5.11: Memory behavior of the q2-DEG measured at $T = 300$ K. The resistance and sheet-conductivity (upper panel) of an initially insulating 3 μc sample (sample L73) and the applied back gate voltage (lower panel) are both plotted as a function of time. The data were measured in four-point configuration using a DS current of $1 \mu\text{A}$.

discussed in the following why the $\text{LaAlO}_3/\text{SrTiO}_3$ samples might be special.

Although the memory behavior is reminiscent of ferroelectric field-effect devices [96], such an effect is not known for field-effect devices that use dielectric gate insulators.

To check if the used gate dielectric influences the memory behavior additional experiments were done on 4 μc samples using a top gate contact, so that the electric fields are applied via the LaAlO_3 film. In the experiment the used gate electrode did not cover the whole conducting area and the gate voltage also dropped along the DS channel. For these samples no such memory effects were found. Because no mechanism is known that would yield a memory behavior for an isolated q2-DEG, one has to conclude that the SrTiO_3 plays a significant role.

Indeed, it has been proposed that charge excitations in SrTiO_3 can strongly influence the properties of the q2-DEG [104].

The long and temperature dependent time constants (fast reaction at low T , very slow reaction at high T) suggest that creation and motion of defect states, such as oxygen defects, are controlling the dynamics of the effect. While oxygen defects do not contribute to the formation of the electron gas, as discussed extensively in Sec. 4.2, the presence of a tiny amount of defects can not be excluded. One possible mechanism leading to the memory behavior is that the gate field and also the channel charge give rise to a sheet of positively charged defects or trapping states in the SrTiO_3 . In this model, the strong electric field of the dipole layer, consisting of the resulting q2-DEG and the defect sheet, stabilizes the electron gas as well as the defect sheet. In this way a nominally bistable

configuration can be obtained.

Another property of the substrate material might also be important. SrTiO_3 is a quantum paraelectric, with the phase transition to the ferroelectric state being suppressed by quantum fluctuations only, so already undisturbed bulk SrTiO_3 is almost ferroelectric [25,32]. Deformation of the bulk SrTiO_3 structure at the interface by the presence of the LaAlO_3 film might favor this state, so that a situation similar to ferroelectric field effect devices appears.

While all these effects can influence the samples, the exact mechanism of the memory behavior in the $\text{LaAlO}_3/\text{SrTiO}_3$ heterostructures at high temperatures is not resolved yet.

The transition between insulating and conducting interfaces found between 3 uc and 4 uc of LaAlO_3 film thickness was observed without exception during the complete time of this thesis. In contrast to this observation a slight drift was observed for the tunability by electric field. At the beginning of the experiments it was possible to drive 3 uc samples into the conducting state by electric field and 4 uc samples stayed conducting at all applied gate voltages. This situation changed over the years. After some time, the q2-DEG could not be induced in 3 uc samples, and also the observed photoconductivity was smaller. At the same time it became possible to drive 4 uc samples into the insulating state by electric field. This change indicates that the metal-insulator transition shifted slightly from being closer to 3 uc to be found closer to 4 uc. To induce the q2-DEG in initially insulating samples then required to use samples where the LaAlO_3 film deposition was stopped at an incomplete coverage of about 3.2 uc. In comparison to completed LaAlO_3 layers the spatially inhomogeneous number of unit cells in samples with 3.2 uc of LaAlO_3 is a badly defined situation and therefore was not studied further. It is presently not clear what caused these slight changes in the field effect tunability. At the same time the electronic transport properties of conducting $\text{LaAlO}_3/\text{SrTiO}_3$ interfaces were not affected at all.

It is stressed again here, that $d_c = 4$ uc was valid for the complete time. This stability of d_c together with the fact that this value was reproduced in various labs worldwide indicates that the critical thickness phenomenon is not related to specific preparation setups and conditions. Whether samples with 3 uc or 4 uc of LaAlO_3 can be tuned across the metal-insulator transition by electric field can in contrary be lab-specific.

Because these field effects are present at 300 K and show a large on/off ratio they are of potential interest for device applications. Memory devices might be fabricated for example. A special approach, that was followed in the course of this work, that potentially yields a very high data density will be presented at the end of this chapter (Sec. 5.4).

Of course, it still has to be clarified whether the stability, integrability, and device parameters are suitable for any practical implementation. One obvious issue is the generated photoconductivity in the samples, which requires to keep them in darkness to observe only the q2-DEG caused by electronic reconstructions.

Another big drawback for using the heterostructure in a device is the high gate voltage (100 V), which had to be applied up to now. Additional experiments were therefore performed to reduce the necessary voltage to acceptable levels of about 1 V and less. These studies are described shortly in the following.

5.3 Field Effect Using a Top Gate Contact

By making the gate dielectric of the plate capacitor formed by gate electrode and DS channel thinner, smaller gate voltages are needed to generate similar electric field strengths and changes in sheet carrier density.

One option to obtain a thinner dielectric is to reduce the thickness of the SrTiO₃ substrate by polishing, but samples with the thickness decreased by a factor of ten (100 μm substrate) are already very difficult to handle experimentally and easily break when they are removed from the heater. Therefore this approach was not followed.

The other option to obtain a thin dielectric layer is to use the LaAlO₃ film on top of the electron gas at the interface as the gate dielectric. In this setup the thickness of the plate-capacitor is reduced to several nanometers, while the sample thickness is not affected. The dielectric constant of LaAlO₃ ($\kappa \approx 25$), which also affects the capacity of the FET device, is considerable lower than for SrTiO₃ (κ up to 25000 at 4 K), especially at low T , but the tremendous lowering of the necessary gate voltage by reducing the thickness of the dielectric from mm to nm will nevertheless have a strong effect. Experimentally this option is realized by depositing Au on top of the LaAlO₃ film without prior ion-etching. This top gate electrode is then contacted by glueing a gold wire with silver paint instead of wire-bonding, which would result in a short to the q2-DEG.

The LaAlO₃ films were found to be excellent insulators, as shown in Fig. 5.12 for a sample with 4 uc of LaAlO₃. Up to fields of \approx MV/cm the gate currents were very small (on the order of 0.1 μA/cm²) as measured over a gate area of 12 mm².

The previously reported large electric field effects at the interface via a back gate and the excellent insulating properties of LaAlO₃ were promising for experiments via a top gate. Much smaller top gate voltages $V_{G,t}$ were expected to be necessary for comparable field effects. This promising perspective motivated the diploma thesis of Christoph Richter [105] in our group, who studied the tunability of the interface conductivity in LaAlO₃/SrTiO₃ samples by electric field effect using the LaAlO₃ film as gate dielectric. The samples he investigated were structured bridges and not plain LaAlO₃ films, which

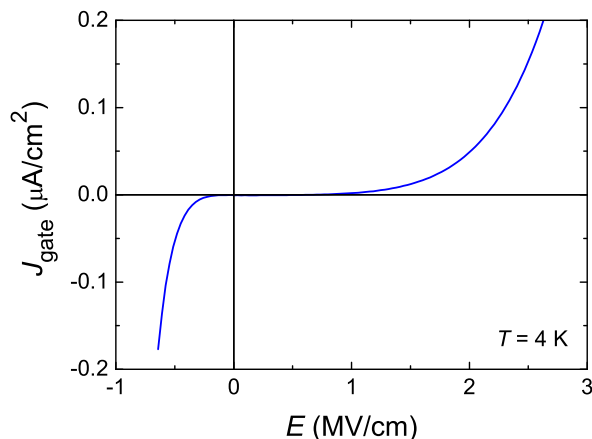


Figure 5.12: Gate-current density as a function of applied electric field at $T = 4$ K. The data were taken on a sample with 4 uc of LaAlO₃ (sample L48) and were measured in a 2-point configuration with one contact at the conducting interface and the other on the Au top gate (gate area 12 mm²).

became feasible due to the development of the patterning process as described in Chapter 6. Gold top gates then covered the whole DS channel. A schematic sketch of the sample setup is shown in Fig. 5.13.

These top gate experiments were successfully performed. As an example of the large field effects which were obtained Fig. 5.14 shows the change of resistance as a function of applied gate voltage for a sample with 5 uc of LaAlO₃ on SrTiO₃. At low temperatures ($T=15$ K) R can be tuned by $\approx 4\%$ by the application of top gate voltages of 0.5 V. Obviously the necessary gate voltages have been reduced by more than one order of magnitude compared to the back gate experiments. Much larger resistance changes are found at room temperature. While for positive gate voltages R is reduced by 40%, the opposite polarity increased R by a factor of 13 for $V_{G,t} = -0.5$ V.

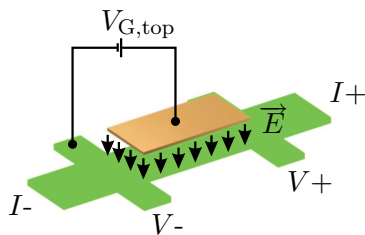


Figure 5.13: Schematic sketch of the sample setup for field effect experiments via $V_{G,top}$. A Au top gate sits above a patterned bridge containing the electron gas, shown in green, and the thin LaAlO₃ film (omitted in the sketch) is used as gate dielectric.

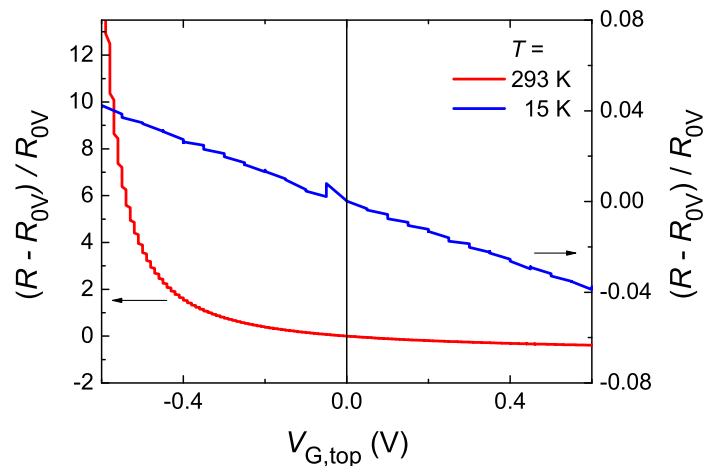


Figure 5.14: Resistance change of a 5 uc thick channel (sample SL3) as a function of $V_{G,top}$ measured at 15 K and 293 K. The resistance was measured in a four-point configuration with $I_{DS}=1$ μ A and leakage currents smaller than 5 nA. A large tunability is observed with a 13-fold change at $T=293$ K and $V_{G,top}=-0.5$ V. For this sample the resistance with no gate voltage applied is $R_{0V} = 10$ k Ω at 293 K and $R_{0V} = 72$ Ω at 15 K. The step-like structure in the data is caused by the measurement procedure, which waits for R to stabilize before another gate voltage is set (see Ref. [105]). The measurement was done by Christoph Richter.

A more detailed description of all the top-gate experiments and results is provided in Ref. [105].

These successful top gate experiments moved us into a position to study whether the electron gas can be tuned locally by electric field effects and especially on which length scales this tuning occurs at the interface. These studies are summarized in the following.

5.4 High-Resolution Patterning Technique Using a Scanning Probe

In the experiments described before a static gate contact was used for electric field effects. The idea behind the project presented next was to use instead of a static gate contact a biased AFM tip⁷ as tiny, movable top gate electrode. This allowed to investigate the local electronic tunability of the $\text{LaAlO}_3/\text{SrTiO}_3$ heterostructure properties.

These experiments were done in collaboration with Cheng Cen and Prof. Jeremy Levy from the University of Pittsburgh (USA) [52]. $\text{LaAlO}_3/\text{SrTiO}_3$ samples with contacts were prepared in Augsburg and then sent to Pittsburgh for all the experiments using a biased AFM tip. By continuous feedback from their group the film thickness and contact geometry were optimized for their investigations. Later Birgit Kießig studied this subject in her diploma-thesis also in Augsburg [106].

As shown in Sec. 5.2, the largest field effects are found for heterostructures with 3 uc thick LaAlO_3 films on SrTiO_3 . For these samples an insulator-to-metal transition can be induced by electric field effect using the SrTiO_3 substrate as gate dielectric. Additionally a pronounced memory effect is observed at room temperature. Due to their strong tunability these samples were chosen for this project.

Three unit cell thick films of LaAlO_3 were grown on TiO_2 -terminated SrTiO_3 substrates by PLD under our standard conditions, and a set of contacts with a spacing of $150\ \mu\text{m}$ was made by Ar-ion etching defined holes and filling these with sputtered gold. Then these samples were transferred to Pittsburgh. There they were mounted in a AFM setup and kept in dark environment to suppress carrier photoexcitation. A conducting AFM tip, which was biased at V_{tip} with respect to the interface, was subsequently scanned from one electrode to the other, while the resistance between both electrodes was measured as a function of the tip position with a lock-in amplifier. Figure 5.15 summarizes the key results.

Like for the field effect experiments described before, an electron gas is induced at the $\text{LaAlO}_3/\text{SrTiO}_3$ interface below the AFM tip, if the tip is biased positively with respect to the interface. These conducting regions also display a similar memory effect as observed for the back gate experiments and are found to be stable over a 24 hour interval. Therefore one can obtain larger conducting regions by scanning the biased tip. This was utilized in the experiments by performing the following sequence. First, rectangular, conducting pads were written at the interface by moving the tip over the corresponding area. In this way the gap between the conducting electrodes was reduced to $40\ \mu\text{m}$, which allowed

⁷A sharp conducting tip at the end of a cantilever is the important part. As the used microscope is mainly operated as AFM and not as STM the term AFM tip will be used in the following.

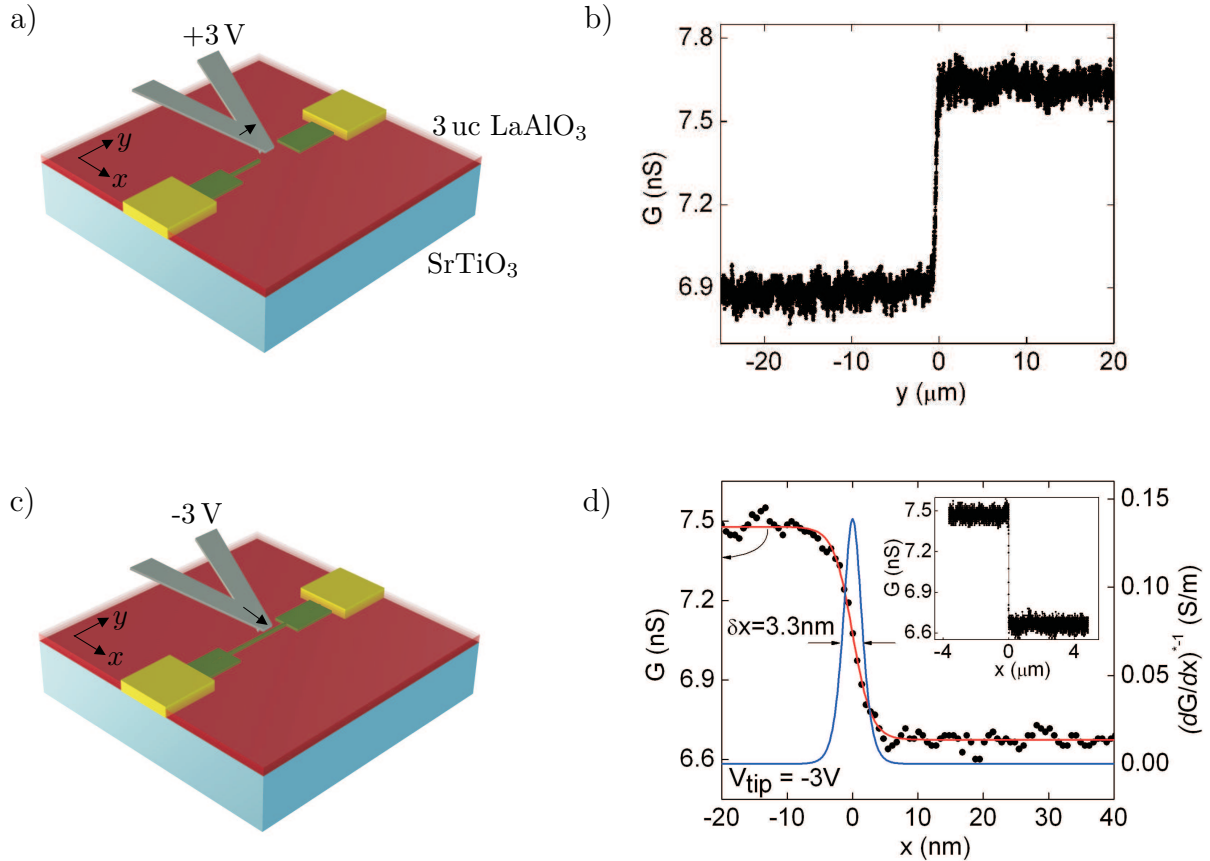


Figure 5.15: Writing and erasing nanowires at the LaAlO₃/SrTiO₃ interface of a sample with 3 uc of LaAlO₃ (sample L77). **a**, Schematic diagram of the experimental setup for writing a conducting wire. **b**, Conductance between the two electrodes measured while writing a conducting wire with the tip biased at +3 V. A step increase in conductance is observed when the tip reaches the second electrode ($y = 0 \mu\text{m}$). **c**, Schematic diagram of the experimental setup for cutting a conducting wire. **d**, Conductance between the two electrodes measured as a function of the tip position, while the tip, biased at -3 V, is scanned across the wire. A sharp drop in conductance occurs when the tip passes the wire ($x = 0 \mu\text{m}$). The deconvolved differential conductance $(dG/dx)^{-1}$ (blue curve, right axis) shows a full-width at half-maximum $\delta x = 3.3 \text{ nm}$. **Inset**, Conductance measured over the entire $8 \mu\text{m}$ scan length. The measurements and sketches were done by C. Cen and J. Levy at the University of Pittsburgh (USA). Published in Ref. [52].

to have the following movements completely in the limited scan field of the used AFM. In later experiments the photolithographically defined distances between the ion etched contacts were adjusted such that the writing of the rectangular pads was not necessary any more.

Then the tip was scanned from one electrode to the other with a positive V_{tip} applied (Fig. 5.15a). In the data of conductance G as a function of tip position y in Fig. 5.15b one can see a pronounced and abrupt increase of $\Delta G \approx +0.8 \text{ nS}$, as soon as the tip arrives at the second electrode (at $y = 0 \mu\text{m}$). This jump can be explained by a conducting, persistent line that has been written between both electrodes. The data shown were obtained with a tip bias of +3 V. For higher voltages the increase in conductance upon connecting both

electrodes via a conducting line gets larger, up to several μS for $V_{\text{tip}} = +10\text{ V}$. From this result one can not yet determine the lateral extensions of the written line.

Experimentally it is found that a negative tip voltage erases the previously induced electron gas, just like discussed before in the back gate experiments. The reversibility of the writing process is demonstrated by scanning the tip perpendicularly across the written line at a reverse bias of -3 V (see Fig. 5.15c). When the AFM tip crosses the wire, the conductance decreases abruptly by $\Delta G \approx -0.8\text{ nS}$ (Fig. 5.15d) to the value it had before any conducting line was written. This experiment also provides information on the width of the wire, as the conductivity only gets back to the initial value if the complete wire is “cut”. Assuming the erasure process to have a resolution similar to the writing process, the deconvolved differential profile $(dG/dx)^{-1}$ exhibits a full-width at half-maximum of $\delta x = 3.3\text{ nm}$ (see Fig. 5.15d). This tiny value corresponds to the width of the previously written wire. The wire width depends sensitively on the bias voltage, increasing by three orders of magnitude if V_{tip} is raised from 3 V to 10 V .

Scanning the AFM tip again with a positive bias voltage across the previously erased area restores the conductance of the wire. This shows that one can reversibly write and erase conducting areas of nanometer dimensions in the q2-DEG at the interface.

One possible application for this scanning probe method is patterning of the electron gas. A clear disadvantage is that exposing the sample to light makes the whole $\text{LaAlO}_3/\text{SrTiO}_3$ interface photoconducting and thus erases all previously written structures. Therefore a completely different method was developed for patterning the electron gas at the interface, which was widely used in the rest of this work. This method is presented in the next chapter.

Due to the nanometer dimensions of the written structures, the AFM lithography is also of potential interest for memory applications. Several measurements were performed to determine the limits of memory density and writing speed of this method. In these experiments the AFM tip was again scanned from one electrode to the other, but now V_{tip} is not applied continuously to the tip. Instead, voltage pulses are applied at defined separations d . In this way a line of conducting dots is formed between the contacts (see Fig. 5.16a), with the dot size depending on both the pulse voltage V_{pulse} and the pulse width. For simplicity we keep V_{pulse} fixed at 10 V . As before, the change in conductance ΔG when these dots reach the second electrode is measured. The results of the experiments for various dot spacings and pulse durations are shown summarized in Fig. 5.16b.

Let us first focus on the data for a fixed pulse duration, like e.g. 5 ms . For spacings larger than $\approx 20\text{ nm}$ one obtains $\Delta G \approx 0\text{ }\mu\text{S}$, which implies that the written conducting dots are separated from each other, and no continuous, conducting path is formed between both electrodes. By further reducing the spacing between the dots they will start to overlap for some critical distance and form a complete, conducting line. In this situation a finite ΔG is observed. For 5 ms pulses this critical value is found to be 15 nm , which is a direct measure of the diameter of the written dots. By reducing the pulse width down to $50\text{ }\mu\text{s}$ and less, the diameter of the dots is observed to saturate at a value of $\approx 1\text{ nm}$.

If it was possible to fabricate memory devices with these nanoscale dot dimensions the resulting densities can exceed 10^{14} inch^{-2} in these $\text{LaAlO}_3/\text{SrTiO}_3$ heterostructures. Of course device stability and integrability still has to be checked in detail. The cantilever

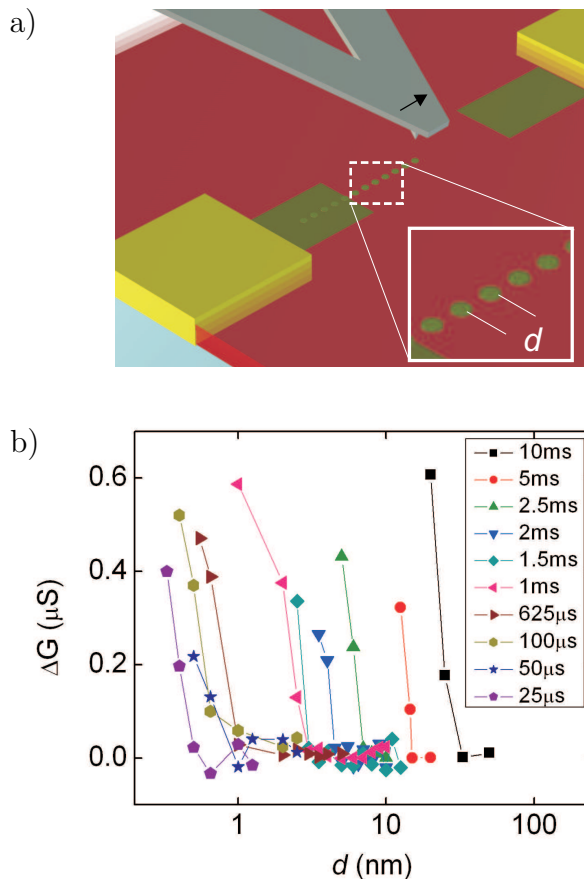


Figure 5.16: Measuring the limits of conducting island density. **a**, Schematic diagram of the measurement method. Voltage pulses are applied to the AFM tip, while scanning from one contact to the other. **b**, Changes of conductance when the dotted lines reach the second electrode, for various spacings d between dots and different pulse durations. The measurements and sketches were done by C. Cen and J. Levy at the University of Pittsburgh (USA). Published in Ref. [52].

necessary for this method is technologically more demanding than a pure electronic read and write method, but the applied lithography with a scanning probe can potentially well be combined with the IBM millipede setup [107], which uses an array of cantilevers.

Some checks were performed to proof that the conductivity of the written lines is related to the electronic reconstruction at the interface, with the observed critical LaAlO_3 film thickness of 4 uc for the formation of the electron gas. Already the reversibility of the writing process is a strong hint against chemical changes of contamination layers on the sample surface being responsible for the induced conductivity. For further tests, samples with 0 uc and 2 uc (sample L159) of LaAlO_3 were studied. It was not possible to induce isolated, conducting structures in these samples, and upon trying to write connected structures the sample surface was damaged by 1-2 nm deep trenches, formed by the AFM tip movement. Therefore it is concluded that the writing of conducting features is not possible for heterostructures with up to 2 uc of LaAlO_3 , in accordance with the field effect tunability by back gate voltages described earlier in this chapter. For a heterostructure with 4 uc of LaAlO_3 (sample L160) the initially observed conductance ($> 1 \mu\text{S}$) is much higher as compared to the value for 3 uc samples ($< 1 \text{ nS}$), because the electron gas is already present at the interface. This conductivity can be further enhanced by scanning a positively biased tip, but the changes are much smaller than for the 3 uc samples. For 3 uc and 4 uc thick samples the writing of conducting lines did not produce any observable topographic changes.

This clear dependence of the writing process on the LaAlO_3 thickness indicates that the

biased AFM tip indeed locally induces a metal-insulator transition at the LaAlO₃/SrTiO₃ interface, like observed in the experiments with a back gate electrode.

These experiments, results, and possible applications later led to the diploma thesis of Birgit Kießig [106] in our group, who further tested the patterning process in an AFM setup in Augsburg. The writing and erasing of conducting lines in LaAlO₃/SrTiO₃ heterostructures was reproduced, but the written wires persisted for shorter times. It certainly still has to be clarified which parameters influence the stability of the written conducting nanoscale areas, before this technique can be employed in more experiments.

This chapter will conclude by a short discussion of electric field effects at *p*-type interfaces.

5.5 Field Effect at *p*-Type LaAlO₃/SrTiO₃ Interfaces

As reported before, interfaces between SrO-terminated SrTiO₃ and LaAlO₃, which are expected to be *p*-type, were found insulating in all experiments. One possible explanation was that the *p*-type carriers were compensated by electrons from residual oxygen vacancies, which do not cause conductivity at the interface. Another explanation for the insulating behavior is that only localized holes are present. For these *p*-type samples electric field effect experiments were promising to induce additional charge carriers at the interface.

Some *p*-type samples were prepared with both back and top gates (samples L40, L86, L87). However it was not possible to induce conductivity. Independent of gate voltage polarity the resistances were larger than our measurement limit for $|V_{G,b}| = 100$ V.

5.6 Summary

As shown in this section, the quasi two-dimensionality of the electron gas and the low sheet charge carrier density of $\approx 10^{13}$ cm⁻² allow to efficiently tune the transport properties of LaAlO₃/SrTiO₃ interfaces by the electric field effect. The conductivity in samples with $d_{\text{LAO}} \geq 4$ uc, which are conducting even with no gate voltage applied, can be modulated to a large extent by applying gate voltages up to ± 100 V with the SrTiO₃ substrate as gate dielectric.

In samples with 3 uc of LaAlO₃ a quantum phase transition from an insulating to a conducting state can be induced by electric field. Tremendous conductance changes of seven orders of magnitude are observed at $T = 4.2$ K. This large on/off ratio by far exceeds those of earlier oxide field-effect devices.

It was not possible to drive samples with even thinner LaAlO₃ films ($d_{\text{LAO}} \leq 2$ uc) from the insulating into the conducting state by electric field. This result shows that LaAlO₃ layers with the subcritical thickness of $d = 3$ uc still support the formation of the q2-DEG by electric field.

As the induced electron gases exhibit a high mobility of $\approx 10^4$ Vs/cm⁻² (at 4.2 K) one can view the LaAlO₃/SrTiO₃ samples as an oxide analog to semiconductor HEMTs, having the doping from the LaAlO₃ layer spatially separated from the conducting sheet at the interface.

At room temperature a pronounced memory effect is observed. The conductivity changes upon application of a gate voltage V_G and stays altered even when V_G is switched off. For 3 uc samples this shows that the $\text{LaAlO}_3/\text{SrTiO}_3$ interface can be switched between a conducting and an insulating state by applying $V_G = \pm 100$ V via a back gate electrode, and these states are stable for hours even with no gate voltage applied. The persistent changes offer the possibility to use this oxide interface as a memory device.

The high necessary gate voltages of ≈ 100 V hamper the use of the $\text{LaAlO}_3/\text{SrTiO}_3$ heterostructure in this back gate field effect configuration in actual applications. It was shown that these voltages can be strongly reduced, while maintaining excellent tunability of the q2-DEG, by applying the electric field via the highly insulating LaAlO_3 film as gate dielectric instead of the SrTiO_3 substrate.

In additional experiments a conducting AFM tip was used as movable top gate electrode. This technique allows to locally and reversibly induce the electron gas with nanometer resolution in samples with 3 uc of LaAlO_3 on SrTiO_3 , which can potentially be used in memory devices with densities exceeding 10^{14} inch⁻².

The experiments described so far have deepened the knowledge about the $\text{LaAlO}_3/\text{SrTiO}_3$ interface. They even have revealed completely new effects, and have demonstrated the strong tunability of the electronic properties by electric field.

However, apart from the achievements, a severe drawback is still experienced, which is the absence of a patterning technique for the q2-DEG. For many experiments and also devices it is crucial to have conducting areas of defined geometries. The lithography using a scanning probe, which was presented in this chapter, is a first possibility, but the variations in stability of the induced electron gases and the erasure of designed conducting areas by light are factors that do not allow to use this method reliably for all experiments.

Therefore a novel patterning technique was developed, which will be presented in the following chapter.

6 Development of a Technique to Pattern the Electron Gas at LaAlO₃/SrTiO₃ Interfaces

Structuring of the electron gas was a major task to be addressed. This chapter presents a process for patterning the conducting LaAlO₃/SrTiO₃ interface by varying the thickness of the epitaxial LaAlO₃ film on the substrate [108]. This process was developed in the course of this thesis.

Up to this point, all studies of the electron gas, which is generated between LaAlO₃ and SrTiO₃, have been performed on unpatterned samples. Unpatterned implies, that the LaAlO₃ films covered the complete substrate, so also the electron gas at the interface was formed over the complete sample area. These samples were then measured as such without further patterning. However for many studies and possible applications it is crucial to have lithographically defined structures.

The reason why structuring has not yet been realized in this heterostructure is that the standard lithography techniques are not applicable. LaAlO₃ is chemically very stable and thus can not be removed by wet etching. The next straightforward approach for patterning would be Ar-ion etching to remove the LaAlO₃ film, but this technique is not useful, because the ion-beam creates damages and defects, especially oxygen vacancies, in the underlying SrTiO₃, which renders it conducting [98]. The conducting substrate then electronically shunts the electron gas. This problem might be solved by a subsequent low energy ion-milling step, but an uncertainty about possible shunts would remain.

It is obviously desirable to pattern the electron gases without exposing the edges of the conducting channels to the environment or to chemicals to avoid interactions between the electron gas and the defect-rich layers that then exist at the edges.

6.1 Preparation and Characterization of Patterned LaAlO₃/SrTiO₃ Samples

The patterning technique is based on the observed strong dependence of the conductivity at the LaAlO₃/SrTiO₃ interface on the LaAlO₃ film thickness, as described in Sec. 4.1. Due to the existence of the critical thickness of the LaAlO₃ film $d_c = 4$ uc for the interface to become conducting, patterning of samples can be done by growing epitaxial LaAlO₃ of varying thickness on one substrate. In parts which are planned to remain insulating the film has to be grown with $d < d_c$, and in parts where the generation of the electron gas is desired, epitaxial LaAlO₃ films have to be grown with $d \geq d_c$.

It still had to be clarified whether this principle can be experimentally realized, but indeed a special sequence of depositions of amorphous and epitaxial LaAlO₃ allows to grow such structures. The different steps are shown schematically in Fig. 6.1.

As first step, 2 uc⁸ of LaAlO₃ were deposited epitaxially over the complete area of

⁸In fact any subcritical thickness $d_{\text{LAO}} < 4$ uc works, but mainly 2 uc of LaAlO₃ were used because of better protection of the interface compared to $d_{\text{LAO}} = 1$ uc, and because the thickness $d_{\text{LAO}} = 2$ uc is two unit cells less than the critical thickness d_c as compared to only one unit cell difference for $d_{\text{LAO}} = 3$ uc. Therefore areas with 2 uc of LaAlO₃ are well on the insulating side of the metal-insulator-transition.

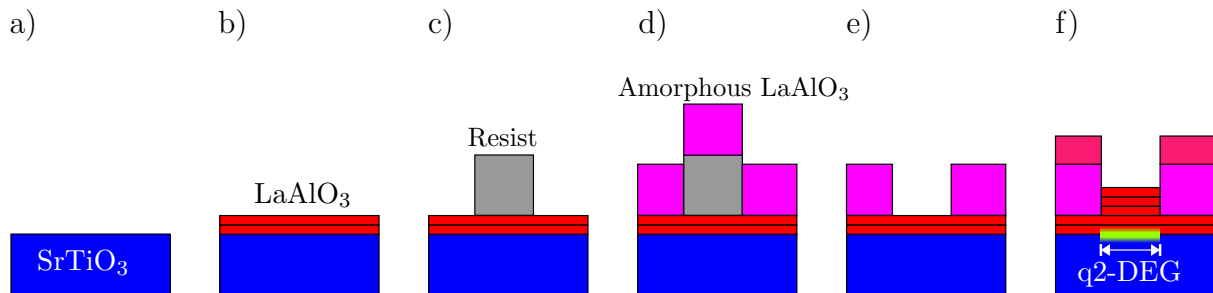


Figure 6.1: Illustration of the patterning technique. **a**, A standard TiO_2 -terminated SrTiO_3 substrate is used. **b**, 2 uc of LaAlO_3 are deposited epitaxially. **c**, By lithography a photoresist lift-off structure is patterned on the sample. **d**, 10 nm of amorphous LaAlO_3 are deposited. **e**, A lift-off step removes the resist from the covered parts, which then have epitaxial LaAlO_3 up to the surface. **f**, Finally 3 uc of LaAlO_3 are deposited. Only in the areas defined in **c**, the growth is epitaxial and the q2-DEG is formed. Procedure published in Ref. [108].

a TiO_2 -terminated SrTiO_3 substrate with the standard deposition conditions and the thickness controlled on the unit cell level by RHEED (see Fig. 6.2). For all subsequent steps of the patterning process the interface between SrTiO_3 and LaAlO_3 which is the crucial part of the sample where the q2-DEG is formed, is therefore protected and capped by 2 uc of LaAlO_3 , so that it is not affected by resists and solvents.

In the next step, by using a photolithography mask, patterns like bridges and bars with widths ranging from $1\ \mu\text{m}$ to $100\ \mu\text{m}$, can be defined with standard optical UV lithography. Smaller structures, with widths down to $\approx 200\ \text{nm}$, were prepared using e-beam lithography (LEO 440 scanning electron microscope (SEM) equipped with lithography system ELPHY Quantum from Raith, Lithography done by German Hammerl). Mostly, bridges which allow four point transport measurements were patterned. The areas which remain covered by photoresist after the developing process will have a q2-DEG formed at the interface at the end of the patterning sequence.

On these lift-off structures 10 nm of LaAlO_3 were deposited on the complete sample area by PLD at room temperature. This low temperature keeps the photoresist intact and results in amorphous growth of the LaAlO_3 , which was checked by XRD.

After a lift-off step with acetone to remove the resist, the sample consists of two different areas (see Fig. 6.1e). A part of the sample surface is now covered with amorphous LaAlO_3 , and the rest has the previously grown 2 uc of epitaxial LaAlO_3 on top.

Finally, LaAlO_3 is grown again using the standard conditions (770°C , $p(\text{O}_2) \approx 10^{-5}\ \text{mbar}$). On the areas that are free of amorphous LaAlO_3 , the film grows homoepitaxially on the present 2 uc of LaAlO_3 . These areas together amount to only a small fraction of the sample surface, so the RHEED signal during growth also shows large contributions from the amorphous surface areas. Nevertheless it is possible to observe the oscillations in RHEED intensity caused by the layer-by-layer homoepitaxial growth of the LaAlO_3 , as shown e.g. in Fig. 6.2.

The film thickness of this deposition was varied from 2 uc to 13 uc, so that always the total thickness of epitaxial LaAlO_3 exceeded the critical thickness of 4 uc in the areas not covered by amorphous LaAlO_3 . Therefore on the completely epitaxial parts of the sample

the electron gas is generated at the interface. On the amorphous LaAlO_3 in contrast the top LaAlO_3 layers grow amorphously, so that in these areas the only epitaxial LaAlO_3 is from the first deposition with a thickness smaller than d_c . Correspondingly no conducting layer is formed (see Fig. 6.1f).

Figure 6.3 shows a sketch of a cross sectional cut through a sample patterned in this way.

As usual, the contacts to the interface were fabricated by ion etching and Au sputtering. To simplify the positioning of the photolithography mask for the contacts on the previously designed contact areas additional markers were used. Photolithographically

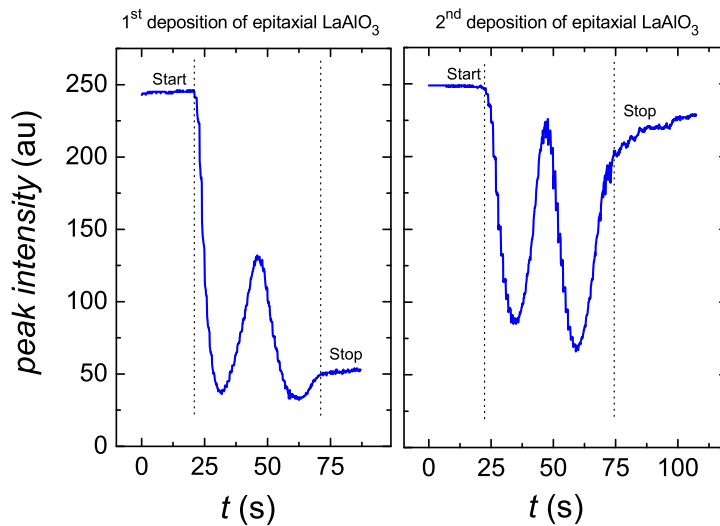


Figure 6.2: RHEED intensity of the specular spot plotted as a function of time for the two depositions of epitaxial LaAlO_3 during the patterning process of a sample with 4 uc of patterned LaAlO_3 in the conducting parts (sample L165). Oscillations are observed for both the initial growth of 2 uc (left) and for the second step (right), where again 2 uc of LaAlO_3 are deposited, but epitaxial growth occurs only on a small fraction of the sample surface.

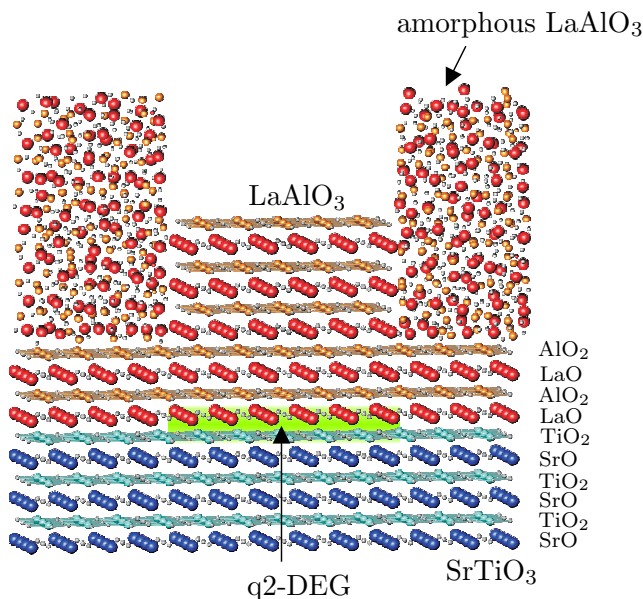


Figure 6.3: Sketch of a cross-sectional cut through a sample, which was patterned by a process as shown schematically in Fig. 6.1.

defined cross shapes were ion-etched some 100 nm deep into the corners of the not yet terminated SrTiO₃ substrates. These are well visible, even underneath a layer of photoresist. The shape of the cross markers was repeated on the masks for the patterning process and the contacts, so that it was possible to correctly align all the structures.

Figure 6.4a shows an optical microscopy image, using a polarizing filter, of a structure fabricated by this method. Although the height differences between the epitaxial and the amorphous LaAlO₃ on the surface is only ≈ 10 nm the patterned bridge, designed for transport measurements, can clearly be seen optically.

Photolithography was used to pattern this sample with conducting tracks (50 μm wide and 1 mm long), which are oriented vertically in the middle of the image. On the left and on the right of the image the track is connected to current contacts. Additionally there are six voltage probes for resistance and Hall measurements, each 300 μm apart, which are connected to contact pads on the top and bottom of the image.

The AFM image in Fig. 6.4b shows a detailed view of the measurement bridge right at

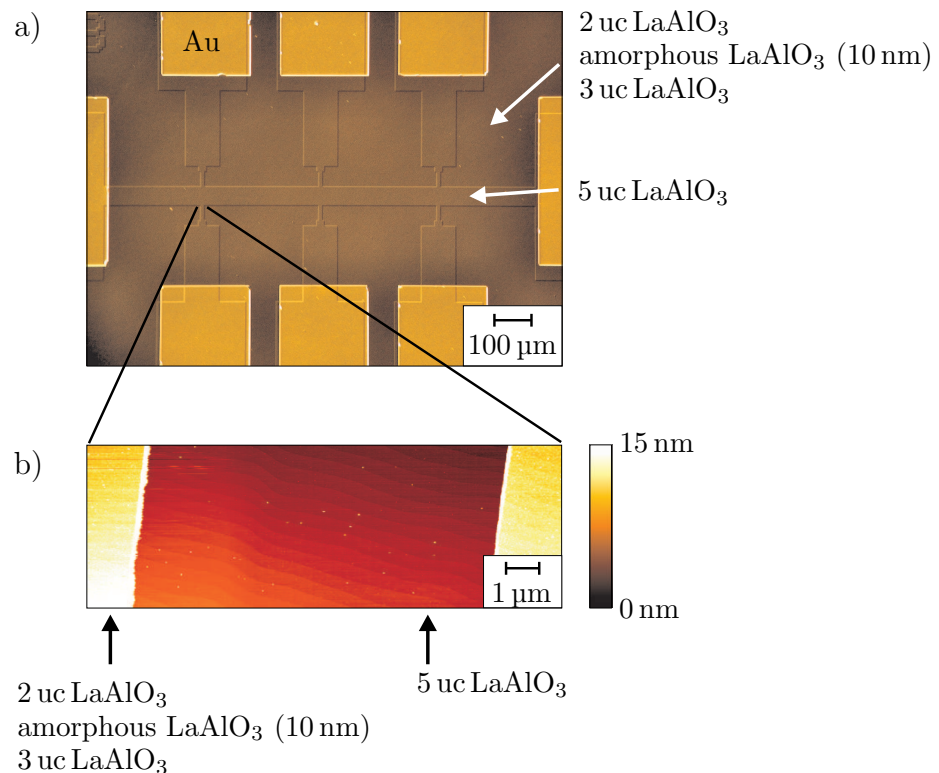


Figure 6.4: Patterning measurement bridge of a LaAlO₃/SrTiO₃ interface (sample L51). **a**, Optical micrograph of a 50 μm wide track of a lithographically defined electron gas. Current contacts (at left and right side) and six voltage contacts (three each at top and bottom of the image) were prepared by ion-etching and sputtering Au, which leads to the yellowish color. The voltage probes for four-point and Hall measurements at the track are placed 300 μm apart. The height difference between the epitaxial and the amorphous LaAlO₃ on the surface is ≈ 10 nm. **b**, AFM image of a part of a voltage probe, which contains sequentially deposited epitaxial and amorphous LaAlO₃. A clear step-and-terrace structure with one unit cell high steps is found on the epitaxially grown LaAlO₃ in the center of the image. Published in Ref. [108].

a voltage probe. In the central part of the image the completely epitaxially grown areas show the flat step-and-terrace structure, which is well known from the non-patterned samples. The step height equals one unit cell of LaAlO_3 . This experiment shows that the surface of the patterned samples has an excellent quality. The amorphous areas show a smooth, yet irregular surface structure. Between the amorphous and the epitaxial LaAlO_3 a steep step is found with a nominal width of less than 2 nm, which is limited by the sharpness of the AFM tip (SuperSharpSilicon™ non-contact AFM tip, typical tip radius ≈ 2 nm).

Figure 6.5 shows an example of a smaller structure, which was patterned using e-beam- instead of photo-lithography. The AFM image shows that the feasible sizes of this patterning technique are smaller than the terrace widths of the samples.

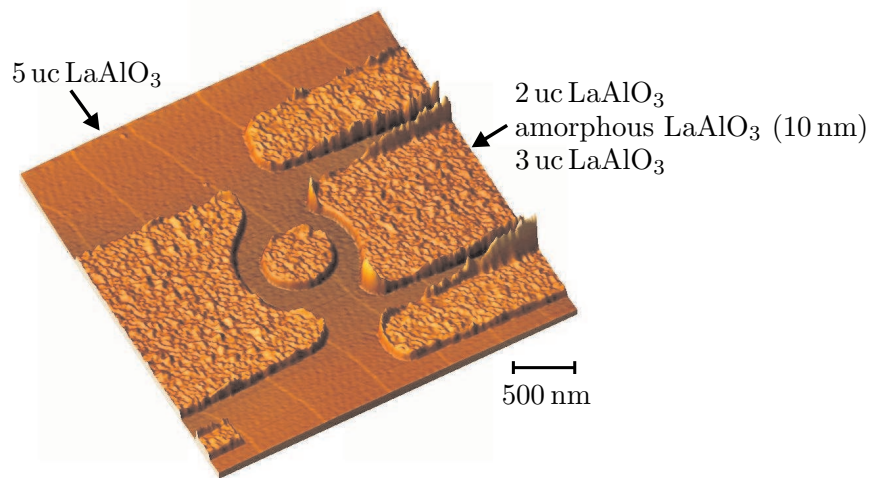


Figure 6.5: AFM image (topographic signal) of a structure containing a ring, which defines a q_2 -DEG with a diameter of $\approx 1.2 \mu\text{m}$ and a track width of ≈ 220 nm (sample L49). Each half of the ring comprises one LaAlO_3 terrace. Published in Ref. [108].

The observed RHEED oscillations and the AFM images, which show a clear step-and-terrace structure in the epitaxial areas, reveal that the samples have grown very well. In the patterning process the epitaxial LaAlO_3 film is grown in two steps, and a photoresist and a developer touch the LaAlO_3 after the first deposition. To clarify whether this affects the formation of the electron gas and the value for the critical thickness, the electronic properties of the conducting interface of structured samples were investigated.

6.2 Electronic Transport Properties of Patterned $\text{LaAlO}_3/\text{SrTiO}_3$ Samples

Standard four-point measurements were used to check the transport properties of the patterned tracks. Areas between separated tracks with 2 uc of epitaxial LaAlO_3 were found to be insulating with resistances exceeding the input impedance ($10^{10} \Omega$) of the voltmeter used (Keithley Model 2000). This insulating behavior proves that the additional deposition of amorphous LaAlO_3 on 2 uc of LaAlO_3 does not change the interface properties for this LaAlO_3 film thickness.

Areas of the patterned tracks with at least 4 uc of LaAlO_3 are found to be conducting. This proves that the critical thickness for the formation of the electron gas is not changed, and that a q2-DEG is only formed in the areas with at least 4 uc of LaAlO_3 .

To be sure that the conducting interface is only formed in the designed tracks and does not extend far beyond the edges, the resistance of two bridges with different widths is measured. As shown in Fig. 6.6, the resistance of the tracks scales well with the structure size. Therefore it is concluded that the q2-DEG indeed only forms in the designed areas with $d_{\text{LAO}} \geq 4$ uc. The exact shape and transition of the electron gas into the adjacent insulating areas at the edges is not known.

Figure 6.7 shows the sheet resistances of an unpatterned sample and a patterned sample with a track of width $1.5 \mu\text{m}$. Both q2-DEG have a very similar temperature dependence of R_s with sheet conductivities of $\sigma_s \approx 5 \times 10^{-3} (\Omega)^{-1}$ at 4.2 K and $\sigma_s \approx 5 \times 10^{-5} (\Omega)^{-1}$ at 300 K. It was possible to operate the electron gases of these structures with current densities as high as $3 \times 10^6 \text{ A/cm}^2$ and $2 \times 10^4 \text{ A/cm}^2$ at 4.2 K and 300 K, respectively.

Hall measurements confirmed that the charge carriers are negatively charged, with densities of $\approx 10^{13} \text{ cm}^{-2}$, like observed for the standard unpatterned samples before.

These experiments clearly show that the electronic properties of the q2-DEG are not changed by the patterning process. The electron gas at the interface therefore now can be studied with true true four-point measurements in a clearly defined geometry. Furthermore, the successful structuring of samples enables the realization of different device layouts. For example, the field-effect experiments with a top gate, which were described in Sec. 5.3, utilized patterned tracks. In this way, the top gates can then cover, and therefore affect, the complete DS channel in these FET structures.

Also a slightly modified route to lithographically pattern the electron gas was explored. In this approach the resist structure was patterned directly onto the TiO_2 -terminated SrTiO_3 surface (sample L54). After deposition of amorphous LaAlO_3 and lift-off, 5 uc of epitaxial LaAlO_3 were grown. As the first step of depositing 2 uc of epitaxial LaAlO_3 is skipped, this technique is simpler and faster, but suffers from the drawback that the

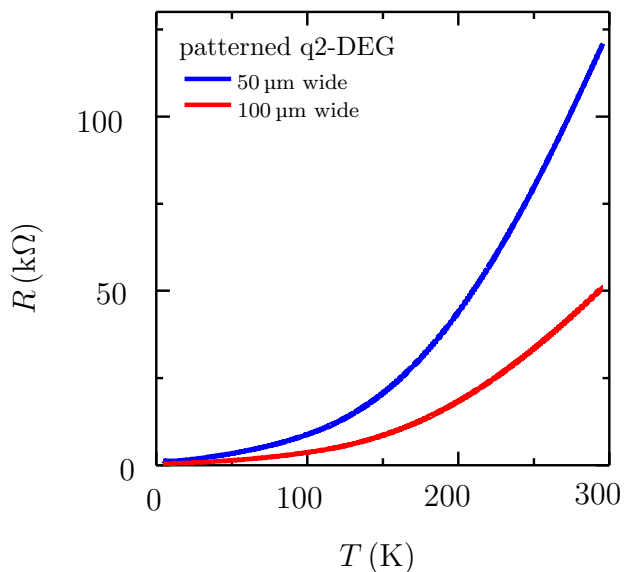


Figure 6.6: Resistance of a patterned q2-DEG (sample L51) measured as a function of temperature. The measurement was done in a four-point configuration on lithographically defined tracks with widths of $50 \mu\text{m}$ and $100 \mu\text{m}$, and $300 \mu\text{m}$ distance between the voltage probes. Published in Ref. [108].

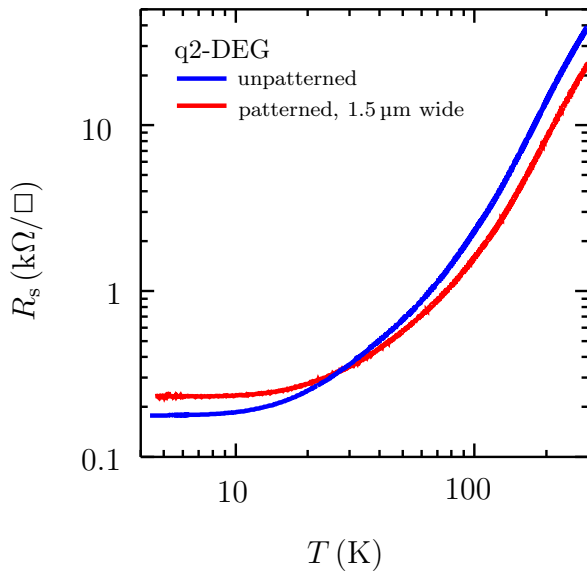


Figure 6.7: Sheet resistance of the q2-DEG as a function of temperature for an unpatterned sample with 6 uc of LaAlO₃ (L29) and for a track with a width of 1.5 μm and 5 uc of LaAlO₃ (sample L52). Published in Ref. [108].

SrTiO₃ surface, which later is crucial for the SrTiO₃/LaAlO₃ interface, is exposed to the resist and the solvents. Therefore the quality of the interface will be reduced. A detrimental effect is indeed observed in transport measurements of structures prepared in this way. The resistances are higher than those of the samples patterned by the standard process. Furthermore, the step-and-terrace structure of the surface topography is slightly rougher.

Due to these findings only the standard patterning process, which initially protects the interface by epitaxial LaAlO₃, is used for the work described in this thesis.

For potential electric field effect experiments via a top gate it is important to also characterize the insulating properties of the patterned epitaxial LaAlO₃. Figure 6.8 shows the I - V curve measured on a patterned sample across a 5 uc thick LaAlO₃ layer in a two-point configuration from the top gate down to the interface.

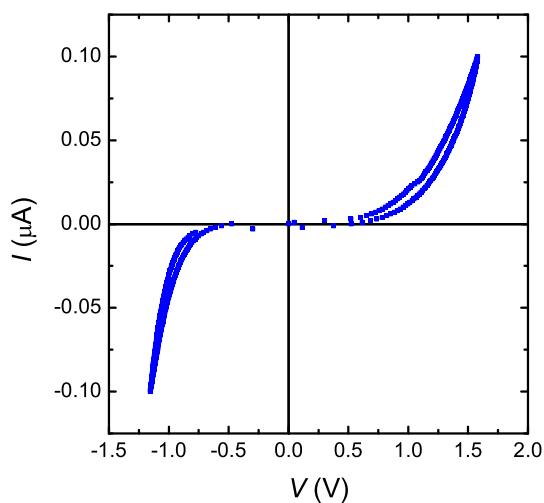


Figure 6.8: Current-voltage characteristic of a sample with 5 uc of epitaxial LaAlO₃ on the patterned, conducting bridge (sample L51) measured in a two-point configuration with one contact at the top gate and the other at the q2-DEG. Leakage currents < 10 nA are found for voltages up to 0.5 V.

A typical resistance value of the LaAlO_3 is $\approx 100 \text{ M}\Omega$ (at 4.2 K and 300 K) with leakage currents $< 10 \text{ nA}$ measured for an area of $50 \times 100 \mu\text{m}^2$. This value corresponds to a resistivity $\rho_{\text{LAO}} \approx 2 \times 10^8 \Omega\text{m}$. Due to these excellent insulating properties patterned bridges were used widely in our group for top gate field effect experiments with defined track geometries [105].

In the following other approaches to patterning, which were investigated in this thesis, will be briefly presented.

6.3 Investigation of Other Patterning Techniques

To pattern the q2-DEG it was also tried to use Ar-ion etching to pre-structure the SrTiO_3 substrate prior to the termination procedure and the film deposition. The structures were covered with photoresist and then patterned by photolithography. After ion etching (acceleration voltage 500 V, beam current 10 mA) the sample for one hour and removal of the resist the previously protected areas form plateaus, which are 220 nm higher than the etched parts. Unfortunately it turned out that the flanks of the plateaus were well conducting so that they shunted the high and low levels of the sample electronically. It was not possible to remove these shunts by a chemical treatment in buffered HF solution. This approach was therefore not followed.

While the developed patterning process makes use of the discovered step in interface conductivity for LaAlO_3 film thicknesses between 3 uc and 4 uc by stepwise increasing the number of unit cells of the epitaxial film to the desired value for the different areas, I also investigated an approach going in the opposite direction. By successively reducing the LaAlO_3 film thickness from $d_{\text{LAO}} \geq 4 \text{ uc}$ to $d_{\text{LAO}} \leq 3 \text{ uc}$ in a controlled way it might be possible to pattern the samples into conducting and insulating areas.

The idea was to try to use an AFM tip of a standard silicon cantilever (force constant 10–130 N/m) to mechanically remove material from the LaAlO_3 film surface to decrease the film thickness to below d_c . After engaging the AFM tip onto the sample surface in standard tapping mode the sample topography was monitored. Then, while scanning a fixed line of several μm length, the cantilever was lowered further to press the tip with increased force onto the sample surface. After some scan lines the tip was lifted to the initial value, and an AFM image of the sample after scratching was taken. The tip was still sharp enough to get good images.

Lowering of only $\approx 4 \mu\text{m}$ did not result in a visible change on the standard step-and-terrace structure. If the sample surface was covered by a dirt layer of some nm, caused by improper storage under ambient conditions for weeks instead of keeping it in a drybox, the scanning of the lowered tip worked like a broom and removed the dirt on the scanned area, so that the step-and-terrace structure was visible again.

Removal of LaAlO_3 from the surface was observed when the tip was lowered by a nominal distance of 15–20 μm . In the used experimental setup the stability of the scan was not sufficient, so that the tip did not scratch along one fixed line, but made several parallel lines. Also it was not possible to determine the depth of the scratch reliably on a unit cell level. On one patterned sample (5 uc thick LaAlO_3 on conducting bridges, separated by insulating areas with 2 uc of LaAlO_3 , sample L52) the AFM tip was scratched

perpendicular to a 2 μm wide transport measurement bridge until a trench of ≈ 4 nm was formed. While the bridge was conducting before, no electronic transport was possible across the scratched line. This observation is another proof against oxygen vacancies extending deep into the SrTiO_3 substrate to be responsible for the observed conductivity in $\text{LaAlO}_3/\text{SrTiO}_3$ heterostructures.

Due to the insufficient accuracy of in-plane position of the tip and depth of the formed trench this approach was not followed further.

Recently, in 2008, another patterning method, which also makes use of the critical thickness $d_c = 4$ uc for $\text{LaAlO}_3/\text{SrTiO}_3$ interfaces was reported in a publication by Caviglia *et al.* [109] from the University of Geneva. On their samples, the LaAlO_3 thickness was reduced from $d_{\text{LAO}} \geq d_c$ down to $d_{\text{LAO}} < 2$ uc in photolithographically defined regions by irradiation with Ar-ions. While the homogeneity of the ion etching in our setup is insufficient to remove LaAlO_3 with unit cell accuracy, the group in Geneva manages to get conducting areas separated by insulating parts with LaAlO_3 films of subcritical thickness and pattern the samples in this way.

This experiment is an additional strong argument against oxygen vacancies at the interface being responsible for the observed conductivity. If the vacancies would be formed during sample preparation, either due to the specifically used deposition pressure or the PLD process itself, the defects and the conductivity are expected to remain even if some unit cells of LaAlO_3 are removed from the surface.

6.4 Summary

During the studies described in the previous chapters it was realized that a crucial, experimental technique was still missing for the $\text{LaAlO}_3/\text{SrTiO}_3$ heterostructures. Up to now it was impossible to structure them, so the conducting interface always extended over the complete sample area.

For this reason a lithography technique was developed that allows to pattern the electron gas formed at the $\text{LaAlO}_3/\text{SrTiO}_3$ interface. It exploits the critical thickness phenomenon, which was presented in Sec.4.1. By a special, sequential deposition of epitaxial and amorphous LaAlO_3 the thickness of epitaxial LaAlO_3 on the sample is varied from $d_{\text{LAO}} < d_c$ (insulating interface) to $d_{\text{LAO}} \geq 4$ uc (conducting interface). The technique does not create unwanted shunts and does not expose the interface to resists or solvents during the patterning process.

For the first time it is now possible to measure the samples in clearly defined geometries and to structure them according to the design requirements of an experiment or a device. The smallest structures realized with the presented method of LaAlO_3 thickness variation were ≈ 200 nm in width.

This method, which is extensively used in the rest of this thesis, is not limited to the $\text{LaAlO}_3/\text{SrTiO}_3$ interface, but can be used for every system with a similar dependence of conductivity on film thickness, like for example in $\text{LaVO}_3/\text{SrTiO}_3$ heterostructures [89].

After this rather technical chapter, the following chapters put their focus again on the electronic properties of the electron gas.

7 Interface Superconductivity

What is the ground state of the electron gas? This chapter presents low-temperature experiments to investigate this fundamental question.

One possibility is that the electron gas condenses into a superconducting state. For field effect transistor configurations it has been proposed that a superconducting, two-dimensional (2D) electron gas can be generated at the SrTiO₃ surface [110]. It was also pointed out that the polarization of the SrTiO₃ layers may cause the electrons on SrTiO₃ surfaces to pair and form at high temperatures a superconducting condensate [104, 111].

Another option for the ground state of the LaAlO₃/SrTiO₃ interface, which was predicted as a result of theoretical calculations carried out in Ref. [46], is charge-ordering with ferromagnetic spin alignment.

7.1 Low Temperature Measurements of LaAlO₃/SrTiO₃ Heterostructures

To investigate the ground state of the electron system, patterned LaAlO₃/SrTiO₃ samples were grown using our standard conditions. Patterned bridges of width 100 μm and lengths of 300 μm–700 μm were prepared with $d_{\text{LAO}} \geq d_c$, which were separated by 2 uc thick LaAlO₃ layers for reference. These heterostructures were first characterized by transport measurements carried out in four-point configuration using our setup in Augsburg. The temperatures was varied between 300 K and 4.2 K. As always, the samples were kept in the dark for at least 20 hours before the experiments to avoid photoconduction effects in the measurements.

The samples are found to be conducting with the standard values for sheet resistances and sheet carrier densities. At 4.2 K a positive magnetoresistance is observed for a magnetic field up to 8 T applied perpendicular to the interface plane. The 2 uc thick structures on the same sample were insulating ($R > 30 M\Omega$) at all T . All these observations resemble the typical behavior found for our samples grown at standard conditions, as described in previous sections.

After finishing these experiments the samples were sent to N. Reyren and A.D. Caviglia in the group of J.-M. Triscone at the University of Geneva (Switzerland) to be measured in a He³/He⁴ dilution refrigerator. This setup allows to cool the samples to $T \approx 30$ mK.

Figure 7.1 shows the electronic transport properties of two samples. Both were measured after being kept in darkness for about one day to exclude photoconduction. At very low temperatures, which were not accessible in our previous experiments, a pronounced drop in resistance is observed. Around 200 mK the samples undergo a transition into a state for which no resistance could be measured. These measurements were the first to show that the interface between the insulators LaAlO₃ and SrTiO₃ can be superconducting.

This transition into the superconducting state is found for all LaAlO₃/SrTiO₃ samples measured at very low temperatures, which were grown using our standard conditions

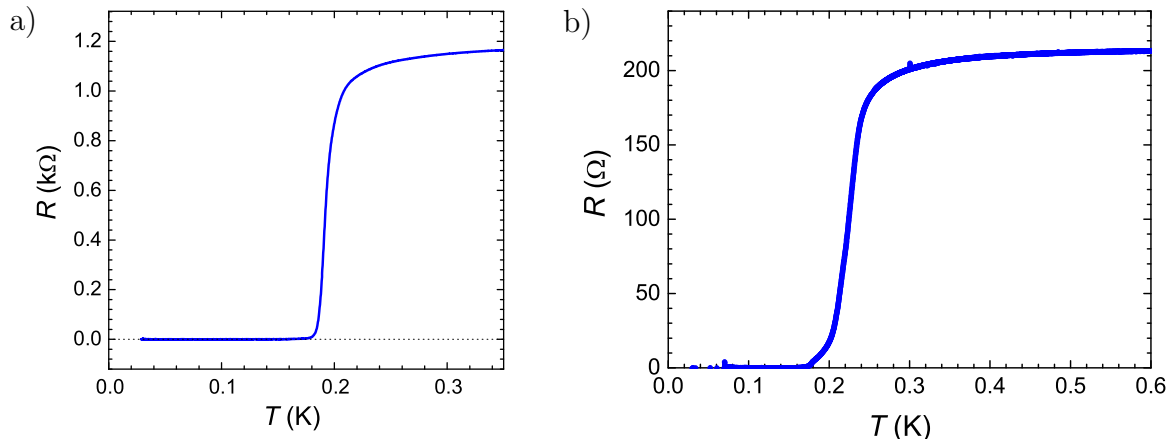


Figure 7.1: Resistance as a function of temperature of $\text{LaAlO}_3/\text{SrTiO}_3$ heterostructures at low T . A measurement current of 100 nA was used. For both samples with **a**, 8 uc (sample L120) and **b**, 6 uc of LaAlO_3 (sample L131) a superconducting transition is observed at $T \approx 200$ mK. For the 6 uc sample only one van-der-Pauw contact configuration was measured, therefore R and not R_s is plotted. The sheet resistance of the patterned 8 uc sample is shown in detail in Fig. 7.2. The measurements were done by N. Reyren and A.D. Caviglia at the University of Geneva.

($p(\text{O}_2) \approx 10^{-5}$ mbar). The experiments on the effect of higher deposition pressures on the ground state of the q2-DEG will be presented and discussed at the end of this chapter.

Similar to the step in conductivity as a function of LaAlO_3 film thickness found before, where the sheet resistance of conducting interfaces is independent of d_{LAO} for $d_{\text{LAO}} \geq 4$ uc, also T_c was always found to be ≈ 200 mK for $d_{\text{LAO}} \geq 4$ uc. If the LaAlO_3 film is only 2 uc thick the interface is found to be insulating in the accessible temperature range of 30 mK – 300 K.

The superconducting properties of the sample with 8 uc thick LaAlO_3 were analyzed in detail, which is presented next.

The width of the transition (20% to 80%) of the sample L120 is $\cong 16$ mK, with the resistance dropping by more than three orders of magnitude to a value within the noise limit of the measurement setup. This limit of the voltage resolution is caused by thermal noise, with an amplitude which is mainly determined by the contact resistance.

If the contact resistance is too high, as found for example for Pt-wires contacted with silver paint instead of wire-bonding on our standard contacts, superconductivity can not be observed in the measurements. This effect shows the need for a very low heat load to the $\text{LaAlO}_3/\text{SrTiO}_3$ samples in these low temperature experiments.

The zero-voltage state was measured by using a small bias current of 100 nA to stay below the critical current.

If the validity of the BCS theory of superconductivity is assumed for this system, the superconducting energy gap Δ can be calculated from the relation $2\Delta (T = 0 \text{ K}) = 3.5 k_B T_c$

(with critical temperature T_c , Boltzmann constant k_B). One obtains $\Delta(T=0\text{ K}) \approx 30\text{ }\mu\text{eV}$ from $T_c \approx 200\text{ mK}$ for the $\text{LaAlO}_3/\text{SrTiO}_3$ interface.

The effect of an applied magnetic field on the zero-resistance state of the sample is shown in Fig. 7.2. As expected from the low value of the energy gap, the superconductivity is weak and the transition is completely suppressed by a small field of 180 mT. The normal state resistance increases for magnetic fields at least up to 8 T. The consequence of this sensitivity for the investigation of the superconducting state at 0 T is that the magnetic field perpendicular to the interface has to be canceled as precisely as possible. This precise alignment was done by minimizing the sample resistance as a function of the current in the magnetic coil. Performing the procedure right at the temperature of the sharp superconducting transition, where R is very sensitive to magnetic fields, allowed adjustment with a precision leading to a residual field estimated to be lower than 0.1 mT.

From these $R_s(T)$ data as a function of magnetic field one can extract the $T_c(H)$ dependence, with T_c defined as $R(T_c) = 0.5 \times R(1\text{ K})$, which provides a measure for the upper critical field $H_{c2}(T)$. Figure 7.3 shows the extracted $H_{c2}(T)$ curve, with an extrapolated value of $H_{c2}(0\text{ K}) \cong 65\text{ mT}$. If BCS theory is assumed to be applicable, one obtains the coherence length $\xi(T=0\text{ K}) \approx 70\text{ nm}$ from the relation $B_{c2} = \Phi_0/2\pi\xi^2$ (Φ_0 being the flux quantum $h/2e$).

To determine the critical currents in this system, voltage-current characteristics were measured at various temperatures. The corresponding data, measured in a four-point setup using a dc technique, are shown in Fig. 7.4a. While ohmic characteristics are observed for high temperatures, the V - I curves show a well defined critical current I_c at low T . As criterion for I_c the current at which the $dV/dI(I)$ value is maximal is taken. The obtained temperature dependence of I_c is shown in Fig. 7.4b. For $T = 30\text{ mK}$, a maximal value $I_c = 98\text{ }\mu\text{A/cm}$ is deduced for the 8 uc sample.

The transition into the superconducting state, which was found for samples grown in Augsburg using our standard conditions, was confirmed by the group at the University of

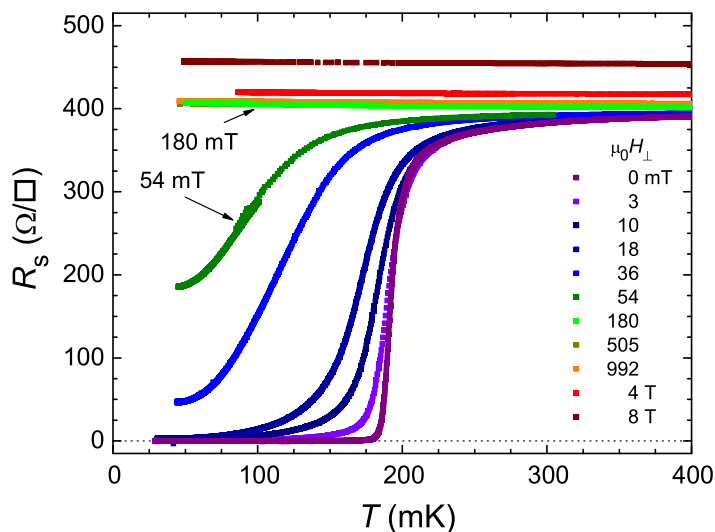


Figure 7.2: Sheet resistance measured as a function of temperature of a sample with 8 uc of LaAlO_3 (sample L120) plotted for different magnetic fields applied perpendicular to the interface. The measurements were done by N. Reyren and A.D. Caviglia at the University of Geneva. Published in Ref. [91].

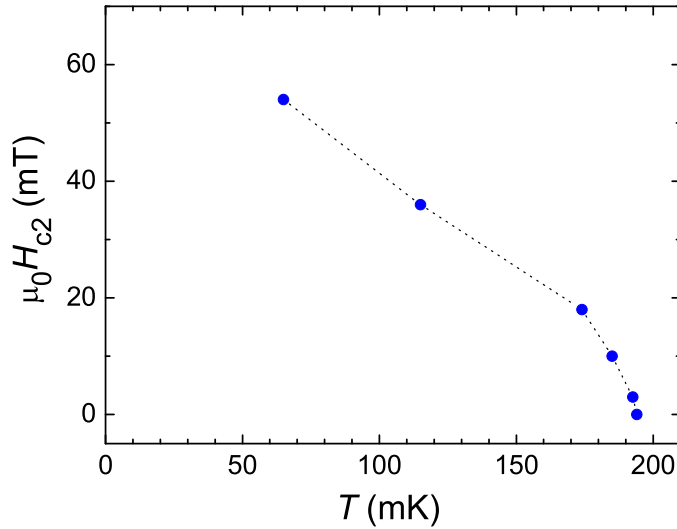


Figure 7.3: Temperature dependence of the upper critical field H_{c2} for a sample with 8 uc of LaAlO_3 (sample L120). The measurements were done by N. Reyren and A.D. Caviglia at the University of Geneva. Published in Ref. [91].

Geneva for $\text{LaAlO}_3/\text{SrTiO}_3$ samples grown in their PLD system with the same deposition parameters. They also find transition temperatures of ≈ 200 mK. T_c is similar, but not identical for the various samples from Augsburg and Geneva. A variation of ≈ 30 mK is observed.

The only exception to the previous statements are the results obtained from the very

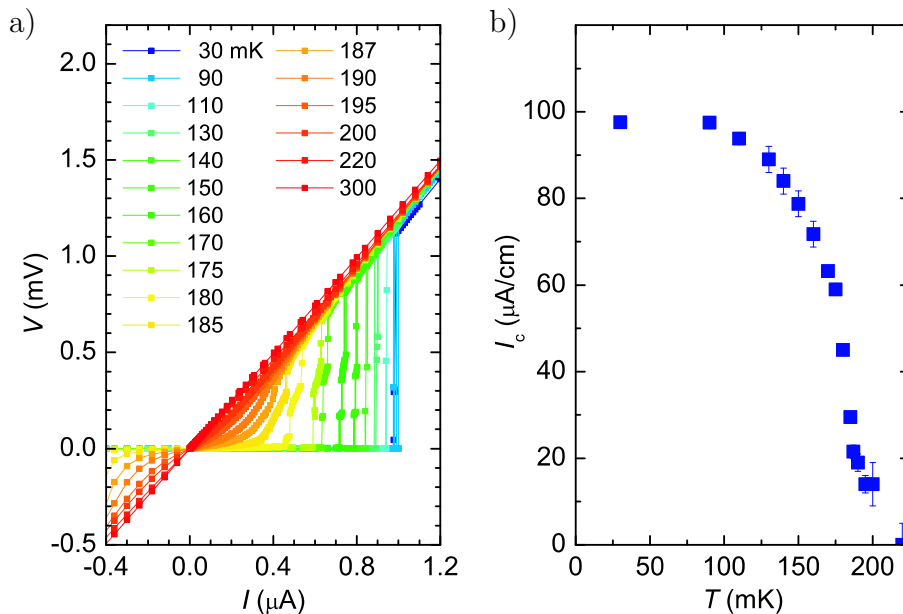


Figure 7.4: Transport measurements of a sample with 8 uc of LaAlO_3 (sample L120). **a**, Temperature-dependent voltage-current characteristics of a $100 \times 300 \mu\text{m}^2$ bridge. **b**, Temperature dependence of the critical current density per bridge width, as obtained from the measurements shown in **a**. The measurements were done by N. Reyren and A.D. Caviglia at the University of Geneva. Published in Ref. [91].

first sample (L95, 15 uc of LaAlO_3 , kept for some months in a drybox) which was measured at very low temperatures. The $R(T)$ data of this sample showed a critical temperature of only 100 mK and additional, small structures in the $R(T)$ curves at lower temperatures. Further differences to the samples described before are a smaller critical field H_{c2} of only 10 mT, much smaller critical currents I_c at 36 mK of about $5 \mu\text{A}/\text{cm}$ (\approx factor 20 less), and a step-like structure in the $V(I)$ curves, which indicates that the low critical current of this sample is caused by inhomogeneities. Due to these findings the transport properties of this probably degraded sample are not compared to the other $\text{LaAlO}_3/\text{SrTiO}_3$ heterostructures.

The occurrence of the zero-resistance state in samples grown in two different PLD systems and the characteristic $R(T,H)$ and $V(I,H)$ dependencies provide clear evidence for superconductivity at the $\text{LaAlO}_3/\text{SrTiO}_3$ interface.

The quasi two-dimensionality of the electron system has some interesting consequences for the superconducting state, which are discussed in the following.

The superconducting samples are transparent at optical frequencies (see Fig.7.5), which sets them apart from other known superconductors, which are opaque and colored even for small film thicknesses. The q2-DEG looks different, because of the smaller charge carrier density and the 2D nature of the conducting layer. The calculated three-dimensional plasma frequency $\omega_{p,3D} = (ne^2/m\epsilon_r\epsilon_0)^{1/2}$ (with electron mass m , electron charge e , dielectric constant ϵ_r , vacuum dielectric constant ϵ_0 , and charge carrier density $n \approx 10^{20} \text{ cm}^{-3}$ for an assumed thickness of about 2 nm) for $\text{LaAlO}_3/\text{SrTiO}_3$ samples is $\omega_{p,3D} \approx 6 \times 10^{14} \text{ Hz}$. This frequency corresponds to a wavelength λ of about $3 \mu\text{m}$ (infrared). As the screening from a two-dimensional sheet is worse than from a 3D bulk material the real plasma frequency $\omega_{p,2D}$ for the quasi two-dimensional electron gas is even below this calculated value, which renders the sample optically transparent.

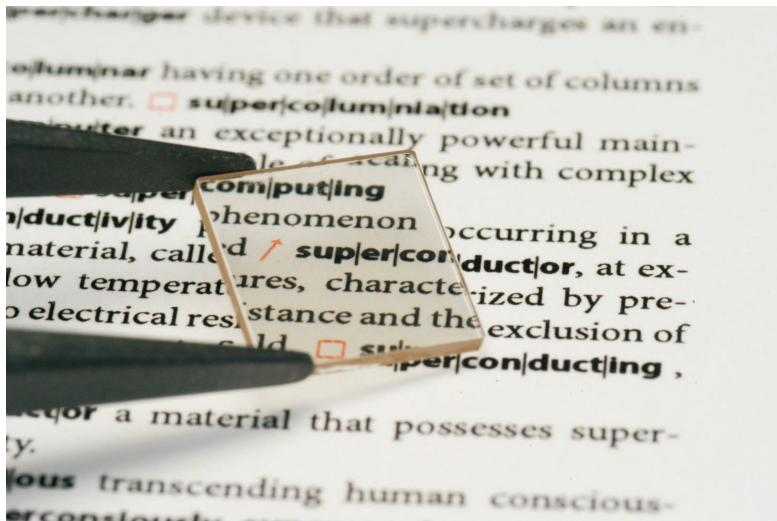


Figure 7.5: Photo of a sample ($10 \times 10 \text{ mm}^2$, sample L151) with 8 uc of LaAlO_3 on a SrTiO_3 substrate with a polished backside. The slight hue of the sample is caused by the SrTiO_3 substrate (see Sec. 2.2).

7.2 Berezinskii-Kosterlitz-Thouless Transition

The focus of this section is on a prediction for the low-dimensional electron gas at low temperatures. If the $\text{LaAlO}_3/\text{SrTiO}_3$ heterostructure interfaces were 2D superconductors, a special transition is expected to be observable: the Berezinskii-Kosterlitz-Thouless (BKT) transition [112–115]. After a general introduction to this effect the analysis of the transport data in our samples will be presented. This analysis provides evidence for the existence of a BKT transition.

The BKT transition is a special transition which was first predicted for the XY model for interacting spin systems (spins constrained to rotate in the plane of the lattice) in two spatial dimensions (2D-XY model). From the Mermin-Wagner theorem it is known that such a system does not have any long-range order and accompanying phase transitions, because the ground state is unstable against low-energy spin-wave excitations. However, it was shown by BKT that another type of transition exists.

In the mentioned 2D-XY model vortices are topologically stable configurations with an energy $E = \kappa \ln(R/a)$, where κ is a constant factor, R is the system size, and a is the radius of the vortex core. However, these vortices are only present in the system above a certain transition temperature. This requirement can be derived from a thermodynamic argumentation. From the total number of possible positions for vortices, which is approximately $(R/a)^2$ (where R is assumed to be much larger than a) one obtains an entropy $S = 2k_B \ln(R/a)$ from Boltzmann's law (k_B is Boltzmann's constant). Then calculating the Helmholtz free energy F results in $F = E - TS = (\kappa - 2k_B T) \ln(R/a)$. Only for $F < 0$ stable vortices can be present in the system. The transition temperature T_{BKT} is thus defined as the temperature for which the condition $F = 0$ is met, which yields $T_{\text{BKT}} = \kappa / (2k_B)$. The excitations are suppressed for temperatures lower than T_{BKT} , while above T_{BKT} the formation of such vortices is thermodynamically favorable.

Below the transition temperature T_{BKT} the excitation energy of a vortex-antivortex dipole is, however, finite (not increasing logarithmically with the system size R). From considerations of the free energy F one then finds that such bound pairs are not thermodynamically forbidden and will be formed. At the BKT transition these pairs dissociate into free vortices.

Already in the first publications on the BKT transition it was pointed out that the previously described scenario is also applicable to neutral superfluids [113, 114]. If a condensate wavefunction can be defined in a local region, it is possible to explore the variation of the phase of the wavefunction from one region to a neighboring region. Then one can obtain a total vorticity within a region by calculating the change of phase along the boundary of the local region, divided by 2π . For this system, the energy of a superfluid vortex increases also logarithmically with the system size, like for the vortices discussed previously.

Kosterlitz and Thouless pointed out that, in contrast to neutral superfluids, for a superconducting condensate the argumentation can not be carried through, because the formation energy of a single flux line is finite. The first ones to show that this energy is finite were Pearl *et al.* [116], who found an interaction energy, which again increases logarithmically with the system size, but only to a characteristic distance $\lambda_{\perp} = \lambda^2/d$, beyond

which the energy falls off as $1/r$ (here λ is the bulk penetration depth of the material of the film, d is the film thickness and λ_{\perp} is the magnetic penetration depth for fields perpendicular to the film). Due to their finite energy the single flux lines are always thermally present and no BKT transition is expected to be observable.

Later, Beasley *et al.* [117] reasoned that in all superconducting systems of interest λ_{\perp} is so large (on the order of a few millimeters), that in practice the situation in superconductors is analogous to that in uncharged superfluids. It should therefore be possible to find BKT transitions in superconducting thin films. Beasley *et al.* expect only some broadening of the vortex-pair dissociation transition in the superconducting case.

While the considerations before show that in principle it might be possible to observe BKT transitions, Gabay *et al.* [118] found that applying the BKT theory to thin superconducting films poses more difficulties, as discussed in the following.

Gabay *et al.* calculate a “critical fugacity” $y_c = \exp(-E_c/k_B T_{\text{BKT}})$, which relates the energy E_c , needed to create a vortex, to the thermal energy $k_B T_{\text{BKT}}$ at the transition. For a superconducting film the value found for y_c is ≈ 300 times larger than typical values for superfluids or granular superconductors. The consequence is that a very dense state is formed, where a crystallization of the vortex-antivortex fluid into an “ionic” crystal occurs. For such a system not the standard BKT transition appears. Instead the melting of the vortex-antivortex lattice represents the BKT transition, which then occurs at lower temperatures.

This discussion concerning the BKT transition shows that in principle such a transition is expected to occur in the $\text{LaAlO}_3/\text{SrTiO}_3$ system if the superconducting sheet is two-dimensional. Theoretical predictions from the BKT theory for the shape of $V(I)$ and $R(T)$ characteristics offer the possibility to indirectly identify the presence of a BKT transition.

An analysis of the measured voltage-current characteristics of $\text{LaAlO}_3/\text{SrTiO}_3$ heterostructures offers one approach to test the predictions by BKT (Fig. 7.6a). Starting from ohmic behavior at high currents the samples develop a small voltage drop below the superconducting transition at I_c . This voltage is proportional to the current and increases with temperature. For 30 mK, the lowest measured temperature, one finds that the associated resistance is at least four orders of magnitude smaller than the normal state resistance. With T increasing from 30 mK to 180 mK this resistance grows exponentially from $\approx 0.1 \Omega$ to 10Ω . Between 180 mK and T_c the step at I_c disappears and power-law type $V(I)$ curves are observed, as illustrated by the short black lines. In the following it will be shown, that this behavior of $V(I)$ is consistent with a BKT transition in finite size systems.

At the BKT transition the current-induced Lorentz force causes dislocation-antidislocation pairs to unbind, which results in a $V \propto I^a$ dependence, with $a(T_{\text{BKT}}) = 3$. In Fig. 7.6a short black lines show the power-law behavior of the $V(I)$ curves directly below and above the transition temperature, and additionally two long black lines are drawn which correspond to $V \propto I$ and $V \propto I^3$. By extracting the exponent a for different temperatures from the $V(I)$ curves one obtains the data shown in Fig. 7.6b. Starting from $a = 1$ at $T = 300$ mK, the exponent approaches $a = 3$ at $T = 188$ mK. Therefore $T_{\text{BKT}} = 188$ mK is identified. It is noted here that the further increase of the exponent a for lower tem-

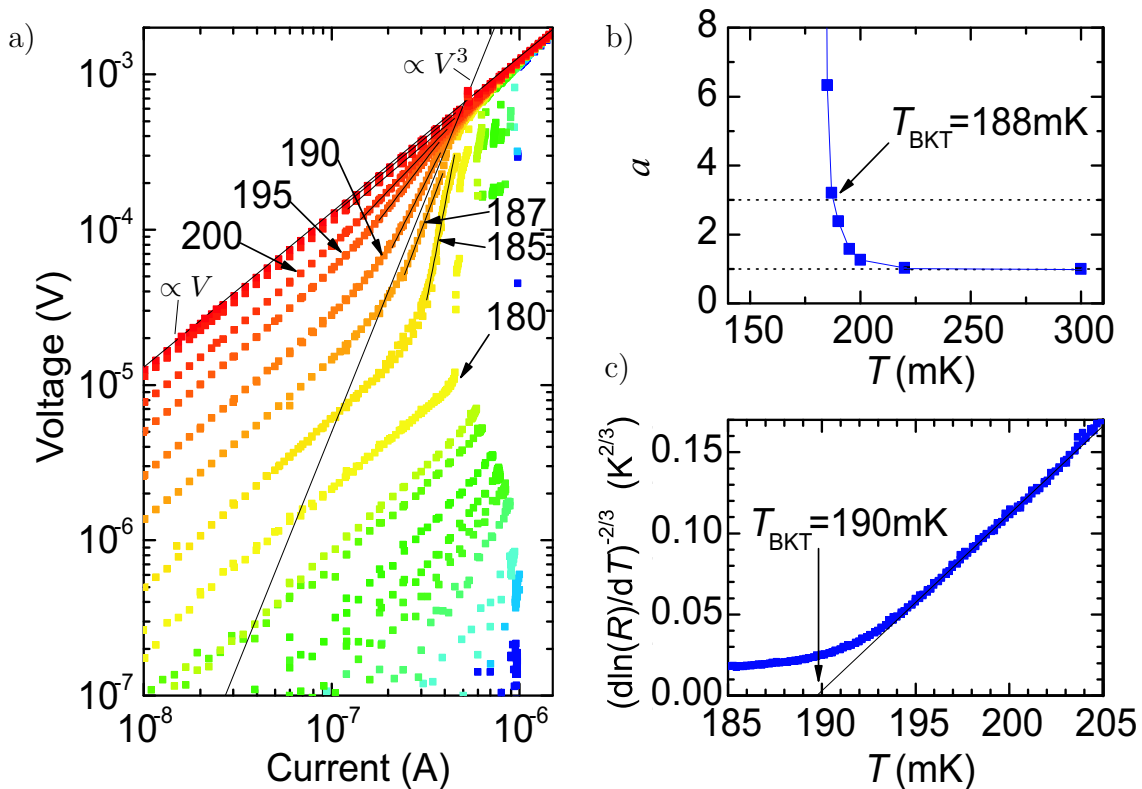


Figure 7.6: Low-temperature transport properties of the 8 uc $\text{LaAlO}_3/\text{SrTiO}_3$ heterostructure (sample L120). **a**, $V(I)$ curves on a logarithmic scale. The color code is the same as in Fig. 7.4a. Additionally the small numbers indicate the temperatures in mK at which the curves were taken. The short black lines are fits to a power-law behavior $V \propto I^a$. The long, black lines correspond to $V \propto I$ and $V \propto I^3$. Between 187 mK and 190 mK the exponent a assumes the value 3, which signals the BKT transition. **b**, Temperature dependence of the power-law exponent a , as deduced from the fits shown in **a**. $T_{\text{BKT}} = 188$ mK is found. **c**, $R(T)$ dependence of the sample plotted on a $(d \ln(R)/dT)^{-2/3}$ scale. The solid line corresponds to the behavior expected for a BKT transition with $T_{\text{BKT}} = 190$ mK. The measurements were done by N. Reyren and A.D. Caviglia at the University of Geneva. Published in Ref. [91].

peratures is not fully consistent with the BKT theory.

Obviously, an ohmic $V \propto I$ dependence is found for smaller currents. Very similar results have been found in simulations treating finite size 2D systems [119]. A detailed analysis⁹ strongly suggests that also in our measurements the ohmic behavior at small currents is caused by finite size effects. Additional information is provided in the supplementary material of Ref. [91].

The $R(T)$ dependence provides another approach to test the predictions by BKT. Close to the BKT transition a $R(t) = R_0 \exp(-bt^{-1/2})$ dependence is expected [120], with material parameters R_0 and b and $t = (T/T_{\text{BKT}}) - 1$. By plotting the data as in Fig. 7.6c one finds that the $R(T)$ characteristic is consistent with the theoretical prediction, which is shown by the black line. From the intersection of this line with the x -axis $T_{\text{BKT}} = 190$ mK is deduced.

⁹Analysis performed by M. Gabay, Laboratoire de Physique des Solides, Université Paris-Sud, France

This value is in very good agreement with $T_{\text{BKT}} = 188 \text{ mK}$, which was obtained before from the analysis of the power exponent a extracted from the voltage-current characteristics.

Therefore, two independent analyses of electronic transport properties are in agreement with a BKT transition in the $\text{LaAlO}_3/\text{SrTiO}_3$ system. Almost the same T_{BKT} is obtained from both methods. Consequently, the superconducting transition in the $\text{LaAlO}_3/\text{SrTiO}_3$ samples is consistent with that expected for a 2D superconducting film.

The exact thickness of the polarity-discontinuity induced electron gas at the interface is still unknown. Unfortunately the fact that a BKT transition is observed only provides a large upper limit, because in the BKT model two-dimensionality is reached for superconducting layers which are thinner than the coherence length ξ . Experimentally we found $\xi \approx 70 \text{ nm}$ for our $\text{LaAlO}_3/\text{SrTiO}_3$ heterostructures, which is not a very small upper limit for the thickness of the q2-DEG.

7.3 Estimation of Superconducting Layer Thickness

Another limit for the superconducting layer thickness is provided by the value of the superconducting transition temperature.

It was already discussed in Sec. 4.2 why oxygen vacancies can not be responsible for the conductivity in our $\text{LaAlO}_3/\text{SrTiO}_3$ samples. But let us for a moment assume, that the conductivity was caused by a thick sheet of oxygen deficient SrTiO_{3-x} , and thus a three-dimensional layer, as suggested in several publications. In this case the well established T_c vs. carrier density diagram for SrTiO_3 [121] is applicable (see Fig. 7.7). The maximum critical temperature of 300 mK is reached for $n \approx 8 \times 10^{19} \text{ cm}^{-3}$, with decreasing T_c for both lower and higher carrier densities. Therefore two possible solutions exist to obtain $T_c = 200 \text{ mK}$, like observed in the experiments. The charge carrier density has to be either $n \approx 3 \times 10^{19} \text{ cm}^{-3}$ or $n \approx 2 \times 10^{20} \text{ cm}^{-3}$. In Hall effect experiments a sheet charge carrier density of $n_s = 3 \times 10^{13} \text{ cm}^{-2}$ was measured in the samples. Therefore, to fit to the two solutions for the carrier density n , the conducting layer has to be either $\approx 13 \text{ nm}$ or $\approx 2 \text{ nm}$ thick. From the experiments so far it is not possible to distinguish between both options.

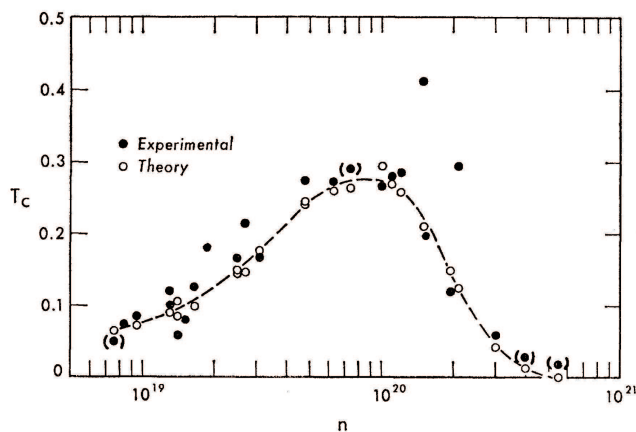


Figure 7.7: Transition temperature (in K) of doped SrTiO_3 as a function of charge carrier concentration (in cm^{-3}). From Ref. [121].

More insight can be gained from field-effect experiments, which were done by N. Reyren and A.D. Caviglia at the University of Geneva. By using a back gate electrode, they were able to modulate the carrier density n of the electron gas, just like in the experiments discussed in Chapter 5. In measurements of a sample grown in Geneva (5 uc of LaAlO₃, sample L07005) it was found that the superconducting transition temperature T_c can be tuned by application of an electric field. Upon increasing the charge carrier density of the q2-DEG by a gate voltage the resistance R is reduced and T_c decreases. This sign of the change of T_c shows that the samples have to be on the high (overdoped) charge carrier density side in the phase diagram¹⁰. This rules out one of the two possible solutions for the carrier density n and thus a thickness limit for the conducting layer of ≈ 2 nm is obtained.

As the charge carrier concentration of a sheet of SrTiO_{3-x} can not be constant, but has to conform to a profile following Poisson's equation, which takes into account the field-dependent susceptibility of SrTiO₃ [122], the upper limit is even smaller than 2 nm.

This value is considerable lower than the 70 nm limit obtained from the analysis of the BKT transition.

All the previously described experiments do not allow to determine whether the observed superconductivity is due to such a thin sheet of doped SrTiO₃ or due to a novel phenomenon occurring at the LaAlO₃/SrTiO₃ interface.

Although the T_c of the LaAlO₃/SrTiO₃ samples falls into the range of values found for oxygen deficient SrTiO_{3-x}, there are clear differences in the transport properties. The Hall constant is less temperature dependent in LaAlO₃/SrTiO₃ heterostructures than in Nb-doped SrTiO₃ films, where a stronger increase is observed below 100 K [123]. Moreover, the critical field H_c of the heterostructures is an order of magnitude smaller than that of Nb-doped SrTiO₃ exhibiting the same T_c . And of course the observation of conducting (even superconducting) and insulating behavior on the same LaAlO₃/SrTiO₃ sample, depending on the epitaxial LaAlO₃ layer thickness, is difficult to explain in a scenario where oxygen vacancies in the SrTiO₃ are responsible for the observed conductivity.

In summary, the transport experiments at very low temperatures have shown that for LaAlO₃/SrTiO₃ samples grown under our standard conditions a superconducting ground state is obtained, which shows clear signatures of a BKT transition predicted for two-dimensional systems. For the first time superconductivity is observed at the interface between two materials that are band-insulators. The nature of the superconducting ground state is not resolved yet and needs further investigation.

The LaAlO₃/SrTiO₃ interface is without doubt a beautiful model system to study low-dimensional interface superconductivity in oxide heterostructures. It offers the additional possibility of substantially changing the carrier density by electric field to, e.g., map the phase diagram.

As already mentioned at the beginning of this chapter, a magnetic ground state for the LaAlO₃/SrTiO₃ interface was predicted from a theoretical calculation [46]. At the same

¹⁰Just recently it was reported that the q2-DEG at the LaAlO₃/SrTiO₃ interface can even be tuned by electric field along almost a complete superconducting dome and finally, through a quantum phase transition, into an insulating state [109].

time when superconductivity was found in our samples grown at standard conditions, A. Brinkman *et al.* [85] from the University of Twente (Netherlands) reported on low temperature magnetic effects in LaAlO₃/SrTiO₃ heterostructures grown at $p(\text{O}_2) = 1 \times 10^{-4} - 2.5 \times 10^{-3}$ mbar. Their samples exhibit a pronounced minimum in $R(T)$ and a logarithmic temperature dependence for low T , accompanied by a hysteretic, negative magnetoresistance. These results have been interpreted in a Kondo scenario as a magnetic effect at the interface. In another publication from their group (Ref. [124]) it is claimed as a general behavior of LaAlO₃/SrTiO₃ samples grown at $p(\text{O}_2) \approx 10^{-3}$ mbar that a $R(T)$ curve like observed in their experiments is found. Furthermore it is speculated in the publication that only the samples grown at lower oxygen pressures become superconducting.

To investigate this suggested dependence of the electronic properties and the ground state of the q2-DEG on deposition conditions transport measurements were done on LaAlO₃/SrTiO₃ samples grown at higher $p(\text{O}_2)$ in our lab. As will be shown in the following, no indications for the proposed magnetic effects were observed in the experiments. Indeed our samples grown at $p(\text{O}_2) \approx 10^{-3}$ mbar are superconducting.

7.4 Transport Properties and Ground State of LaAlO₃/SrTiO₃ Samples Grown at High Oxygen Pressure

As already described in Sec. 4.2, the oxygen pressure during the deposition of the LaAlO₃ films is an important parameter. In samples grown at $p(\text{O}_2) \leq 10^{-6}$ mbar oxygen vacancies are formed in the SrTiO₃ substrate which dominate the electronic transport properties. This is not the case for the LaAlO₃/SrTiO₃ samples studied in this thesis, which usually were deposited at $p(\text{O}_2) \approx 10^{-5}$ mbar.

Additional experiments were done to investigate the effect of a higher deposition pressure on the electronic properties and the ground state of the q2-DEG.

First, LaAlO₃ films were grown at $p(\text{O}_2) = 3 \times 10^{-3}$ mbar on TiO₂-terminated SrTiO₃. Clear RHEED oscillations during film deposition and a smooth step-and-terrace surface structure, with one unit cell high steps, are observed for these samples (see Fig. 7.8).

The transport properties for one sample, which was measured for temperatures ranging from 300 K to 105 mK, are shown in Fig. 7.9 ($R_s(T)$) and Fig. 7.10 ($R(B)$). We find that the sheet resistance values and also the charge carrier density $n_s \approx 10^{13} \text{ cm}^{-2}$ are comparable to those of samples grown at standard conditions. No minimum is observed in $R_s(T)$ and at $T_c \approx 200$ mK the q2-DEG becomes superconducting. Furthermore, a positive magnetoresistance is observed for magnetic fields applied perpendicular to the interface.

These results show that the transport properties of our samples grown at $p(\text{O}_2) 3 \times 10^{-3}$ mbar match those observed for our samples grown at standard pressure ($p(\text{O}_2) \approx 10^{-5}$ mbar). Importantly, none of the features reported in Ref. [85] (minimum in $R(T)$, negative and hysteretic magnetoresistance) is found. This observation proves, in contrast to the claim made in Ref. [124], that these features are not present in all samples grown at $\approx 10^{-3}$ mbar.

For $p(\text{O}_2)$ up to $\approx 10^{-3}$ mbar no detrimental effect was observed on the electronic

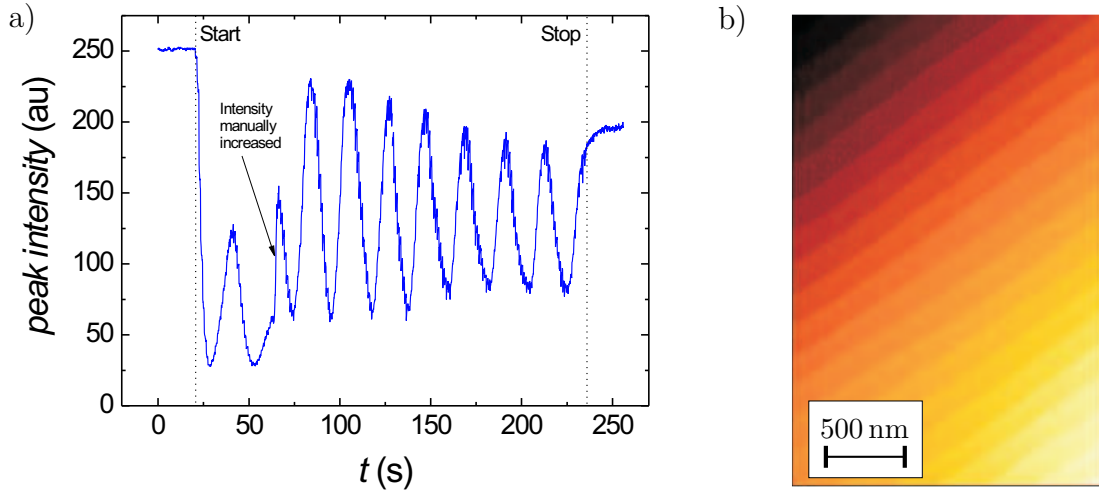


Figure 7.8: RHEED signal and AFM image of a $\text{LaAlO}_3/\text{SrTiO}_3$ sample grown at $p(\text{O}_2) = 3 \times 10^{-3}$ mbar (sample L196). **a**, Clear RHEED oscillations are observed during the deposition of 10 uc of LaAlO_3 . **b**, The AFM image shows a smooth step-and-terrace structure (topographic signal, scan size $2 \times 3 \mu\text{m}^2$, z -scale 10 nm).

properties of the q2-DEG. This changes upon a further increase of the deposition pressure. Sample growth at $p(\text{O}_2) = 1 \times 10^{-2}$ mbar in our PLD setup results in much more noise in the RHEED signal, rapidly damped oscillations, and a rougher surface topography (see Fig. 7.11).

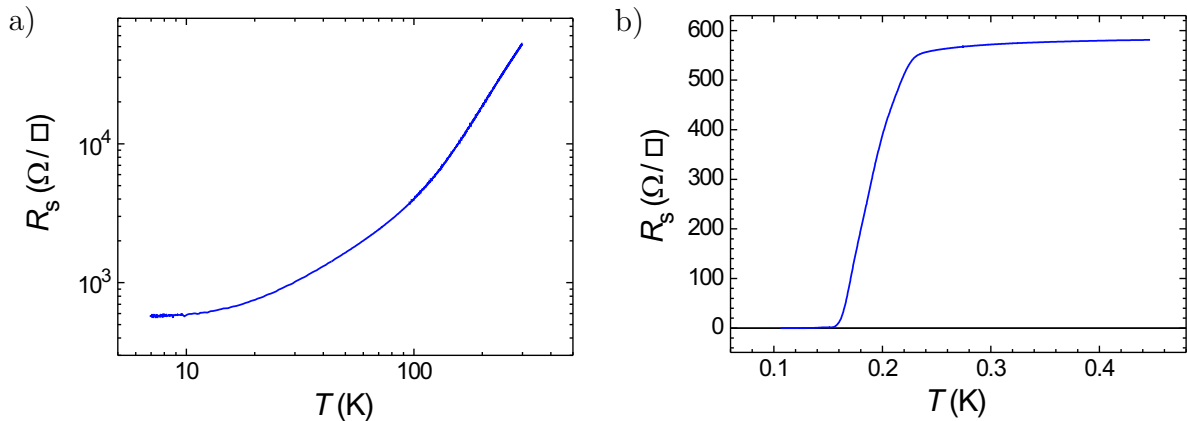


Figure 7.9: Measured sheet resistance as a function of temperature for an unpatterned $\text{LaAlO}_3/\text{SrTiO}_3$ sample grown at $p(\text{O}_2) = 3 \times 10^{-3}$ mbar (sample L196). **a**, No minimum is observed down to 4.2 K. A measurement current of $1 \mu\text{A}$ was used. **b**, Low temperature $R_s(T)$ data showing a transition into the superconducting state at ≈ 200 mK. A measurement current of $1 \mu\text{A}$ was used. The low temperature measurements were done by N. Reyren at the University of Geneva (Switzerland).

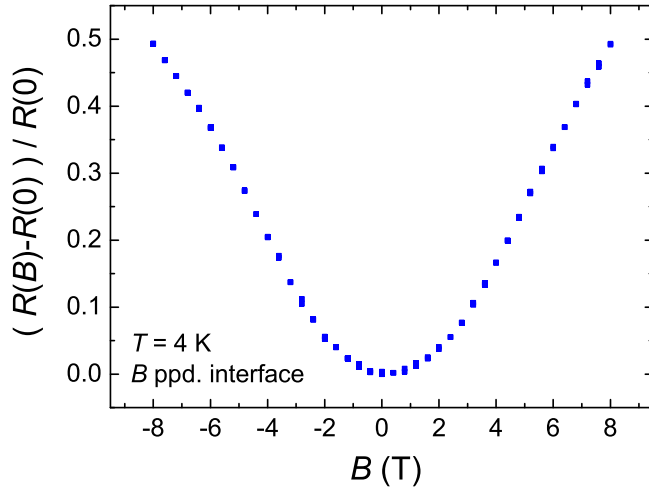


Figure 7.10: Normalized magnetoresistance for an unpatterned $\text{LaAlO}_3/\text{SrTiO}_3$ sample grown at $p(\text{O}_2) = 3 \times 10^{-3}$ mbar (sample L196). The measurement was done at $T = 4$ K with the magnetic field applied perpendicular to the interface. For this measurement a bias current of $1 \mu\text{A}$ was used.

The film growth seems to have changed, and it is therefore concluded that the quality of these $\text{LaAlO}_3/\text{SrTiO}_3$ samples is substantially reduced compared to those grown at $\approx 10^{-5}$ mbar or $\approx 10^{-3}$ mbar.

By analyzing the transport properties of samples grown at 10^{-2} mbar one observes fundamental differences compared to samples grown at lower pressures. Some of the samples are found completely insulating, and others show a peculiar temperature dependence

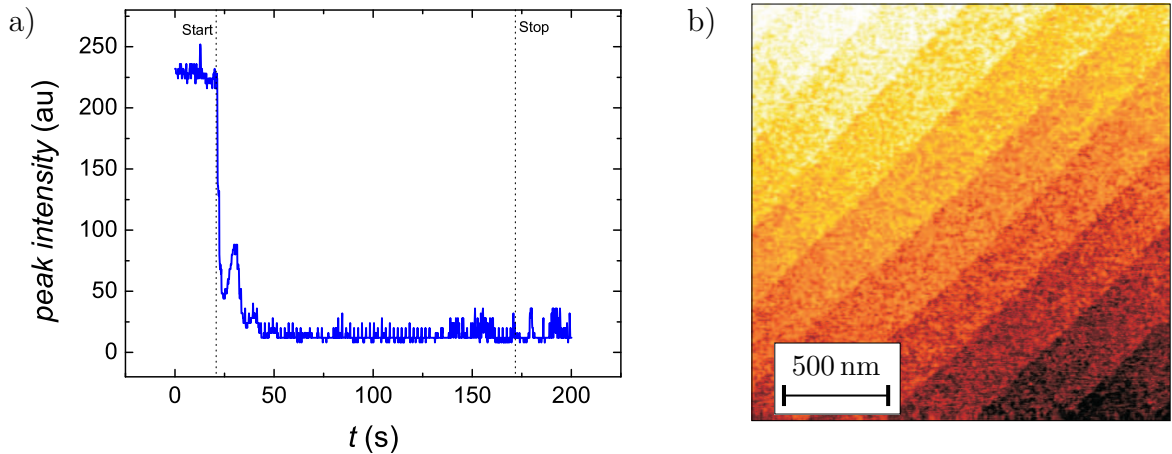


Figure 7.11: RHEED signal and AFM image of a $\text{LaAlO}_3/\text{SrTiO}_3$ sample grown at $p(\text{O}_2) = 1 \times 10^{-2}$ mbar (sample L88). **a**, The RHEED signal is much more noisy than that of standard samples, and only few oscillations are observed during the deposition of 15 uc. **b**, In the AFM image (topographic signal, scan size $2 \times 2 \mu\text{m}^2$, z -scale 5 nm) the step-and-terrace structure is still visible, but the surface is rougher ($\text{RMS} \approx 0.3$ nm) than that of the standard samples.

of the sheet resistance, such as the one shown in Fig. 7.12. At $T = 300$ K, R_s is an order of magnitude larger than the value for standard samples and upon cooling a pronounced minimum is observed at $T \approx 47$ K.

The data shown in Fig. 7.12 looks similar to the results reported in Ref. [85], which were interpreted as magnetic effects at the interface. However, as noted before, the RHEED and AFM data indicate that the film growth is very different and therefore the samples grown at $p(\text{O}_2) = 10^{-2}$ mbar in our PLD setup should not be compared to standard ones.

Supposedly a larger number of dislocations is introduced in the high pressure samples, which severely affect their electronic transport properties. This view will be discussed in the following chapter, where the detailed analysis of the strong influence of dislocations on the q2-DEG is presented.

Therefore it is concluded, that $p(\text{O}_2) \approx 3 \times 10^{-3}$ mbar is the highest deposition pressure for which good quality of the LaAlO_3 films can be assured in our PLD setup.

Triggered by the intense discussions in the scientific community on possible magnetism at the interface it was thoroughly checked if traces of magnetic effects are found in samples grown at our standard pressure ($p(\text{O}_2) \approx 10^{-5}$ mbar). Two different experimental techniques were applied: Superconducting Quantum Interference Device (SQUID) and Superconducting Quantum Interference Filter (SQIF). Neither SQUID magnetometer measurements of magnetic moments, nor experiments with a SQIF device placed directly onto the $\text{LaAlO}_3/\text{SrTiO}_3$ sample (measurements done by C.W. Schneider) showed signatures of magnetism at the interface for temperatures between 300 K and 4 K. These experimental techniques were the most sensitive methods available in our group. However the experiments can of course not exclude the presence of a magnetic layer confined to the interface, because the signal of such a layer would be extremely tiny in both techniques.

It is noted here that all indications for magnetism at the $\text{LaAlO}_3/\text{SrTiO}_3$ interface in Ref. [85] are indirect (resistance and magnetoresistance measurements). As shown before

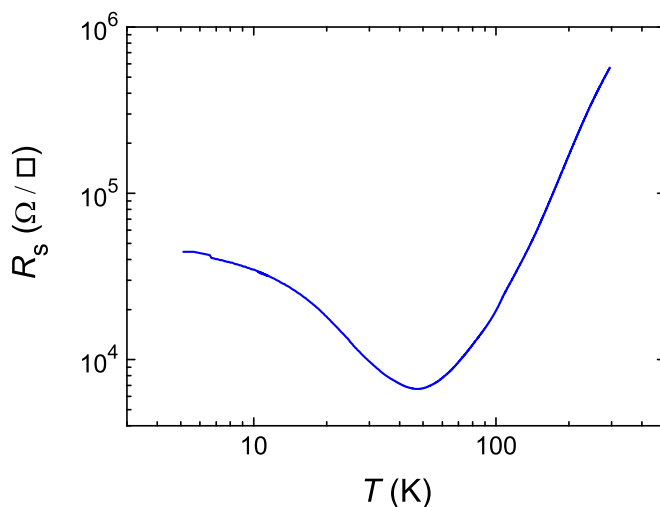


Figure 7.12: Temperature dependence of the sheet resistance for the 15 uc sample grown at $p(\text{O}_2) = 1 \times 10^{-2}$ mbar (sample L88), whose RHEED and AFM data are shown in Fig. 7.11.

in this thesis the special features in the sample transport properties reported in this publication can be caused by other effects, like dislocations in the films (see Chapter 8), and therefore do not proof the presence of a magnetic interface.

7.5 Summary

The studies described in this chapter focused on the investigation of the previously unknown ground state of the electron gas.

Measurements at low temperatures reveal for the first time that the q2-DEG at the interface between the two bandinsulators LaAlO_3 and SrTiO_3 condenses into a superconducting phase. A critical temperature $T_c \approx 200$ mK is found. This observation extends the cases of heterostructures, in which the interfaces have properties which differ from those of the bulk of the constituting materials.

The transition into the superconducting state is observed in all investigated $\text{LaAlO}_3/\text{SrTiO}_3$ heterostructures, which were grown using our standard conditions ($p(\text{O}_2) \approx 10^{-5}$ mbar) and had a LaAlO_3 film thickness $d_{\text{LAO}} \geq 4$ uc. In all these samples T_c is found to be independent of d_{LAO} . Approximately the same T_c values were found in transport measurements on samples grown by the Triscone group at the University of Geneva (Switzerland).

The ground state of one sample with 8 uc of LaAlO_3 was investigated in detail. By application of a magnetic field perpendicular to the interface the superconducting transition is suppressed, with an extrapolated value of the critical field at 0 K of $H_{c2}(0 \text{ K}) \cong 65$ mT. Assuming that the BCS theory of superconductivity is valid the coherence length is calculated to be $\xi(0 \text{ K}) \approx 70$ nm. For the critical current density of the q2-DEG a maximal value of $98 \mu\text{A}/\text{cm}$ is measured.

An analysis of the $R(T)$ and $V(I)$ characteristics of this 8 uc sample shows, that the superconducting transition can be interpreted in the framework of a Berezinskii-Kosterlitz-Thouless transition for 2D superconductors. This result strongly suggests that the (super)conductivity is confined to the $\text{LaAlO}_3/\text{SrTiO}_3$ interface.

From these experiments the upper limit for the possible thickness of the electron gas is given by the coherence length $\xi(0 \text{ K}) \approx 70$ nm.

It was shown that the widely discussed scenario where superconductivity in the samples is caused by oxygen defects in SrTiO_3 is hard to reconcile with our experimental data. If nevertheless such a scenario is assumed, an analysis of the transition temperature and its tunability by electric field provides an independent limit for the thickness of the superconducting layer of ≈ 2 nm in our samples.

A $\text{LaAlO}_3/\text{SrTiO}_3$ sample deposited at higher pressure ($p(\text{O}_2) = 3 \times 10^{-3}$ mbar) is also found to be superconducting, which contradicts the claim of a report [124] concerning a magnetic ground state for all $\text{LaAlO}_3/\text{SrTiO}_3$ samples grown at higher pressures. In further SQUID and SQIF experiments on standard samples no traces of magnetic effects at the interface are observed. A further increase of the deposition pressure does change the transport properties (higher R_s , minimum in $R(T)$), but for such samples the RHEED and AFM data indicate that the film quality is worse than the quality of films grown at

standard pressure. Therefore high pressure samples are not to be compared to samples grown under standard conditions.

A detailed study of the strong dependence of the electron gas properties on dislocations in the samples is presented in the next chapter.

8 Electron Scattering at Dislocations in $\text{LaAlO}_3/\text{SrTiO}_3$ Interfaces

In earlier chapters of this thesis several parameters which control the behavior of the $\text{LaAlO}_3/\text{SrTiO}_3$ interface have already been identified and discussed. First, oxygen defects can dominate the transport properties in samples which are grown at low oxygen pressures ($\leq 10^{-6}$ mbar). Second, the thickness d of the LaAlO_3 films is crucial, as only samples with films of $d \geq 4$ uc form the electron gas at the interface. Third, the conductivity is only achieved if the SrTiO_3 is terminated with a layer of TiO_2 .

To gain a better understanding of the system it is essential to find out whether there are other parameters, like the microstructure of the interface, which play an equally important role for the properties of the q2-DEG.

First hints on a possible effect of film quality on transport properties were found in samples grown at $p(\text{O}_2) = 1 \times 10^{-2}$ mbar, where the electron gas properties differed substantially from the standard ones (see Sec. 7.4).

A thorough analysis became essential when $\text{LaAlO}_3/\text{SrTiO}_3$ samples grown on SrTiO_3 substrates from two new batches showed insulating behavior, although all above mentioned parameters were fulfilled.

To investigate the influence of defects on the q2-DEG the transport properties of $\text{LaAlO}_3/\text{SrTiO}_3$ samples were measured, while systematically altering the microstructure at the interface. This was done by using bicrystalline substrates to add individual grain boundaries with different grain boundary (GB) angles. The growing LaAlO_3 film reproduces the boundary structure, so that defined defects and disorder are formed directly at the boundary.

8.1 Grain Boundary Sample Preparation and Characterization

As substrates (001) oriented, bicrystalline SrTiO_3 substrates containing [001]-tilt grain boundaries were used ¹¹ (Fig. 8.1). The boundary angles θ (2° , 3° , 4° , 24° , and 45°) of the studied bicrystals were confirmed with an accuracy of 0.2° by Laue-diffraction (PW1830/40, Philipps, measurements done by C.W. Schneider, University of Augsburg).

The bicrystalline substrates were treated with our standard procedure of etching in a BHF solution followed by annealing to obtain a TiO_2 termination. Characteristic AFM

¹¹Bicrystals obtained from Furuuchi Chemical Corporation (Fine Trading Division, 6-17-17 Minami-oi, Shinagawa-ku, Tokyo 140-0013, Japan) and Earth Chemical (2-12-1 Kanda-Tsukasamachi, Chiyoda-ku, Tokyo 101-0048, Japan)

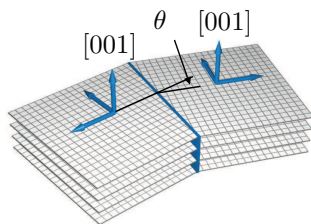


Figure 8.1: Illustration of the crystallographic orientation of the used [001]-tilt grain boundaries with GB angle θ . From Ref. [125].

images are shown in Fig. 8.2. The etching procedure did not lead to trenches at the boundary. In a few percent of the grain boundary length, small holes with diameters up to some 100 nm may be found, which are not visible prior to the etching. On both sides of the boundary smooth step-and-terrace structures are observed. As the orientation of the steps is related to the unavoidable miscut of the substrate, and both single-crystalline parts of the bicrystal have slightly different misorientations towards the [001] direction, the orientations of the steps on both sides of the GB can be different, and are not related to the boundary angle. The transition from one step-and-terrace system of one single-crystalline part to the other therefore causes surface steps to occur locally at the boundary. These steps are typically one unit cell high, but may occasionally reach a height of 2–3 unit cells.

In the grains of some of the investigated bicrystals, steps are bunched up to distances ranging from 100 nm – 3 μm from the grain boundary (see e.g. Fig. 8.2a and b). “Bunching” denotes several single unit cell high steps merging to a larger step. This bunching yields steps that locally are 2–3 unit cells high. Sometimes it also is observed that the step orientation changes close to the GB (see e.g. left of the GB in Fig. 8.2c).

On these substrates patterned LaAlO_3 films were deposited using our standard conditions as described in Chapter 6. The patterns were chosen such that the properties of the bicrystal boundaries and of the adjacent grains can be determined simultaneously by four-point measurements (see Fig. 8.3). Lines of 5 μm , 10 μm or 20 μm width and 20 μm or 30 μm length were used. Contacts of typical side length 400 μm were made using the standard technique of filling Ar ion-etched holes with sputtered gold.

Figure 8.4 shows an AFM image of a patterned bridge across a 4° grain boundary. The

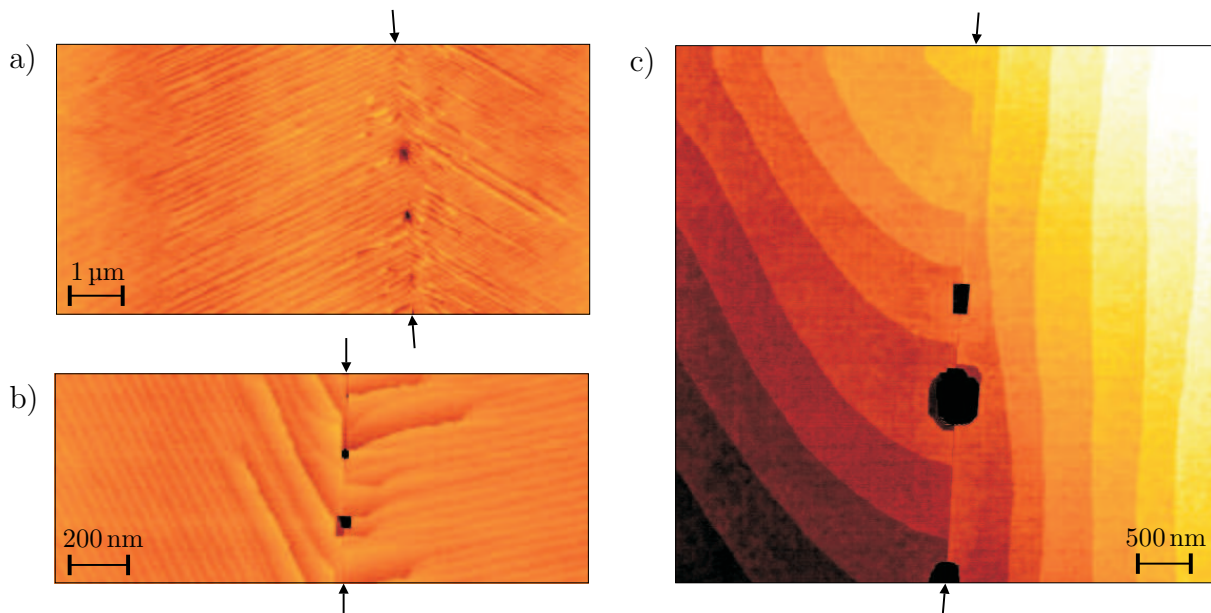


Figure 8.2: Topographic AFM images of TiO_2 -terminated, bicrystalline SrTiO_3 substrates. The position of the boundary is indicated by arrows. **a**, 24° [001]-tilt boundary (Scan size $10 \times 5 \mu\text{m}^2$). **b**, 3° [001]-tilt boundary (Scan size $4.5 \times 1.7 \mu\text{m}^2$). **c**, 4° [001]-tilt boundary (Scan size $2 \times 2 \mu\text{m}^2$).

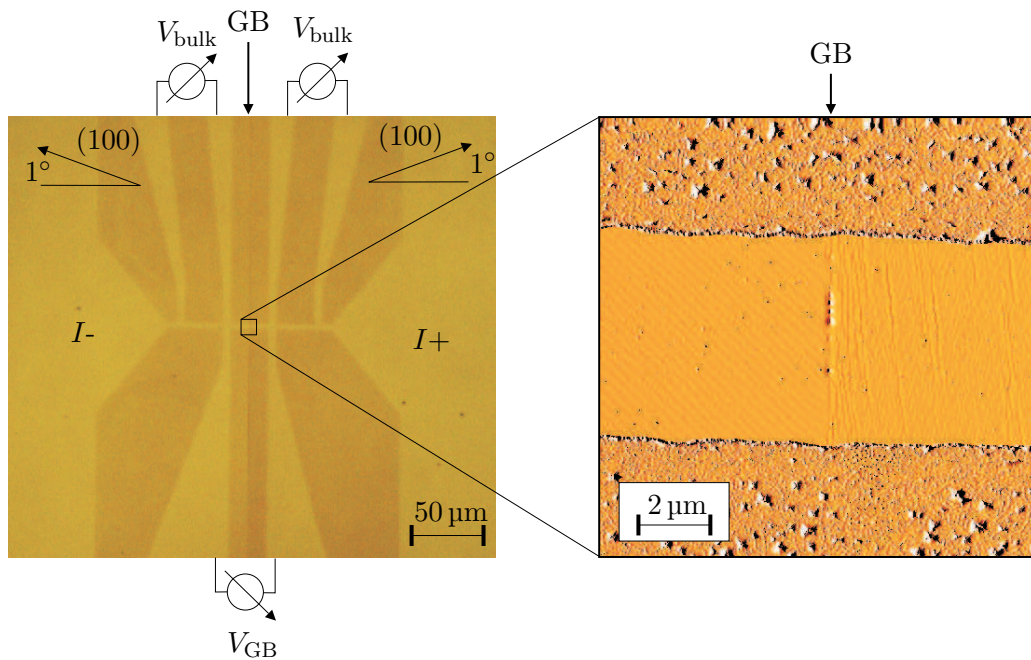


Figure 8.3: Image of a patterned LaAlO_3 film, grown on a bicrystalline SrTiO_3 substrate (sample LGB10). **Left**, Optical micrograph of a patterned bridge crossing a 2° symmetric GB, where in the brighter areas an electron gas is generated at the interface while the darker areas are insulating. Three pairs of voltage contacts allow to determine the bulk and GB transport properties independently in a four-point measurement. **Right**, AFM image (amplitude error signal, scan size $12 \times 12 \mu\text{m}^2$) of the GB. The two areas at the top and bottom of the image show the parts with amorphous LaAlO_3 while the center shows the conducting bridge, which is characterized by the step-and-terrace structure of the epitaxial LaAlO_3 on both sides of the GB, reproduced from the underlying bicrystalline substrate.

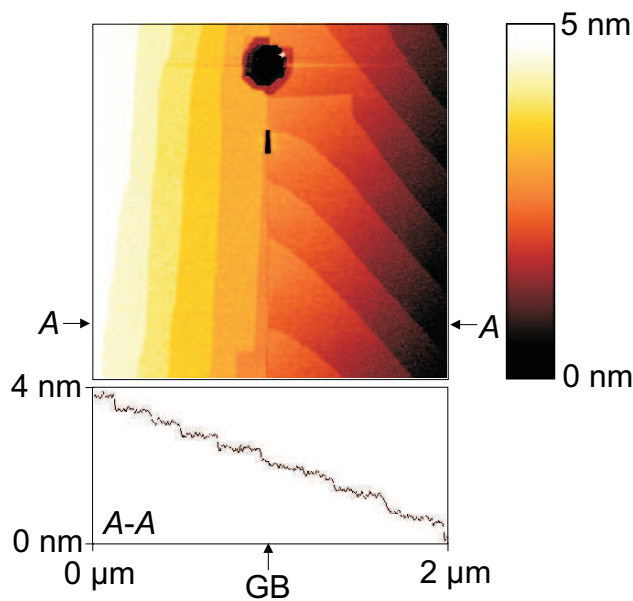


Figure 8.4: Topographic AFM image and linescan (along $A-A$) of a 8 uc thick LaAlO_3 film on a 4° SrTiO_3 bicrystal (sample LGB7), showing the GB (Scan size $2 \times 2 \mu\text{m}^2$).

smooth step-and-terrace structure from the substrate is preserved, and as expected from the studies of the substrate topography, the linescan shows that the transition from one side of the boundary to the other occurs via about one unit cell high steps. Occasionally, these steps may also reach a height of 2–3 unit cells.

The exact step structure (orientation and bunching) varies between samples, and it is not possible to distinguish from the AFM data between large and small boundary angles. Therefore, to analyze the effects of different GB angles, and the accompanying changes of microstructural disorder, it is important to know the atomic structure at the boundary.

For this reason, scanning transmission electron microscopy (STEM) studies were done by L. Fitting Kourkoutis and D.A. Muller at the University of Cornell (USA). Unpatterned samples were prepared by PLD, with the same parameters as used for the patterned samples, and were finally capped with a 5 nm thick protection layer of amorphous Al_2O_3 , which was grown by PLD at ≈ 300 K in an oxygen pressure of 0.1 mbar. These samples were then prepared by wedge polishing followed by low energy ion milling of the backside of the samples to obtain electron transparent plan view samples.

Figure 8.5 shows large scale annular dark field (ADF) STEM images of a 45° and a 4° [001]-tilt boundary. The samples are viewed along the [001] direction, parallel to the interface normals. From the lattice fringes in these images the tilt angles were determined to be $45.2^\circ \pm 0.1^\circ$ and $4.2^\circ \pm 0.1^\circ$ for the two samples. This analysis confirms the angles as determined from the Laue experiments.

The bright islands in these plan view images are probably related to the Al_2O_3 capping layer. This layer was reported in Sec. 3.5.3 to cause problems for cross section images due to La diffusion into the capping, but the in-plane investigation of atomic positions is not influenced by the Al_2O_3 capping.

In the STEM images one can clearly see the grain boundary. It is oriented vertically in the middle of both images. For the 45° tilt sample one observes a continuous dark line with several steps, in contrast to the 4° tilt sample, where a line of isolated dark spots is seen with a single step in the middle of the image.

An enlarged view of the atomic structure directly at the boundary is shown in Figure 8.6. For the 4.2° boundary one finds that the atomic columns bend continuously from one side of the boundary to the other, interrupted only by uniformly spaced, isolated edge dislocations, with an average spacing of $d = 5.2 \pm 0.1$ nm. This value is in very good agreement with the value of 5.3 nm as determined from Frank's formula [126, 127] for pure tilt boundaries, $d = |b|/(2 \sin(\theta/2))$ ($|b|$ is the modulus of the Burgers vector and θ is the tilt angle). The observed microstructure is expected for low angles θ . For $\theta < 4.2^\circ$ the single dislocations will be separated further, and for larger angles the spacing between them will decrease, until finally the dislocation cores merge and form a continuous stripe with a distorted structure. The latter effect can be seen in the image of the 45° tilt grain boundary as a line of reduced ADF intensity (Fig. 8.6a).

Additionally, the chemistry of these tilt boundaries was investigated on the atomic scale by electron energy loss spectroscopy (EELS). Ti-L_{2,3} and O-K EELS spectra were recorded in bulk SrTiO_3 and at the 45° boundary. Significant changes in the near edge structure on and off the dislocation cores were observed for both the Ti-L (Fig. 8.6c) and the O-K (Fig. 8.6d) edges, suggesting a reduction of the Ti valence from 4+ in bulk SrTiO_3

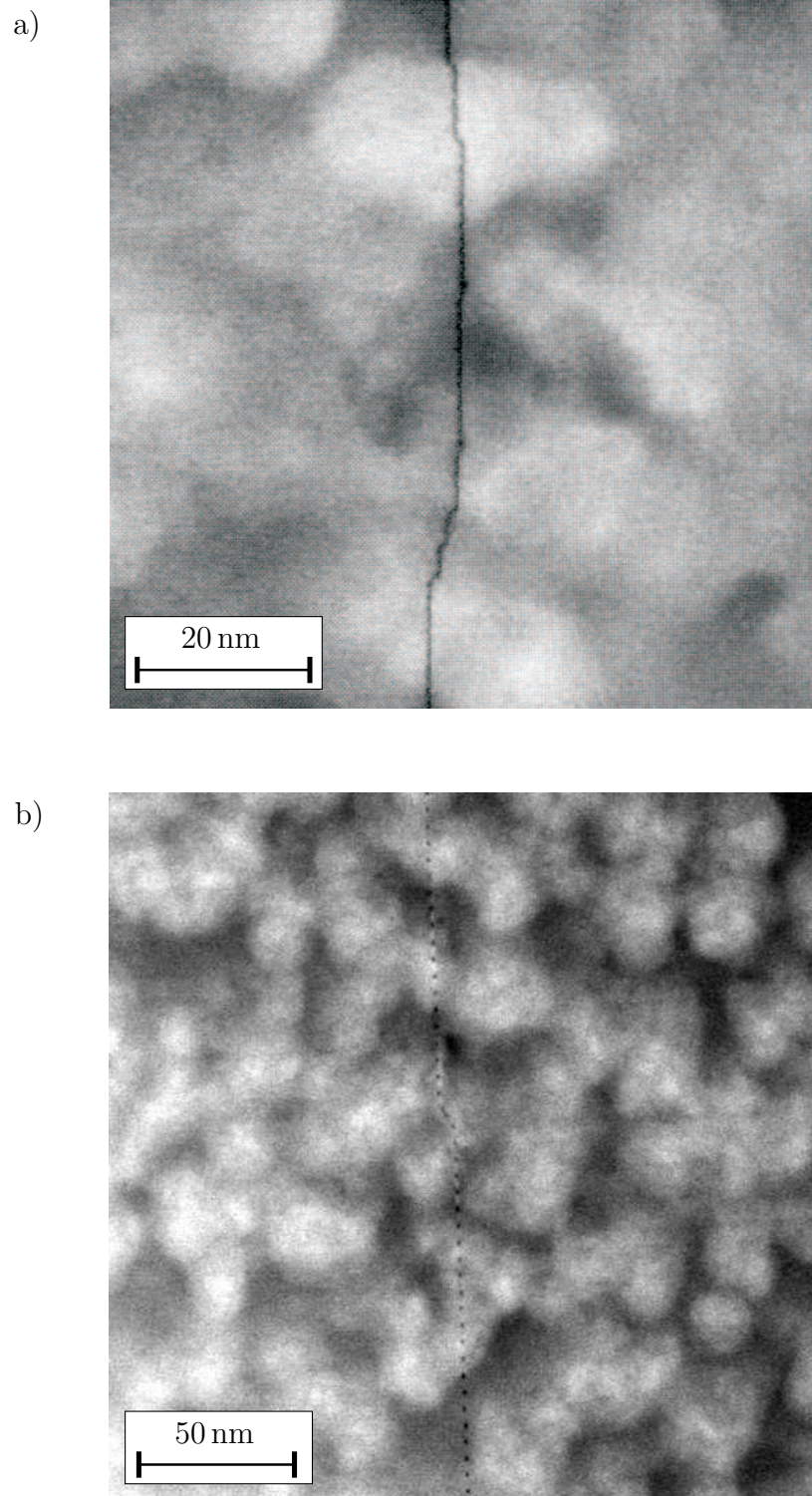


Figure 8.5: Large scale STEM images of **a**, 45° (sample L55) and **b**, 4° (sample L56) [001]-tilt boundaries in samples of 5 μm thick LaAlO_3 grown on SrTiO_3 bicrystals. The STEM experiments were done by L. Fitting Kourkoutis and D.A. Muller at the University of Cornell (USA).

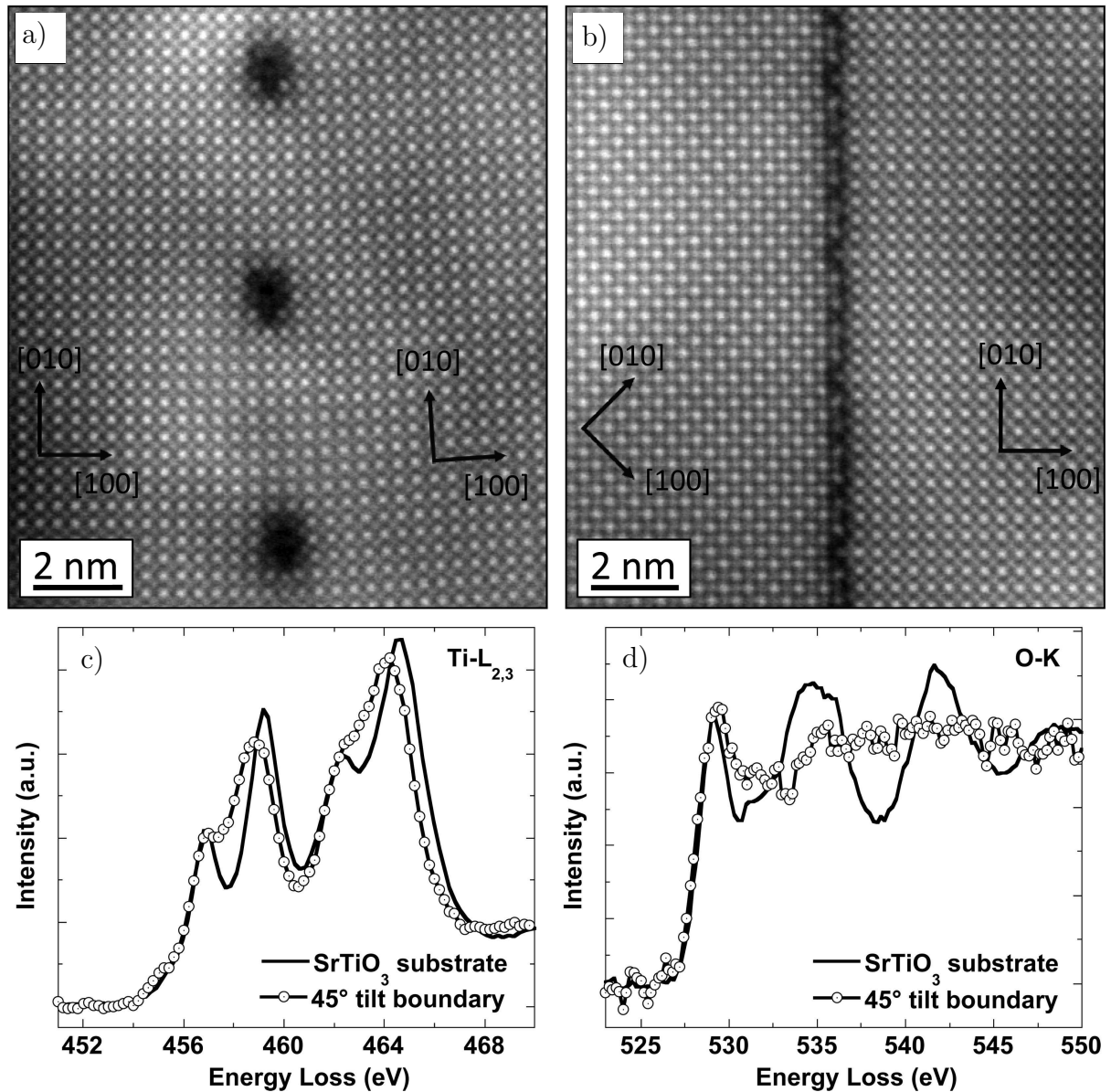


Figure 8.6: High angle annular dark field STEM images of **a**, 4° (sample L56) and **b**, 45° (sample L55) $[001]$ -tilt boundaries in samples of 5 uc thick LaAlO_3 grown on SrTiO_3 bicrystals. The crystallographic directions are indicated by small arrows. **c**, $\text{Ti-L}_{2,3}$ and **d**, O-K electron energy loss spectra measured at the 45° tilt boundary and the SrTiO_3 substrate. The STEM and EELS experiments were done by L. Fitting Kourkoutis and D.A. Muller at the University of Cornell (USA).

and Sr-deficiency in the dislocation cores [92]. Thus the microstructure and chemical composition of the cores differ significantly from undisturbed interfaces.

Therefore, in case the dislocation cores act locally on the electron gas, a scattering cross section of the core diameter (≈ 1 nm) would result. As we will see, this effect only can not explain the observed transport properties.

8.2 Transport Properties of the Grain Boundary Samples

To measure the samples without photo-generated charge carriers being present, transport measurements were done after keeping the samples in dark for at least 24 hours. Within the grains the samples showed the standard transport characteristics as reported in Chapter 4 for single crystalline $\text{LaAlO}_3/\text{SrTiO}_3$ heterostructures. The GB properties, however, differ significantly from the standard electronic properties.

First, it had to be examined whether the unit cell steps, and their occasional bunching affect the transport properties. To clarify this, a set of samples was fabricated, in which the orientation of the measurement bridges, with respect to the steps, was varied. No variation of the bridge resistance beyond the standard scatter ($\approx 10\%$) was observed. A similar result was obtained by Huijben [84]. This implies that the steps do not significantly influence the interface conductivity. These measurements therefore show that the electron gases couple across steps that are one, or possibly two or even three unit cells high. Therefore, if different properties are found for bridges across and adjacent to the GB, this effect has to be related to the GB microstructure and not to the 2–3 uc steps occasionally occurring at the GB.

Initially, large angle grain boundaries were investigated because the continuous, irregular stripe at the GB (see Fig. 8.6b) was expected to have a stronger influence on the q2-DEG, as compared to the almost undisturbed microstructure of low angle boundaries (see Fig. 8.6a).

The 45° boundaries were, however, completely insulating. Recalling the STEM plan view images for this angle, the observation of insulating behavior shows that the transport across an only 1 nm wide, disturbed band at the GB is completely blocked for the electron gas at the interface. For a GB angle of 24° the boundary was also insulating. For the next sample θ was reduced by a large step to 4° . In contrast to the previous samples for this angle the boundary consists of isolated dislocations with an almost undisturbed lattice between the dislocations. The rows of atoms bend continuously from one single-crystalline side to the other. The boundary was nevertheless found to be insulating.

Typical current-voltage curves are shown in Fig. 8.7. Insulating behavior with current flow only starting above a critical voltage, is observed. Transport measurements next to the GB still revealed linear $V(I)$ characteristics with standard values for the sheet resistance, which confirms that the electron gas was still present on the single crystalline sides of the samples.

At a GB angle $\theta \approx 2^\circ$ a rapid increase of the conductivity of the boundary is observed. Yet the GB resistances of the 2° samples still exceeded those of the grains by orders of magnitude. This result shows that isolated dislocation cores still have a large effect, even when separated by ≈ 10 nm, as is the case for a GB angle of 2° . Samples with even smaller angles θ were not investigated because the corresponding bicrystalline substrates were not available.

Ohmic as well as non-linear $V(I)$ characteristics were measured for 2° grain boundaries, as shown in Fig. 8.8a. The contribution of the boundary to the resistance was obtained by measuring the resistance of the bridge crossing the boundary and subtracting the simultaneously measured intragrain resistance of the bridge, as derived from the close reference

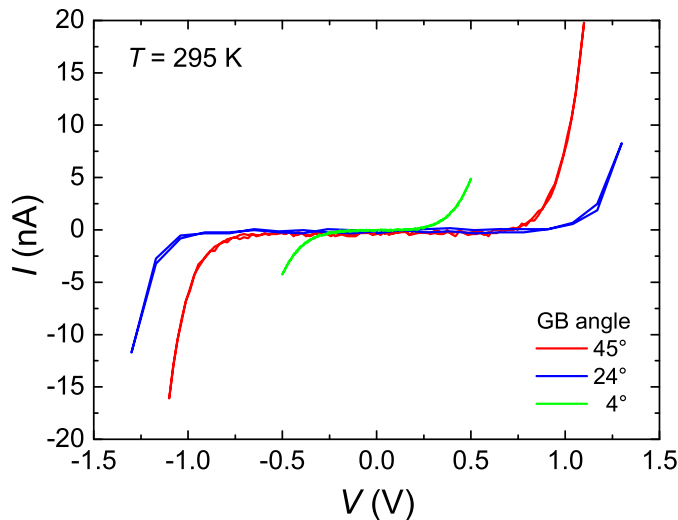


Figure 8.7: Current-Voltage characteristics of bridges crossing the grain boundary for different GB angles. All bridges show an insulating behavior at small voltages.

bridges. To measure the grain boundary characteristics without any contributions from the grains, one sample was cooled to $T < 200$ mK. At this temperature the undisturbed electron gas is superconducting, as described in Chapter 7. The measurements shown in Fig. 8.8b reveal that indeed for the reference bridge in the bulk of the sample superconductivity is observed ($T_c = 200$ mK was obtained from $R(T)$ measurements), while the bridge containing a 2° GB still has a resistance of 4650Ω , which therefore has to be caused by the boundary alone.

The 2° boundary potentially acts as Josephson junction, however the high value of the normal state resistance $R_n = 4650 \Omega$ prevents the observation of Josephson currents across the GB. From the low temperature limit of the Ambegaokar-Baratoff relation $I_c R_n (T \rightarrow 0) = \pi / (2e) \Delta(0)$ (with the critical current I_c , normal state resistance $R_n = 4650 \Omega$, elementary charge e , zero temperature energy gap $\Delta = 30 \mu\text{eV}$ (see Chapter 7)) a critical current $I_c (T = 0 \text{ K})$ of ≈ 10 nA is obtained. For this current to be observed in a measurement at finite temperature the Josephson coupling energy $E_c = \hbar I_c / (2e)$ has to be much higher than the thermal energy $k_B T_c$. For the sample investigated both energies are about $2 \mu\text{eV}$, which makes it impossible to observe a Josephson current, and any Josephson effects, in the experiments.

The conductivity per GB width is examined for comparison of the transport properties of bridges crossing grain boundaries of different angles. The corresponding data is shown in Fig. 8.9 for GB angles from $2^\circ - 45^\circ$ and for temperatures of 4 K and 300 K. The conductivities of the electron gases straddling the grain boundary are very low, and drop precipitously with increasing boundary angle. For the 2° boundaries conductivities up to $10^2 / \Omega\text{m}$ and $3 \times 10^{-1} / \Omega\text{m}$ are observed at 4.2 K and 300 K, respectively. For the 2° GB bridge which was cooled to 184 mK, below the superconducting transition in the bulk, a conductivity of $\approx 11 / \Omega\text{m}$ is found. For bridges crossing a 3° GB the conductivity is further reduced. A boundary resistance exceeding the measurement limit is found for samples with larger angles $\theta \geq 4^\circ$.

To be able to relate these conductivities to the standard values for the q2-DEG, an

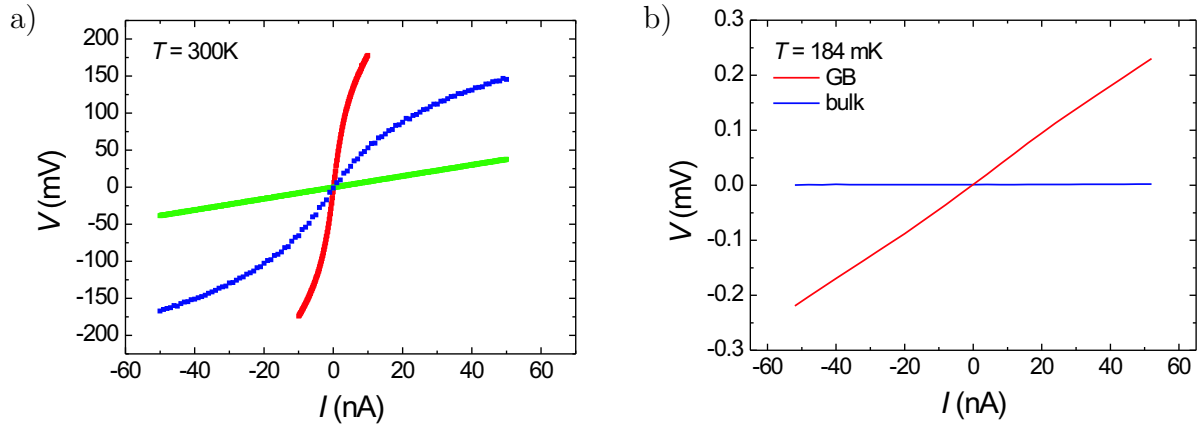


Figure 8.8: Current-voltage characteristics of bridges crossing 2° boundaries. **a**, $V(I)$ curves of three different 2° GB samples measured at $T = 300\text{ K}$. Ohmic as well as non-linear characteristics are found. **b**, $V(I)$ curves for the GB and the adjacent bulk of one 2° sample (LGB16) measured at $T = 184\text{ mK}$. The bridge in the adjacent grain is superconducting, so the observed resistance of $4650\ \Omega$ across the GB is caused by the boundary alone. The measurements at low temperatures were done by A.D. Caviglia and N. Reyren at the University of Geneva.

electronic width of $\approx 5\text{ nm}$ is ascribed to the boundaries. This value will be justified later. Using this assumption, the conductivity of the 2° boundary is 3–7 orders of magnitude smaller than that of the neighboring grains. An increase of the GB angle to 3° reduces the conductivity further to a value which is 8–9 orders smaller than that of the grains.

In the following, only 2° grain boundaries will be discussed. Not only the magnitude of the GB resistance, but also its temperature dependence differs significantly from the standard properties of the grains. Typical $R(T)$ curves for bridges crossing 2° grain

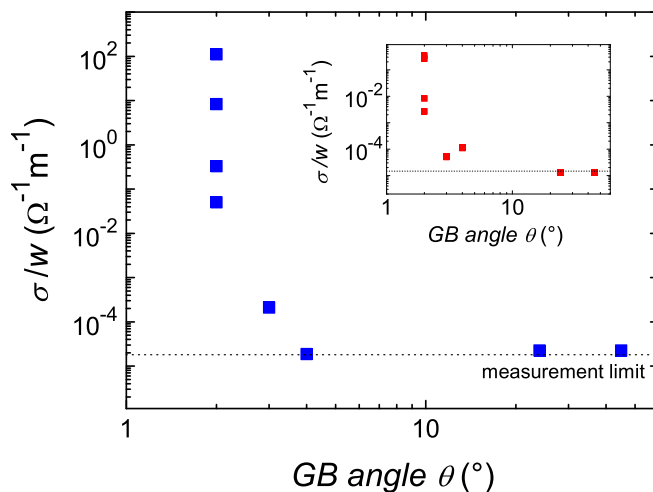


Figure 8.9: Conductivity per GB width as a function of the GB angle at $T = 4\text{ K}$. The values were obtained from the slope of the I - V curves at $V = 0\text{ V}$. **Inset**, Measurement at 300 K .

boundaries and for intragrain bridges are shown in Fig. 8.10. While the grains show the known continuous decrease over more than two orders of magnitude (inset of Fig. 8.10) the boundary shows a minimum around 40 K for measurements from 300 K to 4 K with a correspondingly smaller change in resistance. When measuring while warming the sample from 4 K to 300 K, the boundary resistance develops a pronounced maximum at ≈ 70 K. Some samples exhibit at ≈ 230 K a second maximum. While none of the grains showed any of these maxima, similar humps have been observed by others [86] and by us for films grown on different SrTiO_3 substrates, as presented later in this chapter.

For colossal magneto resistance (CMR) materials an enhanced MR at low fields was observed for grain boundaries [128]. As the grain boundary in the electron gas potentially also shows a larger sensitivity, compared to in the grain, to magnetic and electric fields, the influence of both was investigated.

Up to the largest magnetic fields applied (8 T, parallel to the surface normal), however, the grain boundary resistance did not change noticeably for all temperatures.

Remarkably, electric gate fields have a much more pronounced effect on the grain boundaries. In a field effect transistor configuration like shown in Fig. 5.2 electric fields were applied from the back of the substrate. As before, the polarity of V_G was such that the plus terminal was on the back gate electrode, and the minus terminal contacted the conducting interface. Although the substrates are 1 mm thick, the application of gate voltages V_G of only 10–20 V changes the $V(I)$ characteristics of the electron gas crossing the grain boundary. Figure 8.11 shows two $V(I)$ curves, both taken with no gate field applied. The difference between both measurements is the gate voltage which was applied before. It is found that positive gate voltages reduce the conductivity and result in non-linear $V(I)$ characteristics, while negative gate voltages enhance the conductivity and cause linear $V(I)$ characteristics. During application of gate voltages, the gate leakage currents were smaller than 5 nA. Reminding of the hysteretic field effects of the $\text{LaAlO}_3/\text{SrTiO}_3$ q2-DEG, which were presented in Sec. 5.2, these characteristics remain altered for hours even when V_G is removed. The original characteristics are recovered by

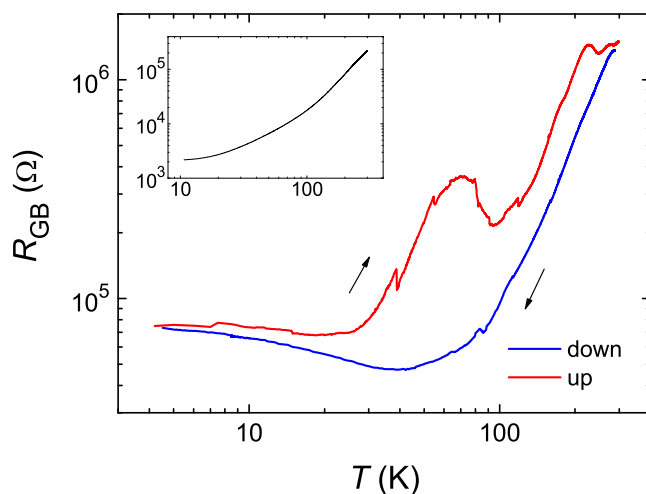


Figure 8.10: Measured GB-Resistance as a function of temperature of a 2° sample (sample LGB10) obtained during cooling and warming. A measurement current of 50 nA was used. **Inset,** Resistance as a function of temperature of the adjacent bulk bridge. The magnitude of the resistance is several orders smaller than for the GB, and no extrema are observed.

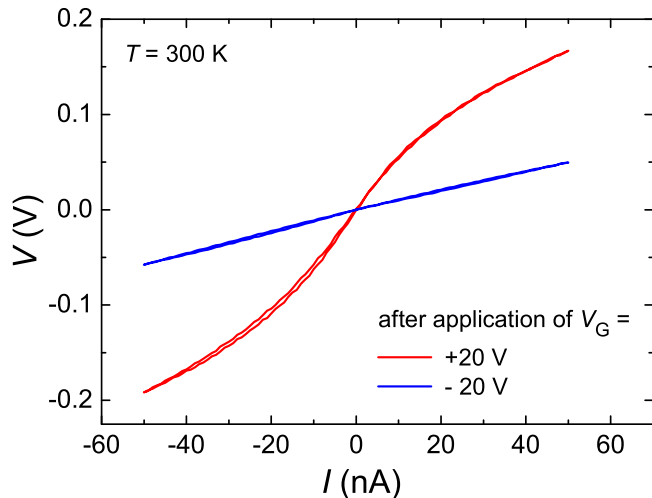


Figure 8.11: $V(I)$ characteristics of a 2° boundary (sample LGB10) measured at $T = 300$ K with no gate voltage applied. These characteristics can be changed by the application of gate voltages of ± 20 V, and remain altered even when these voltages are switched off.

a gate voltage pulse of opposite polarity.

Long timescales are observed in these experiments for the changes in the $V(I)$ curves of bridges crossing the GB. When V_G is switched from -20 V to $+20$ V it takes several minutes until the characteristic is in a stable state.

For the insulating 3° boundaries even the application of $V_G = \pm 100$ V can not drive the GB conducting.

The tuning of the GB conductivity by electric field is probably caused by charging and discharging of dislocation cores. This will be explained below, where a model is presented to explain the extremely high GB resistances.

To explore whether the observed q2-DEG transport behavior across lines of isolated dislocations and grain boundaries is a general property of the interface electron gas or whether it is specific to bicrystal samples, additional experiments were done with SrTiO_3 single crystals having different densities of edge-dislocations.

8.3 Dislocations in SrTiO_3 Substrates

This section first describes the analysis of the number of dislocations in our standard SrTiO_3 substrates. Then special SrTiO_3 single crystals with a higher dislocation density are investigated.

The standard single crystalline SrTiO_3 substrates used in our group are grown by the Verneuil flame-fusion method. As described earlier, these substrates show the typical step-and-terrace structure at the surface upon treatment with buffered HF solution and annealing.

The density of dislocations on the surface of these substrates can be determined by etch-pit formation and counting [129]. In these experiments the substrates are dipped in ultrasonically agitated buffered HF solution ($\text{NH}_4\text{F}:\text{HF} = 87.5:12.5$, Merck) for 30 min

and subsequently cleaned in deionized water and isopropanol. Upon checking the surface topography with AFM, square pyramidal etch pits are observed, which form at positions where dislocations are present (see Fig. 8.12). These pits have the edges aligned to the crystal axes and are some 100 nm deep. By counting the number of pits a typical dislocation density of 10^6 cm^{-2} is found for our standard SrTiO₃ substrates.

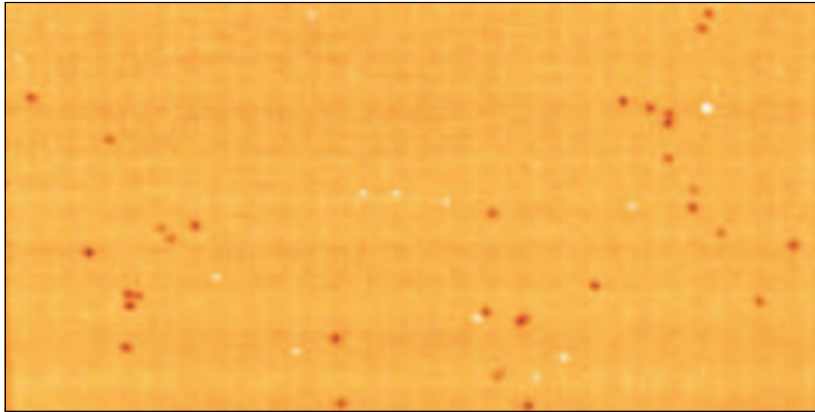


Figure 8.12: Topographic AFM image of a standard, flame fusion grown SrTiO₃ substrate treated in buffered HF for 30 min. Etch pits are formed at dislocations (Scan size $100 \times 50 \mu\text{m}^2$, z -scale 50 nm).

For changing the microstructure of the complete substrate, and not only along one line at the GB, SrTiO₃ single crystals were used that were fabricated by the floating zone (FZ) method¹². These substrates exhibit a very high density of edge dislocations. The dislocations were again revealed by prolonged treatment in buffered HF.

After this procedure many line features can be seen even optically (see Fig. 8.13a), which are absent for good quality standard SrTiO₃ treated in this way. Such lines are also found on a much smaller scale in AFM measurements, as shown in Fig. 8.13b and c. The dislocation density is higher compared to the standard Verneuil grown substrates, yet the distribution of these defects is not homogenous. Most of the dislocations are randomly spread, with a density of 10^6 cm^{-2} (same density as found for standard SrTiO₃), but many of them are arranged in linear arrays, like pearls in a necklet, forming networks of very low angle grain boundaries. In Fig. 8.13c such lines of isolated dislocations can be seen more clearly.

An increased density of dislocations on the surface, as observed for the floating zone grown SrTiO₃ substrates, is not necessarily related to a reduced quality of the bulk single crystal. Dislocations can also be induced by the polishing of the substrate surface, and can thus differ for different batches and suppliers of substrates.

A typical example for this effect can be seen in Fig. 8.14a, where the optical image of a standard SrTiO₃ substrate, which was treated for etch-pit formation, is shown to have a very dense network of lines. In AFM experiments an even higher density of dislocations than for the FZ-SrTiO₃ is found. The straightness of the lines indicates that the dislocations are induced by the polishing process. To test this idea, these substrates were carefully polished a second time by the supplier, removing additional 0.1 mm of the material. After this process a much smaller number of lines was found after treatment for etch pit formation, but still many were present. Therefore it is concluded that also

¹²Floating zone grown SrTiO₃ substrates were obtained from CrysTec GmbH, D-12555 Berlin, Germany.

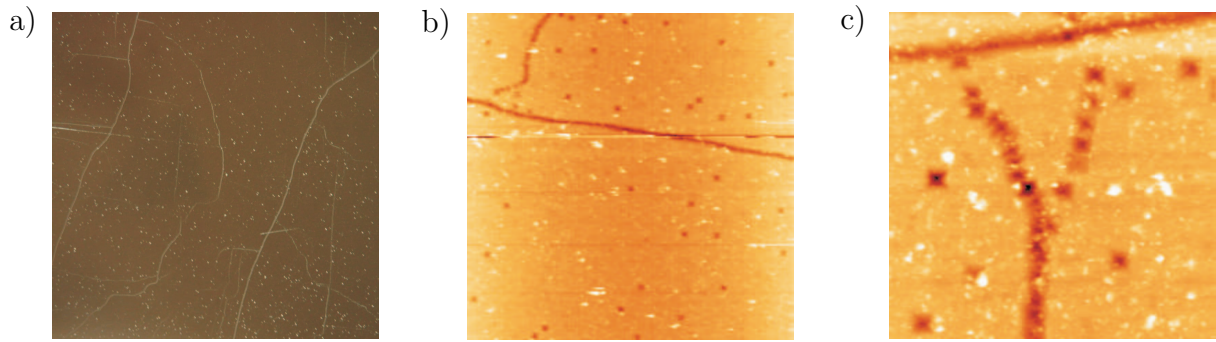


Figure 8.13: Surface of a floating-zone grown SrTiO_3 substrate after 30 min buffered HF treatment for etch pit formation. **a**, Optical image of the surface (Image size $2 \times 2 \text{ mm}^2$). **b**, Topographic AFM image (Scan size $50 \times 50 \mu\text{m}^2$). Linear arrays of dislocations are observed. **c**, Topographic AFM image with an enlarged view, showing lines of isolated dislocations (Scan size $15 \times 15 \mu\text{m}^2$).

flame-fusion grown SrTiO_3 substrates can have a very high dislocation density if polished incorrectly.

A clear difference between standard and “bad” substrates is not only observed after a treatment for etch pit formation, which irreversibly excludes the use of these substrates for $\text{LaAlO}_3/\text{SrTiO}_3$ samples, but also in AFM images of SrTiO_3 which was treated for TiO_2 termination. For “bad” substrates not the perfect step-and-terrace structure with smooth edges is observed, but rather many locations with step-bunches, where several 1 μc high steps merge to a higher step, as shown in Fig. 8.14b. Similar step-bunches on the surface after the TiO_2 -termination procedure are also found on FZ-grown SrTiO_3 , and on SrTiO_3 that was polished by the standard procedure used in our group [130].

As already mentioned in Sec. 3.1, SrTiO_3 substrates that showed step-bunches on the surface after TiO_2 termination were not used for $\text{LaAlO}_3/\text{SrTiO}_3$ heterostructures. The

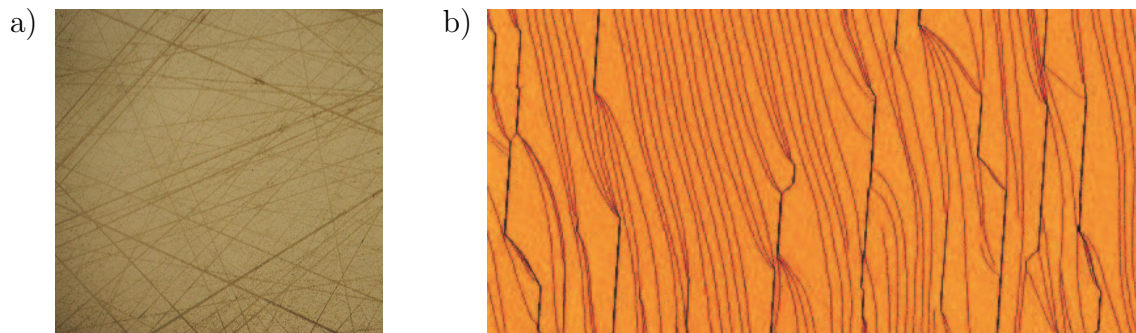


Figure 8.14: Surface of a “bad” SrTiO_3 substrate with polishing induced dislocations. One $10 \times 10 \text{ mm}^2$ substrate was cut into several parts prior to the chemical treatments. **a**, Optical image of the surface of one part of the substrate after 30 min buffered HF treatment for etch pit formation (Image size $2 \times 2 \text{ mm}^2$). **b**, Topographic AFM image of another part of the substrate after treatment for TiO_2 termination (without prior treatment for etch pit formation). Many step bunches, typically 2–4 μc high, are observed (Scan size $5 \times 10 \mu\text{m}^2$).

reason for this selection is that the transport properties of samples grown on step-bunched substrates are very different from the standard properties, which will be shown next.

8.4 Transport Properties of Samples with High Dislocation Density

In the experiments described in this section “bad” substrates were used on purpose to investigate their influence on the transport properties. By presenting results of $\text{LaAlO}_3/\text{SrTiO}_3$ samples grown on these substrates it will be shown that not only the dislocations of grain boundaries, but also high dislocation densities of SrTiO_3 single crystals dramatically affect the properties of the q2-DEG.

Our standard conditions were used to deposit films of LaAlO_3 on SrTiO_3 substrates containing many dislocations. The RHEED patterns and oscillations during growth did not change compared to depositions on standard substrates. AFM images of the sample surface revealed that the bunched step-and-terrace structure from the substrate was reproduced by the LaAlO_3 films, due to the layer-by-layer growth.

Figure 8.15 shows the transport properties of a $\text{LaAlO}_3/\text{SrTiO}_3$ sample with a FZ-grown substrate. An electron gas is generated at the interface, yet the conductivity and mobility are about one order smaller than those of standard samples. The charge carrier density of this sample ($\approx 10^{13} \text{ cm}^{-2}$ for all T) is similar to the standard value. Like the bridge crossing a 2° grain boundary (see Sec. 8.2) these electron gases show a minimum in the $R(T)$ characteristic upon cooling, and go through a resistance peak upon warming (see

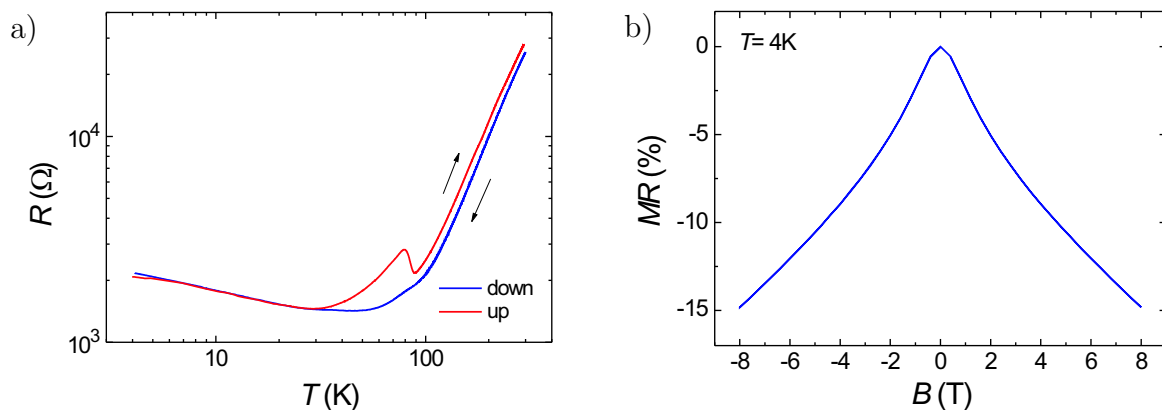


Figure 8.15: Transport properties of an unpatterned $\text{LaAlO}_3/\text{SrTiO}_3$ sample fabricated using a floating-zone grown substrate, containing a high number of dislocations (sample L149). **a**, Resistance as a function of temperature. During cooling down, R goes through a minimum at $\approx 45 \text{ K}$, and upon warming up a peak at $\approx 75 \text{ K}$ is observed. A measurement current of $1 \mu\text{A}$ was used. **b**, A pronounced negative magnetoresistance is found at $T=4 \text{ K}$ with the magnetic field directed perpendicular to the interface plane. The curve is independent of the used sweep speed (2 T/min or 0.2 T/min).

Fig. 8.15a). While these properties match those of 2° [001]-tilt bicrystal boundaries, there is also a difference: the magnetoresistance (MR) of the electron gases on the floating-zone grown SrTiO_3 crystals is large and negative (Fig. 8.15b), while the resistance of the 2° GB did not change noticeably upon application of magnetic fields. For standard samples a positive MR ($\approx 25\%$ at 8 T and $T = 4$ K) is found.

Samples grown on SrTiO_3 substrates which contained an even higher density of dislocation lines on the surface (see e.g. Fig. 8.14) than the above described FZ-grown substrate were not conducting at all.

These results have consequences for the interpretation of some experiments reported earlier in this work.

Although no step-bunches were found on the step-and-terrace structure for samples grown at $p(\text{O}_2) = 1 \times 10^{-2}$ mbar (see Sec. 7.4), the observation of a minimum in the $R(T)$ data of these samples suggests that LaAlO_3 films contain a higher number of dislocations or defects when deposited in this high pressure regime. Therefore the transport properties of those samples should not be compared to the transport properties of standard $\text{LaAlO}_3/\text{SrTiO}_3$ samples.

The experiments described in this chapter can have consequences for the interpretation of experiments done by others. The features in the data of samples, which have been interpreted to be an indication of magnetic effects [85], can also be caused by other factors, like a high dislocation density in the sample, and therefore in my opinion do not prove a magnetic ground state of the q2-DEG (see also Sec. 7.4).

The results described in this chapter provide evidence that very low angle grain boundaries with their isolated dislocations drastically reduce the conductivity of the electron gas at the $\text{LaAlO}_3/\text{SrTiO}_3$ interface. In the following section the origin of this strong influence will be discussed.

8.5 Scattering at Dislocations

Several mechanisms can be responsible for the depressed conductivity in samples containing grain boundaries.

A first candidate is the occasional presence of unit cell steps at the boundaries. But these can not be responsible for the observed larger resistance. Even if the steps completely blocked the current flow where present, the conductance along current paths crossing over step-free areas would be orders of magnitude larger than observed. Further, the surfaces of the Verneuil and floating-zone grown SrTiO_3 crystals are equally flat, so it would be hard to reconcile why the interfaces have so different conductivities.

Therefore it is concluded that the conductivity is reduced by the edge dislocations. The measured dependence of the boundary conductance on the boundary angle can only be accounted for if each dislocation is a scattering center with a cross section of ≈ 5 nm (as 4° boundaries with a dislocation spacing of 5.3 nm are completely insulating). The dislocations generate around their cores insulating disks of diameter D (schematically shown in Fig. 8.16). This model yields, like experimentally observed, for very small GB

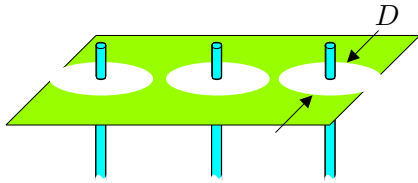


Figure 8.16: Schematic view of the model with charged dislocation cores (blue), which cause insulating disks of diameter D in the electron gas at the interface (green). In our samples $D \approx 5$ nm is found.

angles a strong decrease of the boundary conductivity with increasing misorientation, caused by a smaller distance between the disks of neighboring dislocations.

For 2° samples a strong scatter in conductivity is observed (see Fig. 8.9), because for this angle, small deviations in angle (which can only be measured with an accuracy of 0.2°) or disk diameter D substantially change the width of the conducting paths across the GB.

When the disks start to overlap at a GB angle of $\approx 3^\circ$ the insulating zone is continuous and the GB conductivity is vanishingly small.

Three mechanisms were identified that can possibly cause the insulating disks: mechanical strain, change of oxygen concentration, and space charges. These will now be discussed.

Edge dislocations are surrounded by stress fields. Along the grain boundary line a dislocation causes dilatational strain in one direction, and compressive strain in the other. At first sight, it seems well possible that these lattice distortions suppress the formation of a mobile electron gas. Between two dislocations the stress field changes sign, however, and locally the lattice is virtually stress free. If the conductivity was suppressed by the stress only, these stress-free areas would provide conducting paths crossing the boundaries. The high resistance of the grain boundaries excludes the existence of such paths, so that it is concluded that stress and strain fields do not cause the insulating behavior of the boundaries.

The influence of oxygen vacancies on conductivity was already described earlier in this work, where it was found that in samples grown at low oxygen pressures oxygen vacancies n -dope the SrTiO_3 and the interface. For such samples it then seems possible that during film growth oxygen diffuses along the dislocation cores into the interface so that in the vicinity of the dislocation the oxygen concentration is enhanced. In these areas the n -doping would be reduced, so that the interface could possibly be insulating. While this scenario is valid in principle, it is not applicable to the samples investigated, because oxygen vacancies are not responsible for the conductivity in our $\text{LaAlO}_3/\text{SrTiO}_3$ heterostructures (see Sec. 4.2). Additional experiments were done on a 2° sample (LGB17) which was grown with $p(\text{O}_2)$ increased by a factor of 10 to 5×10^{-4} mbar to investigate whether the small boundary conductivity is associated with the oxygen pressure used during deposition. The boundary conductivity of this sample equals $2 \times 10^{-3} \text{ } \Omega\text{m}$ and $7 \times 10^{-3} \text{ } \Omega\text{m}$ at 4 K and 300 K, respectively, and is therefore comparable to the conductivity of the standard bicrystals.

The third possible mechanism is charged dislocation cores creating space charge layers. These are understood to be the mechanism causing the resistance of grain boundaries in bulk samples of doped SrTiO_3 [131, 132]. In these samples trapped charges and migration

of defects charge the dislocation cores. In case the dislocation cores are negatively charged, as reported for example in [131], they induce in the interface charge depleted disks. Our data do neither provide information on the charge density in the dislocation line nor on the electronic susceptibility of the interface, so a quantitative calculation of the possible space charge disks in the interface can not be provided. Nevertheless, a comparison with the behavior of bulk, *n*-doped SrTiO₃ bicrystals suggests that the screening likely is reduced in the two-dimensional LaAlO₃/SrTiO₃ interfaces as compared to the screening in the bulk. The grain boundaries in bulk doped bicrystals have higher conductivities than those in the LaAlO₃/SrTiO₃ heterostructures: in the bulk, grain boundaries with angles of 36.8° [133, 134] have been found to be conducting, although the carrier density of these bulk samples (10^{17} – 10^{19} cm⁻³) is smaller than the charge carrier density of our LAO/STO interfaces ($\approx 10^{20}$ cm⁻³; this value for a bulk density was calculated by using the known sheet density $n_s \approx 10^{13}$ cm⁻² [75] and assuming a thickness of 4 nm for the q2-DEG, which was found as an upper limit in Chapter 7 [91]).

The model of scattering by space charge layers around charged dislocations is consistent with the measured response of the transport across a 2° grain boundary to gate voltages (see Sec. 8.2). This suggests, that in gate fields additional charges migrate to or are trapped at the dislocations, which happens on the observed long timescales. These additional charges are believed to change the diameter D of the insulating disk around the dislocation, which alters the width of the conducting region between neighboring disks and thus the resistance of the GB.

For angles $\theta \geq 3^\circ$ it is assumed that the disks overlap in the initial state, and that the change of D with gate voltage is too small to produce a conducting path across the GB. This can explain why those samples always stay insulating, even in applied electric fields.

From these considerations one can conclude that from the three identified possible mechanisms only space charge regions around the dislocation cores can explain all the experimental results.

8.6 Summary

In this chapter experiments were described which investigated the effects of microstructural defects on the LaAlO₃/SrTiO₃ interface properties.

To introduce a defined and controllable linear defect, LaAlO₃ films were grown on several bicrystalline [001] tilt SrTiO₃ substrates with different GB angles. STEM images with atomical resolution show a continuous disturbed band at the GB for a GB angle of 45°, while for a 4° GB a linear array of isolated dislocations is found.

The transport across the GB is strongly dependent on the GB angle, with a steep change from completely insulating behavior at a GB angle of 3° to conducting behavior at an angle of $\approx 2^\circ$. This observed conductivity across 2° boundaries is still several orders of magnitude smaller than the conductivity of intragrain bridges located on the same sample next to the boundary. Also the temperature dependence of the GB resistance is different compared to the standard $R(T)$: it shows a minimum and a hump-shaped hysteresis upon cycling from 300 K to 4 K and back to 300 K. The fact that small GB

angles have such a large effect implies that even isolated dislocations strongly affect the transport properties.

Samples deposited on floating-zone grown SrTiO_3 substrates, which contain a larger number of dislocations than standard SrTiO_3 displayed R - T characteristics similar to those of boundaries and additionally a negative magnetoresistance. This shows that the effects of dislocations are not limited to bicrystalline samples.

All experimental results are in agreement with a model proposed in this work, where insulating disks of diameter $D \approx 5$ nm are formed around dislocation cores. The response of the transport properties to electric fields suggests that the disks are caused by space charge layers around the cores, which are charged. In this model, depending on the distance between two dislocations the disks overlap completely (insulating GB) or a conducting path remains (conducting GB). This effect leads to a large scattering cross section of dislocations for interface electrons, which has several important consequences, as listed in the following.

First, it is important for sample preparation to take care of the substrate quality and to check the surface of each one after TiO_2 termination before proceeding (bunching of unit cell high steps indicates an increased dislocation density). In the experiments shown in this chapter only the quality of the substrate, whose structure is reproduced by the film, was changed. Similar effects are expected if the LaAlO_3 film grows with many defects on a good quality SrTiO_3 . This scenario is probably valid for samples grown at very high oxygen pressures like $p(\text{O}_2) = 1 \times 10^{-2}$ mbar and their transport properties should consequently not be compared to those of standard samples. Therefore the microstructural quality of the interface is revealed as a crucial parameter for the properties of $\text{LaAlO}_3/\text{SrTiO}_3$ heterostructures, which has not yet been accounted for in literature.

Moreover, the observed strong dependence of electronic transport on dislocation density offers the possibility to pattern the q2-DEG by artificially introducing defects in defined regions. This can for example be done by using a Focused Ion Beam (FIB) system. In preliminary experiments it was already found that the interface conductivity is completely suppressed by a low-dose irradiation with a Ga ion beam of 4 pA for ≈ 1 s (FIB200, fei company).

Finally, a very promising consequence is that a reduction of the dislocation density might enhance the interface conductivity and mobility of the electron gas, which would make the $\text{LaAlO}_3/\text{SrTiO}_3$ system even more interesting for electronic devices. Such a reduction of the number of defects might be obtained by using different substrate materials, growing high quality SrTiO_3 and LaAlO_3 films on these. DyScO_3 is a possible candidate as substrate for this approach, as SrTiO_3 was grown on this material by MBE with the narrowest rocking curves reported for epitaxial SrTiO_3 up to now [32]. However, one has to keep in mind that by the use of a different substrate material also the strain state is changed. This might be an additional tuning parameter for the electron gas at the interface.

9 Summary and Outlook

The research described in this thesis deals with interfaces in oxide heterostructures. In this field several surprising discoveries were made over the last years, like the observation of completely new properties in multilayers, which are not present in the bulk of the constituting materials. One spectacular example was reported in 2004: A conducting interface is formed between the two band insulators LaAlO_3 and SrTiO_3 [13]. The goal of this thesis was to prepare and study such $\text{LaAlO}_3/\text{SrTiO}_3$ heterostructures to get a better understanding of the interface effects in these samples and of interfaces in oxides in general. Starting from a barely investigated system it developed into one of the most widely studied oxide heterostructure by the end of this work.

For the preparation of the samples the exact atomic stacking at the interface is decisive, therefore a special termination procedure was used to obtain TiO_2 -terminated SrTiO_3 substrates. On these substrates thin films of LaAlO_3 were deposited by Pulsed Laser Deposition (PLD). While complex oxide heterostructures have been studied in this group before, the work described in this thesis opened a new area of research, as for the first time epitaxial oxide films with thicknesses of a few unit cells (some nm) were grown with control on the atomic level. To achieve this precision, a Reflection High Energy Electron Diffraction (RHEED) system was used, which was optimized by reducing the vibrational noise of the setup.

Characterization of the samples confirms a high quality of the films: Atomic Force Microscopy (AFM) reveals a flat surface with a step-and-terrace structure (step height 1 uc, $\approx 4 \text{ \AA}$), and Scanning Transmission Electron Microscopy (STEM) experiments reveal an atomically sharp interface between SrTiO_3 and LaAlO_3 .

A formation of a quasi-two-dimensional electron gas (q2-DEG) right at the interface between the two insulators was confirmed in this work. The focus was on n -type interfaces, which form if the stacking sequence at the interface is TiO_2/LaO .

To contact the conducting layer, which is buried underneath the LaAlO_3 film, a new method was designed. It uses Ar-ion etching and gold sputtering to access the interface.

Detailed investigation of the dependence of interface conductivity on LaAlO_3 film thickness revealed a remarkable transition. For the first time it was observed in this work that a minimum critical thickness $d_c = 4 \text{ uc}$ exists for the formation of the electron gas. Samples with 3 uc of LaAlO_3 or less are completely insulating with resistivities exceeding our measurement limit (sheet resistance $R_s > 5 \text{ G}\Omega/\square$). For film thicknesses of 4 uc or more the interface is metallic (sheet conductivity $\sigma_s \approx 2 \times 10^{-5} \Omega^{-1}$ (at 300 K) and $\sigma_s \approx 3 \times 10^{-3} \Omega^{-1}$ (at 4.2 K)). The sheet charge carrier density is $n_s \approx 10^{13} \text{ cm}^{-2}$ at all temperatures. Several groups confirmed the critical thickness of 4 uc in $\text{LaAlO}_3/\text{SrTiO}_3$ samples. The transition in transport properties between 3 uc and 4 uc of LaAlO_3 was utilized extensively throughout the rest of this work in field effect experiments and for patterning of the samples. It was discussed in this work that the metal-insulator transition (MIT) can be explained by energy considerations for the electrostatic potential of the film in the framework of the polarity discontinuity model.

For samples grown using our standard conditions ($T \approx 770^\circ\text{C}$, $p(\text{O}_2) \approx 10^{-5} \text{ mbar}$) the transport properties were stable over years and were reproducibly obtained throughout

this work.

In this thesis it was shown that it is indeed the interface which is conducting and not the bulk of the used materials. For several years the origin of the electron gas was a highly debated topic. Now it becomes clear that varying results and conclusions were mainly caused by the use of different deposition conditions for LaAlO₃ film growth. At the beginning of this thesis many groups claimed the conductivity in LaAlO₃/SrTiO₃ samples to be caused exclusively by oxygen vacancies in the SrTiO₃ substrate. Of course in this scenario it would be no novel interface effects which are studied, but only known materials properties. Many experiments described in this work show that oxygen vacancies do not dominate the transport properties in our samples. The biggest clue is the observed critical thickness of 4 uc for the formation of the electron gas at the interface. The existence of this critical thickness is hard to reconcile with a pure oxygen vacancy scenario. Supported by this finding, the widely accepted view today is that electronic transport in samples grown at very low oxygen pressure $p(\text{O}_2) \leq 10^{-6}$ mbar is controlled by oxygen vacancies in the SrTiO₃ substrate, resulting in much lower resistances and higher carrier densities compared to our standard samples. For samples grown at $p(\text{O}_2) \geq 10^{-5}$ mbar, like the used standard conditions in this work, the polarity-discontinuity model with electronic reconstructions being responsible for the interface conductivity is now widely accepted. To compare the properties of LaAlO₃/SrTiO₃ samples among publications it therefore is important to consider the preparation conditions.

The quasi two-dimensionality of the conducting interface layer and the low charge carrier density $n_s \approx 10^{13} \text{ cm}^{-2}$ makes the LaAlO₃/SrTiO₃ system an ideal candidate for electric field effect experiments. First it was demonstrated that by using the SrTiO₃ substrate as gate dielectric the resistivities of conducting interfaces can be tuned to a large extent (e.g. from -60% to +170% of the initial value at $T = 4$ K) by application of gate voltages $V_{G,b}$ of ± 100 V. This effect is now used by the group of Prof. Triscone at the University of Geneva (Switzerland) to map the phase diagram of the electron gas as a function of charge carrier density at temperatures of several mK [109].

After the previously mentioned discovery of the metal-insulator transition (MIT) triggered by a critical LaAlO₃ thickness it was important to investigate whether this transition can also be induced electronically. Therefore the electric field effect was used to analyze samples with $d = 3$ uc of LaAlO₃, which are insulating but in close proximity to the MIT. It was shown that by application of gate voltages $V_{G,b} \geq +70$ V an electron gas is generated at the interfaces, having a conductivity similar to samples with $d \geq d_c$. The electric field causes a tremendous change in resistance of up to seven orders of magnitude. While oxide field-effect devices have been prepared before by using other materials, their on-off ratios were orders of magnitude lower.

The high mobility (10^4 Vs/cm²) of the induced q2-DEG allows to view these field effect devices as an oxide analog to high electron mobility transistors built from conventional semiconductors, which shows the large potential of interfaces for oxide electronics.

At room-temperature a special memory effect is observed in samples with 3 uc of LaAlO₃. After generating the electron gas by applying $V_{G,b} = +100$ V the interface stays conducting, even if the gate voltage is switched off. By applying $V_{G,b} = -100$ V insulating behavior is restored, which also persists with $V_{G,b}$ put back to 0 V. The reversible, persis-

tent tunability is of potential interest for memory devices. However, because the origin of this memory effect is not yet resolved, further studies are needed.

For the use of these field effects in devices it is crucial to reduce the necessary voltages. A reduction of the needed gate voltages to some volts was achieved by using the LaAlO_3 film as gate dielectric, instead of the SrTiO_3 substrate.

Further experiments aimed on resolving the spatial resolution of the electron gas tunability. It was shown in this work that nanometer sized, conducting dots and lines can be reversibly induced in samples with 3 uc of LaAlO_3 by using a conducting, movable AFM tip as top gate electrode. Assuming that the thickness of the conducting layer is similar to the lateral extent of the induced structures implies that the electron gas is only several nanometer thick. These studies were done on our samples by C. Cen and Prof. J. Levy at the University of Pittsburgh (USA) who now use this scanning probe technique to generate and investigate multi-terminal devices.

Up to this point, all the $\text{LaAlO}_3/\text{SrTiO}_3$ samples studied used unpatterned films with the electron gas extending over the complete sample area. For the use of $\text{LaAlO}_3/\text{SrTiO}_3$ interfaces in oxide electronics it was a severe drawback that it was not possible to structure defined device geometries. The reason is that standard lithography techniques (like wet-chemical etching or ion etching) are not suitable for this system. This problem was solved in the course of this thesis by developing a patterning technique, which is based on the existence of a critical thickness for the formation of the q2-DEG. This effect offers the possibility to design conducting and insulating parts of the heterostructures by varying the number of unit cells of epitaxial LaAlO_3 on top of the SrTiO_3 . The control of the epitaxial LaAlO_3 thickness is accomplished by a series of depositions at high and low temperatures in lithographically defined areas.

As this procedure allowed for the first time to perform four-point measurements of the electron gas in clearly defined geometries, the patterning process was used extensively in this work. The developed technique is not limited to $\text{LaAlO}_3/\text{SrTiO}_3$ interfaces, but can be used for all systems where a similarly striking dependence of the transport properties on film thickness is found (like e.g. for LaVO_3 on SrTiO_3).

In the next part of this thesis the focus is on the important question whether and how the electron gas orders when the temperature approaches absolute zero. This question is still widely discussed in the scientific community. The ground state of the q2-DEG was explored in a collaboration with the group of Prof. J.-M. Triscone at the University of Geneva (Switzerland).

In these experiments it was discovered on our $\text{LaAlO}_3/\text{SrTiO}_3$ samples grown under standard conditions that the interface electrons condense at $T_c \approx 200$ mK into a superconducting state. This is the first observation of superconductivity confined to an artificially designed interface between two insulating materials. The maximum critical current density per width measured is $98 \mu\text{A}/\text{cm}$, and the estimated critical field is $H_{c2}(0 \text{ K}) \cong 65$ mT. From the latter value a coherence length $\xi(0 \text{ K}) \approx 70$ nm is obtained, assuming the applicability of the BCS theory.

Superconductivity was observed in $\text{LaAlO}_3/\text{SrTiO}_3$ heterostructures grown at oxygen pressures up to 3×10^{-3} mbar. No traces of magnetic effects, which have been reported elsewhere [85], were found in our samples.

From $I(V)$ and $R(T)$ characteristics it was further found that one can describe the system as a 2D superconductor, which undergoes a Berezinskii-Kosterlitz-Thouless transition. In conjunction with the observed tunability of superconductivity by electric field [109] the system therefore is ideally suited to study the superconducting transition in a low-dimensional electron system.

Additionally, these experiments lead to an estimation for the maximum thickness of the superconducting layer. First, for the BKT transition to be observable the superconducting sheet has to be thinner than the coherence length $\xi(0\text{ K}) \approx 70\text{ nm}$. A second estimation comes from the dependence of T_c on the charge carrier density in doped SrTiO_3 . Although the results for the standard samples grown in this work contradict a scenario, where oxygen deficient $\text{SrTiO}_{3-\delta}$ close to the interface causes the conducting layer, it is interesting to note that even in this view the upper limit for the possible thickness of a $\text{SrTiO}_{3-\delta}$ layer is only $\approx 2\text{ nm}$.

The polarity discontinuity model predicts that the electron gas is confined to the interface. Yet the exact thickness of the q2-DEG for our samples grown under standard conditions still needs to be determined. To achieve this, two approaches are pursued right now in collaboration with other groups. On the one hand, hard X-ray photoelectron spectroscopy (HAXPES) and its angle-dependence are analyzed to obtain the distribution profile of Ti^{3+} close to the interface, and on the other hand, electron holography is applied (Appendix B provides a list of ongoing projects).

Finally, when some experimental observations suggested that the transport properties of the samples are strongly affected by microstructural defects and dislocations, their influence on the q2-DEG was studied in detail. For these investigations LaAlO_3 bridges were patterned across a [001]-tilt grain boundary (GB) of bicrystalline SrTiO_3 substrates. The GBs serve as well defined defects. Even across 4° -tilt grain boundaries, where the GB microstructure shows isolated dislocations, which are separated by 5.2 nm , insulating behavior is found. For even larger spacings between the dislocations, adjusted by reducing the GB angle to 2° , the GB gets conducting. However, the resistivities still exceed those of the $\text{LaAlO}_3/\text{SrTiO}_3$ by orders of magnitude. As verified experimentally, the high value of R also prevents the use of such boundaries as Josephson junctions.

It was shown furthermore that the detrimental effects of dislocations on the transport properties are not limited to bicrystalline $\text{LaAlO}_3/\text{SrTiO}_3$ samples, but also are present in samples grown on substrates with a high dislocation density.

The data suggest that the electron gas is blocked in a disk of $\approx 5\text{ nm}$ diameter around single, charged dislocation cores.

The pronounced sensitivity of the q2-DEG properties on dislocations in the sample has two important consequences. First, the quality of the SrTiO_3 substrate is a crucial parameter for the transport properties, which justifies why all substrates have been checked prior to film depositions in this work. It is important to take this parameter into account for all studies of $\text{LaAlO}_3/\text{SrTiO}_3$ heterostructures, and probably for all systems where the properties are dominated by film-substrate interface effects. The second consequence is that reducing the dislocation density to well below the standard 10^6 cm^{-2} in SrTiO_3 has the potential to substantially improve the transport properties of the 2D electron gas at the interface.

In summary, the $\text{LaAlO}_3/\text{SrTiO}_3$ interface has proven to be a very interesting system among the complex oxide heterostructures. Novel properties and amazing effects observed in the experiments, like the critical thickness phenomenon, add to the big potential of oxide interfaces in general. The Science magazine termed the achievements in the field one of the breakthroughs of the year 2007.

Finally, some open questions are listed along with studies and experiments that potentially are necessary in the future development of the field of oxide interfaces.

Experimentally, one promising topic will definitely be if the ultrathin electron gas and its properties can be exploited in actual devices. Right now the $\text{LaAlO}_3/\text{SrTiO}_3$ interface is already successfully used in a diploma project in our group as an oxide diode with unique characteristics, which works at temperatures up to several 100 °C.

A great leap forward for scaling the dimensions of electronics in this system to the nanometer range is the lithography by scanning probe, which was presented in this thesis. The technique allows to write reconfigurable nanowires and electronics. In such structures it might then be possible to study single electron effects, such as coulomb blockade.

$\text{LaAlO}_3/\text{SrTiO}_3$ heterostructures are also promising for sensor applications. The electronic reconstruction, which leads to the conducting interface, might be susceptible to the presence of material on top of the LaAlO_3 film. Especially for samples with a film thickness close to the critical value for the formation of the electron gas the conductivity is potentially changed by putting on top, e.g., chemical solutions or biological samples. Using nanometer-sized structures can additionally enhance the sensitivity of such sensors.

Furthermore it will be important to resolve the real thickness of the conducting layer of the $\text{LaAlO}_3/\text{SrTiO}_3$ heterostructures. In the superconducting phase signatures of two-dimensionality of the conducting layer were observed. However, for the normal conducting phase only some upper limits on the possible thickness were obtained. Scanning tunneling microscopy experiments might provide contributions to this subject. By scanning tunneling spectroscopy signatures of discrete energy levels caused by confinement of the electron gas to the interface can potentially be found in the density of states.

The determination of the origin of the superconductivity of $\text{LaAlO}_3/\text{SrTiO}_3$ interfaces is another important task. Novel pairing mechanisms might exist at interfaces, like pairing in the electron gas induced by the SrTiO_3 [104].

While this work has focused on the interface effects in $\text{LaAlO}_3/\text{SrTiO}_3$ samples, it will also be exciting to design and investigate other combinations of materials. Especially oxides, with their large versatility in properties, allow for a huge number of variations in multilayers. Interface properties might additionally be tuned by exploiting electronic correlation effects in the materials. Such heterostructures potentially show functionalities which can not be realized using semiconductors.

It will also be a big step forward if oxide superlattices containing many interfaces with identical properties can be prepared, which has not been demonstrated up to now. Such samples will allow to study coupling between interfaces and will furthermore simplify investigations by spectroscopic techniques, for which the signal from a single interface is too small to be resolved.

It was theoretically predicted that the thermoelectric figure of merit $Z_{2D}T$ of ther-

moelectric semiconductors can be substantially enhanced by using superlattices with electrons confined in quantum wells [135]. Experimental confirmations were found in a PbTe/Pb_{0.927}Eu_{0.073}Te superlattice [136] and in SrTiO₃/SrTi_{0.8}Nb_{0.2}O₃ superlattices [137]. Therefore two-dimensional electron gases are also very promising in the field of thermoelectrics.

A decisive question for the use of oxide heterostructures in applications will be if the integration with silicon is feasible.

From the theoretical side it will be important to see in how far interface properties are captured in modern band structure calculations and to investigate low-dimensional electron systems and occurring ordering phenomena.

In conclusion, the experiments presented in this thesis have helped to widen the understanding of oxide heterostructure properties. The perspectives and remaining tasks mentioned in the last paragraphs show that also for the following years it will remain thrilling in this field to analyze the fascinating physics of interfaces in oxides.

References

- [1] H. Kroemer. “Nobel Lecture: Quasielectric fields and band offsets: teaching electrons new tricks”. *Rev. Mod. Phys.*, **73**, 783, 2001.
- [2] H. Koinuma. “Chemistry and electronics of oxides from carbon dioxide to perovskite”. *Thin Solid Films*, **486**, 2, 2005.
- [3] E. Dagotto. “When Oxides Meet Face to Face”. *Science*, **318**, 1076, 2007.
- [4] J. Mannhart. “Interfaces in Materials with Correlated Electron Systems”. Springer, 2005.
- [5] A.P. Ramirez. “Oxide Electronics Emerge”. *Science*, **315**, 1377, 2008.
- [6] G. Rijnders and D.H.A. Blank. “Build your own superlattice”. *Nature*, **433**, 369, 2005.
- [7] H.N. Lee, H.M. Christen, M.F. Chisholm, C.M. Rouleau, and D.H. Lowndes. “Strong polarization enhancement in asymmetric three-component ferroelectric superlattices”. *Nature*, **433**, 395, 2005.
- [8] D.P. Norton, B.C. Chakoumakos, J.D. Budai, D.H. Lowndes, B.C. Sales, J.R. Thompson, and D.K. Christen. “Superconductivity in SrCuO₂-BaCuO₂ superlattices - Formation of artificially layered superconducting materials”. *Science*, **265**, 2074, 1994.
- [9] T. Tsurumi, T. Harigai, D. Tanaka, S.-M. Nam, H. Kakemoto, S. Wada, and K. Saito. “Artificial ferroelectricity in perovskite superlattices”. *Appl. Phys. Lett.*, **85**, 5016, 2004.
- [10] K.S. Takahashi, M. Kawasaki, and Y. Tokura. “Interface ferromagnetism in oxide superlattices of CaMnO₃/CaRuO₃”. *Appl. Phys. Lett.*, **79**, 1324, 2001.
- [11] A. Ohtomo, D.A. Muller, J.L. Grazul, and H.Y. Hwang. “Artificial charge-modulation in atomic-scale perovskite titanate superlattices”. *Nature*, **419**, 378, 2002.
- [12] A. Tsukazaki, A. Ohtomo, T. Kita, Y. Ohno, H. Ohno, and M. Kawasaki. “Quantum Hall Effect in Polar Oxide Heterostructure”. *Science*, **315**, 1388, 2007.
- [13] A. Ohtomo and H.Y. Hwang. “A high-mobility electron gas at the LaAlO₃/SrTiO₃ heterointerface”. *Nature*, **427**, 423, 2004; Corrigendum: *Nature*, **441**, 120, 2006.
- [14] J. Nishimura, A. Ohtomo, A. Ohkubo, Y. Murakami, and M. Kawasaki. “Controlled Carrier Generation at a Polarity-Discontinued Perovskite Heterostructure”. *Japan. Journ. of Appl. Phys.*, **43**, L1032, 2004.
- [15] M. Johansson and P. Lemmens. “Perovskites and thin films – crystallography and chemistry”. *J. Phys.: Condens. Matter*, **20**, 264001, 2008.

- [16] P. Chaudhari, R.H. Koch, R.B. Laibowitz, T.R. McGuire, and R.J. Gambino. “Critical-Current Measurements in Epitaxial Films of $\text{YBa}_2\text{Cu}_3\text{O}_{7-x}$ Compound”. *Phys. Rev. Lett.*, **58**, 2684, 1987.
- [17] K.A. Müller, W. Berlinger, and F. Waldner. “Characteristic Structural Phase Transition in Perovskite-type Compounds”. *Phys. Rev. Lett.*, **21**, 814, 1968.
- [18] H.P.R. Frederikse, W.R. Thurber, and W.R. Holser. “Electronic Transport in Strontium Titanate”. *Phys. Rev.*, **134**, A442, 1963.
- [19] W. Luo, W. Duan, S.G. Louie, and M.L. Cohen. “Structural and electronic properties of n-doped and p-doped SrTiO_3 ”. *Phys. Rev. B*, **70**, 214109, 2004.
- [20] J.F. Schooley, W.R. Hosler, and M.L. Cohen. “Superconductivity in Semiconducting SrTiO_3 ”. *Phys. Rev. Lett.*, **12**, 474, 1964.
- [21] J.F. Schooley, W.R. Hosler, E. Ambler, J.H. Becker, M.L. Cohen, and C.S. Koonce. “Dependence of the Superconducting Transition Temperature on Carrier Concentration in Semiconducting SrTiO_3 ”. *Phys. Rev. Lett.*, **14**, 305, 1965.
- [22] G. Binnig, A. Baratoff, H.E. Hoenig, and J.G. Bednorz. “Two-Band Superconductivity in Nb-Doped SrTiO_3 ”. *Phys. Rev. Lett.*, **45**, 1352, 1980.
- [23] J. Mannhart and D.G. Schlom. “The value of seeing nothing”. *Nature*, **430**, 620, 2004.
- [24] D.A. Muller, N. Nakagawa, A. Ohtomo, J.L. Grazul, and H.Y. Hwang. “Atomic-scale imaging of nanoengineered oxygen vacancy profiles in SrTiO_3 ”. *Nature*, **430**, 657, 2004.
- [25] K.A. Müller and H. Burkard. “ SrTiO_3 : An intrinsic quantum paraelectric below 4 K”. *Phys. Rev. B*, **19**, 3593, 1979.
- [26] O.N. Tufte and P.W. Chapman. “Electron Mobility in Semiconducting Strontium Titanate”. *Phys. Rev.*, **155**, 796, 1966.
- [27] T. Sakudo and H. Unoki. “Dielectric Properties of SrTiO_3 at Low Temperatures”. *Phys. Rev. Lett.*, **26**, 851, 1971.
- [28] A. Bhattacharya, M. Eblen-Zayas, N.E. Staley, W.H. Huber, and A.M. Goldman. “Micromachined SrTiO_3 single crystals as dielectrics for electrostatic doping of thin films”. *Appl. Phys. Lett.*, **85**, 997, 2004.
- [29] H.-M. Christen, J. Mannhart, E.J. Williams, and C. Gerber. “Dielectric properties of sputtered SrTiO_3 films”. *Phys. Rev. B*, **49**, 12095, 1994.
- [30] M. Lippmaa, N. Nakagawa, and M. Kawasaki. “Dielectric Properties of Homoepitaxial SrTiO_3 Thin Films Grown in the Step-Flow Mode”. *Journal of Electroceramics*, **4**, 365, 2000.

-
- [31] E. Sawaguchi, A. Kikuchi, and Y. Koderu. “Dielectric Constant of Strontium Titanate at Low Temperatures”. *J. Phys. Soc. Japan*, **17**, 1666, 1962.
- [32] J.H. Haeni, P. Irvin, W. Chang, R. Uecker, P. Reiche, Y.L. Li, S. Choudhury, W. Tian, M.E. Hawley, B. Craigo, A.K. Tagantsev, X.Q. Pan, S.K. Streiffer, L.Q. Chen, S.W. Kirchoefer, J. Levy, and D.G. Schlom. “Room-temperature ferroelectricity in strained SrTiO₃”. *Nature*, **430**, 758, 2004.
- [33] R.W. Simon, C.E. Platt, A.E. Lee, G.S. Lee, K.P. Daly, M.S. Wire, and J.A. Luine. “Low-loss substrate for epitaxial growth of high-temperature superconductor thin films”. *Appl. Phys. Lett.*, **53**, 2677, 1988.
- [34] H. Lehnert, H. Boysen, J. Schneider, F. Frey, D. Hohlwein, P. Radaelli, and H. Ehrenberg. “A powder diffraction study of the phase transition in LaAlO₃”. *Z. Kristallogr.*, **412**, 536, 2000.
- [35] S.A. Hayward, F.D. Morrison, S.A.T. Redfern, E.K.H. Salje, J.F. Scott, K.S. Knight, S. Tarantino, A.M. Glazer, V. Shuvaeva, P. Daniel, M. Zhang, and M.A. Carpenter. “Transformation processes in LaAlO₃: Neutron diffraction, dielectric, thermal, optical, and Raman studies”. *Phys. Rev. B*, **72**, 054110, 2005.
- [36] D. de Ligny and P. Richet. “High-temperature heat capacity and thermal expansion of SrTiO₃ and SrZrO₃ perovskites”. *Phys. Rev. B*, **53**, 3013, 1996.
- [37] B.C. Chakoumakos, D.G. Schlom, M. Urbanik, and J. Luine. “Thermal expansion of LaAlO₃ and (La,Sr)(Al,Ta)O₃, substrate materials for superconducting thin-film device applications”. *Journ. Appl. Phys.*, **83**, 1979, 1998.
- [38] P. Delugas, V. Fiorentini, and A. Filippetti. “Dielectric properties and long-wavelength optical modes of the high- κ oxide LaAlO₃”. *Phys. Rev. B*, **71**, 134302, 2005.
- [39] G.A. Baraff, J.A. Appelbaum, and D.R. Hamann. “Self-Consistent Calculation of the Electronic Structure at an abrupt GaAs-Ge Interface”. *Phys. Rev. Lett.*, **38**, 237, 1976.
- [40] W.A. Harrison, E.A. Kraut, J.R. Waldrop, and R.W. Grant. “Polar heterojunction interfaces”. *Phys. Rev. B*, **18**, 4402, 1978.
- [41] N. Nakagawa, H.Y. Hwang, and D.A. Muller. “Why some interfaces cannot be sharp”. *Nature Materials*, **5**, 204, 2006.
- [42] S. Okamoto and A.J. Millis. “Electronic reconstruction at an interface between a Mott insulator and a band insulator”. *Nature*, **428**, 630, 2004.
- [43] S. Okamoto and A.J. Millis. “Theory of Mott insulator-band insulator heterostructures”. *Phys. Rev. B*, **70**, 075101, 2004.
- [44] F. Lichtenberg, D. Widmer, J.G. Bednorz, T. Williams, and A. Reller. “Phase diagram of LaTiO_x: from 2D layered ferroelectric insulator to 3D weak ferromagnetic semiconductor”. *Z. Phys. B*, **82**, 211, 1991.

- [45] F. Lichtenberg, A. Herrnberger, K. Wiedenmann, and J. Mannhart. “Synthesis of Perovskite-Related Layered $A_nB_nO_{3n+2} = ABO_x$ Type Niobates and Titanates and Study of Their Structural, Electric and Magnetic Properties”. *Prog. Solid State Chem.*, **29**, 1, 2001.
- [46] R. Pentcheva and W.E. Picket. “Charge localization or itineracy at $LaAlO_3/SrTiO_3$ interfaces: Hole polarons, oxygen vacancies, and mobile electrons”. *Phys. Rev. B*, **74**, 035112, 2006.
- [47] M.S. Park, S.H. Rhim, and A.J. Freeman. “Charge compensation and mixed valency in $LaAlO_3/SrTiO_3$ heterointerfaces studied by the FLAPW method”. *Phys. Rev. B*, **74**, 205416, 2006.
- [48] S. Gemming and G. Seifert. “ $SrTiO_3(001)|LaAlO_3(001)$ multilayers: A density-functional investigation”. *Acta Materialia*, **54**, 4299, 2006.
- [49] D.R. Hamann, D.A. Muller, and H.Y. Hwang. “Lattice-polarization effects on electron-gas charge densities in ionic superlattices”. *Phys. Rev. B*, **73**, 195403, 2006.
- [50] J.-M. Albina, M. Mrovec, B. Meyer, and C. Elsässer. “Structure, stability, and electronic properties of $SrTiO_3/LaAlO_3$ and $SrTiO_3/SrRuO_3$ interfaces”. *Phys. Rev. B*, **76**, 165103, 2007.
- [51] U. Schwingenschlögl and C. Schuster. “Surface effects on oxide heterostructures”. *EPL*, **81**, 17007, 2008.
- [52] C. Cen, S. Thiel, G. Hammerl, C.W. Schneider, K.E. Andersen, C.S. Hellberg, J. Mannhart, and J. Levy. “Nanoscale control of an interfacial metal-insulator transition at room temperature”. *Nature Materials*, **7**, 298, 2008.
- [53] M. Kawasaki, K. Takahashi, T. Maeda, R. Tsuchiya M. Shinohara, et al. “Atomic Control of the $SrTiO_3$ Crystal Surface”. *Science*, **266**, 1540, 1994.
- [54] G. Koster, B.L. Kropman, G.J.H.M. Rijnders, and D.H.A. Blank. “Quasi-ideal strontium titanate crystal surfaces through formation of strontium hydroxide”. *Appl. Phys. Lett.*, **73**, 2920, 1998.
- [55] T. Ohnishi, K. Shibuya, M. Lippmaa, D. Kobayashi, H. Kumigashira, M. Oshima, and H. Koinuma. “Preparation of thermally stable TiO_2 -terminated $SrTiO_3(100)$ substrate surfaces”. *Appl. Phys. Lett.*, **85**, 272, 2004.
- [56] S. Karimoto and M. Naito. “Electron doped infinite-layer thin films with T_c over 40 K grown on $DyScO_3$ substrates”. *Appl. Phys. Lett.*, **84**, 2136, 2004.
- [57] T. Ohnishi, K. Takahashi, M. Nakamura, M. Kawasaki, M. Yoshimoto, and H. Koinuma. “A-site layer terminated perovskite substrate: $NdGaO_3$ ”. *Appl. Phys. Lett.*, **74**, 2531, 1999.
- [58] V. Leca. “Heteroepitaxial growth of copper oxide superconductors by Pulsed Laser Deposition”. Ph.D. thesis, University of Twente, 2003.

-
- [59] P.R. Willmot and J.R. Huber. “Pulsed laser vaporization and deposition”. *Rev. of Mod. Phys.*, **72**, 315, 2000.
- [60] A. Schmehl, R.R. Schulz, and J. Mannhart. “Eucentric four-axis ultrahigh vacuum goniometer for reflection high-energy electron diffraction applications”. *Rev. of Scient. Instr.*, **76**, 123901, 2005.
- [61] F.C. Frank and J.H. van der Merwe. “One-Dimensional Dislocations. I. Static Theory”. *Proc. Roy. Soc. London A*, **198**, 205, 1949.
- [62] M. Volmer and A. Weber. “Nucleus formation in supersaturated systems”. *Z. Phys. Chem.*, **119**, 277, 1926.
- [63] I.N. Stranski and Krastanov. “Theory of orientation separation of ionic crystals”. *Acad. Wiss. Math.-Naturw. Klasse IIb*, **146**, 797, 1938.
- [64] T. Frey, C.C. Chi, C.C. Tsuei, T. Shaw, and F. Boszo. “Effect of Atomic Oxygen on the Initial Growth Mode in Thin Epitaxial Cuprate Films”. *Phys. Rev. B*, **49**, 3483, 1994.
- [65] G. Koster, G.J.H.M. Rijnders, D.H.A. Blank, and H. Rogalla. “Imposed layer-by-layer growth by pulsed laser intervall deposition”. *Appl. Phys. Lett.*, **74**, 3829, 1999.
- [66] D.H.A. Blank, G.J.H.M. Rijnders, G. Koster, and H. Rogalla. “A New Approach in Layer-by-layer Growth of Oxide Materials by Pulsed Laser Deposition”. *J. of Electroceramics*, **4**, 311, 2000.
- [67] W. Braun. “Applied RHEED”, volume 154. Springer Tracts in Modern Physics, 1999.
- [68] G.J.H.M. Rijnders, G. Koster, D.H.A. Blank, and H. Rogalla. “In situ monitoring during pulsed laser deposition of complex oxides using reflection high energy electron diffraction under high oxygen pressures”. *Appl. Phys. Lett.*, **70**, 1888, 1997.
- [69] S. Kikuchi. “Diffraction of cathode rays by mica”. *Jpn. J. Phys.*, **5**, 83, 1928.
- [70] J.J. Harris, B.A. Joyce, and P.J. Dobson. “Oscillations in the surface structure of Sn-doped GaAs during growth by MBE”. *Surf. Sci.*, **103**, L90, 1981.
- [71] J. Resh, K.D. Jamison, J. Strozier, A. Bensaoula, and A. Ignatiev. “Phase of reflection high-energy electron-diffraction intensity oscillations during molecular-beam-epitaxy growth of GaAs(100)”. *Phys. Rev. B*, **40**, 11799, 1989.
- [72] H. Karl and B. Stritzker. “Reflection High-Energy Electron Diffraction Oscillations Modulated by Laser-Pulse Deposited $\text{YBa}_2\text{Cu}_3\text{O}_{7-x}$ ”. *Phys. Rev. Lett.*, **69**, 2939, 1992.
- [73] J.P.A. Van der Wagt. “Reflection High-Energy Electron Diffraction during Molecular-Beam Epitaxy”. Ph.D. thesis, Stanford University, 1994.

- [74] G. Rijnders, G. Koster, V. Leca, D.H.A. Blank, and H. Rogalla. “Imposed layer-by-layer growth with pulsed laser intervall deposition”. *Applied Surface Science*, **168**, 223, 2000.
- [75] S. Thiel, G. Hammerl, A. Schmehl, C.W. Schneider, and J. Mannhart. “Tunable Quasi-Two-Dimensional Electron Gases in Oxide Heterostructures”. *Science*, **313**, 1942, 2006.
- [76] Y. Li, C. Weatherly, and M. Niewczas. “TEM studies of stress relaxation in GaAsN and GaP thin films”. *Philosophical Magazine*, **85**, 3073, 2005.
- [77] H. Yamada, M. Kawasaki, and Y. Tokura. “Epitaxial growth and valence control of strained perovskite SrFeO₃ films”. *Appl. Phys. Lett.*, **80**, 622, 2002.
- [78] I.K. Robinson. “Crystal truncation rods and surface roughness”. *Phys. Rev. B*, **33**, 3830, 1985.
- [79] J.-L. Maurice, C. Carretero, M.-J. Casanove, K. Bouzehouane, S. Guyard, É. Larquet, and J.-P. Contour. “Electronic conductivity and structural distortion at the interface between insulators SrTiO₃ and LaAlO₃”. *Phys. Stat. Sol. A*, **203**, 2209, 2006.
- [80] M.M.J. Treacy and J.M. Gibson. “The effects of elastic relaxation on transmission electron microscopy studies of thinned composition-modulated materials”. *J. Vac. Sci. Technol. B*, **4**, 1458, 1986.
- [81] M. Huijben, G. Rijnders, D.H.A. Blank, S. Bals, S. Van Aert, J. Verbeeck, G. Van Tendeloo, A. Brinkman, and H. Hilgenkamp. “Electronically coupled complementary interfaces between perovskite band insulators”. *Nature Materials*, **5**, 556, 2006.
- [82] A.S. Kalabukhov, R. Gunnarsson, J. Börjesson, E. Olsson, D. Winkler, and T. Claesson. “Effect of oxygen vacancies in the SrTiO₃ substrate on the electrical properties of the LaAlO₃/SrTiO₃ interface”. *Phys. Rev. B*, **75**, 121404, 2007.
- [83] L.J. van der Pauw. “A method of measuring specific resistivity and Hall effect of discs of arbitrary shape”. *Philippis Research Reports*, **13**, 1, 1958.
- [84] M. Huijben. “Interface Engineering for Oxide Electronics: Tuning electronic properties by atomically controlled growth”. Ph.D. thesis, University of Twente, 2006.
- [85] A. Brinkman, M. Huijben, M. van Zalk, J. Huijben, U. Zeitler, J.C. Maan, W.G. van der Wiel, G. Rijnders, D.H.A. Blank, and H. Hilgenkamp. “Magnetic effects at interfaces between nonmagnetic oxides”. *Nature Materials*, **6**, 493, 2007.
- [86] W. Siemons, G. Koster, H. Yamamoto, T.H. Geballe, D.H.A. Blank, and M.R. Beasley. “Experimental investigation of electronic properties of buried heterointerfaces of LaAlO₃ on SrTiO₃”. *Phys. Rev. B*, **76**, 155111, 2007.

-
- [87] G. Herranz, M. Basletic, M. Bibes, C. Carrétéro, E. Tafra, E. Jacquet, K. Bouzouane, C. Deranlot, A. Hamzic, J.-M. Broto, A. Barthélémy, , and A. Fert. “Origin and Perspectives of High Mobility in $\text{LaAlO}_3/\text{SrTiO}_3$ Structures”. *Phys. Rev. Lett.*, **98**, 216803, 2007.
- [88] Y. Hotta, Y. Mukunoki, T. Susaki, L. Fitting, D.A. Muller, and H.Y. Hwang. “Growth and epitaxial structure of LaVO_x films”. *Appl. Phys. Lett.*, **89**, 031918, 2006.
- [89] Y. Hotta, T. Susaki, and H.Y. Hwang. “Polar Discontinuity Doping of the $\text{LaVO}_3/\text{SrTiO}_3$ Interface”. *Phys. Rev. Lett.*, **99**, 236805, 2007.
- [90] D. Kan, T. Terashima, R. Kanda, A. Masuno, K. Tanaka, S. Chu, H. Kan, A. Ishizumi, Y. Kanemitsu, Y. Shimakawa, and M. Takano. “Blue-light emission at room temperature from Ar^+ -irradiated SrTiO_3 ”. *Nature Materials*, **4**, 816, 2005.
- [91] N. Reyren, S. Thiel, A.D. Caviglia, L. Fitting Kourkoutis, G. Hammerl, C. Richter, C.W. Schneider, T. Kopp, A.-S. Rüetschi, D. Jaccard, M. Gabay, D.A. Muller, J.-M. Triscone, and J. Mannhart. “Superconducting Interfaces Between Insulating Oxides”. *Science*, **317**, 1196, 2007.
- [92] L. Fitting, S. Thiel, A. Schmehl, J. Mannhart, and D.A. Muller. “Subtleties in ADF imaging and spatially resolved EELS: A case study of low-angle twist boundaries in SrTiO_3 ”. *Ultramicroscopy*, **106**, 1053, 2006.
- [93] J.N. Eckstein. “Watch out for the lack of oxygen”. *Nature Materials*, **6**, 473, 2007.
- [94] W. Siemons, G. Koster, H. Yamamoto, W.A. Harrison, G. Lucovsky, T.H. Geballe, D.H.A. Blank, and M.R. Beasley. “Origin of charge carrier density at LaAlO_3 -on SrTiO_3 hetero-interfaces: possibility of intrinsic doping”. *Phys. Rev. Lett.*, **98**, 196802, 2007.
- [95] M. Basletic, J.-L. Maurice, C. Carrétéro, O. Copie, M. Bibes, É. Jacquet, K. Bouzouane, S. Fusil, and A. Barthélémy. “Mapping the spatial distribution of charge carriers in $\text{LaAlO}_3/\text{SrTiO}_3$ heterostructures”. *Nature Materials*, **7**, 621, 2008.
- [96] C.H. Ahn, J.-M. Triscone, and J. Mannhart. “Electric Field Effect in Correlated Oxide Systems”. *Nature*, **424**, 1015, 2003.
- [97] C.H. Ahn, A. Bhattacharya, M. Di Ventra, J.N. Eckstein, C.D. Frisbie, M.E. Gershenson, A.M. Goldman, I.H. Inoue, J. Mannhart, A.J. Millis, A.F. Morpurgo, D. Natelson, and J.-M. Triscone. “Electrostatic modification of novel materials”. *Rev. of Mod. Physics*, **78**, 1185, 2006.
- [98] A. Sawa, C.W. Schneider, and J. Mannhart. “Unusual current-voltage characteristics of single crystalline and bicrystalline $\text{La}_{0.7}\text{Ca}_{0.3}\text{MnO}_3$ films”. *Ann. Phys. (Leipzig)*, **13**, 595, 2004.
- [99] H.L. Stormer. “Nobel Lecture: The fractional quantum Hall effect”. *Rev. Mod. Phys.*, **71**, 875, 1999.

- [100] I. Pallecchi, G. Grassano, D. Marré, L. Pellegrino, M. Putti, and A.S. Siri. “SrTiO₃-based metal-insulator-semiconductor heterostructures”. *Appl. Phys. Lett.*, **78**, 2244, 2001.
- [101] K.S. Takahashi, D. Matthey, D. Jaccard, J.-M. Triscone, K. Shibuya, T. Ohnishi, and M. Lippmaa. “Electrostatic modulation of the electronic properties of Nb-doped SrTiO₃ superconducting films”. *Appl. Phys. Lett.*, **84**, 1722, 2004.
- [102] K. Ueno, I.H. Inoue, H. Akoh, M. Kawasaki, Y. Tokura, and H. Takagi. “Field-effect transistor on SrTiO₃ with sputtered Al₂O₃ gate insulator”. *Appl. Phys. Lett.*, **83**, 1755, 2003.
- [103] K. Ueno, S. Nakamura, H. Shimotani, A. Ohtomo, N. Kimura, T. Nojima, H. Aoki, Y. Iwasa, and M. Kawasaki. “Electric-Field-Induced Superconductivity in an Insulator”. *Nature Materials*, **7**, 855, 2008.
- [104] V. Körting, Q. Yuan, P.J. Hirschfeld, T. Kopp, and J. Mannhart. “Interface-mediated pairing in field effect devices”. *Phys. Rev. B*, **71**, 104510, 2005.
- [105] C. Richter. “Untersuchung des Feldeffektes an SrTiO₃/LaAlO₃-Heterostrukturen”. Diplomathesis, Universität Augsburg, 2007.
- [106] B. Kießig. “Rastersondenmikroskopische Modifikation von Grenzflächen in oxidischen Heterostrukturen”. Diplomathesis, Universität Augsburg, 2008.
- [107] M.I. Lutwyche, M. Despont, U. Drechsler, U. Dürig, W. Häberle, H. Rothuizen, R. Stutz, R. Widmer, G.K. Binnig, and P. Vettiger. “Highly parallel data storage system based on scanning probe arrays”. *Appl. Phys. Lett.*, **77**, 3299, 2000.
- [108] C.W. Schneider, S. Thiel, G. Hammerl, C. Richter, and J. Mannhart. “Microlithography of electron gases formed at interfaces in oxide heterostructures”. *Appl. Phys. Lett.*, **89**, 122101, 2006.
- [109] A.D. Caviglia, S. Gariglio, N. Reyren, D. Jaccard, T. Schneider, M. Gabay, S. Thiel, G. Hammerl, J. Mannhart, and J.-M. Triscone. “Electric Field Control of the LaAlO₃/SrTiO₃ Interface Ground State”. *Nature*, **456**, 624, 2008.
- [110] M. Gurvitch, H.L. Stormer, R.C. Dynes, J.M. Graybeal, and D.C. Jacobson. In J. Bevk and A.I. Braginski, editors, Proceedings of the MRS, pages 47–49. Materials Research Society, Warrendale, PA, 1986.
- [111] N. Pavlenko and T. Kopp. “Electrostatic interface tuning in correlated superconducting heterostructures”. *Phys. Rev. B*, **72**, 174516, 2005.
- [112] V.L. Berezinskii. “Destruction of Long-Range Order in One-Dimensional and Two-Dimensional Systems with a Continuous Symmetry Group. II. Quantum Systems”. *Zh. Eksp. Teor. Fiz.*, **61**, 1144, 1971.
- [113] V.L. Berezinskii. “Destruction of Long-Range Order in One-Dimensional and 2-Dimensional Systems Possessing a Continuous Symmetry Group. II. Quantum Systems”. *Sov. Phys. JETP*, **34**, 610, 1972.

-
- [114] J.M. Kosterlitz and D.J. Thouless. “Ordering, metastability and phase transitions in two-dimensional systems”. *J. Phys. C: Solid State Phys.*, **6**, 1181, 1973.
- [115] P. Minnhagen. “The two-dimensional Coulomb gas, vortex unbinding, and superfluid-superconducting films”. *Rev. of Mod. Phys.*, **59**, 1001, 1987.
- [116] J. Pearl. *Low Temp. Phys.*, **LT9**, 566, 1965.
- [117] M.R. Beasley, J.E. Mooij, and T.P. Orlando. “Possibility of Vortex-Antivortex Pair Dissociation in Two-Dimensional Superconductors”. *Phys. Rev. Lett.*, **42**, 1165, 1979.
- [118] M. Gabay and A. Kapitulnik. “Vortex-Antivortex Crystallization in Thin Superconducting and Superfluid Films”. *Phys. Rev. Lett.*, **71**, 2138, 1993.
- [119] K. Medvedyeva, B.J. Kim, and P. Minnhagen. “Analysis of current-voltage characteristics of two-dimensional superconductors: Finite-size scaling behavior in the vicinity of the Kosterlitz-Thouless transition”. *Phys. Rev. B*, **62**, 14531, 2000.
- [120] B.I. Halperin and D.R. Nelson. “Resistive transition in superconducting films”. *J. Low Temp.*, **36**, 599, 1979.
- [121] C.S. Koonce, M.L. Cohen, J.F. Scholey, W.R. Hosler, and E.R. Pfeiffer. “Superconducting Transition Temperatures of Semiconducting SrTiO₃”. *Phys. Rev.*, **163**, 380, 1967.
- [122] K. Ueno. “Field-Effect Transistors Based on perovskite oxides”. Ph.D. thesis, University of Tokyo, 2003.
- [123] K.S. Takahashi, M. Gabay, D. Jaccard, K. Shibuya, T. Ohnishi, M. Lippmaa, and J.-M. Triscone. “Local switching of two-dimensional superconductivity using the ferroelectric field effect”. *Nature*, **441**, 195, 2006.
- [124] G. Rijnders and D.H.A. Blank. “An atomic force pencil and eraser”. *Nature Materials*, **7**, 270, 2008.
- [125] G. Hammerl. “Neue Verfahren zur Optimierung von Bandsupraleitern”. Ph.D. thesis, Universität Augsburg, 2004.
- [126] F.C. Frank. *Conference on Plastic Deformations of Crystalline Solids (Mellon Institute)*, page 150, 1950.
- [127] A.P. Sutton and R.W. Balluffi, editors. “Interfaces in Crystalline Materials”. Clarendon Press, Oxford, 1995.
- [128] N.D. Mathur, G. Burnell, S.P. Isaac, T.J. Jackson, B.-S. Teo, J.L. MacManus-Driscoll, L.F. Cohen, J.E. Evetts, and M.G. Blamire. “Large low-field magnetoresistance in La_{0.7}Ca_{0.3}MnO₃ induced by artificial grain boundaries”. *Nature*, **387**, 266, 1997.

- [129] G.C. Spalding, W.L. Murphy, T.M. Davidsmeier, and J.E. Elenewski. “Faceting of Single-Crystal SrTiO₃ during Wet Chemical Etching”. *Mat. Res. Soc. Symp.*, **587**, O6.4.1, 2000.
- [130] A. Widuch. “Optimierung des Polierprozesses von einkristallinen und bikristallinen SrTiO₃-Substraten zur Epitaxie von Hochtemperatursupraleitern”. Diplomathesis, Fachhochschule Nürnberg, 2001.
- [131] Z. Zhang, W. Sigle, and M. Rühle. “Atomic and electronic characterization of the $a[100]$ dislocation core in SrTiO₃”. *Phys. Rev. B*, **66**, 094108, 2002.
- [132] R.A. De Souza, J. Fleig, J. Maier, O. Kienzle, Z. Zhang, W. Sigle, and M. Rühle. “Electrical and Structural Characterization of a Low-Angle Tilt Grain Boundary in Iron-Doped Strontium Titanate”. *J. Am. Ceram. Soc.*, **86**, 922, 2003.
- [133] R. Shao, J. Vavro, and D.A. Bonnell. “Low-temperature study of nonlinear transport across oxide grain boundaries”. *Appl. Phys. Lett.*, **85**, 561, 2004.
- [134] R. Shao, M.F. Chisholm, G. Duscher, and D.A. Bonnell. “Low-Temperature Resistance Anomaly at SrTiO₃ Grain Boundaries: Evidence for an Interface-Induced Phase Transition”. *Phys. Rev. Lett.*, **95**, 197601, 2005.
- [135] L.D. Hicks and M.S. Dresselhaus. “Effect of quantum-well structures on the thermoelectric figure of merit”. *Phys. Rev. B*, **47**, 12727, 1993.
- [136] L.D. Hicks, T.C. Harman, X. Sun, and M.S. Dresselhaus. “Experimental study of the effect of quantum-well structures on the thermoelectric figure of merit”. *Phys. Rev. B*, **53**, R10493, 1996.
- [137] H. Ohta, S. Kim, Y. Mune, T. Mizoguchi, K. Nomura, S. Ohta, T. Nomura, Y. Nakanishi, Y. Ikuhara, M. Hirano, H. Hosono, and K. Koumoto. “Giant thermoelectric Seebeck coefficient of a two-dimensional electron gas in SrTiO₃”. *Nature Materials*, **6**, 129, 2007.

Appendix A: List of Publications

1. S. Thiel
“Transport Measurements of Oxide Heterostructures”.
Diploma-Thesis, University of Augsburg, 2004
2. A. Weber, C.W. Schneider, S. Hembacher, C. Schiller, S. Thiel, and J. Mannhart
“Transport properties of low angle grain boundaries in $Y_{1-x}Ca_xBa_2Cu_3O_{7-\delta}$ films at high magnetic fields”.
Applied Physics Letters, **88**, 132510, 2006
3. S. Thiel, G. Hammerl, A. Schmehl, C.W. Schneider, and J. Mannhart
“Tunable Quasi-Two-Dimensional Electron Gases in Oxide Heterostructures”.
Science, **313**, 1942, 2006
4. L. Fitting, S. Thiel, A. Schmehl, J. Mannhart and D.A. Muller
”Subtleties in ADF imaging and spatially resolved EELS: A case study of low-angle twist boundaries in $SrTiO_3$ ”.
Ultramicroscopy, **106**, 1053, 2006
5. C.W. Schneider, S. Thiel, G. Hammerl, C. Richter, and J. Mannhart
“Microlithography of electron gases formed at interfaces in oxide heterostructures”.
Applied Physics Letters, **89**, 122101, 2006
6. N. Reyren, S. Thiel, A.D. Caviglia, L. Fitting Kourkoutis, G. Hammerl, C. Richter, C.W. Schneider, T. Kopp, A.-S. Rüetschi, D. Jaccard, M. Gabay, D.A. Muller, J.-M. Triscone, and J. Mannhart
“Superconducting Interfaces Between Insulating Oxides”.
Science, **317**, 1196, 2007
7. A. Schmehl, V. Vaithyanathan, A. Herrnberger, S. Thiel, C. Richter, M. Liberati, T. Heeg, M. Röckerath, L. Fitting Kourkoutis, S. Mühlbauer, P. Böni, D.A. Muller, Y. Barash, J. Schubert, Y. Idzerda, J. Mannhart, and D.G. Schlom
“Epitaxial integration of the highly spin-polarized ferromagnetic semiconductor EuO with silicon and GaN”.
Nature Materials, **6**, 882, 2007
8. C. Cen, S. Thiel, G. Hammerl, C.W. Schneider, K.E. Andersen, C.S. Hellberg, J. Mannhart, and J. Levy
“Nanoscale control of an interfacial metal-insulator transition at room temperature”.
Nature Materials, **7**, 298, 2008
9. A.D. Caviglia, S. Gariglio, N. Reyren, D. Jaccard, T. Schneider, M. Gabay, S. Thiel, G. Hammerl, J. Mannhart, and J.-M. Triscone
“Electric Field Control of the $LaAlO_3/SrTiO_3$ Interface Ground State”.
Nature, **456**, 624, 2008

-
10. S. Thiel, C.W. Schneider, L. Fitting Kourkoutis, D.A. Muller, N. Reyren, A.D. Caviglia, S. Gariglio, J.-M. Triscone, and J. Mannhart
“Electron Scattering at Dislocations in $\text{LaAlO}_3/\text{SrTiO}_3$ Interfaces”.
Physical Review Letters, **102**, 046809, 2009
 11. C. Cen, S. Thiel, J. Mannhart, and J. Levy
“Oxide Nanoelectronics On Demand”.
Science, **323**, 1026, 2009
 12. M. Sing, G. Berner, K. Goss, A. Muller, A. Ruff, A. Wetscherek, S. Thiel, J. Mannhart, S.A. Pauli, C.W. Schneider, P.R. Willmott, M. Gorgoi, F. Schafers, and R. Claessen
“Profiling the Interface Electron Gas of $\text{LaAlO}_3/\text{SrTiO}_3$ Heterostructures by Hard X-Ray Photoelectron Spectroscopy”.
arXiv/0809.1917, Manuscript submitted to *Physical Review Letters*, 2008
 13. M. Salluzzo, G. Ghiringhelli, J.C. Cezar, N.B. Brooks, V. Bisogni, G.M. De Luca, C. Richter, S. Thiel, J. Mannhart, M. Huijben, A. Brinkman, and G. Rijnders
“Orbital Reconstruction and Two-Dimensional Electron Gas at the $\text{LaAlO}_3/\text{SrTiO}_3$ Interface”.
Manuscript submitted to *Physical Review Letters*, 2008
 14. A. Savoia, D. Paparo, P. Perna, Z. Ristic, M. Salluzzo, F. Miletto Granozio, U. Scotti di Uccio, C. Richter, S. Thiel, J. Mannhart, and L. Marrucci
“Polar Catastrophe and Electronic Reconstructions at the $\text{LaAlO}_3/\text{SrTiO}_3$ Interface: Evidence from Optical Second Harmonic Generation”.
Manuscript submitted to *Physical Review Letters*, 2008

Appendix B: Ongoing Projects

Here a brief overview of still ongoing promising projects is given, which were started during this thesis, but have not advanced enough yet to be covered in the main part. As summarized in the tables, many $\text{LaAlO}_3/\text{SrTiO}_3$ samples were grown for the different experiments.

Inductance Measurements

Shashank Shuler-Misra and Prof. Dr. Ali Yazdani from the University of Princeton (USA) are analyzing the inductance of the electron gas at low temperatures, especially in the superconducting state, where information on the superfluid density can be obtained.

Sample Name	Date of Deposition	Substrate Size	d_{LAO}	Contacts
L189	01/23/2008	$10 \times 10 \times 1 \text{ mm}^3$	4 uc	Yes
L206	06/06/2008	$10 \times 10 \times 1 \text{ mm}^3$	8 uc	Yes

Photoemission Studies

Hard X-ray photoelectron spectroscopy (HAXPES) of our $\text{LaAlO}_3/\text{SrTiO}_3$ heterostructures are performed by Götz Berner, Dr. Michael Sing, and Prof. Dr. Ralph Claessen from the University of Würzburg (Germany) to study the valency of Ti at the interface and its spatial distribution.

Sample Name	Date of Deposition	Substrate Size	d_{LAO}	Contacts
L134	06/18/2007	$10 \times 10 \times 1 \text{ mm}^3$	6 uc	No
L145	07/13/2007	$10 \times 10 \times 1 \text{ mm}^3$	10 uc	No
L146	07/17/2007	$10 \times 10 \times 1 \text{ mm}^3$	2 uc	No
L168	11/19/2007	$10 \times 10 \times 1 \text{ mm}^3$	4 uc	No
L179	12/14/2007	$10 \times 10 \times 1 \text{ mm}^3$	2 uc	No
L194	02/11/2008	$5 \times 10 \times 0.5 \text{ mm}^3$	4 uc	Yes
L212	08/27/2008	$5 \times 10 \times 1 \text{ mm}^3$	6 uc	Yes

Electron Holography

Electron holography experiments on our $\text{LaAlO}_3/\text{SrTiO}_3$ samples are done by Dr. Dorin Geiger and Prof. Dr. Hannes Lichte at the Technical University of Dresden (Germany) to study the charge distribution at the interface.

Sample Name	Date of Deposition	Substrate Size	d_{LAO}	Contacts
L188	01/21/2008	$5 \times 10 \times 1 \text{ mm}^3$	5 uc	No
L192	02/04/2008	$5 \times 10 \times 1 \text{ mm}^3$	3 uc	No

Surface X-Ray Diffraction

Stephan Pauli and Philip Willmott from the Paul-Scherrer-Institute in Villigen (Switzerland) use surface X-ray diffraction to determine exactly the atomic structure of LaAlO_3 films on SrTiO_3 .

Sample Name	Date of Deposition	Substrate Size	d_{LAO}	Contacts
L182	01/03/2008	$10 \times 10 \times 1 \text{ mm}^3$	2 uc	No
L183	01/04/2008	$10 \times 10 \times 1 \text{ mm}^3$	5 uc	No
L184	01/07/2008	$10 \times 10 \times 1 \text{ mm}^3$	3 uc	No

Irradiation with He-Ions

The effects of irradiation with He-Ions on the properties of $\text{LaAlO}_3/\text{SrTiO}_3$ samples are studied by Prof. Dr. Wolfgang Lang from the University of Vienna (Austria) and Prof. Dr. Johannes Pedarnig from the University of Linz (Austria).

Sample Name	Date of Deposition	Substrate Size	d_{LAO}	Contacts
L203	04/23/2008	$5 \times 5 \times 1 \text{ mm}^3$	3 uc	Yes
L204	04/25/2008	$5 \times 5 \times 1 \text{ mm}^3$	4 uc	Yes

Appendix C: Danksagung

Besonders bedanken möchte ich mich bei meinem Doktorvater Prof. Dr. Jochen Mannhart, der mich ein spannendes neues Projekt beginnen ließ, das ich hier unter perfekten Bedingungen bearbeiten konnte. Die intensive persönliche Betreuung und stete Diskussionsbereitschaft hat maßgeblich zum Erfolg der Arbeit beigetragen. Speziellen Dank auch für die Möglichkeit der Teilnahme an zahlreichen internationalen Konferenzen.

Prof. Dr. Armin Reller danke ich für die bereitwillige Übernahme des Zweitgutachtens meiner Doktorarbeit.

Un grand merci au Prof. Jean-Marc Triscone pour avoir accepté d'être le rapporteur externe de cette thèse.

Bei unseren Laboringenieuren Dipl. Ing. (FH) Alexander Herrnberger und Dipl. Ing. (FH) Klaus Wiedenmann bedanke ich mich herzlich für die stete Unterstützung bei allen grafischen, fotografischen, (elektro)technischen und sonstigen Problemen.

Danke auch an die "alte Garde" Dr. Christof Schneider, Dr. German Hammerl und Dr. Andreas Schmehl. Ihr habt mich von Anfang an über all die Jahre mit den Anlagen und Laboren vertraut gemacht und wart immer mit Rat und Tat zur Stelle.

Ein ganz spezieller Dank geht an meinen langjährigen Bürokollegen Dipl. Phys. Rainer Held für die tolle Zeit, Gespräche, Überlegungen, Hilfen, Motivationen, usw. die den Raum 286S zu meinem Zuhause am Lehrstuhl gemacht haben.

Stete Unterstützung, spannende Diskussionen zur Mensa-Zeit, helfende Hände, und vieles mehr gab es von allen Mitarbeitern vom Lehrstuhl Experimentalphysik VI. Danke Jungs und Mädels! Ich habe die schöne Zeit mit euch allen sehr genossen.

Bei Prof. Dr. Thilo Kopp möchte ich mich für die geduldigen Erklärungen und Diskussionen bei diversen theoretisch-physikalischen Problemen bedanken.

I benefited from international collaborations with many groups. They all contributed to the success of my thesis. Especially I would like to send a big "Thanks" to

- Prof. Jean-Marc Triscone and his group at the University of Geneva (Switzerland), in particular Nicolas Reyren, Andrea D. Caviglia, and Dr. Stefano Gariglio, for performing the demanding low-temperature measurements.
- Prof. Dave A. Muller and Lena Fitting Kourkoutis at Cornell University (USA) for their fantastic STEM work on the samples.

-
- Prof. Jeremy Levy and Cheng Cen at the University of Pittsburgh (USA) for the great collaboration on patterning by scanning probe.
 - Prof. Ralph Claessen and his group at the University of Würzburg (Germany), in particular Götz Berner and Dr. Michael Sing, for performing detailed HAXPES experiments.
 - Prof. Darrell G. Schlom and his group at Penn State University (USA), for fruitful discussions and the growth of samples by MBE.
 - Prof. Dave H.A. Blank, Dr. Guus J.H.M. Rijnders, Prof. Hans Hilgenkamp, Dr. Alexander Brinkman, Dr. Mark Huijben, and Jeroen Huijben at the University of Twente (Netherlands) for the hospitality and help during my stay at the beginning of my thesis and the collaborations in the years that followed.

Bedanken möchte ich mich auch bei allen Mitarbeitern der feinmechanischen Werkstatt, die mir immer wieder schnell und unkompliziert bei technischen Problemen geholfen haben.

Ein großes “Danke” geht natürlich an meine Familie, die mich während des Studiums und der Promotion optimal unterstützt haben.

Ganz zum Schluss gilt mein besonderer Dank meiner Frau Yvonne, die mir immer wieder geholfen hat meinen vor Physik brummenden Kopf zu beruhigen, mich aufgemuntert hat wenn es nötig war, und einfach stets für mich da war. Deshalb schließe ich meine Doktorarbeit mit folgender, komplett unphysikalischer Feststellung: S♡Y

Appendix D: Curriculum Vitae

Name: Stefan Patrick Thiel
Geburtstag: 30. Mai 1979
Geburtsort: Coburg
Familienstand: verheiratet

Schulbildung:

1985 - 1989 Fröbel-Grundschule Augsburg
1989 - 1998 Holbein-Gymnasium Augsburg
1998 Abitur

Zivildienst:

1998 - 1999 Kompass-Kompakt Drogentherapie Augsburg

Studium:

1999 - 2003 Studium der Physik an der Universität Augsburg
Okt. 2003 - Dez. 2004 Diplomarbeit betreut von Prof. Dr. J. Mannhart
"Transport Measurements of Oxide Heterostructures"
März 2005 Abschluss: Diplom-Physiker (Univ.)

Promotion:

seit Juli 2005 Wissenschaftlicher Angestellter an der Universität Augsburg